Large Magellanic Cloud

Extreme Star Formation In A Low-Metallicity Environment

by

Omnarayani Nayak

A dissertation submitted to The Johns Hopkins University in conformity with the requirements for the degree of Doctor of Philosophy.

Baltimore, Maryland

April, 2018

Abstract

Young stellar objects (YSOs) with high masses (>8$M_\odot$) interact with the interstellar medium (ISM) via accretion and feedback processes on both local and galaxy-wide scales. Massive stars are rare and evolve very quickly, making them difficult to observe. My thesis aims to answer the question: How do massive stars form?

We study the molecular gas observed with ALMA in 30 Doradus, N159, and N79 using dendrograms, a new method that deconstructs the nested hierarchy inherent to the ISM. We find additional YSO candidates missed by initial studies by individually inspecting the spectral energy distribution of the point sources in the ALMA footprints of the three extreme regions. Feedback from turbulence regulates star formation: the energy injected into the ISM can trigger further formation of stars or quench the star formation process. We have measured the contribution of this feedback by comparing size-linewidth relations in 30 Doradus and N159. The size-linewidth relation in 30 Doradus is shifted to higher linewidths for a given clump size in comparison to N159 because of the turbulent feedback and increased star formation

ABSTRACT

activity from the nearly super star cluster (SSC). By looking at where the stars are forming in relation to the molecular gas, we find the gas density necessary to form massive stars in the LMC is at least 500 $M_{\odot}$ pc^{-2}, x5 higher than the gas density necessary to form low-mass stars in the Milky Way.

ALMA observations of H72.97-69.39 in the N79 region of the LMC reveal filaments, outflows, and the first extragalactic detection of a rotating toroid around a cluster. The luminosity of this source is over 2,000,000 $L_{\odot}$, making this one of the most luminous compact source ever discovered. What is this very luminous source? My thesis shows that this object is a embedded early-stage SSC.

This thesis present insights on high-mass star formation in a low-metallicity environment by studying the individual protostars and proto-clusters at high resolution with ALMA.

Primary Reader and Advisor: Dr. Margaret Meixner

Secondary Reader: Dr. Colin Norman

Acknowledgments

I have spent the last 23 years in school and am amazed that it is finally over. It has been a long and tough journey, and would not have been possible without several people in my life. First and foremost, I want to thank my Ph.D. adviser Dr. Margaret Meixner. Margaret's patience in teaching me and her enthusiasm in working on scientific projects with me make her a great instructor. Margaret has opened many academic doors for me in star formation research and sent me around the country and around the world to share my research and form new collaborations. And I am excited to continue to work with her on future JWST observations. I will forever be grateful for her advice on research, life, and everything else in the Universe.

I would also like to thank Dr. Olivia Jones, Dr. Bram Ochsendorf, and Dr. Alec Hirschauer for their support in various collaborative projects as well as reading my postdoctoral job applications. It has been a pleasure to work with them and their words of encouragement as I try to find a job has been invaluable.

ACKNOWLEDGMENTS

My friends Kevin Fogarty and Alice Li have been people I turn to in times of personal difficulties. Whether it is a weekend afternoon or at 2am the day before a major deadline, they always take the time to listen to my gripes and help me work out my problems in research and in life.

I met Gina Quan and Jessica Scholey during my undergraduate studies in California. We all got through impossible problem sets in the dusty old reading room in Le Conte Hall in Berkeley and bonded over our love of food. Coincidentally, we all independently decided to move to the east coast for graduate school and ended up living a few hours away from each other. They are both the kindest and smartest people I have had the privilege of being friends with. And I am always thinking of what next restaurant to eat with them or recipe to make for them.

Sean Jackson, I could not have done this without you. Your unwavering support through the trials and tribulations of graduate school and life in general is beyond what I could ever have dreamed of. You make my life better with your witty humor and endless compassion.

I thank my parents Biranchi and Gitanjali Nayak for their endless support and encouragement. They have both been there for me when I needed it the most. And they have believed in me, even when I did not believe in myself. I also thank my best

friend and quite possibly the best dog that ever lived, Ralph. Somehow he came into my life when I was 14-years-old and always managed to make me smile, on even the worst days of my life.

Dedication

To Papa, Mama, & Ralph.

Contents

List of Tables

List of Figures

Chapter 1

Introduction

1.1 Why Study Massive Star Formation?

The Universe's average star formation rate peaked at 3.5 billion years after the Big Bang (redshift z $\approx$ 2), and was almost ten times higher than the current star formation rate in the Milky Way (Madau & Dickinson, 2014). The few stars that were born and subsequently exploded in the first few billion years of the Universe had only just started to release heavy metals into the local environment. The peak of star formation in the early Universe occurred in a metal-poor environment. It is therefore crucial to understand how massive stars ($M>8_{M_\odot}$) form at low metallicity.

The formation of massive stars has a profound impact on the physical structure and chemical composition of galaxies. Their strong stellar winds and powerful outflows

increase the kinetic energy of surrounding interstellar medium (ISM) (Hopkins et al., 2012). These winds compress and shock gas in the vicinity, triggering further star formation or quenching future star formation. High intensity UV radiation from massive stars ionizes the surrounding and changes the thermodynamic state of the gas. All massive stars die in a supernova explosion (Heger et al., 2003; Smartt et al., 2009; Woosley et al., 2002), which is one of the most energetic phenomena in the Universe and can be as far away as redshift z $\approx$ 3.9 (Cooke et al., 2012). The heavy elements produced in the lifetime of a massive star get expelled out during a supernova, further enriching the ISM and increasing the metallicity content of a galaxy.

The questions my thesis aims to answer are:

1. How do massive stars form?

2. Are there special conditions in certain molecular gas clouds that lead to the formation of massive stars?

3. Is there a previously undiscovered super star cluster in the Large Magellanic Cloud, a satellite galaxy to the Milky Way?

1.2 Three Theories on How Massive Stars Form

There are currently three competing theories on how massive stars form: monolithic collapse (Tan & McKee, 2004; Zinnecker & Yorke, 2007), competitive accretion (Bonnell et al., 2004), and filamentary collision (Inoue & Fukui, 2013). It is possible that all three scenarios occur in nature, dependent on the initial conditions of the cloud in which massive stars form.

Monolithic Collapse: This theory hypothesizes that all the mass that will turn into a star is gathered before the star formation process takes place. Yorke & Sonnhalter (2002) calculate numerically the collapse of massive clumps that are 30 $M_\odot$, 60 $M_\odot$, and 120 $M_\odot$. They assume the massive stars accreting material via accretion disk and take into account the frequency dependence of the opacity. Gas clumps that are originally 30 $M_\odot$, 60 $M_\odot$, and 120 $M_\odot$ form stars that have masses of 13 $M_\odot$, 33.6 $M_\odot$, and 42.9 $M_\odot$. Therefore assuming all the mass in a clump forms a single star, simulations show more massive clumps lead to the formation of a more massive protostar. Recent observational evidence also support stars forming via monolithic collapse. De Buizer et al. (2017) use the Stratospheric Observatory For Infrared Astronomy Massive (SOMA) Star Formation Survey to image with the FORCAST instrument which covers a wavelength range of 10-40μm. Their images show extended mid-infrared and

far-infrared emission along the direction of outflows of the massive protostars with shorter wavelength peak flux positions displaced from the protostar due to extinction, both predictions of the monolithic collapse theory.

Competitive Accretion: In the competitive accretion theory the star's mass depends not only on the parental gas cloud, but also the size (and therefore gravity) of other nearby stars. Local environmental factors (mass of gas cloud, location of star within the cloud) are important, however stars that have initially accreted more mass get even bigger and steal away material from other smaller stars. Similar to the monolithic collapse theory, a more massive gas cloud will lead to the formation of more massive protostars. However, protostars forming at the center of a cluster will have more favorable conditions to grow since the gas will settle into the deepest part of the gravitational potential (i.e. the center). The stars on the outskirts of a cluster will lose out on accreting material because the gas cloud itself will have a greater potential in the center, as well as the stars in the center will have more favorable conditions and therefore be bigger and have a greater gravitational sphere of influence.

Filamentary Collision: Filamentary collisions can compress gas and allow for cores to collapse and form massive stars. NANTEN2, a 4m submillimeter telescope in Chile capable of observing between 2.6mm and 350μm, was used to observe O-stars in the Milky Way to show that massive protostars are forming due to collisions between

clouds (Furukawa et al., 2009). Filamentary collisions have also been observed in the HII region M20 (Torii et al., 2011), super star cluster NGC 3603 (Fukui et al., 2014), and RCW 120 (Torii et al., 2015). Magnetohydrodynamic cloud-cloud collision simulations show molecular gas colliding and creating dense cores in the compressed interface where densities are $>10^4 \mathrm{cm}^{-3}$, one to two orders of magnitude higher than before the collision (Inoue & Fukui, 2013). On larger scales, simulations show filamentary collisions between clouds happen every 10 Myr (Dobbs et al., 2015).

Figure 1.1 shows a cartoon of the current three theories on how massive stars form. The left panel is of monolithic collapse where dense cores are collapsing within a low-density clump. The center panel is of competitive accretion where the cores and competing for material with each other. And the right panel is of filamentary collision which shows a blue-shifted and red-shifted filament, and at the center of this collision is a massive star. These three theories are not mutually exclusive. Different scenarios could be possible depending on initial clump mass conditions, location of a protostar, scale-size being observed, and evolutionary stage of the cloud and the protostar.

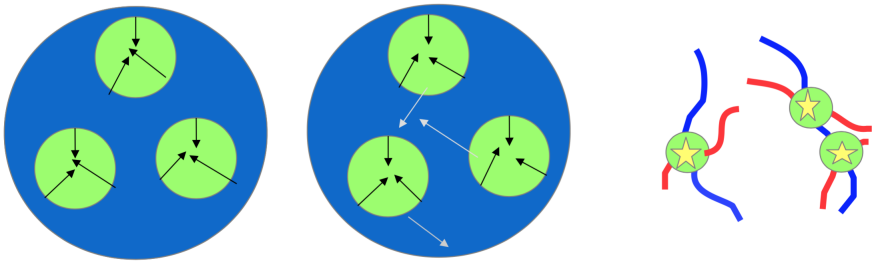

Figure 1.1: Cartoon example of monolithic collapse (left), competitive accretion (middle), and filamentary collision (right).

1.3 Difficulty in Observing Massive Protostars

1.3.1 Observational Difficulties

Even though high mass star formation has impacted the evolution of the Universe on all size scales, their formation process still remains a mystery. High mass star formation is rare and occurs at large distances (>1kpc), which requires high angular resolution observations. Star formation takes place when the protostars are deeply embedded in their parental molecular gas cloud, and the high extinction due to all the gas and dust around the forming star make it impossible to observed this phenomena at optical or near-infrared wavelengths. A high mass protostars takes 10 million years in its early evolution phase until it can be observed in optical wavelengths (no longer obscured by gas and dust), however a low mass star takes 10 billion years to shed its outer parental cloud layers. High mass stars evolve very quickly, making it difficult

to capture the early accretion-phase process.

1.3.2 High-Mass Star Formation is Not Scaled-Up Version of Low-Mass Star Formation

High mass star formation is not a simple scaled up version of low mass star formation. Low mass stars are more abundant than high mass stars (Salpeter, 1955) and several low mass star forming regions lie much closer to the Sun, therefore low mass star formation is better understood than high mass star formation. However, there are more complex physical processes that are associated with high mass star formation. Radiative forces have little to no effect on low mass star formation, however the intense radiation of high mass stars affects the ionization state of the local gas cloud. UV photons of high mass stars can disperse the disks of surrounding low mass stars. Gravitational interactions play a much more important role in high mass star formation. Massive stars can steal material away from local low mass stars (i.e. competitive accretion theory). In addition, massive stars are often found in a small cluster of low mass stars and have a higher companion fraction than smaller mass stars. A third difference between high mass and low mass star formation is that massive stars start burning hydrogen as they are still accreting material in the protostellar phase. However smaller mass stars take up to 30 Myr (three times the timescale for massive stars to be born, accrete material, and stars to be observable in optical wavelengths)

as contracting pre-main sequence stars that have yet to start burning hydrogen.

1.4 The Large Magellanic Cloud

1.4.1 History of Finding Protostars in the Large Magellanic Cloud

Observations of massive star formation in our Galaxy are plagued by distance ambiguities, line of sight confusion, and extinction by dust. Massive star formation is also relatively rare in the solar neighborhood. The lower metallicity Large Magellanic Cloud (LMC, $0.5Z_{\odot}$) is close enough that we can resolve individual star formation sites. Studying massive star formation in the LMC is key to understanding the massive star formation in the low-metallicity early Universe. The distances to the LMC is 50 kpc (Schaefer, 2008) and the galaxy has a face-on orientation. The proximity and orientation allow astronomers to map entire molecular gas clouds with just a few pointings, depending on the specific instrument. The line-of-sight thickness (2.5kpc, Subramanian & Subramaniam (2009)) is thin, allowing observers to associate massive young stellar objects (YSO) to their parental gas cloud with relative certainty. With a complete sample of YSOs in a single galaxy (the LMC), it should be possible to answer questions such as "Where do massive stars form within a gas clump?" or "What is the feedback effect of massive star formation?"

The first extragalactic YSO labelled P1 was discovered by Gatley et al. (1981) in the N159 region of the LMC. They used the 3.9-m Anglo-Australian Telescope and the Infrared Photometer-Spectrometer to image the N159 region in J (1.2 μm), H (2.2 μm), and K (3.5 μm) bands. By comparing the brightness and color of this object to other protostars in the Milky Way, Gatley et al. (1981) determined this was indeed a protostar in the LMC. From the early-1980's to the mid-2000's, only a handful of other protostars were discovered in the LMC and only in the largest giant molecular cloud (GMC) complexes: N160 and N105 (Epchtein et al., 1984), N11 (Walborn & Parker, 1992), and 30 Doradus (Hyland & Jones, 1991; Scowen et al., 1993; Walborn & Blades, 1987). Observing a large sample of protostars as well as observing the parental molecular gas for a statistical sample was observationally inaccessible until recently.

With the *Spitzer* Space Telescope, astronomers were able to map the entirety of the LMC for the first time with parsec-size resolution in the near-infrared and mid-infrared wavelengths. Whitney et al. (2008) used the Surveying the Agents of a Galaxy's Evolution (SAGE) survey (Meixner et al., 2006) and identified point-like sources with excess infrared emission to detect over 1000 YSOs. These protostars are bright in the infrared, and therefore surrounded by a lot of dust that reprocesses the radiation from the central star into the infrared range. Gruendl & Chu (2009) also

analyzed images from the SAGE survey and found almost 1400 YSO candidates in the LMC. These two big papers that found over 1000 massive YSOs used different color-color and color-magnitude selection criteria. The number of YSO candidates in specific regions of the LMC were extended to lower mass protostars in focused studies (Carlson et al., 2012; Romita et al., 2010). The addition of observations from the HERschel Inventory of the Agents of Galaxy Evolution (HERITAGE) more than doubled the number of YSO candidates in the LMC (Seale et al., 2014). The far-infrared wavelengths better constrained the spectral energy distribution (SED) of the embedded protostars. The details of the *Spitzer* and *Herschel* observations are explained in Section 1.4.2. My work on the N159 region (Chapter 2, Nayak et al. (2016)) and 30 Doradus region (Chapter 3, Nayak et al. (2018)) shows that a case-by-case analysis of the *Spitzer* and *Herschel* photometry can increase the number of known YSO candidates by a factor of 2.

1.4.2 Surveys of Protostars in the Large Magellanic Cloud

1.4.2.1 *Spitzer* Space Telescope

SAGE is an unbiased *Spitzer* imaging survey of the LMC, covering a region of 7°x7° (Meixner et al., 2013). The science goals of SAGE include: i) detection of diffuse ISM to examine dust processes, ii) study of evolved stars and how much heavy metals

they shed into the local environment, and iii) early stage YSOs deeply embedded in a molecular gas cloud. Images are taken with the Infrared Array Camera (IRAC) at 3.6 μm, 4.5 μm, 5.8 μm, and 8.0 μm. Images are also taken with the Multiband Imaging Photometer (MIPS) at 24 μm, 70 μm, and 160 μm. Figure 1.2 shows a three-color image with IRAC 3.6 μm (red), IRAC 4.5 μm (green), and MIPS 24 μm (blue). The self-propagating nature of star formation through stellar winds and supernovae (Oey & Massey, 1995), could also lead to the quenching of star formation by dissipating the local ISM (Israel et al., 2003). The unbiased SAGE survey is sensitive to YSOs $>8M_{\odot}$ in various evolutionary stages. The 1000s of YSOs that have been discovered are still currently being analyzed to better characterize their feedback effects on local and galactic scales.

Objects from the IRSF and MCPS have been matched to *Spitzer* IRAC sources using nearest neighbor matching with a 2" search radius because the SAGE point source catalog is based on PSF photometry to the IRAC images Meixner et al. (2006). The initial results of the SAGE survey are described in Meixner et al. (2006).

1.4.2.2 *Herschel* Space Telescope

The HERITAGE survey used the 100μm and 160μm Photodetector Array Camera and Spectrometer (PACS) as well as the 250 μm, 350 μm, and 500 μm on Spectral and Photometric Imaging Receiver (SPIRE) (Meixner et al., 2013). Very early stage

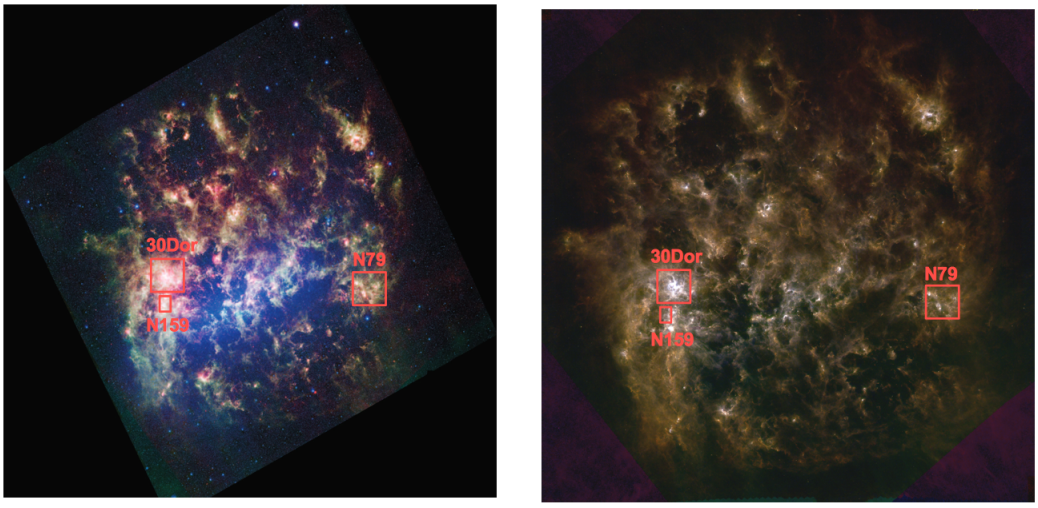

Figure 1.2: Left: *Spitzer* mosaic image of epoch 1 observations: (red) IRAC 3.6 μm, (blue) IRAC 4.8 μm, (green) MIPS 24 μm (Meixner et al., 2006). Right: *Herschel* image of the LMC. Red corresponds to SPIRE 250μm, green to PACS 160μm, blue to PACS 100μm. The location of N159, 30 Doradus, and N79 are boxed in red.

YSO candidates are deeply embedded in cold dust, making the HERITAGE survey crucial in identifying YSO candidates tens of thousands of years old or younger.

Seale et al. (2014) used the cross-band matched catalog between *Spitzer* IRAC/MIPS and *Herschel* PACS/SPIRE point source catalogs to further investigate the dusty objects in the LMC. They first matched *Herschel* PACS/SPIRE point sources to the *Spitzer* MIPS 24μm point source catalog, then bootstrapped the IRAC point sources through the MIPS 24μm matches. If a *Herschel* PACS/SPIRE point source has a MIPS 24μm match, then the photometry of the nearest IRAC source within 1.5" is adopted. *Herschel* PACS/SPIRE point sources are not directly matched to *Spitzer* IRAC point sources due to the difference in angular resolution. Large surveys like

the HERITAGE survey are a necessity for identifying protostars and removing contaminant sources reliably.

1.5 Molecular Gas and YSOs

1.5.1 Molecular Gas Surveys of the LMC

Cohen et al. (1988) were the first to map the CO molecular gas in the LMC. The 6° x 6° coverage of the LMC was taken with the 1.2m Millimeter-Wave Telescope at CITO in Chile. They were able to identify 40 molecular gas clouds with the 8.8' (130 pc) resolution. Observations were taken at a much higher resolution (Israel et al., 1986; Johansson et al., 1994, 1998) with the Swedish-ESO Submillimeter Telescope (SEST). The SEST observations were done at a resolution of 10 pc or better, however they were limited to covering < 1 square degree.

The second complete survey of the LMC was taken with NANTEN (nan=southern in Japanese, ten=heaven or sky in Japnese, Fukui et al. (2008)). The ^{12}CO observations were taken with a 2' resolution and identified 272 different molecular gas clouds in the LMC with a completeness above $5 \times 10^4 M_\odot$. Kawamura et al. (2009) compare the clouds identified by Fukui et al. (2008) to optical and radio HII regions in order to classify the clouds. Type I clouds show no signature of massive star formation; Type II clouds are associated with relatively small HII regions; and Type III clouds

have both HII regions and young stellar clusters. The evolutionary sequence is used to age date the clouds.

The Magellanic Mopra Assessment (MAGMA) survey was limited in total to 3.6 square degrees and only covered known CO clouds detected by NANTEN (Wong et al., 2011). They found a higher CO luminosity increases the likelihood of a YSO being associated with the parental cloud, and more luminous YSOs are more likely to be coincident with CO emission. Ochsendorf et al. (2017a) use the MAGAMA survey to derive star formation properties of 150 star forming clouds in the LMC. They conclude that the most important factor in determining the properties of star forming giant molecular clouds and setting their star formation rates is local stellar feedback, and not global turbulence on large scales.

1.5.2 ALMA - Studying the LMC at Resolution Comparable to Previous Milky Way Studies

This work builds on previous molecular gas studies. We choose three extreme star forming regions previously observed with NANTEN and MAGMA, and follow-up these regions with high resolution observations with the Atacama Large Millimeter Array (ALMA). ALMA uses 54 12m antennas and 12 7m antennas which can observe at frequencies ranging from 31 GHz to 900 GHz. Chapter 2 discusses ALMA observa-

tions of 30 Doradus, Chapter 3 is about ALMA observations of N159, and Chapter 4 shows ALMA observations of the first extragalactic toroid rotating around a potential super star cluster in N79. The sub-arcsecond resolution capabilities (and therefore sub-parsec resolution at distances of the LMC) make this the ideal telescope to study molecular gas comparable to Milky Way molecular gas studies in the past. Massive star formation exclusively takes place on sub-parsec scales and ALMA has revealed the high density cores and filaments in the LMC within which star formation takes place.

1.6 Methods of Analyzing Protostars and Molecular Gas Clouds

1.6.1 Spectral Energy Distribution Fitting

Fitting SEDs involves taking the optical, near-IR, and far-IR photometry and matching it to one of the 200,000 models by Robitaille et al. (2006). These models include 14 parameters: stellar mass, stellar radius, envelope accretion rate, disk mask, total luminosity, and age are just some of the parameters. The parameters cover a wide range of values and all parameters are computed for 10 different viewing angles. The SED fitter does have its limitations. The SED fitter seems to interpret double peaked SEDs that have a large far-IR excess to be a Stage I YSO viewed pole on. As discussed

below, these YSOs may be more evolved than Stage I and hence may show a limitation of using the YSO fitter which assumes the geometric stages more suited to low mass YSOs. Also the resolution of these instruments (20-30" for *Herschel*) means that we are looking at the SED of a small cluster of stars and other dusty objects at distances of the LMC. We are making an assumption that the SED we fit is dominated by a single massive and luminous YSO, and contamination from other sources is negligible.

Lada (1987) divided the protostars in the Milky Way into four different groups based on the shape of of their SEDs: Class 0, Class I, Class II, Class III. Figure 1.3 shows the four stages. Robitaille et al. (2006) determine the 'Stage' of a protostar based on the physical properties of the best fit models to the SEDs: Stage 0/I objects have $\frac{\dot{M}_{env}}{M_{star}} > 10^{-6}$ yr^{-1}, Stage II objects are those that have $\frac{\dot{M}_{env}}{M_{star}} < 10^{-6}$ yr^{-1} and $\frac{M_{disk}}{M_{star}} > 10^{-6}$, and Stage III objects have $\frac{\dot{M}_{env}}{M_{star}} < 10^{-6}$ yr^{-1} and $\frac{M_{disk}}{M_{star}} < 10^{-6}$. These mathematical properties are based on the physical conditions as the protostar goes through its evolutionary sequence. A protostar begins to form with the collapse of a core, at which point it is a Stage 0 object. Once formed, the protostar accretes material via a rotating disk which accreted material from an outer envelope (Stage I). Bi-polar outflows perpendicular to the disk are often observed with Stage I protostars. It is difficult to observe Stage 0 protostars since they are short-lived, therefore oftentimes Stage 0 and Stage I get grouped into one classification: Stage 0/I. Strong winds from the central protostar will eventually slow down the accretion process and sometimes there

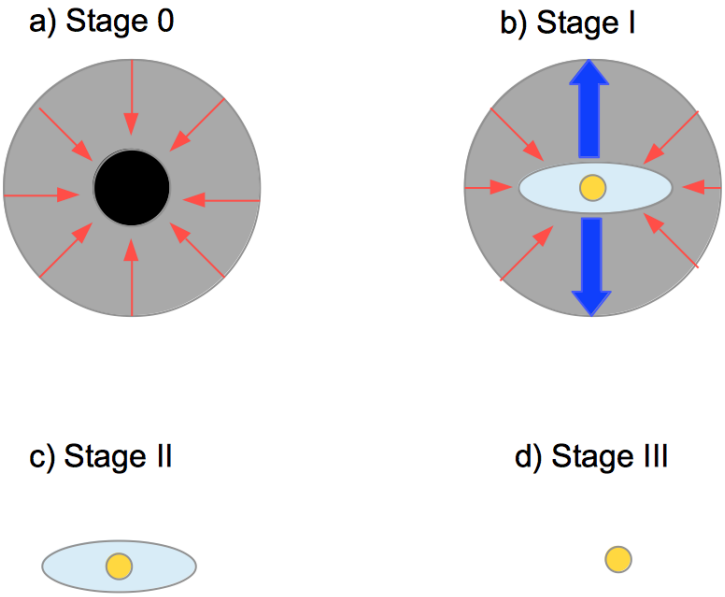

Figure 1.3: a) A core is collapsing to form a Stage 0 protostar. b) At Stage I a protostar is surrounded by a disk, which is surrounded by an outer envelope. There are also bi-polar jets. c) Winds and high intensity radiation has blown away the outer envelope. Sometimes a thin disk remains at Stage II. d) The protostar has shed all its outer layers and is visible at optical wavelengths.

is evidence of a disk around the young star during Stage II. Eventually the accretion process will come to a complete stop and winds will blow away what is remaining of the original accretion disk at Stage III, at which point the star will be visible in optical wavelengths.

1.6.2 Dendrogram Algorithm

The molecular cloud structure determines where star formation occurs and the mass distribution of stars in a cluster. Molecular cloud sizes range several orders of magnitudes: high density parsec size clumps are nested within larger low density clumps that span several tens of parsecs (Lada, 1992). We use dendrograms (Rosolowsky et al., 2008) as a way to study the hierarchical structure of the ^{12}CO (2-1) and ^{13}CO (2-1) emission from molecular clouds in Chapters 2 and 3. We define clumps to mean any entity that is bound by an iso-intensity surface. Dendrogram algorithms look for the largest scale sizes first and then for smaller clumps embedded within the larger ones. The dendrogram of a position-position-velocity (PPV) data cube is a way to keep track of the iso-intensity surfaces over a range of size scales. If the intensities of a structure are not contiguous, then this structure is split into separate entities. The low-density gas is represented at the bottom of the hierarchical structure in a dendrogram, the starting branch of the structure. This branch connects to other branches and leaves that represent smaller and denser clumps embedded in the low-density media. The leaves and branches correspond to the different volumes in the data cube bounded by a given isosurface level.

Dendrogram method is different than previous studies, such as CLUMPFIND (Williams et al., 1994), which look at individual clumps and not nested structures. CLUMPFIND cannot define structures that are inside another. When you have a

crowded molecular gas structure, CLUMPFIND tends to cut apart features that are part of a single entity. Dendrogram allows us to understand how, where, and why denser objects are nested inside a lower-density gas. Figure 1.4 shows a cartoon cloud (top panel) and the resulting dendrogram structure (bottom panel). The higher density gas embedded in the lower density gas is broken down in a tree-like structure with the dendrogram algorithm.

The *astrodendro* program uses what is known as the clipping method to calculate clump properties from a 2D image or a 3D data cube. The clipping method only accounts for emission above a contour level to be associated with an object, as oppose to extrapolating down to a zero intensity isosurface. The user has to input the minimum value to be considered in the data set, the threshold value that determines if a leaf will be a single entity or not, and the minimum number of pixels for a leaf to be considered a single entity. The larger branch breaks down into leaves depending on the three input criteria. The *astrodendro* program outputs the total integrated luminosity of an isosurface (a.k.a. clump), the linewidth (v_{RMS}) of the clump, and the area of the clump, the effective radius of the clump, and the orientation angle of the clump. These properties can be used to calculate relevant astrophysical properties such as the column density or mass.

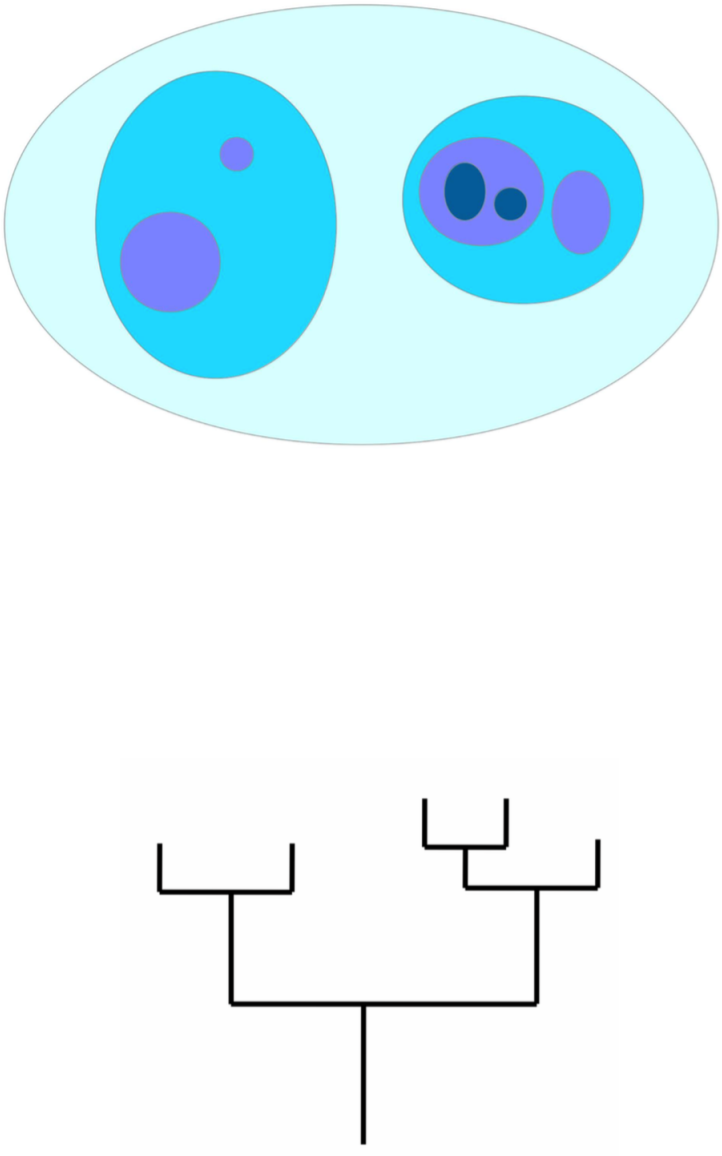

Figure 1.4: Top: Cartoon example of a gas cloud. The largest structure represents the low level emission. The smallest clumps represents high density cores in which star formation is possible. Bottom: The dendrogram tree structure of the cartoon clump. As the clump breaks down into smaller and more dense cores, the dendrogram tree structure splits accordingly.

1.7 Dissertation Overview

We strive to understand how massive stars form. In doing so we observe massive protostars in many different wavelength regimes and try to connect observations to models. The three massive star formation regions in the LMC that are part of my thesis include 30 Doradus, N159, and N79. These three regions have extreme star forming conditions: R136 super star cluster (SSC) at the heart of 30 Doradus, high intensity CO emission observed in N159 indicates this region could potentially turn into a SSC (Minamidani et al., 2008), and an overdensity of YSOs in N79 and increase in star formation rate (SFR) in N79 also signs this region can also become a SSC (Ochsendorf et al., 2017b). Massive star formation requires extreme densities, shocks, and turbulent conditions. Such conditions are often found in SSCs. Recent studies show that very massive stars form via filamentary collision (Fukui et al., 2015; Nayak et al., 2016) and even stellar collisions (Zinnecker & Yorke, 2007). These formation processes only become viable in dense (high gas density and high stellar density) environments which are inherent to SSCs. The plethora of O stars in SSCs make such clusters an ideal location to study massive star formation. However SSCs are rare, and finding one that is just at its early formation stages in rarer. My thesis aims to study massive star formation near currently known SSCs (R136 in 30 Doradus) and star formation in what could potentially be the next 30 Doradus (N159 and N79).

Chapter 2 described the analysis of high-mass YSOs and low-mass pre main sequence

(PMS) stars in the 30 Doradus region, about 10 kpc away from the central R136 SSC. For this region we use HST observations in addition to *Spitzer* and *Herschel* observations. We find 4 new YSO candidates in the region by fitting SEDs to the SAGE point sources in the ALMA footprint of the region. The high-resolution ALMA images reveal that high-mass stars are associated with clumps with higher masses and mass densities. Often the low-mass PMS stars are not associated with any visible molecular gas.

Chapter 3 we apply the method of finding new YSOs from the previous chapter to N159 West (N159W) and N159 East (N159E). We find 6 new YSO candidates in N159W and 4 new candidates in N159E. Both N159 and 30 Doradus are extreme star forming environments, however the proximity of the SSC in 30 Doradus adds to the turbulence of the region. This additional turbulence is evident in the linewidths (proportional to the kinetic energy) of the clumps. We also find that high mass star formation in the LMC forms in gas x5 more dense that low-mass star formation in the Solar Neighborhood.

In Chapter 4, we discuss potential SSC H72.97-69.39 in the N79 region of the LMC. Figure 1.5 shows the SED of this luminous source. This region appears to be a younger and more embedded twin of 30 Doradus, with both regions lying at the tips of tidal arms (see Figure 4.1). The molecular gas is filamentary on large scales (20-50pc)

and on small scales (< 1-3 pc). ALMA observations show the different kinematics involved in the formation of this potential SSC. We find colliding filaments, bi-polar outflows, a photodissociation region (PDR), and a rotating toroid associated with this object.

We use ALMA observations to study the molecular gas properties in three extreme star forming regions in the LMC. We have measured the contribution of turbulent feedback by comparing size-linewidth relations in 30 Doradus (location of the R136 SSC) and N159 (one of the most massive giant molecular clouds in the LMC that can potentially become a SSC). We identify new massive YSOs in the ALMA footprints and compare our observations to analytical models (Krumholz et al., 2005) to show very massive stars are more likely forming via monolithic collapse, and not via competitive accretion. We anticipate our new approach in findings YSOs will profit future studies on massive star formation in the Large Magellanic Cloud. Our observations of ^{12}CO and ^{13}CO molecular gas (ALMA) show the presence of a rotating toroid around potential SSC H72.97-69.39, making this the first time such a structure has been detected outside the Milky Way.

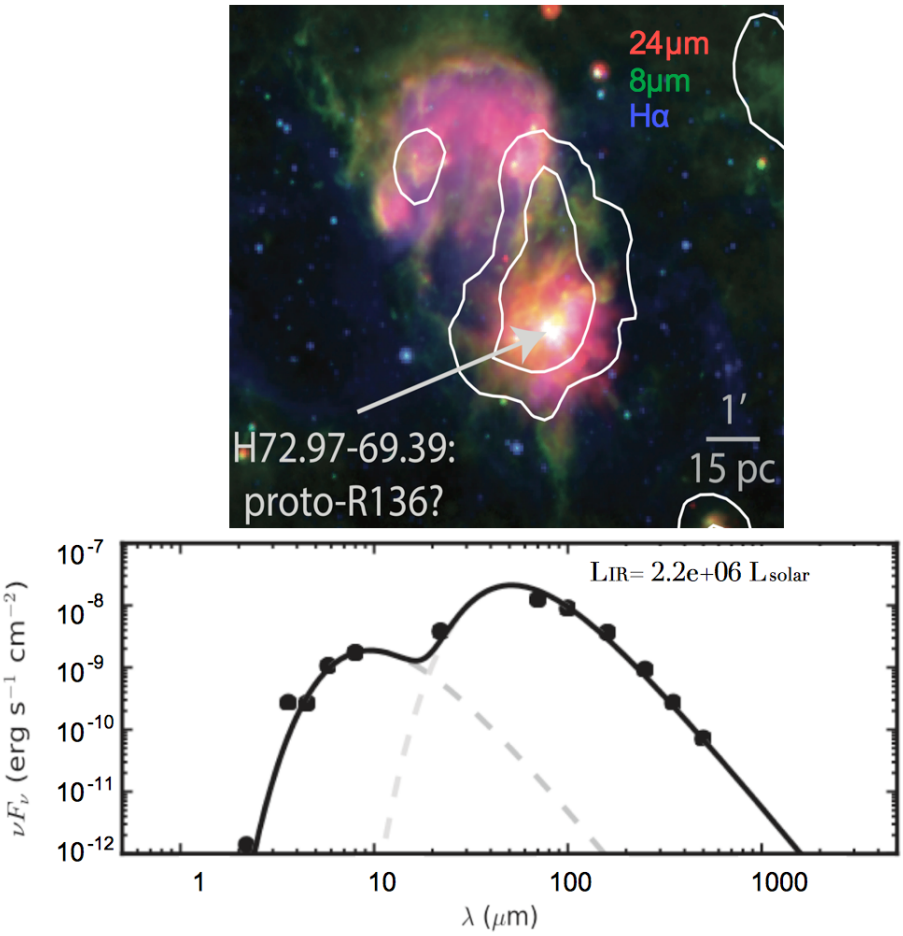

Figure 1.5: Top: Three color image of the proto-SSC H72.97-69.39. Bottom: The SED of the proto-SSC shows the luminosity of this source is greater than 2,000,000$L_{\odot}$ (Ochsendorf et al., 2017b).

Chapter 2

Massive Protostars and Molecular Clumps in 30 Doradus

Abstract

We present ^{12}CO and ^{13}CO molecular gas data observed by ALMA, massive early stage young stellar objects identified by applying color-magnitude cuts to *Spitzer* and *Herschel* photometry, and low-mass late stage young stellar objects identified via Hα excess. Using dendrograms, we derive properties for the molecular cloud structures. This is the first time a dendrogram analysis has been applied to extragalactic clouds. The majority of clumps have a virial parameter equal to unity or less. The size-linewidth relations of ^{12}CO and ^{13}CO show the clumps in this study have a larger linewidth for a given size (by factor of 3.8 and 2.5, respectively) in comparison to

several, but not all, previous studies. The larger linewidths in 30 Doradus compared to typical Milky Way quiescent clumps are probably due to the highly energetic environmental conditions of 30 Doradus. The slope of the size-linewidth relations of ^{12}CO, 0.65 $\pm$ 0.04, and ^{13}CO, 0.97 $\pm$ 0.12, are on the higher end but consistent within 3σ of previous studies. Massive star formation occurs in clumps with high masses ($>1.83 \times 10^2$ M$_\odot$), high linewidths (v $>$1.18 km/s), and high mass densities ($>6.67 \times 10^2$ M$_\odot$ pc^{-2}). The majority of embedded, massive young stellar objects are associated with a clump. However the majority of more evolved, low-mass young stellar objects are not associated with a clump.

2.1 Introduction

The 30 Doradus region, a.k.a. the Tarantula Nebula, provides a unique opportunity to study star formation over a range of masses and its feedback on the environment. 30 Doradus is one of the most active star formation regions in the Magellanic Clouds and the only Giant HII region in the Local group. At the heart of 30 Doradus is R136, the super star cluster with extraordinarily high stellar densities of $>1.5 \times 10^4 - 10^7$ M$_\odot$ pc^{-3} (Selman & Melnick, 2013), containing the most massive stars known (Crowther et al., 2010). Combining data from the *Spitzer* SAGE survey (Meixner et al., 2006), the *Herschel* Heritage survey (Meixner et al., 2013), and the Hubble Tarantula Treasury Project (HTTP) (Sabbi et al., 2013, 2016) we can study

young and massive YSOs and low-mass and more evolved YSOs over the bulk of the mass function ($0.5 - 35$ $M_\odot$). Studying both low-mass and high-mass stars that are located in the same low-metallicity region can shed some light on the conditions necessary for star formation to occur.

The 30 Doradus region has been previously investigated in the tracers of the interstellar medium (ISM) that fuel the star formation. The dust content has been measured and quantified with the analysis of *Spitzer* SAGE (Meixner et al., 2006) and *Herschel* HERITAGE (Meixner et al., 2013) surveys by Gordon et al. (2014). ^{12}CO (1-0) has been imaged as part of whole LMC surveys at 2.6′ with NANTEN (Fukui et al., 2008) and at 45″ with MOPRA (Wong et al., 2011). ^{12}CO (1-0), (2-1), and (3-2) have been observed in 30 Doradus by SEST (Johansson et al., 1998).

ALMA observations of ^{12}CO (2-1), ^{13}CO (2-1), and C^{18}O (2-1) clumps have been analyzed by Indebetouw et al. (2013). The CO observed in 30 Doradus is very clumpy, similar to that observed in the Milky Way. Analysis of the ALMA data shows a decrease in ^{12}CO (2-1) emission relative to the total gas mass compared to massive star formation regions in the Milky Way, consistent with theory: there is less shielding in a lower-metallicity environment and ^{12}CO (2-1) is not well shielded in comparison to H_2 gas. High density gas tracers such as HCN (1-0) and HCO^+ (1-0) show clumps in 30 Doradus have similar, but slightly larger linewidths than other regions in the

LMC (Anderson et al., 2013). The physical conditions of the gas surrounding the R136 cluster have previously been constrained with ionized gas models (Indebetouw et al., 2009; Lopez et al., 2011; Pellegrini et al., 2011). Indebetouw et al. (2009) find photodissociated regions (PDRs) dominate over collisional excitation of shocks and that the effects of local hot stars play a more important role in shaping the gas chemistry than large scale trends with distance from the R136 cluster. The hot gas in 30 Doradus may be leaking out of the pores of the HII shells, since the X-ray gas pressure is measured to be much weaker than the radiation pressure (Lopez et al., 2011). H_2 gas correlates well with Brγ and CO in the region, implying that the H_2 gas comes from PDRs (Yeh et al., 2015). Further work on PDR modeling has been done by Chevance et al. (2016) who find 90% of [CII] emissions originates from PDRs and 70% of the far infrared luminosity is associated with the ionized gas component. Chevance et al. (2016) conclude that the gas in 30 Doradus is very porous and dominated by photoionization.

Our goal in this chapter is to conduct a thorough investigation of early stage massive YSOs and later stage low-mass YSOs, and their relation to the clump structure of ^{12}CO (2-1) and ^{13}CO (2-1) molecular gas. This comprehensive study of high-mass and low-mass star formation with multi wavelength photometric and spectroscopic observations of molecular gas and dust will help shed light on the physical conditions necessary for high-mass star formation to take place. In Section 2.2 we describe the

observations we use in more detail. In Section 2.3 we describe the results of the dendrogram program we use to study the hierarchical structure of the clumps. In Section 2.4 we describe the YSOs in the study in more detail. In Section 2.5 we discuss the trends we see in molecular gas and how the how star formation is affected by the distribution of molecular gas. Lastly we present our conclusions in Section 2.6.

2.2 Observations

2.2.1 *Spitzer* Surveying the Agents of Galaxy Evolution (SAGE) and *Herschel* HERschel Inventory of the Agents of Galaxy Evolution (HERITAGE) Surveys

We use the *Spitzer* SAGE (IRAC 3.6 μm, 4.5 μm, 5.8 μm, 8.0 μm bands / MIPS 24 μm, 70 μm, 160 μm bands) and *Herschel* HERITAGE (PACS 100 μm, 160 μm bands / SPIRE 250 μm, 350 μm, 500 μm bands) surveys as described in Section 1.4. Several massive YSO candidates we use in this work have previously been studied by Whitney et al. (2008), Gruendl & Chu (2009), Carlson et al. (2012), and Seale et al. (2014) who used the *Spitzer* SAGE (Meixner et al., 2006) and *Herschel* Heritage (Meixner et al., 2013) surveys.

2.2.2 Hubble Tarantula Treasury Project (HTTP)

HTTP is a survey of stellar populations in 30 Doradus that reaches into the sub-solar mass regime (<0.5 $M_{\odot}$) (Sabbi et al., 2013, 2016). The survey includes optical (F555W and F658N with ACS and WFC), infrared (F110W and F160W with WFC3 and IR), and ultraviolet (F257W and F336W with WFC3 and UVIS). In addition, archival monochromatic survey in the F775W filter was used (realized using ACS/WFC and WFC3/UVIS in parallel). HTTP covers a projected area of 14' x 12' in the sky. We focus on the late-stage, low-mass, and more evolved YSOs (Sabbi et al., 2016) that are located within the 30 Doradus ALMA footprint (Indebetouw et al., 2013).

2.2.3 ALMA ^{12}CO (2-1) and ^{13}CO (2-1) Observation

ALMA allows us to resolve giant molecular clouds (GMCs) at the distance of the LMC with comparable resolution as HST, as well as provides us with high spectral resolution data. The frequency axis of the data is converted to velocity and results in a position-position-velocity (PPV) cube. The ALMA Cycle 0 footprint of 30 Doradus is a small region north of R136 and has been mapped with ^{12}CO (2-1), ^{13}CO (2-1), C^{18}O, and H30α (Indebetouw et al., 2013). Indebetouw et al. (2013) analyze the PPV data cubes and calculate mass, velocity, and size of the clumps. Figure 2.1a shows the HST F160W in greyscale, ALMA+APEX ^{13}CO (2-1) in contour, and the location of

the low-mass YSOs. Figure 2.1b shows the HST F160W in greyscale, ALMA+APEX ^{13}CO (2-1) in contour, and the location of point sources from the SAGE catalog that are in the ALMA footprint. We use the ALMA Cycle 0 combined with APEX single dish observations of ^{12}CO (2-1) and ^{13}CO (2-1) made by Indebetouw et al. (2013) in our analysis.

2.3 Results from Dendrogram Analysis

The most dominant molecular species in the ISM is H_2. Unfortunately H_2 does not have any dipole moment, all of the low energy transitions are quadrupole transitions with small transition probabilities and high excitation energies. This means that the H_2 is excited at high temperatures or in the vicinity of strong ultraviolet radiation. The most abundant molecule in the ISM is invisible to direct observation since the majority of ISM conditions cannot excite it. The second most abundant molecule in the ISM is CO and is frequently used to estimate the H_2 gas mass via a conversion factor. Leroy et al. (2011) find the $^{12}\mathrm{CO}-\mathrm{to}-\mathrm{H_2}$ conversion factor (or the X-factor) in the LMC to be $3-9$ $\mathrm{M_\odot\ pc^{-2}\ (K\ km\ s^{-1})^{-1}}$ in the local group which includes: M21, M33, the LMC, NGC 6822, and the SMC. The $\mathrm{M_{mol}/F(^{12}CO\ 1-0)}$ X-factor of 30 Doradus is higher than the average X-factor in the LMC: Indebetouw et al. (2013) compare the calculated molecular mass to the ^{12}CO (2-1) intensity and find that the X-factor is 12 ± 4 $\mathrm{M_\odot\ pc^{-2}\ (K\ km\ s^{-1})^{-1}}$. We calculate the brightness

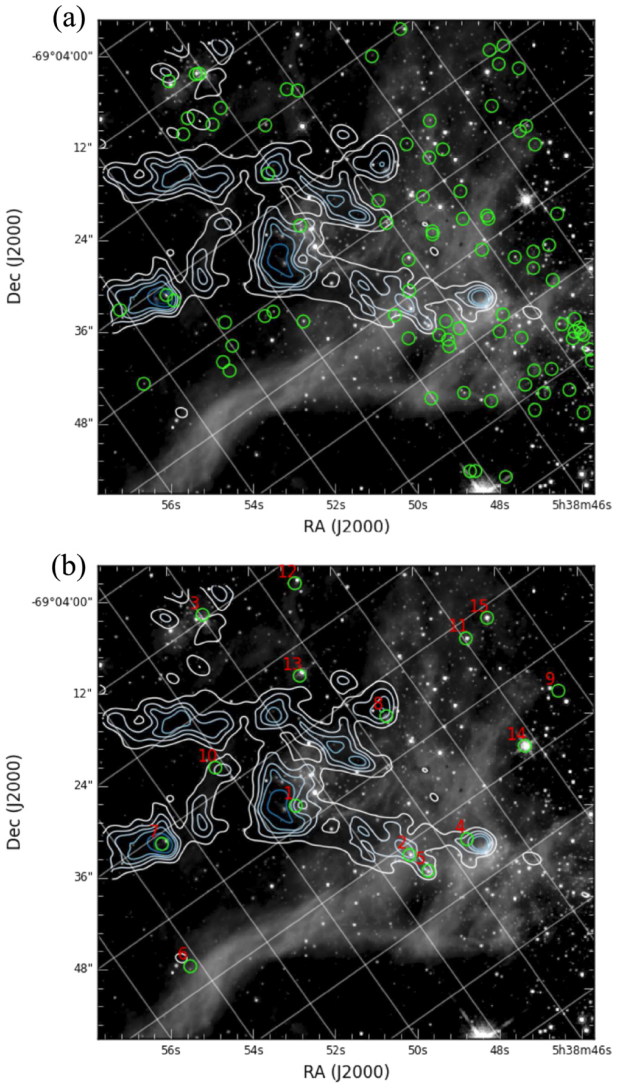

Figure 2.1: **ALMA + HST image of 30 Doradus** Top: HST F160W in greyscale, ALMA+APEX ^{12}CO (2-1) in contour (contour levels signify 10%, 20%, 30%, 40%, 60%, and 80% of peak integrated flux), and the location of more evolved low-mass YSOs (as discussed in section 2.4.1) in green circles . North is to the upper-left in this figure. Bottom: HST F160W in greyscale, ALMA+APEX ^{12}CO (2-1) in contour (contour levels signify 10%, 20%, 30%, 40%, 60%, and 80% of peak integrated flux), and the location of all point sources in the SAGE catalog in green circles. Numbers 1-10 are massive YSO candidates (as discussed in section 2.4.2), and number 11-15 are SAGE point sources in the footprint we do not consider to be YSOs. The number near the YSO candidates indicates rank in mass (1 is the most massive YSO candidate and 10 in the least massive YSO candidate).

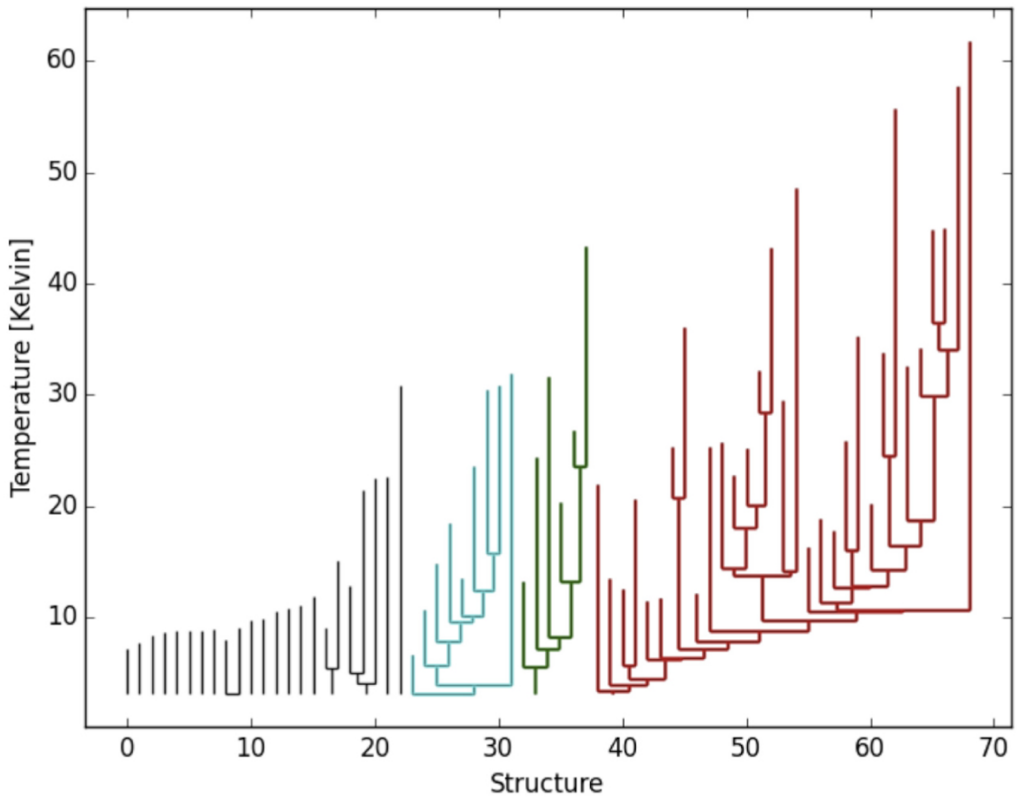

Figure 2.2: **Dendrogram Representation of 12CO** Dendrogram hierarchy of ^{12}CO (2-1) brightness temperature. The trunks represent the lowest lever of emission. The trunks are connected to leaves, which represent higher emission clumps.

temperature integrated over the velocity for ^{12}CO (2-1) and use a X-factor of 12 ± 4 $M_\odot$ pc^{-2} (K km s^{-1})$^{-1}$. The total mass of all dendrogram branches in Figure 2.2 is $1.3 \pm 0.4 \times 10^5$ $M_\odot$. Table 2.1 lists the mass of the ^{12}CO (2-1) clumps.

Table 2.1: Mass Derived from ^{12}CO (2-1)

Clump ID	RA	Dec	Radius [pc]	$F_{^{12}CO}$ [K km s^{-1}]	Total Mass [$M_\odot$]	Linewidth [km/s]
0	84.706989	-69.068853	0.522	21.2 ± 2.55	321 ± 38.6	1.29
1	84.700807	-69.078029	4.61	137 ± 17.5	98900 ± 12600	3.86

Continued on next page

Table 2.1 – continued from previous page

Clump ID	RA	Dec	Radius [pc]	$F_{^{12}CO}$ [K km s^{-1}]	Total Mass [$M_\odot$]	Linewidth [km/s]
2	84.700775	-69.078057	4.59	139 ± 17.2	97300 ± 12100	3.83
3	84.700755	-69.078118	4.57	143 ± 16.7	93700 ± 10900	3.74
4	84.703518	-69.069242	0.457	23.2 ± 2.23	271 ± 26.1	2.18
5	84.700788	-69.078107	4.57	144 ± 16.4	90800 ± 10300	3.69
6	84.703853	-69.071507	0.454	47.2 ± 2.42	647 ± 33.2	2.44
7	84.700814	-69.078139	4.55	148 ± 15.5	83100 ± 8710	3.58
8	84.700823	-69.078138	4.55	148 ± 15.5	83400 ± 8740	3.59
9	84.698556	-69.079379	4.03	151 ± 13.5	63900 ± 5750	3.35
10	84.698567	-69.079381	4.02	151 ± 13.2	61700 ± 5390	3.3
11	84.698536	-69.079390	4.01	152 ± 12.8	58300 ± 4910	3.24
12	84.694103	-69.077254	2.25	148 ± 7.42	19100 ± 958	3.87
13	84.699955	-69.072633	0.287	27 ± 1.47	137 ± 7.45	1.04
14	84.699347	-69.075175	0.497	158 ± 2.40	2130 ± 32.4	3.41
15	84.696479	-69.077376	1.28	153 ± 5.07	9170 ± 304	4.43
16	84.707331	-69.071393	0.298	46.8 ± 1.54	261 ± 8.59	1.62
17	84.699810	-69.069712	1.54	53.6 ± 6.60	5440 ± 669	2.81
18	84.698967	-69.069816	1.36	61.7 ± 5.43	4240 ± 373	2.65
19	84.697151	-69.069254	0.257	35.5 ± 1.31	141 ± 5.21	1.17
20	84.693634	-69.080124	0.337	20.2 ± 1.71	138 ± 11.7	0.991
21	84.697258	-69.079987	0.273	13.7 ± 1.38	60.7 ± 6.11	0.535
22	84.710057	-69.073121	1.38	144 ± 6.82	15600 ± 738	2.18
23	84.695760	-69.082149	0.471	35.4 ± 2.23	411 ± 25.9	1.07
24	84.696537	-69.081386	0.243	21.7 ± 1.19	71.1 ± 3.89	0.511
25	84.689353	-69.081503	0.872	30.1 ± 3.26	749 ± 81.1	0.908
26	84.689385	-69.082348	0.338	34.7 ± 1.79	259 ± 13.4	0.683
27	84.700869	-69.080518	2.68	156 ± 10.0	36600 ± 2350	2.76
28	84.695538	-69.082384	0.311	45.4 ± 1.60	271 ± 9.55	0.84
29	84.702396	-69.079943	2.26	161 ± 9.11	31000 ± 1770	2.73
30	84.689291	-69.080981	0.526	29.7 ± 2.39	396 ± 31.9	0.803
31	84.688452	-69.081129	0.337	32.9 ± 1.76	237 ± 12.7	0.712
32	84.709587	-69.073393	0.864	159 ± 3.63	4900 ± 112	1.76
33	84.700921	-69.080487	2.66	159 ± 9.71	35100 ± 2140	2.70
34	84.702480	-69.079910	2.24	159 ± 9.00	30100 ± 1710	2.71
35	84.701184	-69.082238	0.715	71.3 ± 2.93	1440 ± 59.2	1.47
36	84.700356	-69.082942	0.372	62.3 ± 1.75	446 ± 12.5	0.541
37	84.702569	-69.079872	2.20	162 ± 8.61	27900 ± 1480	2.64
38	84.695010	-69.075487	0.358	24.8 ± 1.58	144 ± 9.17	1.70
39	84.700337	-69.069687	1.72	47 ± 7.23	5730 ± 881	2.75
40	84.691066	-69.080654	0.261	26.3 ± 1.30	103 ± 5.09	0.63

Continued on next page

Table 2.1 – continued from previous page

Clump ID	RA	Dec	Radius [pc]	$F_{^{12}CO}$ [K km s^{-1}]	Total Mass [$M_\odot$]	Linewidth [km/s]
41	84.699043	-69.069825	1.33	66.3 ± 4.67	3370 ± 237	1.77
42	84.701829	-69.081685	0.381	68 ± 1.78	502 ± 13.1	0.903
43	84.708896	-69.079471	0.229	26.1 ± 1.13	77.4 ± 3.35	0.606
44	84.719623	-69.076736	1.73	146 ± 8.61	25300 ± 1490	3.54
45	84.715952	-69.071826	0.38	58.4 ± 1.56	332 ± 8.67	0.829
46	84.699158	-69.069782	1.32	65.3 ± 4.22	2710 ± 175	1.50
47	84.692969	-69.085462	0.202	29.9 ± 0.97	66.1 ± 2.14	0.451
48	84.688529	-69.085050	0.621	148 ± 3.26	3670 ± 80.9	1.59
49	84.693965	-69.084531	0.181	33.2 ± 0.84	54.4 ± 1.38	0.361
50	84.702648	-69.079743	2.18	174 ± 8.08	26400 ± 1230	2.28
51	84.719989	-69.076724	1.62	174 ± 7.41	22300 ± 949	3.41
52	84.720925	-69.076775	1.31	201 ± 6.44	19300 ± 621	3.30
53	84.693749	-69.082392	0.171	36.5 ± 0.85	62.1 ± 1.45	0.941
54	84.702724	-69.079712	2.16	175 ± 7.79	24700 ± 1090	2.21
55	84.704743	-69.078626	1.22	211 ± 5.87	16900 ± 471	2.34
56	84.721886	-69.076712	1.08	225 ± 5.57	16300 ± 404	3.17
57	84.715112	-69.070094	0.295	36.3 ± 1.53	201 ± 8.47	0.973
58	84.699190	-69.069651	1.34	63 ± 3.74	2040 ± 121	1.06
59	84.699174	-69.069684	1.35	60.6 ± 3.92	2170 ± 141	1.06
60	84.698488	-69.069178	0.919	70.0 ± 2.7	1190 ± 45.9	1.10
61	84.696900	-69.082925	1.02	115 ± 4.56	5590 ± 222	1.36
62	84.704867	-69.078592	1.15	221 ± 5.39	15100 ± 368	2.31
63	84.695507	-69.078140	0.954	151 ± 4.33	6540 ± 189	2.07
64	84.721953	-69.076703	0.987	242 ± 4.84	13300 ± 266	2.95
65	84.710659	-69.069206	0.731	13.3 ± 2.98	277 ± 62.1	1.08
66	84.696763	-69.069577	0.423	64.1 ± 1.85	511 ± 14.7	1.03
67	84.695439	-69.084713	0.202	90.3 ± 0.990	206 ± 2.26	0.645
68	84.705060	-69.078616	0.95	203 ± 4.18	83100 ± 1710	2.01
69	84.700879	-69.068490	0.321	71.6 ± 1.46	359 ± 7.32	0.949
70	84.705644	-69.078739	0.634	235 ± 3.07	5170 ± 67.5	1.34
71	84.695601	-69.078200	0.798	147 ± 3.60	4440 ± 109	1.94
72	84.695392	-69.078432	0.688	150 ± 3.08	3310 ± 67.9	1.87
73	84.700724	-69.070683	0.419	48.6 ± 2.05	477 ± 20.1	0.769
74	84.721433	-69.076804	0.704	248 ± 3.45	6870 ± 95.6	2.45
75	84.688778	-69.077411	0.932	131 ± 4.09	5110 ± 159	1.24
76	84.690076	-69.075857	0.328	83.4 ± 1.59	490 ± 9.34	1.11
77	84.697577	-69.070949	0.179	17.5 ± 0.820	27.7 ± 1.29	0.263
78	84.704109	-69.068918	0.501	37.7 ± 2.73	657 ± 47.6	1.13
79	84.681270	-69.089642	0.273	36.3 ± 1.39	163 ± 6.24	1.18

Continued on next page

Table 2.1 – continued from previous page

Clump ID	RA	Dec	Radius [pc]	$F_{^{12}CO}$ [K km s^{-1}]	Total Mass [$M_\odot$]	Linewidth [km/s]
80	84.683899	-69.087016	0.414	54.4 ± 2.32	681 ± 29.1	1.00
81	84.696870	-69.082978	0.758	109 ± 3.34	2810 ± 86.1	0.993
82	84.688625	-69.077588	0.751	142 ± 3.70	4530 ± 118	1.21
83	84.714477	-69.077183	0.61	103 ± 3.10	2310 ± 69.5	1.66
84	84.681043	-69.088247	0.272	25.6 ± 1.41	118 ± 6.49	0.951
85	84.692264	-69.083296	0.211	33.6 ± 0.990	76.6 ± 2.26	0.413
86	84.701799	-69.079815	0.332	68.9 ± 1.54	384 ± 8.58	0.571
87	84.692210	-69.079778	0.184	52.7 ± 0.840	86.7 ± 1.38	0.495
88	84.698923	-69.070512	0.253	39.4 ± 1.24	142 ± 4.47	0.614
89	84.696715	-69.069817	0.209	19.9 ± 1.04	50.3 ± 2.63	0.357
90	84.692520	-69.083699	0.278	35.7 ± 1.36	154 ± 5.87	0.529
91	84.697617	-69.076296	0.218	78.5 ± 1.03	194 ± 2.54	0.814
92	84.703864	-69.079984	0.162	66.4 ± 0.750	88.1 ± 0.995	0.494
93	84.711315	-69.080377	0.322	9.25 ± 1.57	53.1 ± 9.01	0.403
94	84.694719	-69.079030	0.306	166 ± 1.48	851 ± 7.59	0.976
95	84.710370	-69.079071	0.311	36.2 ± 1.54	201 ± 8.55	0.492
96	84.702161	-69.078375	0.455	85.9 ± 1.99	793 ± 18.4	0.842
97	84.703010	-69.078498	0.251	82.0 ± 1.19	271 ± 3.93	0.422
98	84.696271	-69.077918	0.194	68.2 ± 0.890	125 ± 1.63	0.469
99	84.724458	-69.075500	0.165	40.9 ± 0.770	56.9 ± 1.07	0.361
100	84.701233	-69.078210	0.284	63.6 ± 1.25	233 ± 4.58	0.383
101	84.727933	-69.079484	0.738	11.7 ± 2.72	203 ± 47.2	0.934
102	84.728497	-69.079548	0.842	11.9 ± 2.98	249 ± 62.4	1.00
103	84.712801	-69.078013	0.273	31.5 ± 1.40	143 ± 6.34	0.965
104	84.709897	-69.076059	0.664	60.7 ± 3.18	1440 ± 75.4	1.49
105	84.731833	-69.079910	0.215	13.8 ± 1.07	36.6 ± 2.84	0.774
106	84.716524	-69.077616	0.247	27.3 ± 1.15	84.6 ± 3.56	0.368
107	84.702366	-69.075318	0.366	25.7 ± 1.85	206 ± 14.8	0.816
108	84.728531	-69.083668	0.605	22.5 ± 2.89	439 ± 56.4	1.17
109	84.728261	-69.083084	0.244	20.5 ± 1.20	68.7 ± 4.02	0.631
110	84.726557	-69.081757	0.398	34.1 ± 2.15	367 ± 23.1	0.817
111	84.668852	-69.081488	0.315	22.9 ± 1.59	134 ± 9.31	0.943
112	84.728558	-69.084019	0.35 0	24.9 ± 1.73	173 ± 12.01	0.569
113	84.723553	-69.078390	0.524	20.8 ± 2.40	179 ± 20.7	1.04
114	84.669455	-69.075850	0.262	15.8 ± 1.30	61.7 ± 5.08	0.655
115	84.729553	-69.081604	0.267	14.3 ± 1.30	55.9 ± 5.08	0.469

Column 1: The ID we give each clump. Column 4: The geometric mean radius calculated using the major and minor axis of the best-fit ellipse: $\sqrt{\text{major axis x minor axis}}$. Column 6: The total H_2 mass. We use a X_{CO} conversion factor of 8.4 ± 3 $M_\odot$ pc^{-2} (K km s^{-1})$^{-1}$ (Indebetouw et al., 2013). Column 7: The measured linewidth.

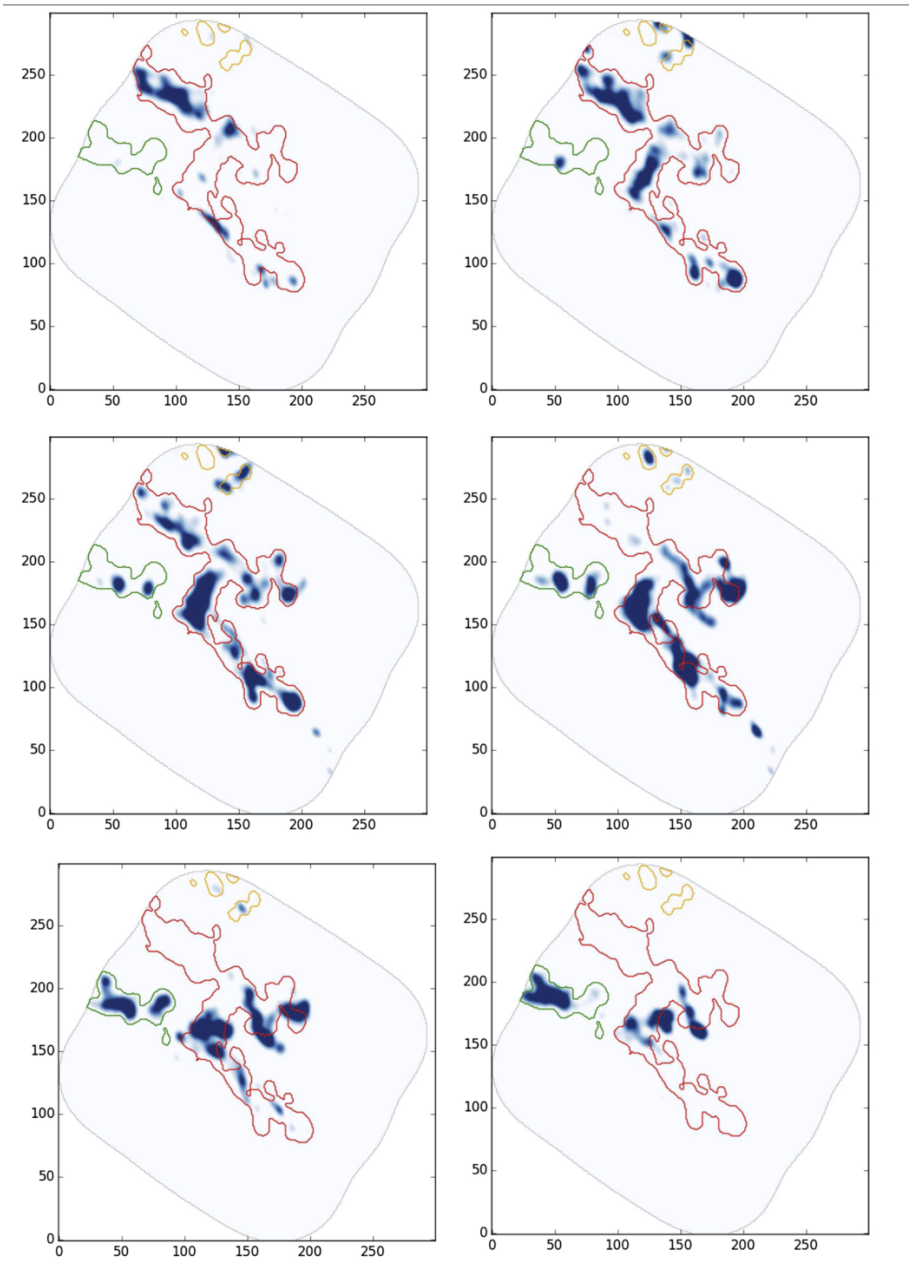

Figure 2.3: **12CO Velocity Cube Slice** Slices of the ^{12}CO (2-1) brightness temperature velocity cube is shown in blue color. From left-to-right, top-to-bottom the channel velocities are 245.17 km/s, 247.17 km/s, 249.17 km/s, 251.17 km/s, 253.17 km/s, and 255.17 km/s. The red, green, and orange molecular structures highlighted correspond to the red, green, and cyan dendrogram structure in Figure 2.2.

Table 2.2 lists column density and mass values we obtain on the ^{13}CO (2-1) clumps. The equations we used to convert the ^{13}CO (2-1) column density to the H_2 mass can be found in Appendix A. We use a $H_2/^{13}$CO abundance ratio of 5×10^6 to convert the ^{13}CO column density to the H_2 column density, the same abundance factor that was used by Indebetouw et al. (2013). The total H_2 mass we obtain by summing up the masses of each dendrogram trunk in Figure 2.4 is 6.7×10^4 $M_\odot$. The mass estimated from ^{13}CO (2-1) and ^{12}CO (2-1) in this work are consistent with each other as well as those estimated by Indebetouw et al. (2013) using dust continuum emission ($6.0 \pm 1.0 \times 10^4$ $M_\odot$) and LTE analysis of ^{13}CO (2-1) (6.8×10^4 $M_\odot$).

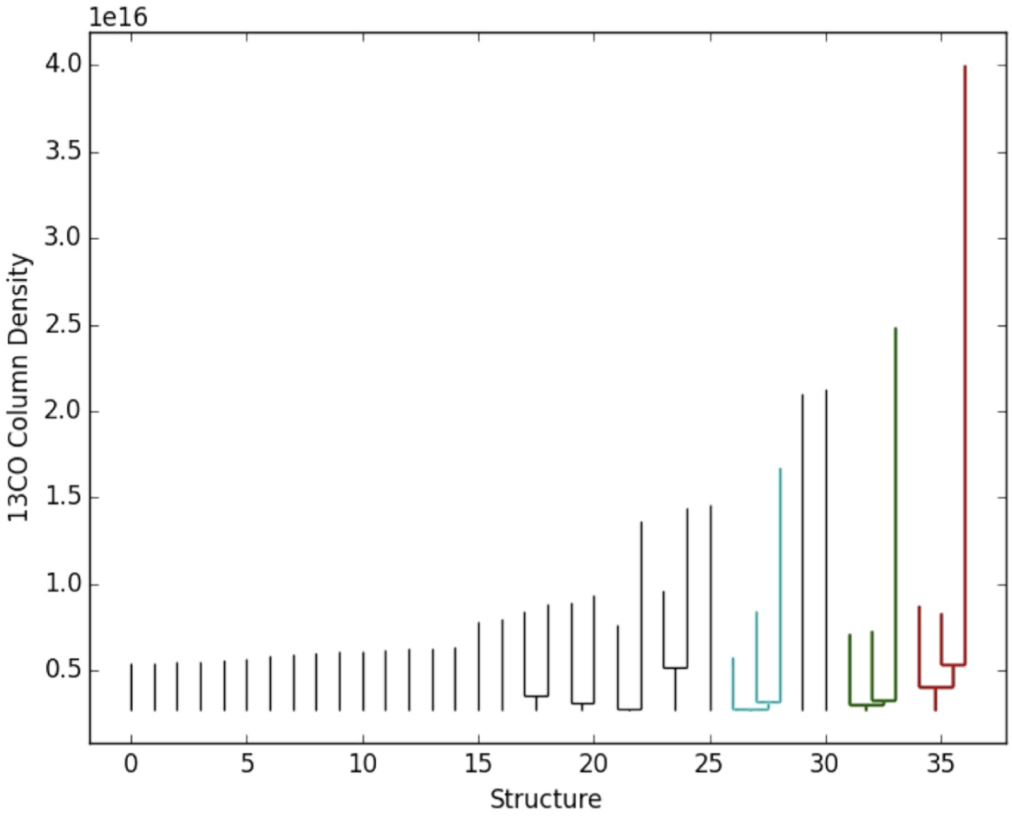

Figure 2.4: **Dendrogram Representation of 13CO** Dendrogram hierarchy of ^{13}CO (2-1) column density.

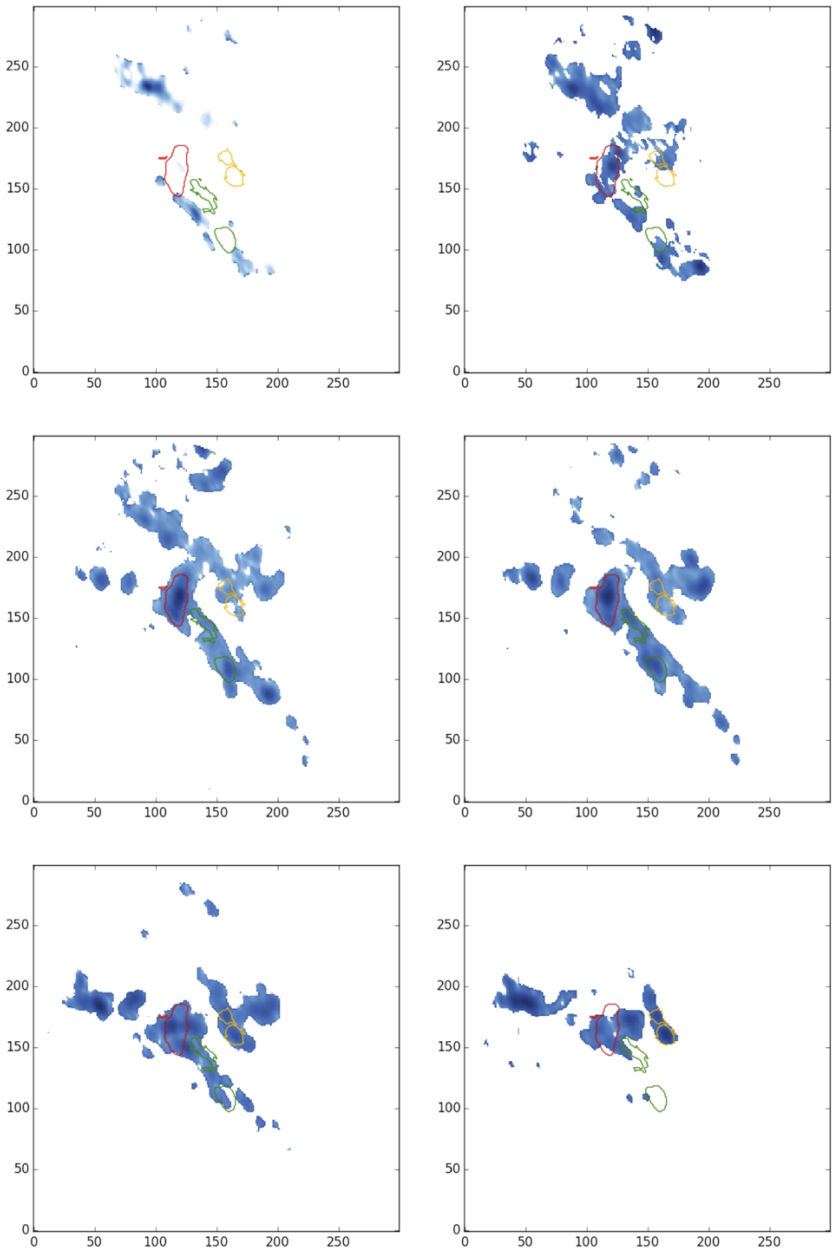

Figure 2.5: **13CO Velocity Cube Slice** Slices of the ^{13}CO (2-1) column density velocity cube is shown in blue color. From left-to-right, top-to-bottom the channel velocities are 245.17 km/s, 247.17 km/s, 249.17 km/s, 251.17 km/s, 253.17 km/s, and 255.17 km/s. The red, green, and orange molecular structures highlighted correspond to the red, green, and cyan dendrogram structure in Figure 2.4.

Table 2.2: Column Densities and Mass Derived from 13CO

Clump ID	RA	Dec	Radius [pc]	$N_{^{13}CO}$ [cm^{-2}]	N_{H_2} [cm^{-2}]	Total H_2 Mass [$M_\odot$]	Linewidth [km/s]
0	84.689449	-69.082378	0.373	$7.44 \pm 0.13 \times 10^{15}$	$3.72 \pm 0.07 \times 10^{22}$	297 ± 5.59	0.394
1	84.687939	-69.081210	0.320	$6.87 \pm 0.11 \times 10^{15}$	$3.43 \pm 0.05 \times 10^{22}$	183 ± 2.67	0.388
2	84.709746	-69.073602	0.936	$2.02 \pm 0.32 \times 10^{16}$	$1.01 \pm 0.02 \times 10^{23}$	4510 ± 89.3	1.87
3	84.711099	-69.073085	0.501	$2.39 \pm 0.21 \times 10^{16}$	$1.19 \pm 0.01 \times 10^{23}$	2310 ± 19.4	1.86
4	84.695409	-69.082384	0.347	$7.39 \pm 0.13 \times 10^{15}$	$3.69 \pm 0.07 \times 10^{22}$	281 ± 5.33	0.477
5	84.708707	-69.079363	0.312	$6.13 \pm 0.07 \times 10^{15}$	$3.06 \pm 0.04 \times 10^{22}$	71.5 ± 0.935	0.556
6	84.701895	-69.081726	0.359	$9.14 \pm 0.14 \times 10^{15}$	$4.57 \pm 0.07 \times 10^{22}$	396 ± 6.07	0.665
7	84.691777	-69.086031	0.226	$5.56 \pm 0.07 \times 10^{15}$	$2.78 \pm 0.01 \times 10^{22}$	53.3 ± 0.192	0.429
8	84.687966	-69.085250	0.434	$3.38 \pm 0.20 \times 10^{16}$	$1.69 \pm 0.10 \times 10^{23}$	2910 ± 172	0.969
9	84.721610	-69.076879	0.837	$4.96 \pm 0.39 \times 10^{16}$	$2.48 \pm 0.19 \times 10^{23}$	16700 ± 1280	2.81
10	84.697005	-69.069689	0.571	$1.74 \pm 0.22 \times 10^{16}$	$8.68 \pm 0.01 \times 10^{22}$	1960 ± 2.26	1.11
11	84.705166	-69.078640	1.010	$4.11 \pm 0.46 \times 10^{16}$	$2.06 \pm 0.02 \times 10^{23}$	19300 ± 187	1.94
12	84.707623	-69.074421	0.515	$1.57 \pm 0.20 \times 10^{16}$	$7.86 \pm 0.98 \times 10^{22}$	1350 ± 168	0.774
13	84.697312	-69.082689	1.170	$1.55 \pm 0.41 \times 10^{16}$	$7.73 \pm 0.21 \times 10^{22}$	5920 ± 161	1.15
14	84.696562	-69.083241	0.849	$1.78 \pm 0.33 \times 10^{16}$	$8.90 \pm 0.02 \times 10^{22}$	4380 ± 9.84	1.16
15	84.695307	-69.084753	0.294	$1.23 \pm 0.12 \times 10^{16}$	$6.15 \pm 0.06 \times 10^{22}$	385 ± 3.76	0.579
16	84.693610	-69.082348	0.323	$6.25 \pm 0.09 \times 10^{15}$	$3.12 \pm 0.04 \times 10^{22}$	112 ± 1.44	0.553
17	84.705443	-69.078644	0.784	$5.30 \pm 0.36 \times 10^{16}$	$2.65 \pm 0.02 \times 10^{23}$	15400 ± 116	1.51
18	84.705570	-69.078625	0.654	$6.73 \pm 0.29 \times 10^{16}$	$3.37 \pm 0.01 \times 10^{23}$	12700 ± 37.7	1.30
19	84.715115	-69.070060	0.261	$9.88 \pm 0.10 \times 10^{15}$	$4.94 \pm 0.05 \times 10^{22}$	214 ± 2.17	0.482
20	84.696728	-69.069400	0.375	$1.56 \pm 0.14 \times 10^{16}$	$7.82 \pm 0.07 \times 10^{22}$	711 ± 6.36	0.419
21	84.710215	-69.069043	0.333	$4.54 \pm 0.09 \times 10^{15}$	$2.27 \pm 0.04 \times 10^{22}$	81.4 ± 1.43	0.279
22	84.700917	-69.068526	0.317	$1.69 \pm 0.13 \times 10^{16}$	$8.44 \pm 0.06 \times 10^{22}$	612 ± 4.35	0.727
23	84.700929	-69.070926	0.566	$5.82 \pm 0.18 \times 10^{15}$	$2.91 \pm 0.88 \times 10^{22}$	405 ± 122	0.607
24	84.714332	-69.077009	0.682	$1.52 \pm 0.27 \times 10^{16}$	$7.60 \pm 0.01 \times 10^{22}$	2520 ± 3.32	1.58

Continued on next page

Table 2.2 – continued from previous page

Clump ID	RA	Dec	Radius [pc]	$N_{^{13}CO}$ [cm^{-2}]	N_{H_2} [cm^{-2}]	Total H_2 Mass [$M_\odot$]	Linewidth [km/s]
25	84.696657	-69.083134	0.688	$2.06 \pm 0.28 \times 10^{16}$	$1.03 \pm 0.01 \times 10^{23}$	3660 ± 35.5	0.906
26	84.697115	-69.070046	0.308	$1.03 \pm 0.12 \times 10^{16}$	$5.13 \pm 0.06 \times 10^{22}$	325 ± 3.80	0.266
27	84.683912	-69.087133	0.275	$8.84 \pm 0.11 \times 10^{15}$	$4.42 \pm 0.05 \times 10^{22}$	232 ± 2.62	0.482
28	84.701028	-69.080010	0.463	$1.03 \pm 0.18 \times 10^{16}$	$5.16 \pm 0.09 \times 10^{22}$	735 ± 12.8	0.629
29	84.688237	-69.077655	0.673	$2.34 \pm 0.28 \times 10^{16}$	$1.17 \pm 0.01 \times 10^{23}$	4210 ± 36.0	1.03
30	84.688363	-69.077495	0.843	$2.03 \pm 0.32 \times 10^{16}$	$1.01 \pm 0.02 \times 10^{23}$	4760 ± 94.3	1.00
31	84.714727	-69.077451	0.332	$1.31 \pm 0.14 \times 10^{16}$	$6.55 \pm 0.07 \times 10^{22}$	563 ± 6.02	0.529
32	84.681295	-69.089657	0.237	$5.46 \pm 0.08 \times 10^{15}$	$2.73 \pm 0.04 \times 10^{22}$	72.7 ± 1.07	0.374
33	84.690069	-69.085793	0.299	$6.63 \pm 0.11 \times 10^{15}$	$3.31 \pm 0.54 \times 10^{22}$	174 ± 28.4	0.523
34	84.694844	-69.078758	0.756	$1.89 \pm 0.30 \times 10^{16}$	$9.47 \pm 0.02 \times 10^{22}$	3870 ± 8.17	1.14
35	84.689538	-69.076042	0.365	$9.50 \pm 0.14 \times 10^{15}$	$4.75 \pm 0.07 \times 10^{22}$	443 ± 6.53	0.545
36	84.695008	-69.078698	0.680	$2.22 \pm 0.26 \times 10^{16}$	$1.11 \pm 0.01 \times 10^{23}$	3410 ± 30.7	1.01
37	84.714061	-69.076682	0.481	$1.36 \pm 0.19 \times 10^{16}$	$6.80 \pm 0.09 \times 10^{22}$	1070 ± 14.2	0.585
38	84.692053	-69.079906	0.386	$5.14 \pm 0.13 \times 10^{15}$	$2.57 \pm 0.01 \times 10^{22}$	201 ± 0.782	0.356
39	84.696185	-69.077785	0.336	$2.02 \pm 0.14 \times 10^{16}$	$1.01 \pm 0.07 \times 10^{23}$	934 ± 64.7	1.07
40	84.703806	-69.080023	0.208	$1.18 \pm 0.08 \times 10^{16}$	$5.90 \pm 0.01 \times 10^{22}$	182 ± 0.308	0.387
41	84.694412	-69.079160	0.422	$2.50 \pm 0.19 \times 10^{16}$	$1.25 \pm 0.10 \times 10^{23}$	2050 ± 164	0.820
42	84.692162	-69.083837	0.314	$5.88 \pm 0.12 \times 10^{15}$	$2.94 \pm 0.06 \times 10^{22}$	184 ± 3.76	0.358
43	84.701180	-69.078147	0.349	$1.02 \pm 0.14 \times 10^{16}$	$5.10 \pm 0.07 \times 10^{22}$	438 ± 6.01	0.407
44	84.728132	-69.083090	0.270	$9.00 \pm 0.10 \times 10^{15}$	$4.50 \pm 0.05 \times 10^{22}$	206 ± 2.29	0.706
45	84.726124	-69.081820	0.306	$9.63 \pm 0.12 \times 10^{15}$	$4.81 \pm 0.06 \times 10^{22}$	285 ± 3.56	0.451
46	84.668881	-69.081515	0.263	$8.44 \pm 0.10 \times 10^{15}$	$4.22 \pm 0.05 \times 10^{22}$	183 ± 2.17	0.873

Column 1: The ID we give each clump. Column 4: The geometric mean radius calculated using the major and minor axis of the best-fit ellipse: $\sqrt{\text{major axis x minor axis}}$. Column 6: The H_2 column density. We use a $\frac{H_2}{^{13}CO(2-1)}$ conversion factor of 5×10^6 Indebetouw et al. (2013). Column 8: The measured linewidth.

2.4 Massive YSOs and Low-Mass YSOs

The molecular clump sizes range from 0.2 - 1.4 pc. To trace star formation at this scale we need an inventory of the forming stars. We use recent surveys (HTTP, *Spitzer* SAGE, *Herschel* HERITAGE) to make a catalog of all the low-mass and massive YSOs. We define the stage of the YSO candidates in our sample by the following: Stage 0/I objects have $\frac{\dot{M}_{env}}{M_{star}}>10^{-6}$ yr^{-1}, Stage II objects are those that have $\frac{\dot{M}_{env}}{M_{star}}<10^{-6}$ yr^{-1} and $\frac{M_{disk}}{M_{star}}>10^{-6}$, and Stage III objects have $\frac{\dot{M}_{env}}{M_{star}}<10^{-6}$ yr^{-1} and $\frac{M_{disk}}{M_{star}}<10^{-6}$ (Chen et al., 2010; Robitaille et al., 2007, 2006).

2.4.1 Stage III Low-Mass YSOs

Stage III low-mass YSOs are usually identified by their location in an optical color-magnitude diagram, which leads to two problems: 1) contamination by older field stars and the effects of differential extinction that may lead to an overestimate of the actual number of candidates 2) older YSOs that are close to the main sequence (MS) cannot be identified accurately (De Marchi et al., 2011c). An alternate method of looking for Stage III low-mass YSOs is by Hα excess from accretion shocks (De Marchi et al., 2011c). Strong and fast variability of the Hα line intensity has been detected spectroscopically (e.g., Alencar et al., 2005, 2001; Fernandez et al., 1995; Reipurth et al., 1996; Smith et al., 1999; Sousa et al., 2016) that can move a star above and below our 10 Angstrom equivalent width threshold in a few days and

sometimes in a few hours. Comparing observations of the SN 1987A field taken at 3 different epochs (Panagia et al., 2000; Romaniello, 1998) revealed that the number of stars that have strong Hα excess is essentially the same at all epochs, but only about about 1/3 of them are that strong at all epochs. This suggests a duty cycle of about 1/3. An ongoing study of the PMS stars in NGC 346, based on the original work of De Marchi et al. (2011b) and De Marchi et al. (2011a) revealed that the number of Hα strong PMS stars in the 'classical' region of the color magnitude diagram (CMD) (i.e. stars brighter and redder than the MS) are between 1/3 and 2/3 of all the stars in the same region (De Marchi & Panagia, private communication). Note that in the case of NGC 346 the reddening is not so high ($A_v \approx 0.5$) and, therefore, there is no serious problem of contamination in that region of the CMD. All those elements taken together suggest that the duty cycle of relatively young PMS stars (those still above and redder than the MS) should be of the order of 1/3.

We have used the HTTP catalog (Sabbi et al., 2016) to select the low-mass Stage III YSO candidates with Hα excess within the ALMA footprint using the stringent selection criteria as defined by De Marchi et al. (2011c). In particular, all selected stars must have uncertainties lower than 0.1 mag in each of the V, I and Hα bands, simultaneously. Furthermore, they must display V-Hα excesses higher than the 4σ level as compared to stars of the same V-I color. There are 87 stars that meet the above criteria and are located within the ALMA footprint.

Figures 2.6a and 2.6b shows the F160W versus F110W - F160W color-magnitude diagram (CMD) with isochrones and mass evolutionary tracks overplotted. We plot isochrones and mass evolutionary tracks taken from the Padova code (Bressan et al., 2012; Chen et al., 2015) on these figures. For our purposes we use Milky Way extinction of $A_v = 0.06$ and metallicity of $Z = 0.008$ to redden the Padova isochrones to their location in the LMC. In addition we use the local extinction of 30 Doradus as calculated by De Marchi et al. (2016) to de-redden the low-mass YSOs. The majority of stars fall between $10^5 - 10^7$ yrs isochrones and $1 - 3$ $M_\odot$ mass evolutionary tracks. Table 2.3 lists the approximate masses of these low-mass YSOs. These masses were calculated by the best fit mass evolutionary track from F160W versus F110W - F160W for each source. When we check these mass estimates with the best fit mass evolutionary track to F775W versus F555W - F775W for each source, we find that 75% of the masses do not match. The masses from the best fit evolutionary track to F775W versus F555W - F775W are always lower than those from F160W versus F110W - F160W. We choose the near infrared CMD mass evolution tracks to determine the mass because these wavelengths are not as contaminated from extinction as optical bands. All masses of low-mass YSOs have an uncertainty of ± 0.25 $M_\odot$. This is due to the the 0.5 $M_\odot$ spacing between the mass evolutionary track (Figure 2.6b).

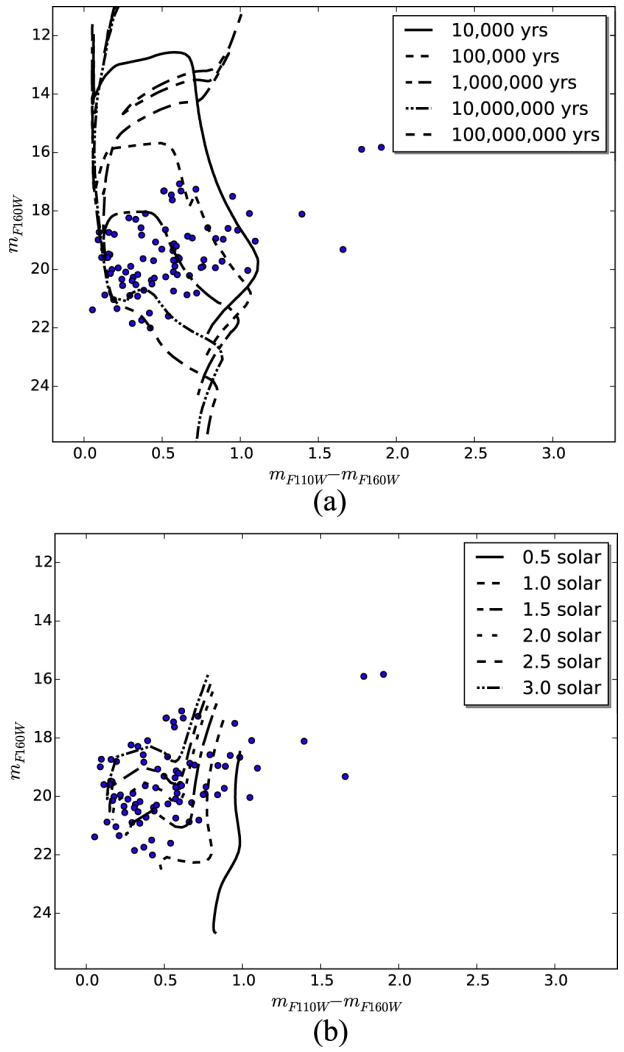

Figure 2.6: **Color Magnitude Diagram with Isochrones** (a) F160W versus F110W - F160W CMD with isochrones. The isochrones are from the Padova code Bressan et al. (2012); Chen et al. (2015). The points are more evolved low-mass YSOs that have been selected via Hα excess and have been de-reddened De Marchi et al. (2016). (b) This is the same as Figure a, however we plot F160W versus F110W - F160W CMD.

Table 2.3: Magnitude and Mass of Pre-Main-Sequence Protostars

ID	RA	Dec	mag	err	mag	err	mag	err	mag	err	mag	err	mag	err	mag	err	Mass
ID	RA	Dec	275	275	336	336	555	555	658	658	775	775	110	110	160	160	[$M_\odot$]
1	84.701393	-69.091209	23.952	11.111	23.267	0.01	22.361	0.038	21.595	0.046	21.684	0.08	21.096	0.014	20.713	0.037	2.5
2	84.700844	-69.091339	25.854	1.585	24.366	0.394	22.735	0.016	21.325	0.039	21.561	0.03	20.605	0.032	19.721	0.077	2.5
3	84.698189	-69.092331	27.005	3.316	25.313	0.537	23.901	0.063	22.201	0.079	22.474	0.1	20.977	0.332	19.319	0.278	1.5
4	84.694267	-69.089218	20.805	0.01	20.652	0.063	20.515	0.03	19.76	0.043	20.274	0.0	20.184	0.061	20.006	0.05	3.0
5	84.690453	-69.090652	19.027	0.049	18.941	0.005	19.438	0.008	19.063	0.015	19.232	0.00	19.077	0.004	18.987	0.002	3.0
6	84.685699	-69.091995	23.538	0.735	22.406	0.243	21.454	0.02	20.393	0.074	20.615	0.029	19.928	0.049	19.359	0.006	3.0
7	84.728310	-69.079735	24.373	0.354	23.11	0.293	21.554	0.027	20.095	0.061	20.297	0.02	19.147	0.041	18.088	0.1	3.0
8	84.688332	-69.090294	24.766	0.465	23.007	0.053	21.771	0.031	20.535	0.047	20.521	0.005	19.52	0.009	18.598	0.005	3.0
9	84.696457	-69.088234	21.887	0.088	20.39	0.01	19.361	0.014	18.385	0.032	18.446	0	17.832	0.002	17.322	0.001	3.0
10	84.718658	-69.081444	25.214	0.731	24.044	0.171	23.416	0.044	21.513	0.014	22.818	0.04	22.106	0.001	21.737	0.065	1.5
11	84.700165	-69.087601	19.105	0.024	19.102	0.004	19.518	0.008	18.823	0.098	19.204	0.01	18.895	0.001	18.736	0.036	3.0
12	84.689651	-69.089500	23.131	0.061	22.369	0.027	21.569	0.023	20.592	0.091	21.036	0	20.586	0.16	20.271	0.046	3.0
13	84.685539	-69.090813	24.617	11.111	24.09	0.18	22.892	0.035	21.34	0.083	21.679	0	20.784	0.054	19.943	0.001	2.5
14	84.718697	-69.080963	25.410	11.111	24.707	0.062	23.868	0.084	21.977	0.099	23.175	0	22.14	0.082	21.6	0.135	1.5
15	84.716599	-69.080612	23.791	0.458	22.922	0.098	22.384	0.008	21.402	0.082	21.76	0.03	21.261	0.076	20.918	0.011	2.5
16	84.694611	-69.086166	22.047	0.065	21.775	11.111	21.237	0.051	20.233	0.021	21.03	0.05	20.36	0.097	20.093	0.035	3.0
17	84.687714	-69.089203	22.63	0.011	22.081	0.019	21.387	0.023	19.703	0.069	21.167	0.01	20.579	0.006	20.337	0.022	3.0
18	84.685844	-69.089600	18.848	0.00	18.821	0.006	19.425	0.017	18.702	0.02	19.221	0	18.996	0.001	18.802	0.001	3.0
19	84.681122	-69.090309	19.398	0.003	19.305	0.003	19.657	0.017	19.152	0.02	19.279	0.0	19.19	0.223	19.462	0.097	3.0
20	84.680565	-69.089874	24.373	0.302	24.17	0.099	23.191	0.02	20.741	0.039	22.118	0.04	20.806	0.043	20.375	0.007	3.0
21	84.715660	-69.079575	25.377	2.033	24.136	0.134	23.716	0.009	22.409	0.048	22.919	0.01	22.427	0.011	22.003	0.099	1.5
22	84.709999	-69.080421	19.673	0.011	19.516	0.003	19.604	0.008	18.975	0.012	19.046	0.01	18.619	0.074	18.288	0.002	3.0
23	84.711174	-69.080360	24.552	0.313	23.915	0.021	23.306	0.032	21.728	0.099	21.856	0.00	20.13	0.042	19.034	0.01	3.0
24	84.707649	-69.081543	22.929	0.054	21.278	0.015	19.564	0.007	18.4	0.031	18.459	0	17.686	0.022	17.075	0.001	3.0

Continued on next page

Table 2.3 – continued from previous page

ID	RA	Dec	mag	err	mag	err	mag	err	mag	err	mag	err	mag	err	mag	err	Mass
ID	RA	Dec	275	275	336	336	555	555	658	658	775	775	110	110	160	160	[$M_\odot$]
25	84.692261	-69.085777	25.221	0.943	24.795	0.516	23.432	0.055	21.361	0.045	22.348	0.09	20.886	0.094	20.211	0.077	2.5
26	84.694832	-69.085495	21.403	0.007	21.625	0.069	21.233	0.006	19.054	0.028	20.674	0.0	19.643	0.009	18.66	0.01	3.0
27	84.693153	-69.085175	25.468	1.708	23.337	11.111	22.243	0.091	20.213	0.045	21.772	0.01	20.779	0.452	20.256	0.063	2.5
28	84.694252	-69.085899	25.125	3.617	23.721	0.402	22.436	0.058	21.091	0.012	21.279	0.05	20.438	0.036	19.671	0.087	2.5
29	84.697914	-69.083656	18.271	0.003	18.413	0.029	19.125	0.008	18.453	0.044	18.538	0.0	17.826	0.004	17.313	0.006	3.0
30	84.698174	-69.084839	24.63	0.767	23.609	0.121	23.154	0.074	21.342	0.071	22.72	0.0	21.912	0.143	21.493	0.042	2.0
31	84.688438	-69.086906	25.489	0.289	25.063	11.111	23.423	0.069	20.814	0.039	22.788	0.01	21.08	0.294	20.035	0.066	2.5
32	84.686890	-69.086388	21.415	0.015	21.337	0.042	21.163	0.023	20.128	0.093	20.792	0.00	20.146	0.262	19.701	0.042	3.0
33	84.686668	-69.087700	20.576	0.117	20.288	11.111	20.394	0.027	19.853	0.011	20.023	0.01	19.66	0.158	19.494	0.046	3.0
34	84.681587	-69.088242	24.7	0.209	23.442	11.111	22.992	0.074	21.031	0.096	22.229	0.0	21.314	0.364	20.741	0.03	2.0
35	84.680145	-69.089180	18.576	0.03	18.55	0.004	19.181	0.017	18.656	0.06	18.954	0.01	18.824	0.013	18.727	0.001	3.0
36	84.680260	-69.089043	19.101	0.00	19.088	0.003	19.562	0.011	18.34	0.043	19.323	0.01	19.164	0.015	18.643	0.004	3.0
37	84.681496	-69.089035	20.331	0.203	20.078	0.028	20.255	0.015	19.576	0.095	20.048	0.0	19.63	0.156	19.473	0.073	3.0
38	84.680847	-69.088844	25.694	4.887	23.776	0.315	22.364	0.018	20.934	0.085	21.213	0.0	20.189	0.047	19.587	0.024	3.0
39	84.679916	-69.088379	24.738	0.994	22.854	11.111	21.546	0.004	20.299	0.019	20.532	0.026	19.619	0.045	18.926	0.016	3.0
40	84.680016	-69.088806	23.422	0.1	21.996	11.111	21.067	0.027	19.927	0.079	20.257	0.0	19.523	0.058	19.065	0.023	3.0
41	84.719650	-69.077087	24.578	0.162	23.923	11.111	22.9	0.025	20.202	0.078	20.897	0.026	17.669	0.013	15.892	0.039	3.0
42	84.719276	-69.077477	24.742	1.02	23.502	0.342	23.176	0.038	22.133	0.078	22.558	0.069	22.158	0.02	21.849	0.003	1.5
43	84.725426	-69.076439	25.037	0.87	24.234	0.302	22.865	0.024	21.62	0.07	21.627	0.05	20.665	0.02	19.904	0.005	2.5
44	84.694695	-69.083130	23.626	0.11	22.407	0.133	21.854	0.085	20.873	0.073	21.394	0.02	20.799	0.315	20.552	0.145	3.0
45	84.692535	-69.081985	23.418	0.21	23.36	0.266	22.533	0.036	21.333	0.074	21.395	0.02	19.786	0.115	18.943	0.133	3.0
46	84.681580	-69.084602	20.725	0.289	20.002	0.009	20.064	0.012	18.832	0.005	19.385	0.02	18.452	0.019	17.501	0.009	3.0
47	84.679291	-69.084869	23.978	0.619	23.60	0.086	22.44	0.028	21.321	0.095	21.499	0.04	20.656	0.055	20.084	0.058	2.5
48	84.680473	-69.085472	24.218	0.904	23.013	0.244	21.825	0.04	20.47	0.084	20.816	0.02	19.806	0.199	19.308	0.032	3.0
49	84.679359	-69.086403	22.02	11.111	21.624	0.008	21.111	0.027	19.982	0.017	20.838	0.032	20.168	0.058	19.949	0.162	3.0

Continued on next page

Table 2.3 – continued from previous page

ID	RA	Dec	mag	err	mag	err	mag	err	mag	err	mag	err	mag	err	mag	err	Mass
ID	RA	Dec	275	275	336	336	555	555	658	658	775	775	110	110	160	160	[$M_\odot$]
50	84.701096	-69.077980	19.052	0.014	19.115	0.006	19.62	0.019	18.665	0.043	19.086	0.01	18.484	0.01	18.091	0.004	3.0
51	84.692154	-69.080086	19.636	0.017	19.721	0.022	20.027	0.012	18.825	0.02	19.17	0.004	18.189	0.003	17.624	0.01	3.0
52	84.688080	-69.081558	22.126	0.247	21.674	0.034	21.073	0.042	20.211	0.028	20.356	0.003	19.527	0.121	18.864	0.013	3.0
53	84.688301	-69.081680	22.141	11.111	21.955	0.09	21.773	0.042	20.386	0.078	21.3	0.041	20.195	0.208	19.896	0.042	3.0
54	84.684372	-69.083496	26.444	0.638	24.486	11.111	23.044	0.068	21.17	0.095	22.455	0.091	21.227	0.022	21.037	0.027	2.5
55	84.677231	-69.085037	24.325	2.261	24.993	0.17	23.349	0.04	22.139	0.093	22.324	0.04	21.53	0.191	20.809	0.091	2.0
56	84.691353	-69.079071	23.208	0.027	22.895	0.127	22.093	0.015	21.138	0.055	21.538	0.01	20.857	0.025	20.525	0.094	3.0
57	84.684090	-69.081886	22.047	0.199	21.94	0.02	22.037	0.04	20.575	0.084	21.282	0.025	20.26	0.088	19.667	0.021	3.0
58	84.686569	-69.080055	18.204	0.011	18.377	0.003	19.192	0.014	18.656	0.047	18.857	0.023	18.526	0.003	18.239	0.001	3.0
59	84.681427	-69.082382	20.446	0.122	20.422	0.007	20.577	0.005	19.773	0.078	20.252	0.036	19.747	0.011	19.595	0.011	3.0
60	84.681511	-69.082527	23.645	1	22.558	0.309	21.584	0.066	19.362	0.072	20.929	0.036	19.701	0.117	19.125	0.071	3.0
61	84.674179	-69.084106	24.864	0.449	24.045	0.15	22.919	0.032	21.645	0.052	21.811	0.016	20.685	0.044	19.936	0.029	2.5
62	84.682388	-69.080818	23.704	0.238	23	0.148	21.976	0.048	20.734	0.017	21.059	0.012	20.261	0.019	19.688	0.008	3.0
63	84.700630	-69.075279	21.251	0.004	21.143	0.048	20.988	0.008	20.515	0.042	20.692	0.017	20.309	0.002	20.14	0.027	3.0
64	84.684479	-69.077736	20.953	11.111	20.351	0.06	19.988	0.02	19.186	0.05	19.377	0.002	18.941	0.006	18.576	0.005	3.0
65	84.683121	-69.078804	23.388	0.285	21.243	0.007	19.748	0.013	18.758	0.054	18.81	0.011	18.01	11.111	17.451	0.013	3.0
66	84.681145	-69.078850	24.586	0.455	23.169	0.163	22.572	0.069	21.311	0.058	22.08	0.066	21.552	0.103	21.341	0.064	2.0
67	84.706413	-69.071678	23.375	0.203	22.644	0.132	22.222	0.035	21.53	0.022	21.647	0.014	21.185	0.017	20.892	0.094	2.5
68	84.671455	-69.081024	23.496	0.461	22.51	0.015	21.653	0.055	20.501	0.095	21.156	0.005	20.521	0.016	20.177	0.016	3.0
69	84.680443	-69.077477	24.546	11.111	22.594	0.046	21.444	0.076	19.966	0.077	20.34	0.042	19.366	0.119	18.574	0.009	3.0
70	84.697449	-69.073441	20.468	0.005	20.087	0.032	20.184	0.012	18.785	0.037	19.018	0.011	17.973	0.002	17.257	0.004	3.0
71	84.702751	-69.072067	24.741	0.111	23.873	0.151	22.527	0.039	21.219	0.067	21.429	0.026	20.474	0.004	19.892	0.013	3.0
72	84.700760	-69.071678	23.645	11.111	22.721	0.105	22.061	0.03	21.197	0.026	21.289	0.018	20.693	0.123	20.385	0.001	3.0
73	84.704803	-69.071213	26.26	4.198	24.966	0.087	23.708	0.061	21.821	0.084	22.775	0.01	21.529	0.021	20.87	0.031	2.0
74	84.673096	-69.078514	22.993	0.209	22.404	0.108	21.963	0.006	21.113	0.087	21.562	0.047	21.009	0.06	20.876	0.032	2.5

Continued on next page

Table 2.3 – continued from previous page

ID	RA	Dec	mag	err	mag	err	mag	err	mag	err	mag	err	mag	err	mag	err	Mass
ID	RA	Dec	275	275	336	336	555	555	658	658	775	775	110	110	160	160	[$M_\odot$]
75	84.671036	-69.080124	23.411	0.078	21.635	0.037	19.874	0.014	18.717	0.032	18.764	0.011	17.94	0.006	17.319	0.001	3.0
76	84.672043	-69.080139	20.922	0.097	20.636	0.036	20.311	0.028	19.598	0.048	19.832	0.024	19.196	0.075	18.827	0.037	3.0
77	84.692680	-69.072685	20.098	0.004	20.085	0.079	20.235	0.018	19.695	0.018	19.973	0.016	19.707	0.009	19.594	0.023	3.0
78	84.691689	-69.073006	22.974	11.111	22.228	0.016	21.377	0.024	19.984	0.098	20.593	0.032	19.795	0.026	19.204	0.005	3.0
79	84.704056	-69.069389	23.665	11.111	23.258	0.265	22.4	0.034	20.781	0.055	21.333	0.008	19.861	0.037	18.97	0.054	3.0
80	84.700874	-69.069824	23.756	0.265	23.379	0.112	22.702	0.043	19.331	0.051	20.07	0.016	17.726	0.033	15.823	0.017	3.0
81	84.700478	-69.069885	23.218	0.389	22.995	0.009	22.792	0.031	20.95	0.098	21.142	0.006	19.505	0.059	18.11	0.057	3.0
82	84.681694	-69.073654	22.861	0.048	22.266	0.005	21.321	0.018	20.124	0.067	20.659	0.038	20.012	0.001	19.634	0.001	3.0
83	84.669319	-69.076431	25.196	0.191	24.124	0.17	22.645	0.016	21.469	0.04	21.797	0.003	20.747	0.003	20.297	0.032	3.0
84	84.669365	-69.077171	23.675	0.15	22.898	0.298	21.919	0.022	20.701	0.074	21.015	0.034	20.237	0.002	19.627	0.068	3.0
85	84.667603	-69.076630	25.749	0.349	23.583	0.323	22.688	0.013	21.151	0.094	21.846	0.023	20.934	0.101	20.499	0.034	3.0
86	84.667641	-69.077843	24.436	0.675	23.754	0.157	23.107	0.023	21.28	0.091	22.691	0.051	21.438	0.064	21.384	0.09	2.0
87	84.676857	-69.073395	25.452	11.111	23.088	11.111	22.445	0.026	20.899	0.08	21.784	0.017	20.781	0.147	20.184	0.064	2.5

Column 1: The ID we give each more evolved low-mass YSOs (discussed in section 2.4.1). Columns 4-17: The magnitude and error of the star in F275W, F336W, F555W, F658N, F775W, F110W, and F160W respectively. Column 18: Mass of star determined from isochrone fitting. Note: The magnitude and errors vary in significant figures. These numbers are the same as Sabbi et al. (2016), therefore we do not change them in order to be consistent.

We are not complete in our catalog of low-mass YSOs due to the Hα duty cycle - selection of low-mass YSOs by Hα excess means at any given time we can observe 1/3 of the stars. Selecting the low-mass YSOs by Hα excess means that we are targeting Stage III objects. Figure 2.10 shows a histogram of all massive and low-mass YSO star masses. The majority of low-mass YSOs in our analysis are 3 $M_{\odot}$. We do not select any Stage I or Stage II low-mass YSO candidates. This is the result of our bias towards selecting low-mass Stage III YSOs by Hα excess.

2.4.2 Stage I Massive YSOs

2.4.2.1 Overview

We include massive YSO stage I candidates found by Gruendl & Chu (2009), Seale et al. (2009), and Seale et al. (2014) in our study. There are no massive stage I YSO candidates from Whitney et al. (2008) that are found in the ALMA CO footprint. Gruendl & Chu (2009) and Whitney et al. (2008) implements color cuts of different kinds, Seale et al. (2009) was a spectroscopic follow-up of Gruendl & Chu (2009) sources, and Walborn et al. (2013) study 10 Spitzer selected YSOs in 30 Doradus in more detail in order to provide mass estimates of these objects. Seale et al. (2009) use *Spitzer* IRS spectra and group YSO candidates in six categories. The S Group objects have silicate absorption features including the 10 μm absorption feature and sometimes including the 18 μm absorption feature, the SE Group objects have both

silicate absorption features (similar to S Group) and strong fine-structure emission lines, the P group objects have strong PAH features, the PE group objects have strong PAH and fine-structure line emission, the E group contain sources that only have very strong fine-structure emission lines, and the F group all other sources whose spectra looks similar to that of a YSO but they do not fit any of the above criteria.

We look at all point source objects in the SAGE catalog that are in the ALMA footprint of 30 Doradus to see if any possible massive YSO candidates were missed by previous galaxy wide studies because of stringent cuts. There are 6 YSO candidates that have previously been identified: J84.703995-69.079110, J84.699755-69.069803, J84.688990-69.084695, J84.695173-69.084857, J84.726173-69.082254, and J84.720292-69.077084. And there are 9 point sources in the ALMA footprint that have not been studied before: J84.695932-69.083807, J84.688372-69.078168, J84.669113-69.081638, J84.674734-69.077374, J84.709403-69.075682, J84.688168-69.071013,
J84.694286-69.074499, J84.676469-69.082774, and J84.671132-69.077168. We fit these sources to the Robitaille et al. (2006) and Robitaille et al. (2007) spectral energy distribution (SED) fitter. We develop a code which we use in conjunction with the Robitaille et al. (2006) SED fitter. This code outputs the maximum likelihood of the YSO parameters such as mass, luminosity, accretion rate, and associated 1σ errors. Tables 2.4 and 2.5 list the near infrared and far infrared photometry we used. For candidates with no PACS or SPIRE photometry we use the upper limit in each far

infrared band as given in Table 2.6 of Meixner et al. (2013). We assume the 6 previously identified YSO candidates are real candidates. For the 9 new point sources in the Spitzer footprint that have not been previously studied we require the reduced χ^2 of the best fit YSO SED to be less than 10 and the reduced χ^2 of the best fit stellar photosphere to be greater than 10. If an object is a good match to a YSO SED and not a good match to a reddened stellar photosphere SED, then we say it is a YSO candidate. With this definition we identify 4 new YSO candidates: J84.695932-69.083807, J84.688372-69.078168, J84.669113-69.081638, and J84.674734-69.077374. There are 5 *Spitzer* point sources that do not meet our χ^2 criteria: J84.709403-69.075682, J84.688168-69.071013, J84.694286-69.074499, J84.676469-69.082774 and J84.671132-69.077168. We look at the ^{12}CO (2-1) map and find that the emission at the location of these 5 sources is less than 3σ. Figures 2.7 and 2.8 shows SEDs of all YSO candidates. Figure 2.9 shows spectra for 3 massive YSO candidates.

Table 2.4: JHK Near Infrared Photometry For SAGE Sources in the ALMA Footprint

Name	J	eJ	H	eH	K	eK
J84.703995-69.079110					1.57011	0.14461
J84.695932-69.083807			3.30100	0.74500	7.93499	0.75269
J84.699755-69.069803	1.38831	0.21737				
J84.688990-69.084695	11.33674	1.46181	8.20918	1.28535	13.30241	1.22519
J84.695173-69.084857			3.30100	0.74500	7.93499	0.75269
J84.726173-69.082254						
J84.720292-69.077084	0.49486	0.09115	1.08218	0.13954	2.53472	0.14007
J84.688372-69.078168			0.36669	0.09798	0.26890	0.10230
J84.669113-69.081638	1.40499	0.09706			0.72229	0.08202
J84.674734-69.077374	3.38299	0.25519	2.24200	0.21950	2.70099	0.24979
J84.709403-69.075682	1.03600	0.08567	0.63669	0.07874	0.87559	0.10589
J84.688168-69.071013	1.89400	0.17440	1.30099	0.17139	1.16499	0.15129
J84.694286-69.074499	6.28200	0.16609	4.59499	0.12399	2.94799	0.09258
J84.676469-69.082774	39.75000	0.87860	27.96999	0.54100	19.31999	0.33799
J84.671132-69.077168	2.13800	0.12620	2.94199	0.19650	3.41899	0.21259

Columns 2-7: JHK photometry and error in mJy.

Table 2.5: *Spitzer* Near Infrared Photometry For SAGE Sources in the ALMA Footprint

Name	I1	eI1	I2	eI2	I3	eI3	I4	eI4
J84.703995-69.079110	21.38444	1.37386	40.415511	2.23344	109.8241473	8.92142	264.88736	26.83673
J84.695932-69.083807	22.27629	1.13999	33.91525	1.57547	57.79999	2.56299		
J84.699755-69.069803	25.38351	1.42744	33.37963	1.84666	87.23642	4.82862	252.96546	16.39286
J84.688990-69.084695	23.79861	1.53435	29.54935	1.95117	88.85826	5.72894	241.58146	17.82829
J84.695173-69.084857	22.27629	1.13999	33.91525	1.57547	57.79999	2.56299		
J84.726173-69.082254	9.7133293	0.66765012	14.2948082	1.03271423	33.45063937	2.21671575	91.7597332	5.56257797
J84.720292-69.077084	11.28633	0.72765	11.33833	0.73174	41.75397	2.69197	103.52881	7.62828
J84.688372-69.078168	2.78999	0.21799			17.13815	1.15499	36.29999	6.95368
J84.669113-69.081638					2.19572	0.33989		
J84.674734-69.077374	1.17999	0.12334	2.5999	0.22548	6.15999	0.33131	16.63815	1.11835
J84.709403-69.075682			0.67424	0.11927				
J84.688168-69.071013	0.95843	0.81513						
J84.694286-69.074499			1.74770	0.38999				
J84.676469-69.082774	9.89999	0.33199	7.49540	0.83999				
J84.671132-69.077168	0.77319	0.71533						

Columns 8-15: IRAC photometry and error in mJy. Note: The flux and errors vary in significant figures. These numbers are the same as those listed in the SAGE catalog as well studies done by Chen et al. (2010); Gruendl & Chu (2009); Seale et al. (2014). Therefore we do not change them in order to be consistent.

Table 2.6: Far Infrared Photometry For SAGE Sources in the ALMA Footprint

Name	PACS 100 μm	error PACS 100 μm	PACS 160 μm	error PACS 160 μm	SPIRE 250 μm	error SPIRE 250 μm	SPIRE 350 μm	error SPIRE 350 μm	SPIRE 500 μm	error SPIRE 500 μm
J84.703995-69.079110	19450	5076	27370	2511	1295	667	5397	698	6875	593
J84.695932-69.083807										
J84.699755-69.069803	13460	2594	14490	1408	6252	597				
J84.688990-69.084695	18340	3100								
J84.695173-69.084857										
J84.726173-69.082254	5890	2529	8198	1126						
J84.720292-69.077084	12520	2699	13480	1567					6875	593
J84.688372-69.078168										
J84.669113-69.081638										
J84.674734-69.077374										
J84.709403-69.075682										
J84.688168-69.071013										
J84.694286-69.074499										
J84.676469-69.082774										
J84.671132-69.077168										

Far Infrared Photometry For SAGE Sources in the ALMA Footprint: Columns 2-5: PACS 100 μm and 160 μm photometry and error in mJy. Columns 6-11: SPIRE 250 μm, 350 μm, and 500 μm photometry and error in mJy. Note: The flux and errors vary in significant figures. These numbers are the same as those listed in the SAGE catalog as well studies done by Chen et al. (2010); Gruendl & Chu (2009); Seale et al. (2014). Therefore we do not change them in order to be consistent.

Table 2.7: Properties of SAGE Sources in the ALMA Footprint

ID Number	Name	RA	Dec	Mass	Luminosity	Reduced	Reduced	Is It A	References
ID Number	Name	RA	Dec	[$M_\odot$]	[$L_\odot$]	$\chi^2_{\rm photosphere}$	$\chi^2_{\rm YSO\ SED}$	YSO Candidate?	References
1	J84.703995-69.079110	84.703995	-69.079110	$23.9^{+23.8}_{-7.01}$	$6.81^{+23.8}_{-4.20} \times 10^4$	209	1.63	yes	a, b, c, d, e
2	J84.695932-69.083807	84.695932	-69.083807	$21.8^{+12.0}_{-8.07}$	$5.62^{+6.49}_{-4.16} \times 10^4$	43.3	0.482	yes	e
3	J84.699755-69.069803	84.699755	-69.069803	$19.0^{+10.5}_{-5.25}$	$5.62^{+6.49}_{-4.16} \times 10^4$	333	2.67	yes	b, c, d, e
4	J84.688990-69.084695	84.688990	-69.084695	$19.0^{+9.13}_{-5.87}$	$4.64^{+5.36}_{-3.17} \times 10^4$	241	8.73	yes	a, b, c, e
5	J84.695173-69.084857	84.695173	-69.084857	$19.0^{+10.5}_{-5.87}$	$5.62^{+6.49}_{-4.16} \times 10^4$	43.3	0.482	yes	d, e
6	J84.726173-69.082254	84.726173	-69.082254	$17.3^{+15.7}_{-7.37}$	$3.16^{+5.09}_{-2.34} \times 10^4$	292	0.025	yes	b, e
7	J84.720292-69.077084	84.720292	-69.077084	$14.8^{+18.3}_{-4.79}$	$3.16^{+6.84}_{-2.48} \times 10^4$	234	9.72	yes	a, b, c, d, e
8	J84.688372-69.078168	84.688372	-69.078168	$11.8^{+21.4}_{-3.43}$	$8.25^{+207}_{-5.09} \times 10^3$	82.1	1.44	yes	e
9	J84.669113-69.081638	84.669113	-69.081638	$8.71^{+4.78}_{-2.96}$	$3.16^{+11.5}_{-2.34} \times 10^3$	36.5	0.003	yes	e
10	J84.674734-69.077374	84.674734	-69.077374	$8.51^{+4.98}_{-1.75}$	$3.83^{+13.9}_{-2.62} \times 10^3$	209	9.64	yes	e
11	J84.709403-69.075682	84.709403	-69.075682	$8.71^{+9.07}_{-2.25}$	$8.25^{+23.4}_{-7.04} \times 10^3$	6.67	2.28	no	e
12	J84.688168-69.071013	84.688168	-69.071013	$8.71^{+5.74}_{-2.68}$	$3.16^{+14.6}_{-2.34} \times 10^3$	2.17	1.13	no	e
13	J84.694286-69.074499	84.694286	-69.074499	$11.2^{+7.83}_{-3.09}$	$8.25^{+30.0}_{-5.64} \times 10^3$	3.21	64.6	no	e
14	J84.676469-69.082774	84.676469	-69.082774	$11.2^{+4.63}_{-1.67}$	$8.25^{+13.3}_{-3.61} \times 10^3$	4.37	935	no	e
15	J84.671132-69.077168	84.671132	-69.077168	$8.51^{+4.67}_{-2.20}$	$3.16^{+11.5}_{-2.16} \times 10^3$	11.3	25.9	no	e

Column 1: ID Number. Columns 5: Mass of the YSO candidate as given by the peak of the liklihood distribution and 1sigma error. Columns 6: Luminosity of the YSO candidate as given by the peak of the liklihood distribution and 1sigma error. Column 7: Reduced χ^2 of the best-fit stellar photosphere (χ^2 divided by the number of fitted points). Column 8: Reduced χ^2 of the best-fit SED model (χ^2 divided by the number of fitted points). Column 10: References: a for Seale et al. (2009), b for Seale et al. (2014), c for Gruendl & Chu (2009), d for Walborn et al. (2013), and e for this work.

Carlson et al. (2012) also used multi-color cuts, but included more of a grey zone with α and β cuts to include bluer sources at a lower reliability in comparison to Gruendl & Chu (2009). The Carlson et al. (2012) cuts are based on *Spitzer* IRAC (3.6 μm, 4.5 μm, 5.8 μm, 8.0 μm) and MIPS (24 μm) color-magnitude diagrams (CMDs). The α cut criteria can be applied to galaxy-wide surveys and has a low contamination rate. Applying α cuts selects the most massive and luminous YSOs. The β cut criteria should be applied to star-forming regions with less contamination from background sources, where it is more likely the cuts will select a YSO. Figure 2.11 shows [3.6] versus [3.5]-[5.8] CMD. YSO candidates numbered 1, 3, 4, and 7 have been previously studied (Gruendl & Chu, 2009; Seale et al., 2009, 2014). These four YSO candidates meet the Carlson et al. (2012) α cut criteria (all located to the right of the orange line). YSO candidates 2, 5, 8, and 10 have not been previously identified. YSO candidate 8 meets the Carlson et al. (2012) α cut criteria. YSO candidates 2, 5, and 10 meet the Carlson et al. (2012) β cut criteria. The YSO numbering refers to ranking from most massive to least massive YSO, as given in Table 2.6.

The 6 previously identified YSO candidates and the 4 new YSO candidates in this work are all Stage I objects as given by the peak of the likelihood distribution of $\frac{\dot{\mathrm{M}}_{\mathrm{env}}}{\mathrm{M}_{\mathrm{star}}}$. Our goal is to find out how massive star formation relates to molecular clumps. Even though we are most likely missing many later stage low-mass YSOs, our catalog of massive Stage I YSO candidates (objects >8 $\mathrm{M}_{\odot}$ in Figure 2.10) is complete.

In addition to Stage, we can characterize the SED by Type. Chen et al. (2010) conduct an empirical analysis by looking at the shape of the SEDs to classify it by Type: Type I YSOs have SEDs with a steady rise in the near infrared and a high peak at 8-24 μm, Type II YSOs have low peak in the optical and a peak in the near infrared as well, Type III have SEDs peaking in the optical with some peak in the near or mid infrared wavelengths. There is correlation between Type I and Stage I YSOs, because these objects are deeply embedding within a molecular cloud. However there is little to no correlation between the any other Type and Stage classification. Below we list each of the YSO candidates in this study and describe the SED morphology in more detail.

2.4.2.2 Details of Each YSO Candidate in Order of Most Massive to Least Massive

J84.703995-69.079110: This massive YSO candidate in our work is located in the central, most massive clump as can be seen in Figure 2.1b. The spectra for this source is shown in the top panel of Figure 2.9. This YSO candidate is in the PE group (Seale et al., 2009). There is a silicon absorption feature visible, as well as strong PAH and fine-structure line emission. There is a steep rise in the SED as shown in Figure 2.7, and a peak in the mid infrared. This object is a Type I YSO. This object also meets one of the Carlson et al. (2012) α cut criteria. Walborn et al.

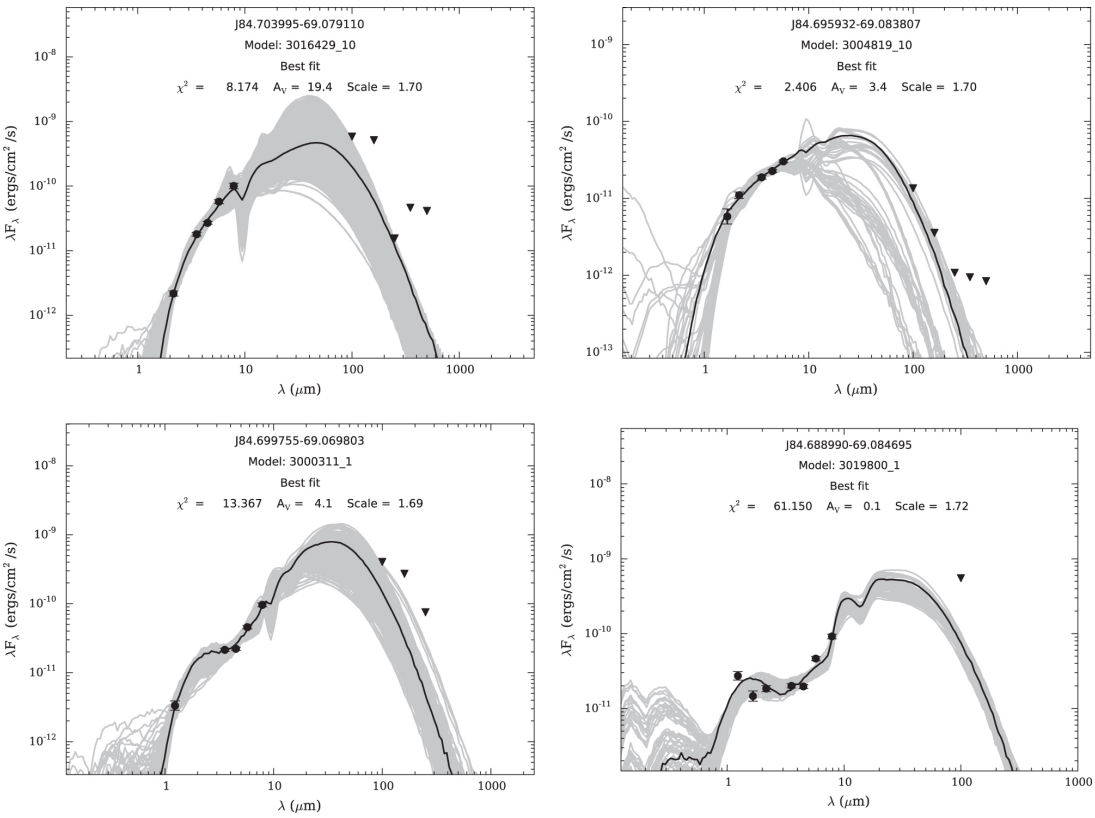

Figure 2.7: **SED fits of Four Most Massive YSOs** SED fits four most massive YSO candidates in the ALMA footprint of 30 Doradus. They are ordered from top to bottom, left to right in order of highest mass to lowest mass. Black dots are the fitted data points, black triangles are upper limits, the black line is the best fit model, and the grey lines are all models that have χ^2<3 relative to the best fit model.

(2013) find there are two water masers associated with this object and the spectral type of the object is O2.

J84.695932-69.083807: This second most massive YSO candidate is located in clump 13 (^{13}CO (2-1) clump as listed in Table 2.1), as well as clumps 14 and 25. This object also meets one of the Carlson et al. (2012) β cut criteria. There is a shallow rise from the near infrared to the far infrared wavelengths in the SED, therefore we say this is a Type II YSO. This object along with J84.695173-69.084857 is a double source and

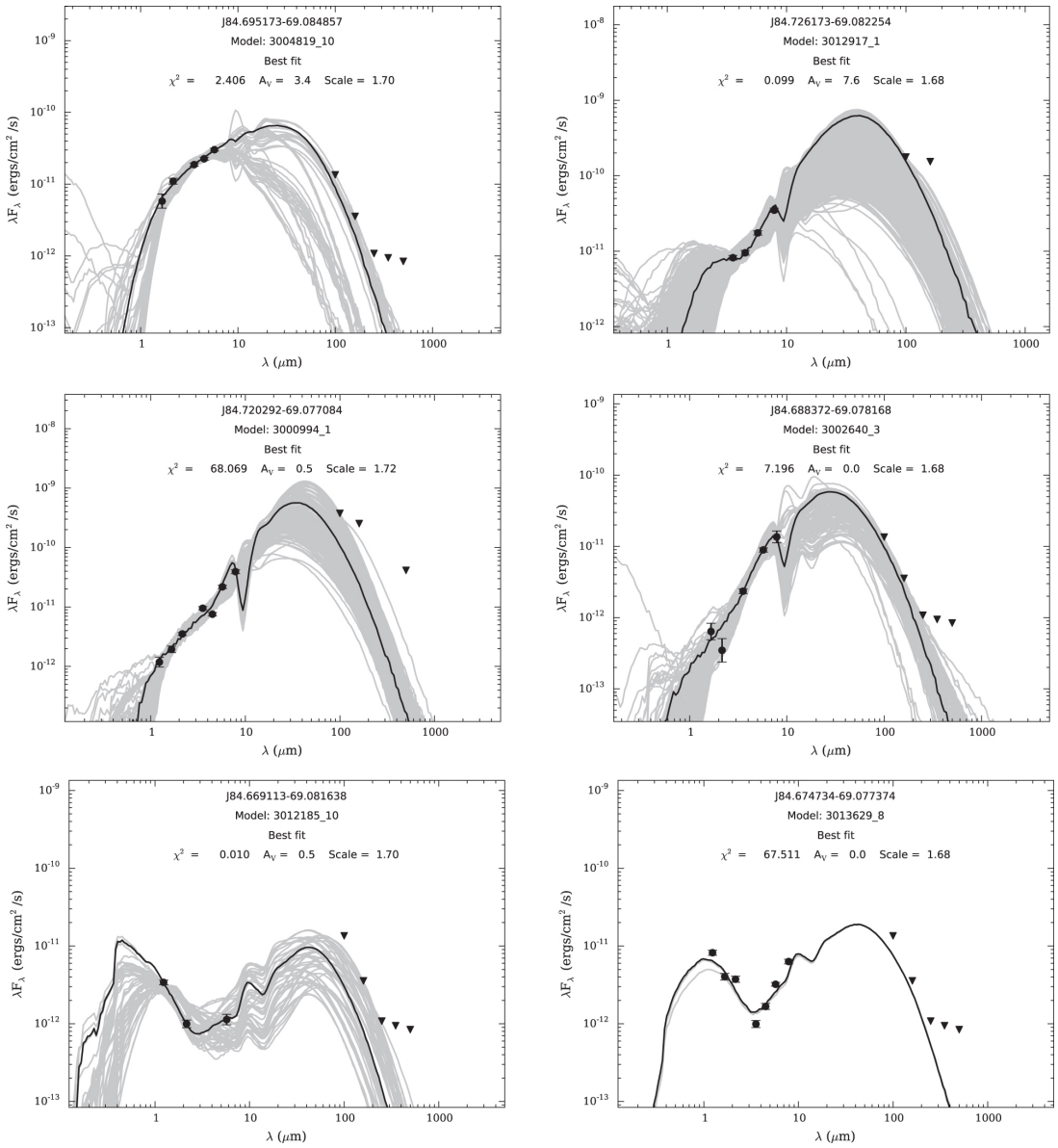

Figure 2.8: **SED fits of Other YSO Candidates** SED fits of six other YSO candidates in the ALMA footprint of 30 Doradus. They are ordered from top to bottom, left to right in order of highest mass to lowest mass. Black dots are the fitted data points, black triangles are upper limits, the black line is the best fit model, and the grey lines are all models that have χ^2<3 relative to the best fit model.

labeled as IRSN 122 and IRSN 126 by Rubio et al. (1998).

J84.699755-69.069803: The SED of the YSO candidate shows a steep rise in the IRAC bands, therefore we say this is a Type I YSO. This object also meets one of the Carlson et al. (2012) α cut criteria. Walborn et al. (2013) find this object to be a bright source surrounded by a cluster of faint sources, and the entire cluster is surrounded by a thick annulus of emission in the *Spitzer*/MIPS 24μm image.

J84.688990-69.084695: Seale et al. (2009) categorize this object to be in the PE group. The spectra is shown in the central panel of Figure 2.9. There is no silicon absorption feature, however there are strong PAH and fine-structure line emission features. A lack of silicon absorption may mean this candidate is more evolved that the other two YSO candidates that have spectra in our work(J84.703995-69.079110 and J84.720292-69.077084). This YSO candidate is located inside clump 8 (^{13}CO (2-1) clump as listed in Table 2.1). There is a double peak in the SED of this object, with one peak in the near infrared and the other peak in the far infrared. Therefore we classify this objects as a Type II YSO candidate. This object also meets one of the Carlson et al. (2012) α cut criteria.

J84.695173-69.084857: This YSO candidate is located inside clump 15 (^{13}CO (2-1) clump as listed in Table 2.1). This object meets Carlson et al. (2012) α and β cut

criteria. There is a shallow rise from the near infrared to the far infrared wavelengths in the SED, therefore we say this is a Type II YSO. This object and J84.695932-69.083807 are part of a double source as studied by Walborn et al. (2013).

J84.726173-69.082254: The SED of the YSO candidate shows a steep rise in the IRAC bands, therefore we say this is a Type I YSO.

J84.720292-69.077084: This object is in the PE group (Seale et al., 2009). The spectra shown in the bottom panel of Figure 2.9 shown silicon absorption, PAH emission, and fine-structure line emission. This YSO candidate is located inside clump 9 (^{13}CO (2-1) clump as listed in Table 2.1). There is a steep rise in the SED as shown in Figure 2.8, and a peak in the far infrared. This object is a Type I YSO. This objects meets Carlson et al. (2012) α cut criteria. Walborn et al. (2013) find a water maser near this object.

J84.688372-69.078168: This YSO candidate is located within ^{13}CO (2-1) clumps 29 and 30. This object also meets one of the Carlson et al. (2012) α cut criteria. This YSO is Type I YSO due to the prominent peak of the SED in mid infrared wavelengths. There is a steep rise in the SED as shown in Figure 2.8, and a peak in the far infrared. This object is a Type I YSO.

J84.669113-69.081638:This YSO candidate is located within ^{13}CO (2-1) clump 46 and meets one of the Carlson et al. (2012) α cut criteria. This object is a Type III YSO candidate due to the similar strength of the near infrared and far infrared peaks in the SED.

J84.674734-69.077374: This object meets the Carlson et al. (2012) α and β cut criteria. This object is a Type III YSO candidate due to the similar strength of the near infrared and far infrared peak in the SED.

2.5 Results and Discussion

2.5.1 Size, Linewidth, and Mass Surface Density

The 'universality' of Larson's law has been verified by other observations (Bolatto et al., 2008; Heyer et al., 2009; Lada, 1985) and simulations (Federrath & Klessen, 2012; Goldbaum et al., 2011). Shetty et al. (2012) study the central molecular zone (CMZ) and analyze N_2H^+, HCN, $H^{13}CN$, and HCO^+ using dendrograms. They find a slope of 0.67, 0.46, 0.78, 0.64 and a coefficient of 2.6, 3.8, 2.6, 2.1 for N_2H^+, HCN, $H^{13}CN$, and HCO^+ respectively. There is a similarity in the slope of the size-linewidth relation that is independent of the local environmental factors and independent of the particular molecular gas that is studied. Bolatto et al. (2008) find the slope to be 0.60 in extra-galactic clouds, Heyer et al. (2009) find the slope to be 0.50 in Milky Way

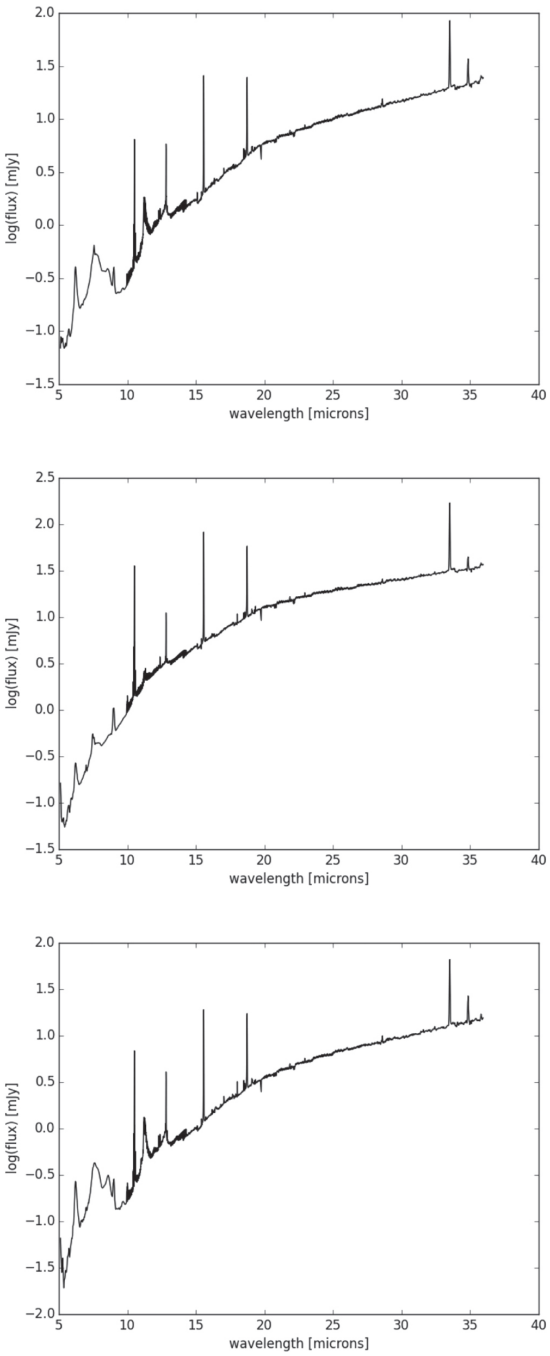

Figure 2.9: **Spectra of YSO Candidates in 30 Doradus** Spectra of YSO candidates in the 30 Doradus ALMA footprint. Top: J84.703995-69.079110. Center: J84.688990-69.084695 . Bottom: J84.720292-69.077084. Prominent features include PAH (6.2 μm), PAH (7.7 μm), PAH (8.6 μm), [ArIII] (8.99 μm), silicon absorption (9.7 μm), H_2 (9.7 μm), [SIV] (10.5 μm), PAH (11.2 μm), H_2 (12.3 μm), [NeII] (12.81 μm), [NeII] (15.55 μm), H_2 (17.1 μm), [SIII] (18.71 μm), [SIII] (33.48 μm), and [SiII] (34.81 μm).

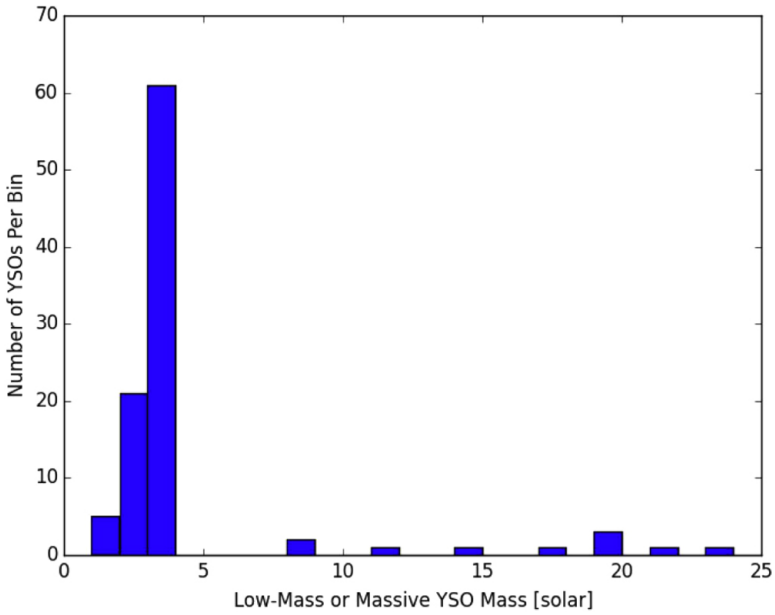

Figure 2.10: **Mass Distribution of Low-Mass YSOs** Mass distribution of low-mass and massive YSOs.

clouds, Shetty et al. (2012) find the slope to range between 0.46 and 0.78 in the CMZ for several high density tracers. This agreement in the slope of the size-linewidth relation is theorized to be because of the universality of turbulence (Heyer & Brunt, 2004).

Figure 2.12 shows the corresponding size-linewidth relation of the ^{12}CO$(2-1)$ brightness temperature clumps. In order to define a radius we use the geometric mean of the major axis radius and minor axis radius of the best-fit ellipse to the clump. The best fit line to the ^{12}CO (2-1) clumps in this study is given by the equation $\sigma = (1.66 \pm 0.06)\mathrm{r}^{(0.65\pm0.04)}$. We find the slope of the ^{12}CO (2-1) size-linewidth relation to be similar to extragalactic clouds studied by Bolatto et al. (2008), but the clumps in this 30 Doradus study have a systematic offset to larger linewidths by a

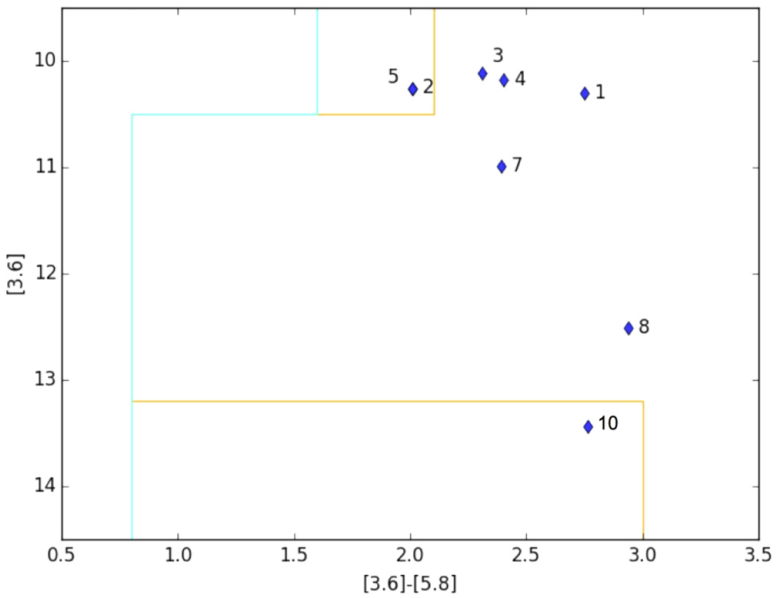

Figure 2.11: **Color Magnitude Diagram** CMD of IRAC [3.6] versus IRAC [3.6] - IRAC [5.8]. Everything to the right of the orange line fits the criteria for the Carlson et al. (2012) α cut and everything to the right of the cyan line fits the Carlson et al. (2012) β cut. Numbers next to each point correspond to the rank of the YSO candidates from most massive to least massive as listed in Table 2.6. Even though we have a total of 11 YSO candidates, we only have 8 objects plotted because a few of them are missing [3.6] or [5.8] photometry.

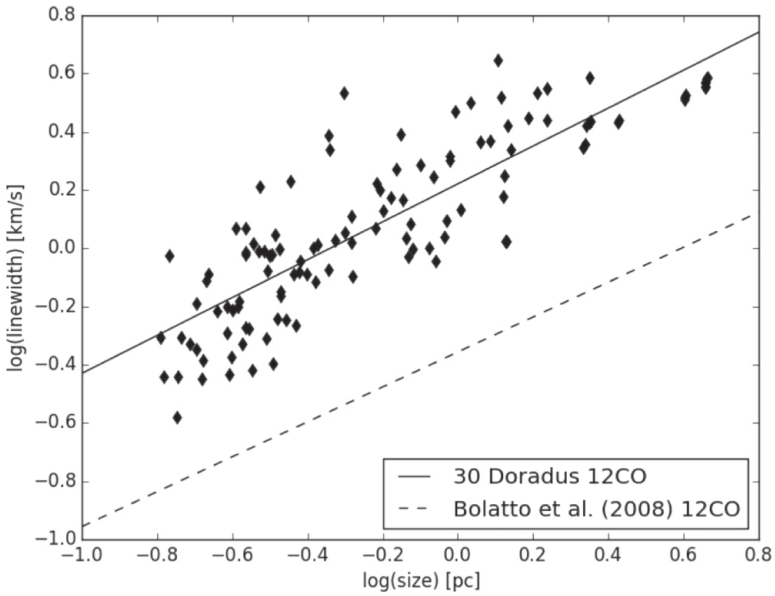

Figure 2.12: **12CO Size-Linewidth Relation** Size-linewidth relation of ^{12}CO (2-1) brightness temperature clumps. The best fit line is given by the equation $\sigma = (1.66 \pm 0.06)\mathrm{r}^{(0.65\pm0.04)}$. The dashed line, given by the equation $\sigma = 0.44\mathrm{r}^{0.60}$, is the best-fit line for extragalactic ^{12}CO molecular cloud analyzed by Bolatto et al. (2008). The ^{12}CO (2-1) linewidths of clumps in 30 Doradus are offset from extragalactic clumps by a factor of 3.8.

factor of 3.8.

Figure 2.13 shows the size-linewidth of $^{13}\mathrm{CO}(2-1)$ clumps analyzed in this work using dendrograms and $^{13}\mathrm{CO}(2-1)$ clumps analyzed by Indebetouw et al. (2013) using cprops. The astrodendro algorithm calculated smaller linewidths for a given clump size. This can be seen in Figure 2.13 and is further explained in Appendix B: the astrodendro clumps have smaller linewidth for a given size. The best-fit line for the $^{13}\mathrm{CO}(2-1)$ clumps from this study is given by the solid black line ($\sigma = (1.58 \pm 0.18)\mathrm{r}^{(0.97\pm0.12)}$). The best-fit line for the $^{13}\mathrm{CO}(2-1)$ clumps from (Indebetouw et al., 2013) is given by the solid cyan line ($\sigma = (2.39 \pm 0.33)\mathrm{r}^{(0.91\pm0.15)}$). The

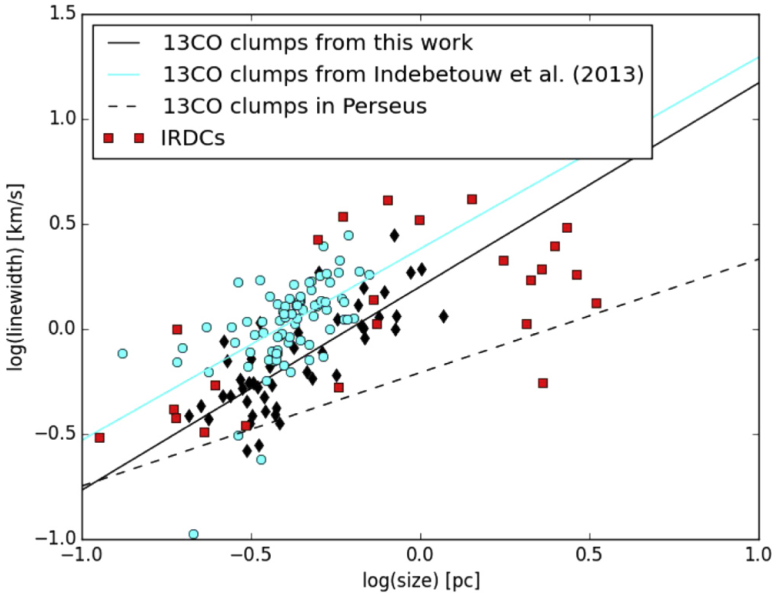

Figure 2.13: **13CO Size-Linewidth Relation** The size (of astrodendro clumps and cprops clumps) is calculated from the weighted second moment in two spatial directions, specifically the direction of greatest spatial extent and perpendicular to that. The radius is then 1.91 times the geometric mean of those two spatial second moments. The linewidth is calculated using the weighted velocity second moment of the pixels assigned to the cprops clump or astrodendro structure. Black diamonds are the size-linewidth values of ^{13}CO (2-1) clumps in this study. The best fit line of astrodendro clumps is given by the equation $\sigma = (1.58 \pm 0.18)\mathrm{r}^{(0.97\pm0.12)}$ and represented by the solid black line. Cyan circles are 30 Doradus ^{13}CO (2-1) brightness temperature size-linewidth clumps from Indebetouw et al. (2013). The Indebetouw et al. (2013) clumps are systematically offset by the clumps in this work by a factor of 1.5. This difference is because astrodendro systematically calculates smaller linewidths for clumps that are comparable in size to the clumps found by cprops. See Appendix B for further details. The best fit line of the cprops clumps is given by the equation $\sigma = (2.39 \pm 0.33)\mathrm{r}^{(0.91\pm0.15)}$ and represented by the solid cyan line. Red squares are size-linewidths from infrared dark cloud studies by Bontemps et al. (2010); Gibson et al. (2009); Peretto et al. (2013). We converted the FWHM to σ by dividing the FWHM values given in the infrared dark cloud studies by a factor of 2.35. The dashed line ($\sigma = 0.62\mathrm{r}^{0.54}$) is the best-fit line for molecular clumps in Perseus analysis by Shetty et al. (2012) using dendrograms. The 30 Doradus clumps are offset from the Perseus clumps by a factor of 2.5.

cyan points in Figure 2.13 use the same regions in position-position-velocity (PPV) space as the clumps defined using cprops and analyzed in (Indebetouw et al., 2013), but a different method to calculate size and linewidth, to be more consistent with the astrodentro calculation. In this chapter we use the same definition of size for both astrodendro clumps and cprops clumps. The size is calculated from the weighted second moment in two spatial directions. The radius is 1.91 times the geometric mean of those two spatial second moments (Solomon et al., 1987). The linewidth is calculated using the weighted velocity second moment of the pixels assigned to the cprops clump or astrodendro structure. More details of the sizes and linewidths from cprops and astrodendro can be found in Appendix C. The analysis in this work is in agreement with Indebetouw et al. (2013): the ^{13}CO$(2-1)$ clumps derived from astrodendro lie in the same parameter space as the clumps analyzed by cprops (Indebetouw et al., 2013).

One comparable analysis to our work in that of the Perseus cloud in the Milky Way by Shetty et al. (2012). The dashed line in Figure 2.13shows the results from Shetty et al. (2012) who analyzed the Perseus cloud, an ordinary Milky Way molecular cloud, using dendrograms. The best-fit equation to the dash line is given by $\sigma = 0.62\mathrm{r}^{0.54}$. The slope of the line that best fits the ^{13}CO$(2-1)$ clumps in this study is within 3σ of the slope of the line that best fits the Perseus clump analysis. The linewidths for a given clumps size in 30 Doradus are larger by a factor of 2.5 than those in Perseus. Linewidths of clumps in high pressure, high density, high star-forming environments

are on average higher than those in quiescent Milky Way clumps. This is similar to studies by Shetty et al. (2012) who find N_2H^+ and HCN clumps in the CMZ are offset by a factor of 5 in comparison to ^{13}CO clumps in Perseus. The results of this work and the results found by Indebetouw et al. (2013) show 30 Doradus clumps to have larger linewidths in comparison to ordinary Milky Way clouds. We use the same data as Indebetouw et al. (2013) in this work. However we do a more thorough analysis: we re-calculate the 'size' and 'linewidth' values output from cprops in order to match the same definition by astrodendro, we fit a line through the cprops size-linewidth relation, and compare our results quantitatively to other studies. The results of this chapter are different and supersede the results of Indebetouw et al. (2013).

Similar offset to higher linewidths has also been seen in infrared dark cloud studies in the Milky Way, as is pointed out by Indebetouw et al. (2013). There are star forming infrared dark clumps in our Galaxy with similar size, mass, linewidth, and mass surface density as those in an extreme environment like 30 Doradus. Peretto et al. (2013) study infrared dark cloud SDC335.579-0.272, located 3.25 kpc away from the Sun. Their ALMA observations show filamentary collisions with two massive star-forming cores at the intersection of the collision. Bontemps et al. (2010) study six massive and dense cores located in Cygnus X. Cygnus X is located 1.7 kpc away and contains 40 known massive dense cores (representative of the earliest phase of massive star formation). Gibson et al. (2009) use the MSX database to probe the physical

conditions of several dozens of infrared dark clouds. We plot the size-linewidth values of infrared dark cloud studies by Gibson et al. (2009), Bontemps et al. (2010), and Peretto et al. (2013) in Figure 2.13. The Milky Way infrared dark clumps are in the same size-linewidth parameter space as 30 Doradus ^{13}CO$(2-1)$ clumps. Clumps in 30 Doradus have a larger linewidths than typical Milky Way clumps, however they have similar linewidth as infrared dark clouds that are very likely forming protostars.

We investigate if the size-linewidth relation is dependent on the individual dendrogram structures. The size-linewidth relation of ^{13}CO (2-1) column density clumps is $\sigma = (1.58 \pm 0.18)\mathrm{r}^{(0.97\pm0.12)}$ (Figure 2.14). The red squares are clumps in the red dendrogram structure in Figure 2.4 ($\sigma = (1.91 \pm 0.31)\mathrm{r}^{(1.14\pm0.19)}$), the green stars are those that are in the green structure in Figure 2.4 ($\sigma = (1.12 \pm 0.11)\mathrm{r}^{(0.58\pm0.11)}$), and the cyan circles are clumps in the cyan structure in Figure 2.4
($\sigma = (1.25 \pm 0.69)\mathrm{r}^{(0.60\pm0.48)}$). For each structure traced in different colors, we fit a slope and intercept. We compare the intercepts with each other and all the intercept values are 1-2σ away from each other. We then compare the slopes of the line fit to the different structures and we find the slopes are also 1-2σ away from each other. We then investigate if the size-linewidth is dependent upon if a clump is forming a star or not. The size-linewidth relation of ^{13}CO (2-1) clumps that are associated with YSOs ($\sigma = (1.58 \pm 0.18)\mathrm{r}^{(0.90\pm0.17)}$) and those that are not ($\sigma = (1.86 \pm 0.26)\mathrm{r}^{(0.91\pm0.14)}$) in Figure 2.15. The size-linewidth of ^{13}CO (2-1) clumps is the same for clumps with

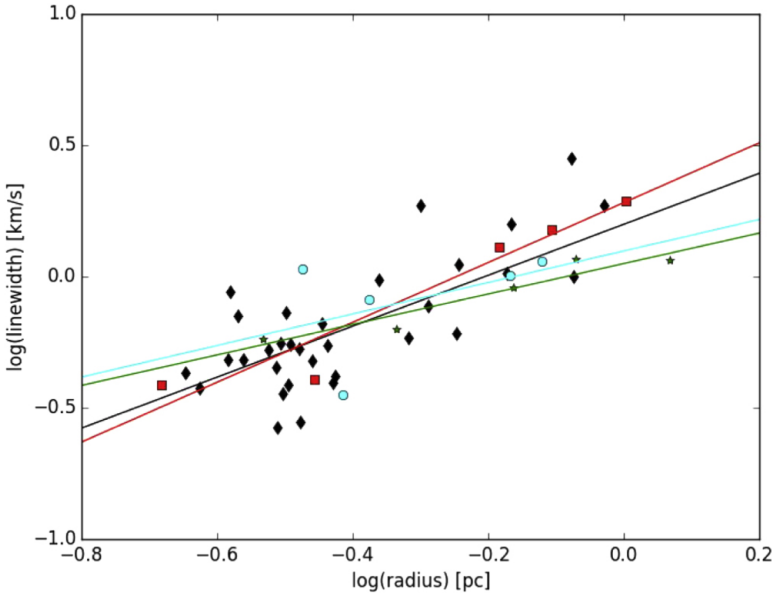

Figure 2.14: **13CO Size-Linewidth Relation in Different Dendrogram Trees** Size - linewidth relation of ^{13}CO (2-1) brightness temperature clumps. The best-fit line of all clumps is given by $\sigma = (1.58 \pm 0.18) r^{(0.97 \pm 0.12)}$. The red squares are clumps in the red dendrogram structure in Figure 2.4 ($\sigma = (1.91 \pm 0.31) r^{(1.14 \pm 0.19)}$), the green stars are those that are in the green structure in Figure 2.4 ($\sigma = (1.12 \pm 0.11) r^{(0.58 \pm 0.11)}$), and the cyan circles are clumps in the cyan structure in Figure 2.4 ($\sigma = (1.25 \pm 0.69) r^{(0.60 \pm 0.48)}$). The red line is the best-fit line to the red squares, the green line is the best-fit line to the green stars, and the cyan line is the best-fit line to the cyan circles. There are a total of five each of red squares, green stars, and cyan circles plotted.

YSOs and those without. Individual star forming clumps have different mass, temperature, pressure conditions. Clumps with star formation taking place within them, and those with no observable star formation also should have different conditions. We thought local variations due to properties of the cloud or star formation happening would result in a different size-linewidth relation. However these differences in the local environment are negligible in comparison to the overall conditions in the regions of 30 Doradus we study in this work.

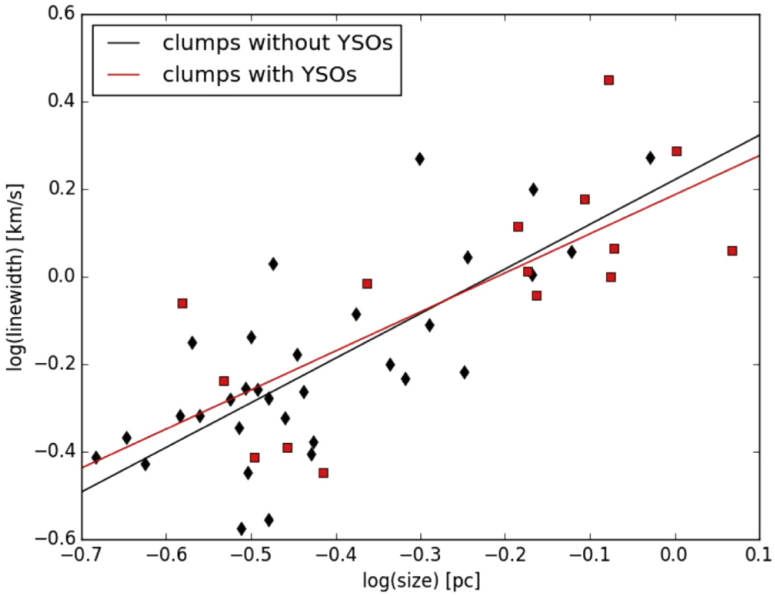

Figure 2.15: **13CO Size-Linewidth Relation of Clumps With and Without Massive Star Formation** Size-linewidth relation of ^{13}CO (2-1) column density clumps. The black diamonds are clumps not associated with any star formation and the best fit line is given by $\sigma = (1.66 \pm 0.31)\mathrm{r}^{(1.02\pm0.17)}$. The red squares show the clumps in our study that are are associated with star formation and the best fit line is given by $\sigma = (1.53 \pm 0.25)\mathrm{r}^{(0.89\pm0.22)}$. There is no noticeable difference in the slope or the intercept of the size-linewidth relation between clumps with active star formation and those without.

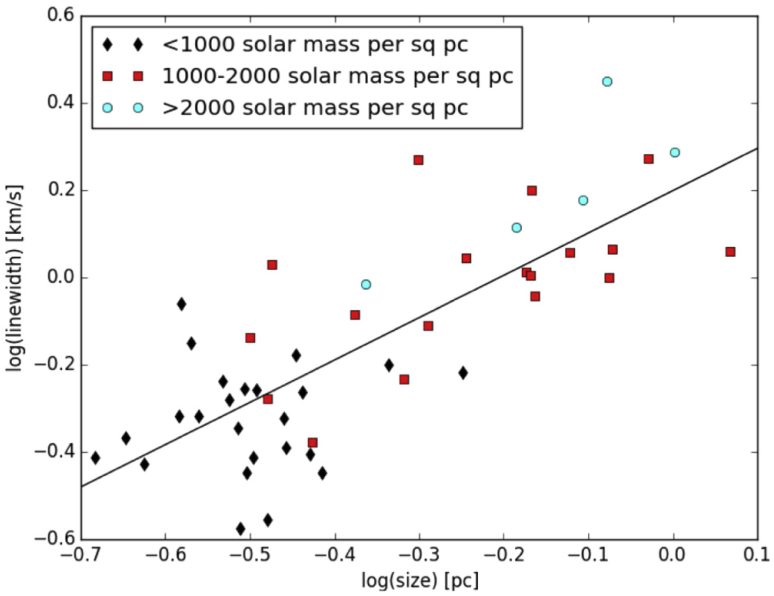

Figure 2.16: **13CO Size-Linewidth Relation of Clumps With Different Densities** Size-linewidth relation of ^{13}CO (2-1) column density clumps. The best fit line is $\sigma = (1.58 \pm 0.18)\mathrm{r}^{(0.97\pm0.12)}$. Black diamonds are clumps with mass density less than 1000 $M_\odot$ pc^{-2}, red squares are clumps with mass density between 1000-2000 $M_\odot$ pc^{-2}, and cyan circles are clumps with mass density above 2000 $M_\odot$ pc^{-2}.

Larson's first law suggests that the linewidth of a clump is only dependent on the size, $\sigma \propto \mathrm{r}^{0.5}$. We look into whether the universality of Larson's first law applied to the clumps in 30 Doradus. We assume the clumps are self-gravitating and say the observed cloud mass is the virial mass:

$$M_{obs} = \frac{5\sigma^2 r}{G}. \tag{2.1}$$

We can substitute the molecular gas surface density ($\Sigma = \frac{\mathrm{M_{obs}}}{\pi \mathrm{r}^2}$) and solve for the linewidth:

$$\sigma = \left(\frac{\pi G}{5}\right)^{0.5} \Sigma^{0.5} r^{0.5}. \tag{2.2}$$

The linewidth of a clump depends on the spatial extent as well as the mass surface density. Figure 2.16 shows the size-line width for ^{13}CO (2-1) colorized by mass surface density: black diamonds for clumps with mass density less than 1000 $\mathrm{M_\odot\ pc^{-2}}$, red squares are clumps with mass density between 1000-2000 $\mathrm{M_\odot\ pc^{-2}}$, and cyan circles are clumps with mass density above 2000 $\mathrm{M_\odot\ pc^{-2}}$. We find clumps with larger sizes and linewidths tend to have larger mass surface densities.

We follow a similar approach to Heyer et al. (2009) and look at the dependence of the size and linewidth on the mass surface density. Heyer et al. (2009) find that Larson's scaling relations are not universal. If Σ in Equation 2 is constant, then you can recover Larson's first law ($\sigma = \nu\ \mathrm{r}^{0.5}$, where ν is a constant). This means that $\frac{\sigma}{\mathrm{r}^{0.5}}$

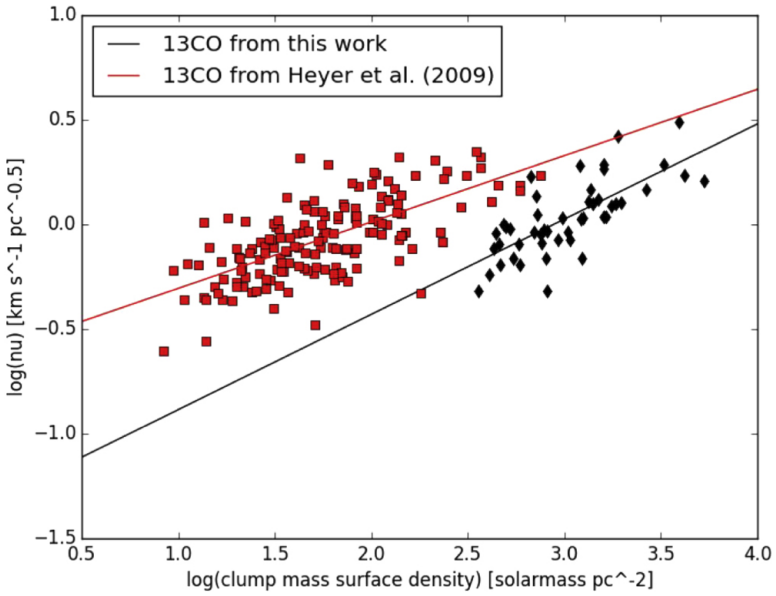

Figure 2.17: $\frac{\sigma}{r^{0.5}}$ **Versus** Σ The black line ($\nu = (0.04 \pm 0.02)\Sigma^{(0.45\pm0.06)}$) is the best-fit line is going through ν versus Σ of 30 Doradus clumps in this study. The red line ($\nu = (0.24 \pm 0.02)\Sigma^{(0.31\pm0.04)}$) is the best-fit line going through ν versus Σ of clumps studied by Heyer et al. (2009). The dependence on Σ is contradictory to Larson's scaling relation, but consistent with the slope found by Heyer et al. (2009).

$= (\frac{\pi G\Sigma}{5})^{0.5} = \nu$, which is a constant. If Larson's first law is to hold, then we should see a flat horizontal line when we plot ν versus Σ. Figure 2.17 shows that ν is not constant with respect to Σ, which is contradictory to Larson's first scaling law. We find that $\nu \propto \Sigma^{0.45}$. This is similar to the study done by Heyer et al. (2009). They too find a dependence of $\frac{\sigma}{r^{0.5}}$ on Σ (Figure 7 in their paper). The slope of the line is not reported in their paper. We take the linewidth, size, and mass values they report and calculate ν and Σ. Heyer et al. (2009) results show that $\nu \propto \Sigma^{0.31}$. Our findings of scaling relations between size, linewidth, and mass surface density lead us to the same conclusion as Heyer et al. (2009): Larson's velocity scaling relationships are not universal.

2.5.2 Energy Balance

We can further analyze the dynamics of the clumps by comparing the kinetic energy and the gravitational energy. We define the virial parameter, α, to be equal to $\frac{5\sigma^2\,\mathrm{r}}{\mathrm{G\,M}}$ - the ratio of the kinetic potential energy to the gravitational potential energy (McKee & Zweibel, 1992; Rosolowsky et al., 2008). When $\alpha<1$, the object is self-gravitating. Figure 2.18 shows the virial parameter as a function of clump mass on a log-log plot. The smaller mass clumps embedded within the larger mass clumps have a larger kinetic energy compare to the larger mass. We find larger clumps to have a larger gravitational potential energy than the smaller clumps: 72% of the ^{13}CO (2-1) clumps have a virial parameter equal to 1 or less. Larger clumps in this study tend to have multiple YSO candidates, whereas smaller clumps tend to have one or no YSO candidates associated with them.

We compare our results with Milky Way studies in order to see how star-forming clumps in two different galaxies differ from each other. We plot virial parameter versus clump mass of infrared dark clouds studied by Gibson et al. (2009), Bontemps et al. (2010), and Peretto et al. (2013) in Figure 2.18. These Milky Way clumps found via analysis of dark clouds could contain a few massive YSOs or hundreds of low-mass YSOs (Bontemps et al., 2010). Mass constraints on these stars have not been placed yet. ALMA observations of Dark cloud SDC335.579-0.272 show that it is one of the most massive, compact protostellar cores ever observed in the Galaxy and could potentially form an OB cluster similar to the Trapezium cluster in Orion

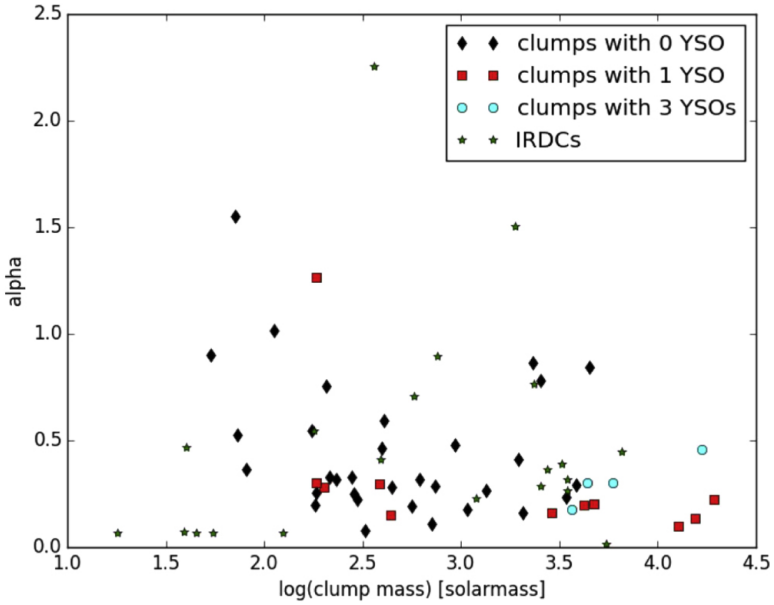

Figure 2.18: **Virial Parameter Versus Clump Mass** Figure showing the relation between the virial parameter versus the mass of the clump. We define α to equal to $\frac{5\sigma^2 \, \mathrm{r}}{\mathrm{G\,M}}$. Black diamonds are clumps with no YSO candidates, red squares are clumps with 1 YSO candidate, and cyan circles are clumps with 3 YSO candidates. Green stars are from infrared dark cloud studies by Bontemps et al. (2010); Gibson et al. (2009); Peretto et al. (2013).

(Peretto et al., 2013). The virial parameter versus mass value of this cluster is located close to the gravitationally bound massive star forming clumps in Figure 2.18 (the green star located at the bottom right). Orion is the nearest region of massive star formation, and therefore Orion and massive star formation sites similar to Orion provide the best comparison to 30 Doradus. Figure 2.18 shows star formation can take place in a wide range of conditions within infrared dark clouds: there are several low-mass gravitationally-unbound clumps that are forming stars and gravitationally-bound clumps 1000s of solar masses in size that are forming stars. However the virial conditions of dark cloud SDC335.579-0.272, a potential massive star formation location in the Milky Way, seems similar to massive star forming clumps in 30 Doradus.

There are a total of 15 star forming clumps, out of which 14 have a virial parameter equal to 1 or less. The majority (75%) of clumps with masses greater than log(clump mass)=3.5 are associated with a YSO, but only 17% of clumps with masses less than log(clump mass)=3.5 are associated with a newly forming star. It is possible that the ^{13}CO (2-1) line is not fully thermalized, therefore leading to an underestimate of the true mass. If the mass we report is underestimated, then the virial parameter we calculate would be overestimated. The points in Figure 2.18 would shift down and to the right in this hypothetical scenario if we could calculate the true mass. We would still find 14, or perhaps even all 15, of the star forming clumps to be gravitationally bound (α<1). We would also still find the majority of high-mass clumps are asso-

ciated with star formation. We do not have the whole CO ladder to calculate the true mass, however the possibility of ^{13}CO (2-1) not being fully thermalized does not affect our conclusions about the dynamical state of the clumps.

2.5.3 Which Clumps Have Newly Forming Stars and Which Do Not

We use the effective radius of the column density clumps to determine if there are any YSOs associated with the clumps. We find 7/87 more evolved low-mass YSOs and 7/10 massive young YSO candidates are associated with clumps. The 7 massive YSOs that are found within a clump are: J84.703995-69.079110 [1], J84.695932-69.083807 [2], J84.688990-69.084695 [4], J84.695173-69.084857 [5], J84.720292-69.077084 [7], J84.688372-69.078168 [8], J84.669113-69.081638 [9] (the numbers are the same as those in Table 2.6). The reason for a higher percentage of massive YSOs to be associated with clumps than low-mass YSOs is consistent with massive YSOs being at an earlier evolutionary stage. The molecular cloud surrounding stars quickly dissipate due to the strong UV radiation from the central stars. Massive YSOs are much younger than low-mass YSOs in this study and therefore still can sometimes be found in their parental cloud. We are missing low-mass embedded YSOs. Tachihara et al. (2001) study the Lupus star-forming region with ^{12}CO NANTEN data and find 40% of the more evolved low-mass YSOs in their study are

associated with clumps less than <20 $M_{\odot}$, which suggests that more evolved low-mass YSOs form in small clouds and then the parental cloud rapidly dissipates. We see more evolved low-mass YSOs (stars less than 3 $M_{\odot}$ in Figure 2.20a) projected against, and thus perhaps forming in clouds a few hundred solar masses to several tens of thousands solar masses. It is not clear if the lack of many more evolved low-mass YSOs associated with clumps is due to them moving away from the parental clump over time or if the parental clump of the young star has dissipated over time. Another reason of finding a smaller fraction of more evolved low-mass YSOs associated with clumps is because low-mass YSOs are fainter and harder to detect due to the sensitivity limits of the surveys.

Figure 2.19 shows the difference in clump mass and H_2 mass surface density distributions between clumps that do contain massive or low-mass YSOs versus clumps that do not. The distributions of clumps with massive or low-mass YSOs and those without are very different. The mass distribution of clumps without massive or low-mass YSOs is quasi normal, and the mass surface density distribution of clumps without massive or low-mass YSOs is uniform. Both the mass distribution and the mass surface density distribution of clumps with massive or low-mass YSOs are mostly uniform, but do have a noticeable peak in the center. The mass distribution and mass surface density distribution of clumps with star formation span a higher range in values than those without star formation: for example Figure 2.19 shows clumps

without any stars have masses up to log(clump mass) = 3.75, but clumps with YSOs have masses up to log(clump mass) = 4.50. The average mass, column density, and mass surface density of clumps without any YSOs are 957 $M_\odot$, 6.1×10^{22} cm^{-2}, and 957 $M_\odot$ pc^{-2}. The distribution of clumps with massive or low-mass YSOs is centered at x6 higher mass, x2 higher column density, and x2 higher mass surface density. Figure 2.20a shows the mass of YSO versus the clump mass. Structures are designed such that the clumps may be concentric (one clump within another clump), therefore there are stars that are counted more than once. If a YSO is associated with a small clump, then it is also associated with the larger clump the smaller clump is embedded in. Only 20% of clumps smaller than 1778 $M_\odot$ ($10^{3.25}$ $M_\odot$) have a YSO above 10 $M_\odot$, whereas 66% of clumps larger than 1778 $M_\odot$ have a YSO above 10 $M_\odot$. Figure 2.20b shows that 46% of clumps with H_2 mass surface density less than 2512 $M_\odot$ pc^{-2} ($10^{3.40}$ $M_\odot$ pc^{-2}) have a massive YSO, but 71% of of clumps with mass surface density more than 2512 $M_\odot$ pc^{-2} have a massive YSO. Larger mass clumps are more likely to form larger mass stars than smaller mass clumps.

The lowest surface density clump with a massive YSO forming in it provides us with a lower limit on the threshold above which high-mass star formation can occur: massive star formation appears to occur in clumps with mass $>1.83 \times 10^2$ $M_\odot$, surface density $>6.67 \times 10^2$ $M_\odot$ pc^{-2}, and turbulence >1.18 km/s. It is possible there are clumps with lower masses and lower surface densities forming low-mass YSOs. Future studies that find lower mass YSOs may push this mass surface density value lower.

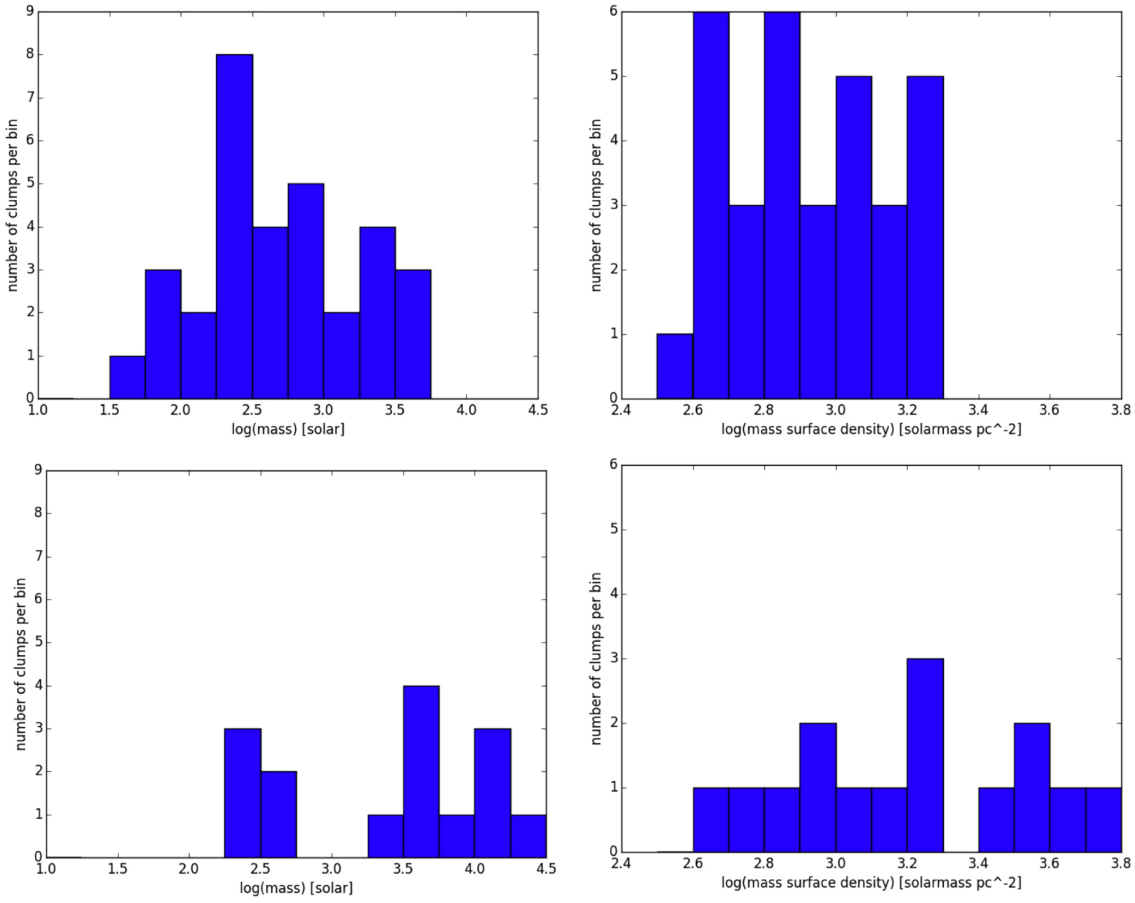

Figure 2.19: **Mass and Density Distribution of Clumps With and Without YSOs** Left Column: Mass distribution of clumps without (top) and with (bottom) YSO candidates. Right Column: Mass surface density distribution of clumps without (top) and with (bottom) YSO candidates.

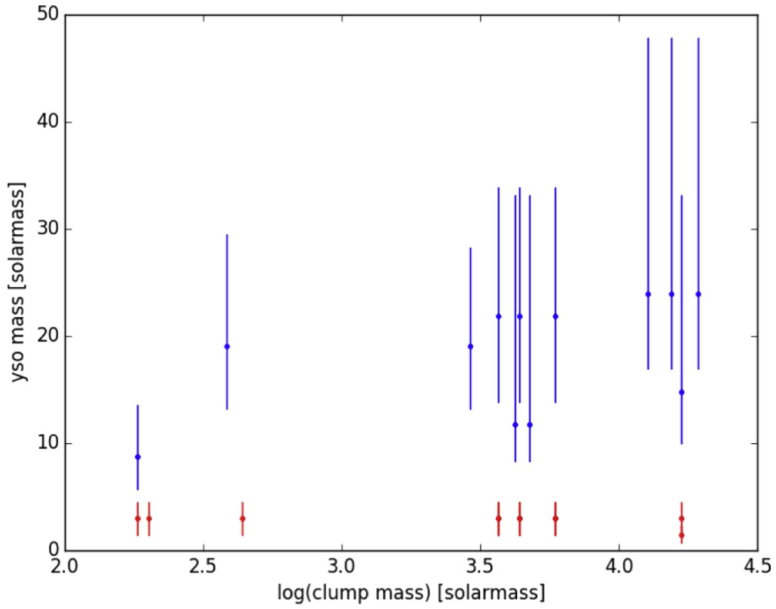

(a)

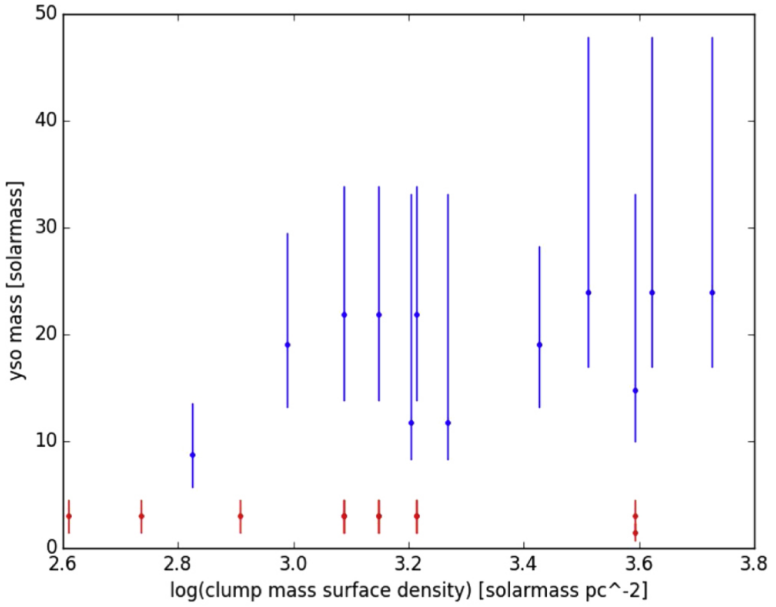

(b)

Figure 2.20: **Protostar Mass Versus Clump Mass** (a) Star mass versus clump mass for each newly forming star. Red circles represent the low-mass more evolved YSO candidates selected via Hα excess. Blue circles represent the massive YSO candidates selected by SED fitting. (b) Star mass versus clump mass surface density for each newly forming star. Red circles represent the low-mass more evolved YSO candidates selected via Hα excess. Blue circles represent the massive YSO candidates selected by SED fitting.

However, 30 Doradus is a very extreme star forming environment and more turbulent than typical GMCs in the Milky Way. The specific region we are analyzing in this study is 10 pc North of the R136 supercluster and is most likely influenced by the radiation field of R136. If there is more turbulence, then we would need higher densities and mass surface densities for star formation to occur. The mass surface density threshold in this study is 5 to 6 times higher than mass thresholds necessary to form stars as observed by Heiderman et al. (2010), Lada et al. (2010), and Kennicutt & Evans (2012). Heiderman et al. (2010) use extinction maps to determine the gas surface density of Galactic star forming regions and find a threshold of 129 $M_\odot$ pc^{-2}. Lada et al. (2010) find similar values for the gas surface density: 116 $M_\odot$ pc^{-2}. The thresholds determined from Galactic studies applies to low-mass star formation. The surface density threshold of $>6.67 \times 10^2$ $M_\odot$ pc^{-2} we place in the ALMA footprint of 30 Doradus is for massive star formation.

Dunham et al. (2011) study high density gas tracer NH_3 and measure an average mass density threshold of 176 $M_\odot$ pc^{-2} for star forming clumps in the Milky Way. Rathborne et al. (2014) study nearby clouds and compare them to clouds in the CMZ. Observations of solar neighborhood clouds suggest a column density threshold of 1.4×10^{22} cm^{-2} (Lada et al., 2010). However the universality of this value is questioned since theoretical models predict the threshold for star formation is dependent on the density and the Mach number (Krumholz et al., 2005). Even though

the CMZ has a much higher column density than 1.4×10^{22} cm^{-2}, it is producing orders of magnitude fewer stars than predicted. Rathborne et al. (2014) find that the density threshold for star formation locally is 10^4 cm^{-3}, however the CMZ with much higher turbulence has a density threshold of 10^8 cm^{-3}. Star formation is dependent on the local environment, with regions of high turbulence having a higher threshold to overcome in order for the star formation process to occur.

2.6 Conclusion

We look at YSOs that are within the ALMA CO footprint of 30 Doradus to conduct a comprehensive analysis of the molecular gas and the stars that form within them. We analyze the CO clumps using dendrograms. The ^{13}CO (2-1) molecular gas clumps analyzed using dendrograms have sizes that range from 0.23 - 1.17 pc, masses that range from 53 - 19300 $M_\odot$, and linewidths that range from 0.27 - 2.81 km/s. There are several conclusions we come to with our analysis of CO clumps and YSOs as listed below.

1. We find ^{13}CO (2-1) clumps to have a larger linewidth for a given size than previous studies done with the Perseus cloud (Shetty et al., 2012). A larger linewidth is not dependent on the size scale, and not dependent on if star formation is taking place in a clump or not. Local environmental factors (high star formation rate, high densities, and high pressures) in 30 Doradus can explain why we find clumps to have a larger

linewidth for a given size. Our result is similar to studies by Shetty et al. (2012) who find clumps in the CMZ have a slope of 0.5 in the size-linewidth relation, but are offset higher compared to the Perseus cloud due to the local environmental conditions. We find the slope of the size-linewidth relation of ^{12}CO (2-1) and ^{13}CO (2-1) molecular gas to be consistent within 3σ of previous studies (Bolatto et al., 2008; Heyer et al., 2009; Shetty et al., 2012).

2. Higher mass clumps have a tendency to have a lower viral parameter and contain multiple YSOs in comparison to lower mass clumps.

3. We find a total of 10 massive YSOs (4 new YSO candidates) with masses between 8.5-24.0 $M_\odot$, and 87 more evolved low-mass YSOs with masses between 1-3 $M_\odot$ in the region of interest.

4. There is a difference in distribution of the mass and H_2 column density of clumps that do not contain any newly forming stars and those that do. The mass and column density of clumps without stars falls off quickly and tend to be lower on average than clumps with stars. The clumps that has the lowest surface density, but still hosts a massive YSO candidate provides us with lower limits necessary for star formation. It is necessary for clumps to have high masses ($>1.83 \times 10^2$ $M_\odot$), high linewidths (v >1.18 km/s), and high mass densities ($>6.67 \times 10^2$ $M_\odot$ pc^{-2}) in order for massive

star formation to occur. This threshold was found by looking at the least massive ^{13}CO clump that is forming a massive YSO.

5. A higher fraction of young and massive YSO candidates are found within clumps (7/10) than the more evolved low-mass YSOs (7/87). This is because the more evolved low-mass YSOs in this study are older, and therefore have moved away from their parental clump. Our inventory of young forming stars is not sensitive to the very embedded low-mass YSOs.

6. We look at the dependence of the size-linewidth relation to the mass surface density. There is a dependence of $\frac{\sigma}{\mathrm{r}^{0.5}}$ on Σ. This is contradictory to Larson's scaling relationships. Assuming the clumps are is gravitational equilibrium and making relevant substitutions (see Section 2.5.1), we derive $\sigma = \left(\frac{\pi G}{5}\right)^{0.5} \Sigma^{0.5} r^{0.5}$. Larson's third scaling relation states that Σ is approximately constant for all clouds. Re-arranging the equation we derived and taking into account Larson's third scaling relations leads to the conclusion that the slope of $\frac{\sigma}{\mathrm{r}^{0.5}}$ versus Σ should be 0. However we do not find the slope to be 0 (Figure 2.17). It is possible that Larson's scaling relationships are not universal.

7. The virial parameter of massive clumps in 30 Doradus forming multiple YSOs is similar to SDC335.579-0.272, an infrared dark cloud in the Milky Way that is most

likely forming massive stars.

2.7 Acknowledgements

This research made use of astrodendro, a Python package to compute dendrograms of Astronomical data (http://www.dendrograms.org). This research also made use of Astropy (http://www.astropy.org). Meixner, Indebetouw, and Nayak were supported by NSF grant 1312902. Sabbi and Panagia were supported by STScI grant GO-12939. We are grateful for discussions with the following astronomers while writing this chapter: Dr. Marta Sewilo, Dr. Olivia Jones, Dr. Bram Ochsendorf, Kirill Tchernyshov.

Chapter 3

Molecular Cloud Structures and Massive Star Formation in N159

Abstract

The N159 star forming region is one of the most massive giant molecular clouds (GMCs) in the Large Magellanic Cloud (LMC). We show the ^{12}CO, ^{13}CO, CS molecular gas lines observed with ALMA in N159 West (N159W) and N159 East (N159E). We relate the structure of the gas clumps to the properties of 24 massive young stellar objects (YSOs) that include 10 newly identified YSOs based on our search. We use dendrogram analysis to identify properties of the molecular clumps such as: flux, mass, linewidth, size, and virial parameter. We relate the YSO properties to the molecular gas properties. We find that the CS gas clumps have a steeper size-linewidth

relation than the ^{12}CO or ^{13}CO gas clumps. This larger slope could potentially occur if the CS gas is tracing shocks. The virial parameters of the ^{13}CO gas clumps in N159W and N159E are low (<1). The threshold for massive star formation in N159W is 501 $M_{\odot}$ pc^{-2}, and the threshold for massive star formation in N159E is 794 $M_{\odot}$ pc^{-2}. We find that ^{13}CO is more photodissociated in N159E than N159W. The most massive YSO in N159E has cleared out a molecular gas hole in its vicinity. All the massive YSO candidates in N159E have a more evolved spectral energy distribution Type in comparison to the YSO candidates in N159W. These differences lead us to conclude that the giant molecular cloud complex in N159E is more evolved than the giant molecular cloud complex in N159W.

3.1 Introduction

Our goal in this chapter is to relate the massive young stars to the sub-parsec molecular gas clumps in order to better understand current star formation theories. One of the most studied clusters in the LMC is the R136 supercluster, located at the center of 30 Doradus. The R136 supercluster contains over 70 O stars, making the 30 Doradus region one of the most bright at optical wavelengths. The previous chapter discuesses the ALMA observations of molecular gas in 30 Doradus in relation to the YSOs in the region. Even though 30 Doradus is one of the brightest sources in optical wavelengths, N159 is the most massive GMC in the galaxy. N159 is a significantly

younger region in comparison to 30 Doradus and is located at the South-West tip of 30 Doradus. Studies of the CO gas content of N159 reveal the complex chemistry and physical conditions under which star formation takes place. Fukui et al. (2008) surveyed the LMC in $^{12}CO(1-0)$ emission line using NANTEN and found N159 shows the highest $^{12}CO(1-0)$ intensity out of the 272 total clouds surveyed. GMCs are the birthplace of massive stars. Therefore N159 is an ideal location to study the very early stages of massive star formation where several of the protostars are less than 100 Myrs old (Fukui et al., 2015). N159 is also the location where the first extragalactic protostar was identified by Gatley et al. (1981).

We use high resolution ALMA data (Fukui et al., 2015; Saigo et al., 2017) in conjunction with the YSO candidates identified via multi-wavelength photometry to get a better understanding of the effect of massive star formation on their prenatal environment. In Section 3.2 we discuss the observations used in this study. Section 3.3 describes our ALMA results in N159W and N159E. Section 3.4 gives details on how we select massive YSO candidates. In Section 3.5 we implement a dendrogram method to make a catalog of the clumps. In Section 3.6 we relate our results to several star formation theories. We compare our findings to previous analysis of the N159 region, as well as the 30 Doradus region and the Milky Way. Our conclusions are given in Section 3.7.

3.2 Observation of Molecular Gas Clouds and Massive Young Stellar Objects

3.2.1 ALMA Observations of N159W and N159E

We observe N159W and N159E in ALMA Cycle 1 using the Band 3 (86-116 GHz) and Band 6 (211-275 GHz) receivers (Project Code: 2012.1.00554.S, PI: Y. Fukui). The Band 6 12m observations of N159W were taken at an average elevation of 29°, consists of 33 pointings using 25 antennae, and cover a map size of 80" x 50" (19 pc x 12 pc at a distance of 50 kpc). The Band 3 12m observations of N159W were taken at an average elevation of 20°, consists of 7 pointings using 25 antennae, and covers a map size of 80" x 50". The Band 6 12m observations of N159E were taken at an average elevation of 28°, consists of 33 pointings using 27 antennae, and cover a map size of 63" x 74" (15 pc x 18 pc at a distance of 50 kpc). The Band 3 12m observations of N159E were taken at an average elevation of 29°, consists of 7 pointings using 27 antennae and covers a map size of 63" x 74". ALMA 7m observations of N159W Band 3 (map size: 80" x 50", pointings: 3), N159W Band 6 (map size: 80" x 50", pointings: 11), N159E Band 3 (map size: 63" x 74", pointings: 14), and N159E Band 6 (map size: 63" x 74", pointings: 3) were taken, however we do not use this data in our analysis. The sensitivity of the 7m observations (which depends on total integration and sky conditions) was not good. This made the quality of the flux recovered from

ALMA 7m observations poor. Band 6 mosaic observations included four spectral windows with three molecular lines observations and one continuum observation in a single correlator setup. The molecular gas lines in Band 6 include ^{12}CO$(2-1)$, ^{13}CO$(2-1)$, and C^{18}O$(2-1)$. Band 3 mosaic observations included three spectral windows with three molecular lines observations in a single correlator setup. The molecular gas lines in Band 3 include ^{13}CO$(1-0)$, C^{18}O$(1-0)$, and CS$(2-1)$ In this chapter we focus on the ^{12}CO$(2-1)$ and ^{13}CO$(2-1)$ molecular line data in N159 W and N159E, previously discussed in Fukui et al. (2015) and Saigo et al. (2017). We also show for the first time the CS$(2-1)$ molecular line observation in N159W and N159E. The C^{18}O$(2-1)$, C^{18}O$(1-0)$, and ^{13}CO$(1-0)$ will be discussed in an upcoming paper (Tokuda et al., in prep). The properties of of the N159W and N159E ALMA fields are listed in Table 3.1. Figure 3.1 shows the ^{12}CO$(2-1)$, ^{13}CO$(2-1)$, and CS$(2-1)$ ALMA observations of N159W and N159E.

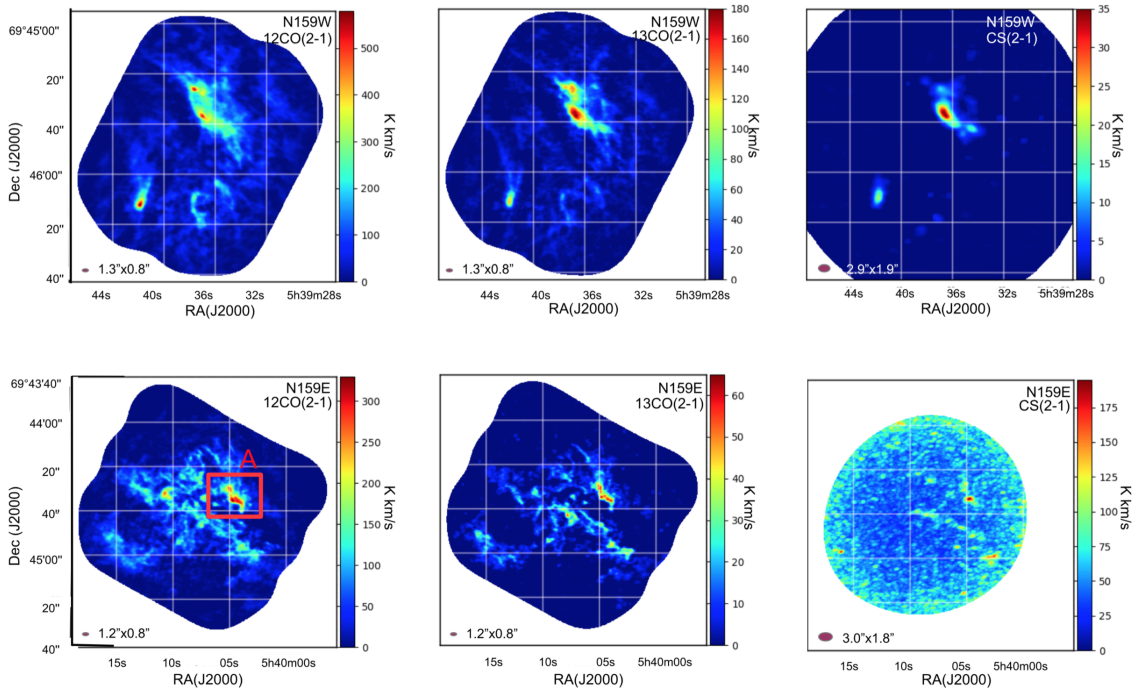

Figure 3.1: The integrated ^{12}CO, ^{13}CO, and CS ALMA 12m observations of N159 West (N159W) and N159 East (N159E) in the top and bottom row, respectively. The top left panel shows the N159W ^{12}CO map. The top middle panel shows the N159W ^{13}CO map. The top right panel shows the N159W CS map. The bottom left panel shows the N159E ^{12}CO map. The location of the Papillon Nebula is shown with the red box labeled A. The bottom middle panel shows the N159E ^{13}CO map. The bottom right panel shows the N159E CS integrated map.

Table 3.1: ALMA Observations Properties

Object	Line	Transition	Frequency [Ghz]	Bandwidth	Channel Width Resolution [km/s]	Beam Size	Precipitable Water Vapor [mm]
N159W	^{12}CO	2-1	230.356	58.6 MHz (76.3 km/s)	30.52 kHz (0.040 km/s)	1.35" x 0.86"	0.2	0.50
N159W	^{13}CO	2-1	220.224	58.6 MHz (79.8 km/s)	30.52 kHz (0.042 km/s)	1.35" x 0.86"	0.2	0.50
N159W	CS	2-1	97.903	58.6 MHz (179.4 km/s)	30.52 kHz (0.093 km/s)	2.89" x 1.96"	0.2	0.54
N159W	C^{18}O	2-1	219.387	58.6 MHz (80.1 km/s)	30.52 kHz (0.042 km/s)	1.56" x 0.89"	0.2	0.50
N159E	^{12}CO	2-1	230.356	58.6 MHz (76.3 km/s)	30.52 kHz (0.040 km/s)	1.21" x 0.84"	0.2	0.61
N159E	^{13}CO	2-1	220.224	58.6 MHz (79.8 km/s)	30.52 kHz (0.042 km/s)	1.27" x 0.87"	0.2	0.61
N159E	CS	2-1	97.903	58.6 MHz (179.4 km/s)	30.52 kHz (0.093 km/s)	3.05" x 1.86"	0.2	2.11
N159E	C^{18}O	2-1	219.387	58.6 MHz (80.1 km/s)	30.52 kHz (0.042 km/s)	1.29" x 0.91"	0.2	0.61

Column 1: The object. Column 2: The molecular line observed. Column 3: The molecular line transition. Column 4: Frequency of the line. Column 5: Spectral Window bandwidth. Column 6: Spectral window channel width. Column 7: Beam size of the observation. Column 8: Spectral resolution of the observation. Column 9: The precipitable water vapor.

Table 3.2: ALMA Noise and Flux Properties

Object	Line	Transition	Noise [K]	Flux [K km s^{-1}]
N159W	^{12}CO	2-1	0.74	580
N159W	^{13}CO	2-1 0.74	181	
N159W	CS	2-1	1.75	34.7
N159W	C^{18}O	0.59	9.73	
N159E	^{12}CO	1.04	328	
N159E	^{13}CO	1.04	61.9	
N159E	CS	2-1	1.17	192
N159E	C^{18}O	0.75	3.51	

Column 1: The object. Column 2: The molecular line observed. Column 3: The molecular line transition. Column 4: Noise in the channel map with a channel width of 0.5 km s^{-1}. Column 5: The peak flux of the position-position-velocity 3D data cube.

Band 6 12m observations of N159W were taken on November 30, 2013. Band 3 12m observations of N159W were taken on December 1, 2013. Band 6 12m observations of N159E were taken on December 2, 2013. Band 3 12m observations of N159E were taken on December 3, 2013. The calibration of complex gains was done with observations of three quasars (J0635-7516 and J0601-7036 in Band 6, J0635-7516 in Band 3), the bandpass calibration was done with observations of four quasars (J1058+0133 and J0538-4405 in Band 6, J0006- 7516 and J0334-4008 in Band 3), and flux calibration was done with three solar system objects (Pallas and Ganymede in Band 6, Uranus in Band 3). Butler-JPL-Horizons 2012 model (https://science.nrao.edu/facilities/alma/aboutALMA /Technology/ALMA_Memo_Series/alma594/abs594) was used for the flux calibration of the solar system objects. The data was processed using the Common Astronomy Software Application (CASA version 4.5.0, http://casa.nrao.edu). As previously reported by Fukui et al. (2015), we used natural weighting for both Band 3 and Band 6 data, providing synthesized beam sizes of ≈2.5" x 1.8" (0.6 x 0.4 pc at a distance of 50 kpc) and ≈1.3" x 0.8" (0.3 x 0.2 pc at a distance of 50 kpc), respectively. The rms noises of the molecular lines of Band 3 and Band 6 are ≈40 mJy/beam and ≈20 mJy/beam, respectively, in emission-free channels. The channel width of the map where the rms noises were measured is 0.5 km s^{-1} in both Band 3 and Band 6. The properties of the final data cubes used in this chapter are listed in Table 3.1.

The baseline length of the 12m array ranges from 16 to 395m. Extended emission larger than the maximum recoverable scale (ex: for ^{12}CO$(2-1)$ $0.6\lambda/\mathrm{L_{min}} \approx 10$", 2.4 pc at a distance of 50 kpc) is missing in our data sets. The convolved image of 12m array data to the ACA 7m resolution is similar to the ACA image, and therefore we do not think there is significant missing extended emission in this region. We do not use the ACA data in our analysis because the ACA data quality is too poor to be combined with the 12m array data. These different lines were observed to sample different critical densities of gas in the region. We list the critical densities of ^{12}CO$(2-1)$, ^{13}CO$(2-1)$, C^{18}O$(2-1)$, and CS$(2-1)$ in Table 3.2.

Table 3.3: List of Critical Densities

Line	Critical Density [cm^{-3}]
^{12} CO (2-1)	2.7 x 10^3
^{13} CO (2-1)	2.0 x 10^4
CS (2-1)	6.0 x 10^5
$C^{18}O$ (2-1)	3.0 x 10^3

The ALMA observed line (column 1) and the critical density of the line (column 2)

3.2.2 Optical and Infrared Photometry of Massive Young Stellar Objects

In this chapter we use the *Spitzer* Surveying the Agents of Galaxy Evolution (SAGE) survey and the HERschel Inventory of The Agents of Galaxy Evolution (HERITAGE) survey to identify the very early stage YSO candidates. The surveys are detailed in Section 1.4. Multi-wavelength photometry in optical and infrared is important to identify or rule out different YSO candidates from other dusty sources. The optical MCPS photometry for N159W/N159E is given in Tables 3.3 and 3.4, the JHK photometry for N159W/N159E is given is Tables 3.5 and 3.6, the *Spitzer* near-IR photometry for N159W/N159E is given in Tables 3.7 and 3.8, and the *Herschel* far-IR photometry for N159W/N159E is given in Tables 3.9 and 3.10.

Table 3.4: MCPS Optical Photometry For SAGE Sources in the ALMA Footprint of N159W

Name	U	U error	B	B error	V	V error	I	I error
J84.906560-69.756949								
J84.907135-69.769883								
J84.904533-69.760199								
J84.905770-69.770930								
J84.924542-69.769972								
J84.932938-69.765721								
J84.920395-69.760427								
J84.919917-69.775556								
J84.933226-69.760410								
J84.931984-69.762191								
J84.900254-69.767791	0.3293464837	0.0491409701	0.3266230443	0.0427179936	0.5343476141	0.0787443744		
J84.918707-69.754816								
J84.932298-69.761194								
J84.869420-69.761424			0.004365629	0.0011218291	0.0117875589	0.0024449385	0.0237408864	0.003323657
J84.935925-69.764660								

All fluxes are in units of mJy. The upper limit in U, B, V, I bands are 0.0047 mJy, 0.0018 mJy, 0.0025 mJy, 0.0035 (respectively) (Zaritsky et al., 1997).

Table 3.5: MCPS Optical Photometry For SAGE Sources in the ALMA Footprint of N159E

Name	U	U error	B	B error	V	V error	I	I error
J85.018920-69.743290								
J85.000623-69.736783								
J85.002866-69.744235								
J85.075276-69.745452								
J85.010292-69.735677								
J85.039540-69.748190			0.0078181691	0.0008	0.0207191578	0.002		
J84.986630-69.739733								
J85.004318-69.735780	0.2696826648	0.0548935079	0.2681926196	0.0338409908	0.4649688668	0.0394420233	0.3943636976	0.0232462329
J85.021921-69.733424	0.3432835802	0.0505881379	0.1152515626	0.0187886583	0.2564625018	0.0514939312		

All fluxes are in units of mJy. The upper limit in U, B, V, I bands are 0.0047 mJy, 0.0018 mJy, 0.0025 mJy, 0.0035 (respectively) (Zaritsky et al., 1997).

Table 3.6: IRSF JHK Photometry For SAGE Sources in the ALMA Footprint of N159W

Name	J	eJ	H	eH	K	eK
J84.906560-69.756949	0.09088419	0.009	0.11436680	0.010	0.35639406	0.030
J84.907135-69.769883	0.24349403	0.020			0.50110698	0.050
J84.904533-69.760199	0.08442835	0.008	0.15642276	0.010	0.92030219	0.090
J84.905770-69.770930						
J84.924542-69.769972	0.09088419	0.009			3.16177132	3.200
J84.932938-69.765721						
J84.920395-69.760427						
J84.919917-69.775556	0.30373040	0.030	0.22197290	0.020	0.40172650	0.040
J84.933226-69.760410						
J84.931984-69.762191						
J84.900254-69.767791	0.10926682	0.010			1.08625167	1.000
J84.918707-69.754816	0.03500000	0.003	0.05900000	0.007	0.06600000	0.008
J84.932298-69.761194	0.05734400	0.005	0.11865880	0.010	0.24656445	0.020
J84.869420-69.761424						
J84.935925-69.764660						

Columns 2-7: JHK photometry and error in mJy. The upper limits in J, H, K bands are 0.048, 0.077, and 0.153 (respectively) (Kato et al., 2007).

Table 3.7: IRSF JHK Photometry For SAGE Sources in the ALMA Footprint of N159E

Name	J	eJ	H	eH	K	eK
J85.018920-69.743290	3.6282649556	0.36	2.7740816227	0.28	2.7529741775	0.28
J85.000623-69.736783						
J85.002866-69.744235	0.4871999919	0.0314100012	0.5094000101	0.038660001	0.3095000088	0.0471000001
J85.075276-69.745452						
J85.010292-69.735677						
J85.039540-69.748190	0.099948012	0.009	0.1264915185	0.01	0.1698495934	0.016
J84.986630-69.739733						
J85.004318-69.735780	0.3720000088	0.0273700003	0.4241000116	0.0364900008	0.263500005	0.0420299992
J85.021921-69.733424						

Columns 2-7: JHK photometry and error in mJy. The upper limits in J, H, K bands are 0.048, 0.077, and 0.153 (respectively) (Kato et al., 2007).

Table 3.8: Spitzer Near to Mid Infrared Photometry For SAGE Sources in the ALMA Footprint of N159W

Name	I1	eI1	I2	eI2	I3	eI3	I4	eI4	M1	eM1
Name	[3.6]	[3.6]	[4.5]	[4.5]	[5.8]	[5.8]	[8.0]	[8.0]	[24]	[24]
J84.906560-69.756949	11.92756355	1.200	23.68907359	2.400	66.78790802	6.700	226.49636679	22.600		
J84.907135-69.769883	19.25536428	1.900	24.80550523	2.500	89.68046271	9.000	301.34309185	30.000	9279	928
J84.904533-69.760199	12.60525800	1.300	24.12948635	2.400	71.89485967	7.200	146.91334257	14.700		
J84.905770-69.770930	4.16424459*	1.175*	3.75885073*	1.589*	23.79537464*	5.219*	65.97003689*	15.695*		
J84.924542-69.769972	52.54746132	5.300	90.89669176	9.000	182.26271713	18.000	327.38685648	33.000	6911	690
J84.932938-69.765721	0.13603970*	0.021*	0.09795605*	0.022*	1.17599693*	0.145*	3.39855933*	0.368*	392*	183*
J84.920395-69.760427	0.22330729*	0.036*	0.28980604*	0.046*	2.26094037*	0.208*	6.11739137*	0.530*	620*	300*
J84.919917-69.775556	3.50390029	0.300	4.55562610	0.400	15.72888150	1.500	39.72475610	3.900	539	54
J84.933226-69.760410	0.90757608*	0.035*	1.35898116*	0.027*	2.82775899*	0.223*	4.68226577*	0.575*	410*	39*
J84.931984-69.762191	0.37268457*	0.076*	0.43804591*	0.105*	1.50172657*	0.216*	4.08765632*	0.493*	250*	135*
J84.900254-69.767791	11.28630388	1.100	11.02930323	1.100	42.14032108	4.200	117.77720396	11.800	1643	16
J84.918707-69.754816	0.21200000	0.030	0.14900000	0.027	0.84300000	0.141				
J84.932298-69.761194	1.19275636	0.110	1.71612168	0.170	2.94237377	0.290	6.96724752	0.690	170	17
J84.869420-69.761424	0.04960000	0.007					0.63900000	0.098	101*	16*
J84.935925-69.764660	0.26425677*	0.025*	0.25392960*	0.023*	1.70103435*	0.165*	3.87280683*	0.364*	179*	100*

Columns 2-9: IRAC photometry and error in mJy. Columns 10-11: MIPS photometry and error in mJy. The upper limit in [3.6], [4.5], [5.8], [8.0], [24] bands are 0.0127 mJy, 0.0834 mJy, 0.1001 mJy, 0.1288 mJy, 0.2110 mJy (respectively) (Meixner et al., 2006). Note: The SED fitter cannot make any fits if there are two or less photometric values input. Therefore we do aperture photometry to extract the IRAC and MIPS photometry from the images for the respective bands for two situations: if an object only had PACS and SPIRE photometry available, or if an object was not previously classified as a YSO and had two or less photometry points available. The values followed by an asterisk are those taken from aperture photometry we did, and not from the *Spitzer* point-source catalog.

Table 3.9: Spitzer Near to Mid Infrared Photometry For SAGE Sources in the ALMA Footprint of N159E

Name	I1	eI1	I2	eI2	I3	eI3	I4	eI4	M1	eM1
Name	[3.6]	[3.6]	[4.5]	[4.5]	[5.8]	[5.8]	[8.0]	[8.0]	[24]	[24]
J85.018920-69.743290	33.794238	0.34	48.865865	4.89	136.722117	13.67	460.647427	46		
J85.000623-69.736783	0.460487663*	0.136871208*	0.27993104*	0.113906631*	1.28419564*	0.154482015*	3.12927766*	0.322451076*	663.470897*	123.567706*
J85.002866-69.744235	0.244000	0.041400			2.619999	0.288199				
J85.075276-69.745452	0.288865842*	0.08153421*	0.278716743*	0.18603473*	1.87059381*	0.46115945*	4.79938659*	0.88529053*	557.15728*	66.6950113*
J85.010292-69.735677	0.250348672*	0.0334659227*	0.119932365*	0.0272229627*	1.48746973*	0.169333687*	3.3931821*	0.428439926*	554.808279*	204.98691*
J85.039540-69.748190	4.222005	0.4	2.853589	0.28	27.760236	2.77	80.039291	8	1881.597567	188
J84.986630-69.739733	0.43367868*	0.0720696*	0.42917871*	0.08275276*	1.73509679*	0.18435275*	4.29370887*	0.45973264*	357.7611417*	27.22318169*
J85.004318-69.735780	0.194000	0.017100	0.135000	0.017999	0.458000	0.072159				
J85.021921-69.733424	0.261000	0.030799	0.195999	0.028799	0.976000	0.152899				

Columns 2-9: IRAC photometry and error in mJy. Columns 10-11: MIPS photometry and error in mJy. The upper limit in [3.6], [4.5], [5.8], [8.0], [24] bands are 0.0127 mJy, 0.0834 mJy, 0.1001 mJy, 0.1288 mJy, 0.2110 mJy (respectively) (Meixner et al., 2006). Note: The SED fitter cannot make any fits if there are two or less photometric values input. Therefore we do aperture photometry to extract the IRAC and MIPS photometry from the images for the respective bands for two situations: if an object only had PACS and SPIRE photometry available, or if an object was not previously classified as a YSO and had two or less photometry points available. The values followed by an asterisk are those taken from aperture photometry we did, and not from the *Spitzer* point-source catalog.

Table 3.10: Herschel Far Infrared Photometry For SAGE Sources in the ALMA Footprint of N159W

Name	PACS 100 μm	error PACS 100 μm	PACS 160 μm	error PACS 160 μm	SPIRE 250 μm	error SPIRE 250 μm	SPIRE 350 μm	error SPIRE 350 μm	SPIRE 500 μm	error SPIRE 500 μm
J84.906560-69.756949	32150	5260	27330	3704	22320	2752				
J84.907135-69.769883	17020	3820	14660	2338			4473	716	3573	988
J84.904533-69.760199	14730	3182	16010	2418	22320	2752	7357	112	3573	658
J84.905770-69.770930	5731	4116	14660	2338	953	921	4473	716		
J84.924542-69.769972										
J84.932938-69.765721										
J84.920395-69.760427										
J84.919917-69.775556										
J84.933226-69.760410										
J84.931984-69.762191										
J84.900254-69.767791										
J84.918707-69.754816										
J84.932298-69.761194										
J84.869420-69.761424										
J84.935925-69.764660										

Columns 2-5: PACS 100 μm and 160 μm photometry and error in mJy. Columns 6-11: SPIRE 250 μm, 350 μm, and 500 μm photometry and error in mJy. The upper limit for PACS 100 μm, PACS 160 μm, SPIRE 250 μm, SPIRE 350 μm, SPIRE 500 μm bands are 450 mJy, 190 mJy, 90 mJy, 110 mJy, 140 mJy (respectively) (Meixner et al., 2013).

Table 3.11: Herschel Far Infrared Photometry For SAGE Sources in the ALMA Footprint of N159E

Name	PACS 100 μm	error PACS 100 μm	PACS 160 μm	error PACS 160 μm	SPIRE 250 μm	error SPIRE 250 μm	SPIRE 350 μm	error SPIRE 350 μm	SPIRE 500 μm	error SPIRE 500 μm
J85.018920-69.743290	20450	3802	18960	2662	4429	866.4	4446	1238		
J85.000623-69.736783										
J85.002866-69.744235										
J85.075276-69.745452										
J85.010292-69.735677										
J85.039540-69.748190										
J84.986630-69.739733										
J85.004318-69.735780										
J85.021921-69.733424										

Columns 2-5: PACS 100 μm and 160 μm photometry and error in mJy. Columns 6-11: SPIRE 250 μm, 350 μm, and 500 μm photometry and error in mJy. The upper limit for PACS 100 μm, PACS 160 μm, SPIRE 250 μm, SPIRE 350 μm, SPIRE 500 μm bands are 450 mJy, 190 mJy, 90 mJy, 110 mJy, 140 mJy (respectively) (Meixner et al., 2013).

3.3 Overview of ALMA Results in N159

Figure 3.1 shows the $^{12}CO(2-1)$, $^{13}CO(2-1)$, and $CS(2-1)$ integrated image in N159W and N159E. The distribution of the $^{12}CO(2-1)$ and $^{13}CO(2-1)$ in N159W is filamentary, with the filaments having straight or arc-like morphologies. We are not concerned with filtering of large scale structures in the maps shown in Figure 3.1. The RMS noise in channels without any signal to be the same as the RMS noise in channels with signal. Therefore, we are not missing a significant amount of large scale flux. The $^{12}CO(2-1)$ traces more diffuse emission than the $^{13}CO(2-1)$, therefore the filaments appear more structured and distinctive in $^{13}CO(2-1)$. The typical length of these filaments in $^{12}CO(2-1)$ and $^{13}CO(2-1)$ are 5-10 pc, and the typical widths of these filaments are 0.5-1.0 pc. The existence of filaments in regions of high star formation activity seems to be ubiquitous (Dhabal et al., 2016; Marsh et al., 2016; Xu et al., 2016). The two filaments in the Southern region of N159W form a V-shape structure. The shorter filament on the right is blue-shifted and the long curved filament on the left is red-shifted. The blue-shifted and red-shifted can be seen separately when integrating over two separate velocity ranges (Figure 3.2). The blue-shifted filament is seen when integrating over 234-237km/s, and the red-shifted filament is seen when integrating over 237-240km/s. At the heart of this collision lies the fifth most massive YSO in the N159W region (Fukui et al., 2015).

The $^{12}CO(2-1)$ and $^{13}CO(2-1)$ in N159E is different in morphology in comparison to N159W. Figure 3.1 shows the $^{12}CO(2-1)$ and $^{13}CO(2-1)$ in N159E to still

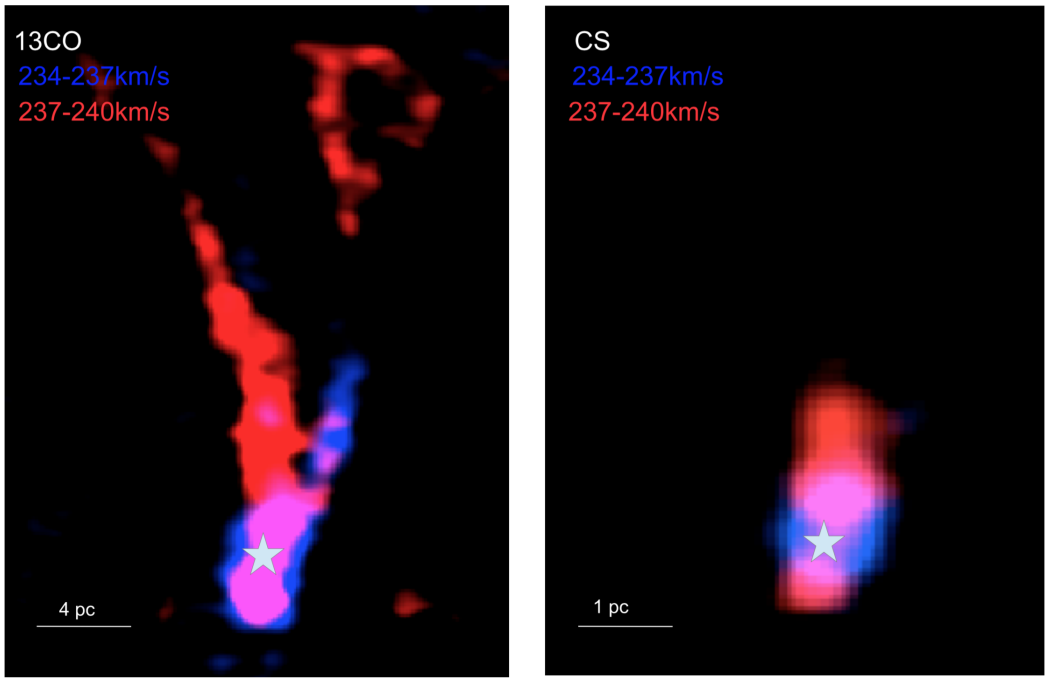

Figure 3.2: The blue-shifted and red-shifted filaments that are colliding in the South region of N159W at the location of YSO candidate 'w5'. Left: The ^{13}CO blue-shifted (blue) and red-shifted (red) colliding filaments. Right: The CS blue-shifted and red-shifted colliding filaments. The blue-shifted emission image is made by summing the channels between 234-237 km/s. The red shifted emission image is made by summing the channels between 237-240 km/s. The star-symbol shows where the massive YSO at the center of the collision is located.

be elongated into arc-like structures with the low-level emission. However the high intensity emission (>150K km/s in ^{12}CO$(2-1)$ and >30 K km/s in ^{13}CO$(2-1)$) is not contiguous in nature. The filaments seem to have broken up into smaller clumps. The region marked as A in N159E in Figure 3.1 is where the Papillon Nebula YSO is located. Figure 6 in Saigo et al. (2017) shows that the Papillon Nebula YSO in at the center of three colliding filaments. After correcting for the velocity of the LMC, the two blue-shifted filaments have velocity ranges from -8 to -1.6km/s, and -1.4 to -1.0 km/s. The red-shifted filament has a velocity range of 1.2 to 7.8km/s (Saigo et al., 2017).

The CS$(2-1)$ gas is not as abundant as ^{12}CO$(2-1)$ and ^{13}CO$(2-1)$. This can be seen in the right panels of Figure 3.1 (N159W on top right, N159E on bottom right). CS$(2-1)$ has a critical density of $2 \times 10^5 \mathrm{cm}^{-3}$, much higher than critical densities of ^{12}CO$(2-1)$ or ^{13}CO$(2-1)$ (see Table 3.2 for details). The morphology of the CS$(2-1)$ gas appears clumpy in N159W and N159E, with the CS$(2-1)$ gas found only in the immediate vicinity of very massive (>20M$_\odot$) YSOs. Figure 3.1 shows the oval/round clumpy structure of the CS$(2-1)$ gas.

3.4 Details on YSO Candidates

Star formation occurs on sub-parsec scales at the most dense knots in the clumpy filamentary molecular gas structure. We make a catalog of all the massive YSO candidates in N159W and N159E by using the *Spitzer* SAGE and *Herschel* HERITAGE surveys. There are 9 YSO candidates in N159W and 5 YSO candidates in N159E, within the ALMA footprint of N159W and N159E, that have previously been studied by Whitney et al. (2008), Gruendl & Chu (2009), Carlson et al. (2012), and Seale et al. (2014). We look for possible additional YSO candidates that could have been missed from stringent cuts applied (see Section 3.3.3). We identify 6 new YSO candidates in N159W and 4 new YSO candidates in N159E. The *Spitzer* SAGE survey (Meixner et al., 2006) was used by Whitney et al. (2008), Gruendl & Chu (2009), Carlson et al. (2012), and Seale et al. (2014) in order to fit SEDs (Robitaille et al., 2006) to the photometry and identify possible YSOs. We list the UBVI, JHK, *Spitzer* IRAC and MIPS, and *Herschel* PACS and SPIRE photometry in Tables 3.3/3.4, 3.5/3.6, 3.7/3.8, and 3.9/3.10 for N159W/E (respectively). Figure 3.3 shows N159W and N159E (respectively), with the location of massive YSOs in circles. The total number of YSOs included in our study is 24 with 15 YSOs in N159W and 9 YSOs in N159E.

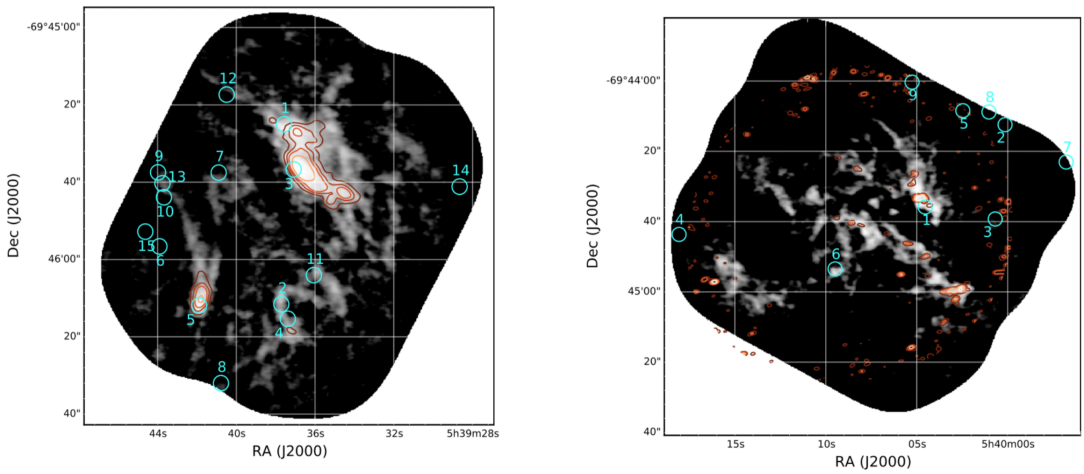

Figure 3.3: Left: ALMA ^{13}CO(2-1) brightness temperature of N159W in greyscale, ALMA CS (2-1) brightness temperature in contour (contour levels signify 10%, 20%, 30%, 50%, and 80% of peak integrated emission), and the location of massive YSO candidates in cyan circles. The ^{13}CO(2-1) peak integrated emission is 180.9 K km s^{-1}. The number near the YSO candidates indicates rank in mass (1 is the most massive YSO candidate and 16 in the least massive YSO candidate). More details about the properties of massive YSOs can be found in Section 3.4 and Table 3.11. The numbers correspond to the same as the numbers in Figures 3.5-3.8, Table 3.11, and the text (1 is w1, 2 is w2, etc). Right: ALMA ^{13}CO(2-1) brightness temperature of N159E in greyscale, ALMA CS (2-1) brightness temperature in contour (contour levels signify 50%, 60%, 70%, and 80% of peak integrated emission), and the location of massive YSO candidates in cyan circles. The ^{13}CO(2-1) peak integrated emission is 61.8 K km s^{-1}. The number near the YSO candidates indicates rank in mass (1 is the most massive YSO candidate and 11 in the least massive YSO candidate). More details about the properties of massive YSOs can be found in Section 3.4 and Table 3.12. The numbers correspond to the same as the numbers in Figures 3.9-3.11, Table 3.12, and the text (1 is e1, 2 is e2, etc).

Table 3.12: Properties of SAGE Sources in the ALMA Footprint of N159W

ID Number	Name	Mass [$M_\odot$]	Luminosity [$L_\odot$]	$\dot{M}/M$	Stage	Type	^{12}CO Association?	^{13}CO Association?	CS Association?	References
1	J84.906560-69.756949	$35.5^{+13.5}_{-12.0}$	$2.15^{+1.01}_{-1.15} \times 10^5$	3.16×10^{-5}	Stage 0/I	I	y	y	n	a,b,c,g,i
2	J84.907135-69.769883	$34.7^{+14.3}_{-13.8}$	$2.15^{+1.01}_{-1.59} \times 10^5$	2.15×10^{-5}	Stage 0/I	I/II	y	y	n	a,b,c,f,g,i
3	J84.904533-69.760199	$26.9^{+22.1}_{-9.93}$	$1.21^{+1.95}_{-0.75} \times 10^5$	2.15×10^{-5}	Stage 0/I	I	y	y	y	a,b,c,d,e,i
4	J84.905770-69.770930	$26.9^{+13.8}_{-9.93}$	$1.21^{+0.94}_{-0.89} \times 10^5$	3.16×10^{-5}	Stage 0/I	II	y	n	n	b,i
5	J84.924542-69.769972	$25.7^{+15.0}_{-5.75}$	$0.83^{+1.78}_{-0.36} \times 10^5$	4.64×10^{-6}	Stage 0/I	I/II	y	y	y	a,c,d,e,f,h,i
6	J84.932938-69.765721	$13.2^{+5.01}_{-5.05}$	$0.83^{+1.78}_{-0.56} \times 10^4$	6.81×10^{-6}	Stage 0/I	II	y	n	n	i
7	J84.920395-69.760427	$12.0^{+9.36}_{-3.51}$	$0.83^{+4.79}_{-0.51} \times 10^4$	1.00×10^{-5}	Stage 0/I	II	y	n	n	i
8	J84.919917-69.775556	$11.7^{+9.14}_{-3.43}$	$0.83^{+3.82}_{-0.51} \times 10^4$	6.81×10^{-6}	Stage 0/I	II	n	n	n	c,g,i
9	J84.933226-69.760410	$11.7^{+6.03}_{-3.62}$	$0.83^{+2.33}_{-0.56} \times 10^4$	6.81×10^{-6}	Stage 0/I	II	n	n	n	i
10	J84.931984-69.762191	$11.7^{+6.03}_{-4.16}$	$0.32^{+2.29}_{-0.14} \times 10^4$	1.00×10^{-5}	Stage 0/I	II	n	n	n	i
11	J84.900254-69.767791	$11.7^{+5.23}_{-2.20}$	$1.00^{+2.16}_{-0.44} \times 10^4$	2.15×10^{-6}	Stage 0/I	I	y	n	n	a,c,f,g,i
12	J84.918707-69.754816	$11.2^{+6.98}_{-3.63}$	$0.83^{+1.78}_{-0.65} \times 10^4$	1.00×10^{-5}	Stage 0/I	II	n	n	n	d,i
13	J84.932298-69.761194	$9.77^{+5.02}_{-2.53}$	$0.32^{+1.46}_{-0.17} \times 10^4$	6.81×10^{-6}	Stage 0/I	III	y	n	n	c,d,g,i
14	J84.869420-69.761424	$8.32^{+2.90}_{-2.69}$	$1.78^{+3.85}_{-1.46} \times 10^3$	1.00×10^{-5}	Stage 0/I	II/III	n	n	n	i
15	J84.935925-69.764660	$7.24^{+7.21}_{-2.46}$	$3.16^{+6.84}_{-2.78} \times 10^3$	1.00×10^{-5}	Stage 0/I	II/III	n	n	n	i

Column 1: ID Number. Columns 3: Mass of the YSO candidate as given by the peak of the likelihood distribution and 1sigma error. Columns 4: Luminosity of the YSO candidate as given by the peak of the likelihood distribution and 1sigma error. Column 5: Accretion rate over YSO mass. Column 6: Stage of YSO candidate. Column 7: Type of YSO candidate. Column 8: Is the YSO candidate associated with ^{12}CO gas? Column 9: Is the YSO candidate associated with ^{13}CO gas? Column 10: Is the YSO candidate associated with CS gas? Column 11: References: a for Seale et al. (2009), b for Seale et al. (2014), c for Chen et al. (2010), d for Carlson et al. (2012), e for Jones et al. (2005), f for Testor et al. (2006), g for Indebetouw et al. (2004), h for Nakajima et al. (2005), and i for this work.

Table 3.13: Properties of SAGE Sources in the ALMA Footprint of N159E

ID Number	Name	Mass [$M_\odot$]	Luminosity [$L_\odot$]	$\dot{M}/M$	Stage	Type	^{12}CO Association?	^{13}CO Association?	CS Association?	References
1	J85.018920-69.743290	$35.0^{+15.1}_{-13.0}$	$2.15^{+1.01}_{-1.15} \times 10^5$	1.47×10^{-5}	Stage 0/I	III	y	y	y	a,b,c,d,i
2	J85.000623-69.736783	$13.5^{+9.95}_{-5.17}$	$2.15^{+1.01}_{-1.59} \times 10^5$	4.64×10^{-5}	Stage 0/I	II/III	n	n	n	i
3	J85.002866-69.744235	$13.5^{+4.29}_{-5.17}$	$1.21^{+1.95}_{-0.75} \times 10^5$	6.81×10^{-6}	Stage 0/I	III	n	n	n	d,i
4	J85.075276-69.745452	$12.0^{+9.36}_{-3.71}$	$1.21^{+0.94}_{-0.89} \times 10^5$	1.00×10^{-5}	Stage 0/I	II/III	y	n	n	i
5	J85.010292-69.735677	$12.0^{+9.36}_{-3.71}$	$0.83^{+1.78}_{-0.36} \times 10^5$	1.00×10^{-5}	Stage 0/I	II	n	n	n	i
6	J85.039540-69.748190	$11.7^{+15.2}_{-2.63}$	$0.83^{+1.78}_{-0.56} \times 10^4$	6.81×10^{-6}	Stage 0/I	I/II	y	y	n	a,c,d i
7	J84.986630-69.739733	$11.7^{+7.31}_{-3.62}$	$0.83^{+4.79}_{-0.51} \times 10^4$	1.00×10^{-5}	Stage 0/I	II	n	n	n	i
8	J85.004318-69.735780	$9.33^{+1.89}_{-3.71}$	$0.83^{+3.82}_{-0.51} \times 10^4$	1.47×10^{-6}	Stage 0/I	III	n	n	n	d,i
9	J85.021921-69.733424	$8.51^{+2.71}_{-2.35}$	$0.83^{+2.33}_{-0.56} \times 10^4$	1.00×10^{-6}	Stage 0/I	III	n	n	n	d,i

Column 1: ID Number. Columns 3: Mass of the YSO candidate as given by the peak of the likelihood distribution and 1sigma error. Columns 4: Luminosity of the YSO candidate as given by the peak of the likelihood distribution and 1sigma error. Column 5: Accretion rate over YSO mass. Column 6: Stage of YSO candidate. Column 7: Type of YSO candidate. Column 8: Is the YSO candidate associated with ^{12}CO gas? Column 9: Is the YSO candidate associated with ^{13}CO gas? Column 10: Is the YSO candidate associated with CS gas? Column 11: References: a for Seale et al. (2009), b for Seale et al. (2014), c for Chen et al. (2010), d for Carlson et al. (2012), e for Jones et al. (2005), f for Testor et al. (2006), g for Indebetouw et al. (2004), h for Nakajima et al. (2005), and i for this work.

3.4.1 Description of Previously Identified YSO Candidates From The Most Massive to Least Massive

J85.018920-69.743290 (Papillon Nebula YSO, 'e1'): The Papillon Nebula YSO was one of the first YSOs discovered in the LMC (Swings & Andrillat, 1979). This massive YSO has been studied extensively since its discovery with studies done on the molecular gas (Bachiller et al., 1990; Heydari-Malayeri et al., 1999), SED modeling (Carlson et al., 2012; Chen et al., 2010), and isochrone fits Meynadier et al. (2004). The SED modeling of the Papillon Nebula YSO by Chen et al. (2010) gives a mass estimate of $20M_{\odot}$. Saigo et al. (2017) added the far infrared *Herschel* PACS and SPIRE photometry to the SED fits and found the mass of the Papillon Nebula to be $35M_{\odot}$ (this is the mass that is listed in Table 3.12). However the mass is most likely closer to the Meynadier et al. (2004) estimate of $50M_{\odot}$ found by fitting isochrones. This makes the Papillon Nebula YSO the most massive candidate on our list. This YSO candidate is associated with ^{13}CO and CS molecular gas, as observed by ALMA.

SED modeling is based on the assumption that none of the ionizing photons are escaping and the infrared photometry we use is a good estimate of the photon flux. However, there is a CO-hole surrounding the Papillon Nebula YSO (Saigo et al., 2017). It is plausible the photons are escaping due to the density in the vicinity of

the YSO being low. The conditions necessary for the formation of a $50M_{\odot}$ can be possible with colliding filaments. It is believed that the Papillon Nebula YSO formed by the collision of three filaments (Saigo et al., 2017). Seale et al. (2009) classify the Papillon Nebula YSO as a PE object because the spectrum shows PAH and fine structure line emissions.

J84.906560-69.756949 (Fukui et al. (2015) YSO-N, 'w1'): The velocity distribution of the ALMA CO spectrum (Fukui et al., 2015) of YSO-N shows a blue-shifted high velocity wing, indicative of an outflow. Indebetouw et al. (2004) look at 3cm continuum observations and find YSO-N to be a O5.5 star and determine it is a UCHII object. YSO-N is associated with ^{12}CO molecular gas and ^{13}CO molecular gas.

J84.907135-69.769883 ('w2'): VLT images in the J band (Figure 5 in Testor et al. (2006)) show that 'w2' is actually formed by a cluster of six stars embedded in a nebulosity with a radius of 0.45 pc. The VLT spectrum of 'w2' shows Brγ and H_2 2.121μm emission lines. There is no He I 2.113μm emission line detected, which means there are no O stars in the cluster. This is a PE object as classified by Seale et al. (2009). Indebetouw et al. (2004) classify this object as a UCHII source. YSO candidate 'w2' is associated with ^{12}CO molecular gas and ^{13}CO molecular gas.

J84.904533-69.760199 ('w3'): This is a PE object as classified by Seale et al. (2009).

This YSO also shows silicate absorption at 10μm in the spectrum analyzed by Seale et al. (2009). YSO candidate 'w3' is associated with ^{12}CO, ^{13}CO, CS and C^{18}O molecular gases.

J84.905770-69.770930 ('w4'): This YSO candidate was identified in the *Herschel* HERITAGE point source catalog by Seale et al. (2014). YSO Candidate 'w4' is associated with only ^{12}CO molecular gas.

J84.924542-69.769972 (Fukui et al. (2015) YSO-S, 'w5'): The filamentary collision taking place, and most likely leading to the formation of YSO-S, can clearly be seen in the ALMA ^{13}CO data as shown in Figure 3.2. Fukui et al. (2015) find the length of the two filaments colliding to be 10pc and 5pc. High velocity wings show a red-shifted and blue-shifted outflow from the protostar. YSO-S is associated with ^{12}CO, ^{13}CO, CS and C^{18}O molecular gases. Seale et al. (2009) find the spectrum of YSO-S to have PAH features and fine structure emission lines, therefore classify it as a PE object. Jones et al. (2005) targeted a few dozen candidates in the N159 region with *Spitzer* and identify five protostars in the region, one of which is YSO-S. SED fitting, color-magnitude (CMD) cuts, and comparison to optically identified stars leads Jones et al. (2005) to conclude that YSO-S will evolve into B2 or B3 main-sequence stars. Testor et al. (2006) use VLT J and K images, as well as VLT spectroscopy to further study N159. High resolution images, non-detection of He 2.113 μm, and weak Brγ

emission lead Testor et al. (2006) to conclude that YSO-S ('P2' in Testor et al. (2006)) is actually two individual sources (objects 121 and 123 in Testor et al. (2006)) at a very early stage of star formation. Nakajima et al. (2005) classify this object as a HAeBe star. Figure 3.2 shows the colliding filaments that result in the formation of massive YSO candidate 'w5'. The two colliding filaments are more extended (5-10pc) in $^{12}CO(2-1)$ and $^{13}CO(2-1)$. However the two filaments are very compact in $CS(2-1)$.

J84.919917-69.775556 ('w8'): Nakajima et al. (2005) classify this object as a HAeBe star.

J84.900254-69.767791 ('w11'): Indebetouw et al. (2004) find 'w11' is coincident with a 6 cm radio peak. YSO candidate 'w11' is seen as a tight cluster formed by five stars in VLT images by Testor et al. (2006). Brγ and He I 2.113μm emission lines are detected in the spectrum of this source, with a He I 2.11μm/Brγ ratio of 0.021. This cluster most likely contains a late O-type star. Martín-Hernández et al. (2005) estimated the N_{Lyc} flux and found it to be consistent with an O8 star. This is a PE object as classified by Seale et al. (2009). Nakajima et al. (2005) classify this object as a HAeBe star. YSO candidate 'w11' is associated with only ^{12}CO molecular gas.

J84.932298-69.761194 ('w13'): Nakajima et al. (2005) classify this object as a HAeBe

star. YSO candidate 'w13' is associated with only ^{12}CO molecular gas.

Candidates J84.918707-69.754816 ('w12'), J85.002866-69.744235 ('e3'), J85.039540-69.748190 ('e6'), J85.004318-69.735780 ('e8'), and J85.021921-69.733424 ('e9') do not have much written about them in literature other than being identified as a YSO candidate.

3.4.2 Description of New YSO Candidates Identified in This Chapter

The past searches for YSOs were incomplete and biased towards the most massive YSOs. Therefore, we searched the SAGE and HERITAGE catalogs in order to increase the number of YSO candidates in the region for our analysis. We first extract all the *Spitzer* SAGE survey and *Herschel* HERITAGE survey point sources within the ALMA footprint of N159W and N159E. If a point source has already been identified as a massive YSO candidate (Carlson et al., 2012; Chen et al., 2010; Jones et al., 2005; Seale et al., 2009, 2014), then we keep this object as part of our candidate list. There are a total of 9 YSO candidates that have previously been identified in N159W, and 5 YSO candidates that have previously been identified in N159E. There are only a handful of point sources within the ALMA footprint of N159W and N159E, therefore we can look at each object individually. We fit Robitaille et al.

(2006) SEDs to the optical and infrared photometry to all other point sources within the ALMA footprint that have previously not been identified as a candidate. If the reduced χ^2 is less than 10, then we keep this object for further analysis. If the reduced χ^2 is greater than 10, then we reject this object as a YSO candidate. We then fit stellar photosphere SEDs to the *Spitzer* point sources that remain. If an object has a good fit to a stellar photosphere (reduced χ^2 is less than 10), then we remove this object from our candidate list. Therefore we identify new YSO candidates as those that have a good fit to a YSO SED, but not a good fit to a stellar photosphere SED. For all candidates without far-infrared photometry, we fit SPIRE detection upper limits (Meixner et al., 2006).To further remove any contamination we look at HST images (private communication with R. Indebetouw) in order to remove any sources that look extended and therefore may be a galaxy. These new candidates do have the potential to be other dusty sources: evolved stars, planetary nebulae, supernovae remnants, etc. We check the new candidates we find with Riebel et al. (2015) and Jones et al. (2015) to rule out other possible source contamination and we find none of our new YSO candidates to be in these two dusty evolved star source catalogs. With this method we identify 6 new YSO candidates in the ALMA footprint of N159W: J84.932938-69.765721, J84.920395-69.760427, J84.933226-69.760410, J84.931984-69.762191, J84.869420-69.761424, and J84.935925-69.764660. And we identify 4 new candidates in N159E: J85.000623-69.736783, J85.075276-69.745452, J85.010292-69.735677, J84.986630-69.739733.

Carlson et al. (2012) use *Spitzer* IRAC (3.6μm, 4.5μm, 5.8μm, 8.0μm) and *Spitzer* MIPS (24μm) to implement multi-color cuts and identify YSO candidates. They have two different color-cut criteria: α cuts and β cuts. The α cut criteria is used for galaxy-wide surveys where contamination is high. The β cut criteria is used in star-forming regions where contamination for evolved stars and galaxies is low. The β cut is best used in dusty star forming regions, but when applied to a whole galaxy can lead to significant contamination from non-YSO sources. Carlson et al. (2012) applied a stringent cut in identifying their candidates: they use five different CMD diagrams, and they select sources as YSOs if the sources meet their α cut or at least two β cut criteria. The new sources in this chapter were not identified as YSO candidates by Carlson et al. (2012) because these objects had many of the IRAC and MIPS photometry missing. Some of our sources only had photometry in one of the near-IR bands, however had *Herschel* detections. Other sources had U, B, V, I photometry but no near-IR photometry. These sources had a good fit to YSO SEDs, however without the near-IR photometry we could not compare to Carlson et al. (2012) results. Therefore we extract the near-IR and mid-IR photometry from doing aperture photometry on the IRAC and MIPS 24μm bands, and we list the photometry with an asterisk next to the number (in Tables 3.7 and 3.8) to denote that these measurements that are not from literature. Figure 3.4 shows the YSO candidates in a color-magnitude-diagram (CMD). The orange line indicates α cut and the cyan line

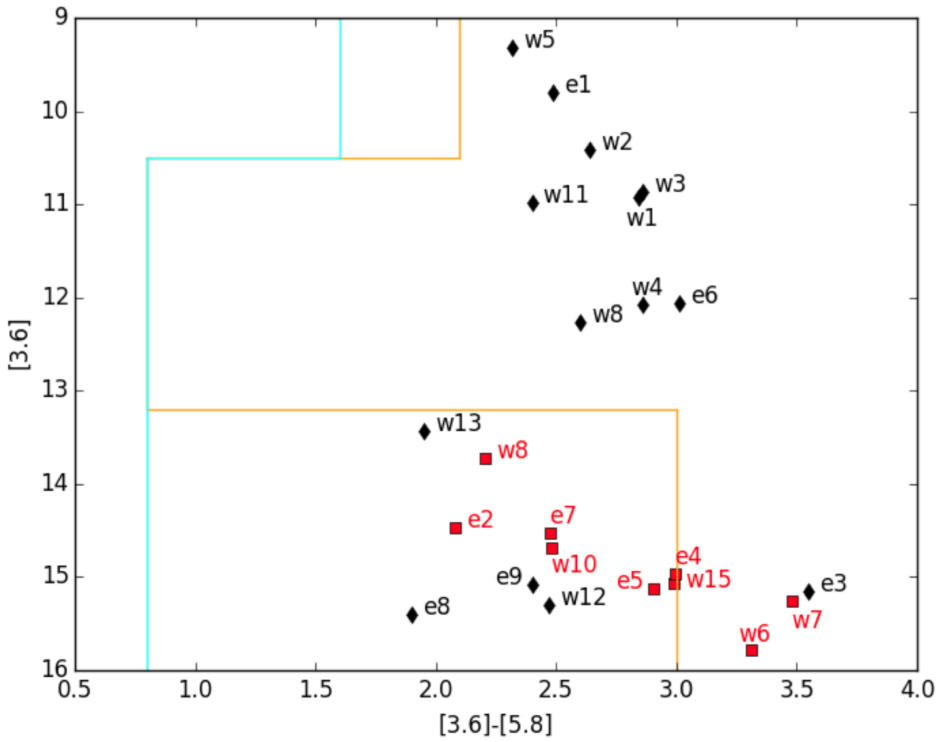

Figure 3.4: YSO candidates shown in a [3.6]-[5.8] versus [3.6] CMD. All candidates that are to the right of the orange line are in agreement with Carlson et al. (2012) α cuts, and all candidates that are to the right of the cyan line are in agreement with Carlson et al. (2012) β cuts. Black diamonds are previously identified YSO candidates, red squares are new YSO candidates we identify in this work.

indicates β cut by Carlson et al. (2012). Figure 3.4 shows that the majority of the old YSO candidates (in black diamonds) are three to four magnitudes brighter than the new candidates (red squares). The majority of the new candidates meet the β cut criteria, but not the α cut criteria. The majority of the new YSO candidates are also much fainter than the previously identified candidates and have masses (Robitaille et al., 2006) of 8-10$M_{\odot}$.

3.4.3 Fitting SEDs to the Photometry of the YSO Candidates

We re-fit the previously identified candidates as well as the new YSO candidates from this chapter. We add the *Herschel* HERITAGE PACS and SPIRE photometry to all sources for the SED fits to get a better constraint on the far-IR dust. The SEDs are shown in Figures 3.5 - 3.8 (N159W) and 3.9 - 3.11 (N159E). ALMA continuum observations of N159W and N159E are of the ionized gas continuum, and not the dust continuum. Therefore we do not fit the ALMA continuum data when using the SED fitter. All YSO candidates in this chapter are Stage 0/I objects. We reference the candidates by rank: 'w1' is the most massive candidate in N159W and 'w15' is the least massive candidate in N159W, 'e1' is the most massive candidate in N159E and 'e9' is the least massive candidate in N159E. We list the properties of YSO candidates in N159W in Table 3.11 and the properties of YSO candidates in N159E in Table 3.12. All the YSO candidates in this chapter are Stage 0/I objects. Stage 0/I candidates are those with $\frac{\dot{M}_{env}}{M_{star}}>10^{-6}$ yr^{-1} (Robitaille et al., 2006).

We have edited the Robitaille et al. (2006) SED fitter code to output the maximum likelihood of the YSO parameters and associated 1σ errors. The mass and luminosity of these YSO candidates can be found in Tables 3.11 and 3.12. We list the YSO candidates from most massive to least massive in these tables. The location of the

YSO candidates in N159W/N159E with respect to the ^{13}CO and CS gas can be seen in Figure 3.3.

3.4.4 An Alternative Classification Method

The term 'Stage' as defined in Section 3.3.3 has to do with the physical properties of the YSO (i.e., accretion rate, stellar mask, and disk mask). Another classification scheme to define YSOs is 'Type'. YSOs are characterized by Type depending on the shape of their SED, rather than physical quantities that define the Stage. Chen et al. (2010) define YSO Type I as the following: YSOs which have SEDs with a steep rise from the near-IR to mid-IR because they are deeply embedded. These Type I YSOs are generally not visible in the optical or J band, but visible in the K band and bright in 24-70μm wavelength range. Type II YSOs have SEDs with a low peak in the optical and a high peak in the mid-IR wavelengths (8-24μm) as the optical stellar core stars to become more visible but the circumstellar dust also still exists. Type III YSOs are those with SEDs that peak in the optical, but still have some remnant dust and circumstellar material left to still visible in the IR. Chen et al. (2010) categorize YSO candidates 'w1', 'w2, 'w3', and 'w5' as Type I, Type I/II, Type I, and Type I/II respectively. YSO candidate 'w4' was not studied by Chen et al. (2010) since it did not have any near-IR photometry. We extract the near-IR photometry for YSO candidate 'w4' by doing aperture photometry with the IRAC images and we input the PACS and SPIRE observed photometry. In doing so, we see that this candidate

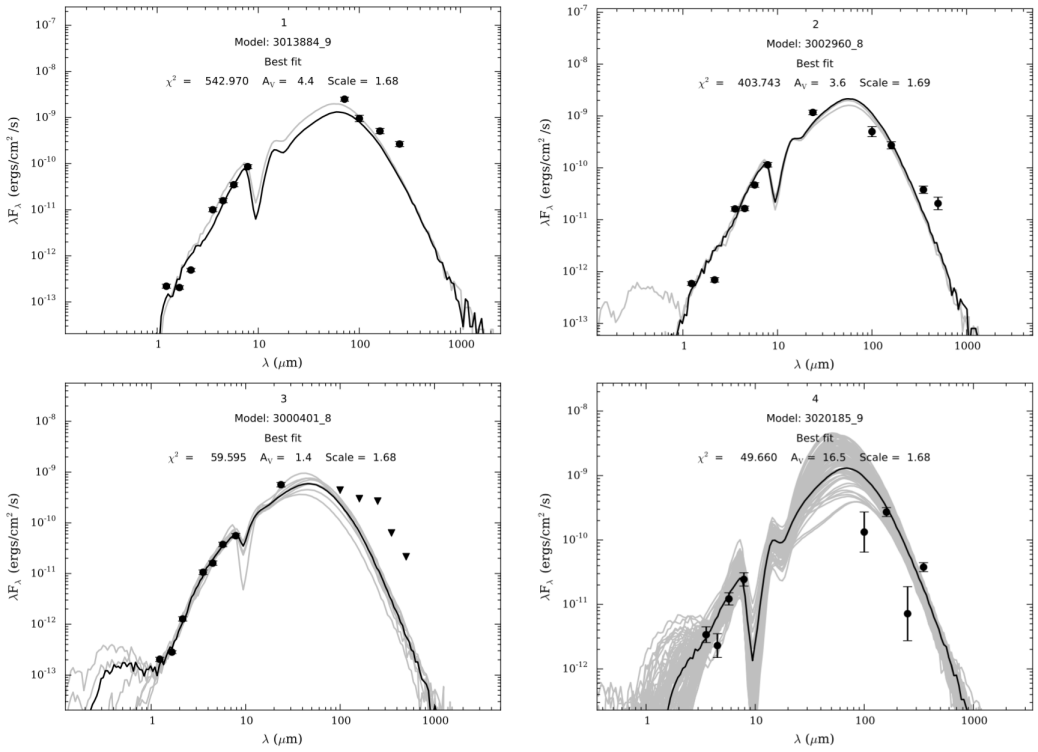

Figure 3.5: SED fits of YSO candidates 1-4 in the ALMA footprint of N159W. They are ordered from top to bottom, left to right in order of highest mass to lowest mass. Black dots are the fitted data points, black triangles are upper limits, the black line is the best fit model, and the grey lines are all models that have χ^2<3 relative to the best fit model. The YSO candidate number corresponds to the same number in Table 3.11.

is a Type I YSO (SED of YSO #4 shown in Figure 3.5). Out of the 5 total YSO candidates >20$M_\odot$ in N159W, 3 of them are Type I objects and two of them are Type I/II objects. The Papillon Nebula YSO in N159E (YSO candidate 'e1') is classified as a Type III object by Chen et al. (2010). This is consistent with this YSO being more evolved and having enough time to clear out molecular gas in its vicinity, forming a CO-hole.

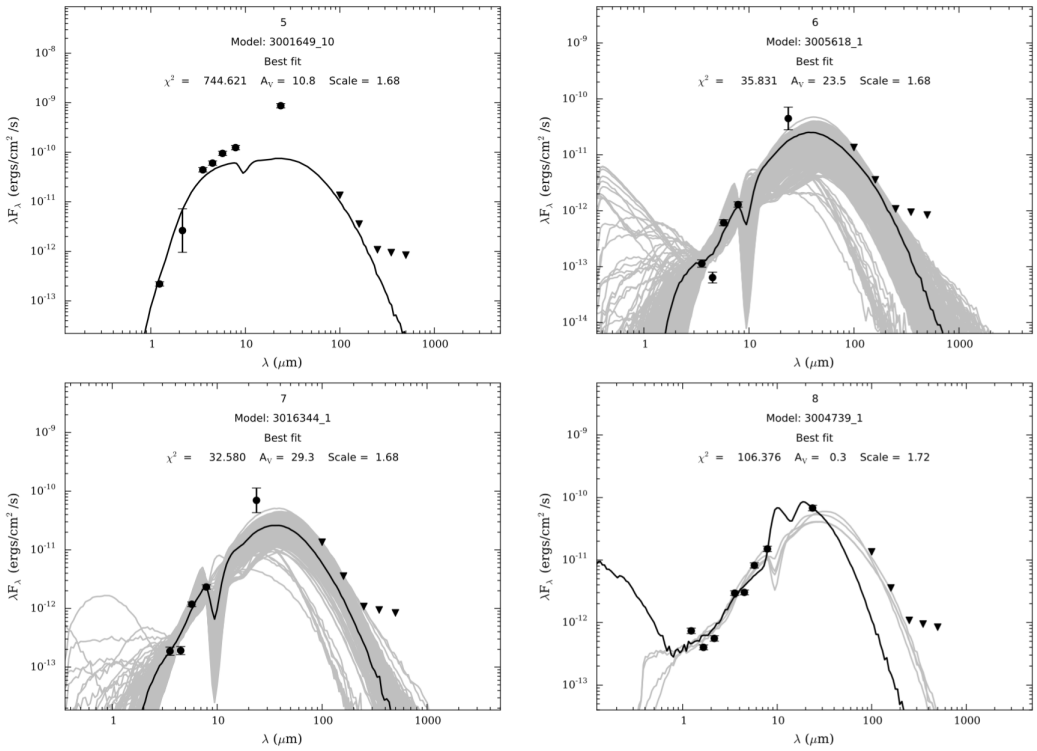

Figure 3.6: SED fits of YSO candidates 5-8 in the ALMA footprint of N159W. They are ordered from top to bottom, left to right in order of highest mass to lowest mass. Black dots are the fitted data points, black triangles are upper limits, the black line is the best fit model, and the grey lines are all models that have χ^2<3 relative to the best fit model. The YSO candidate number corresponds to the same number in Table 3.11.

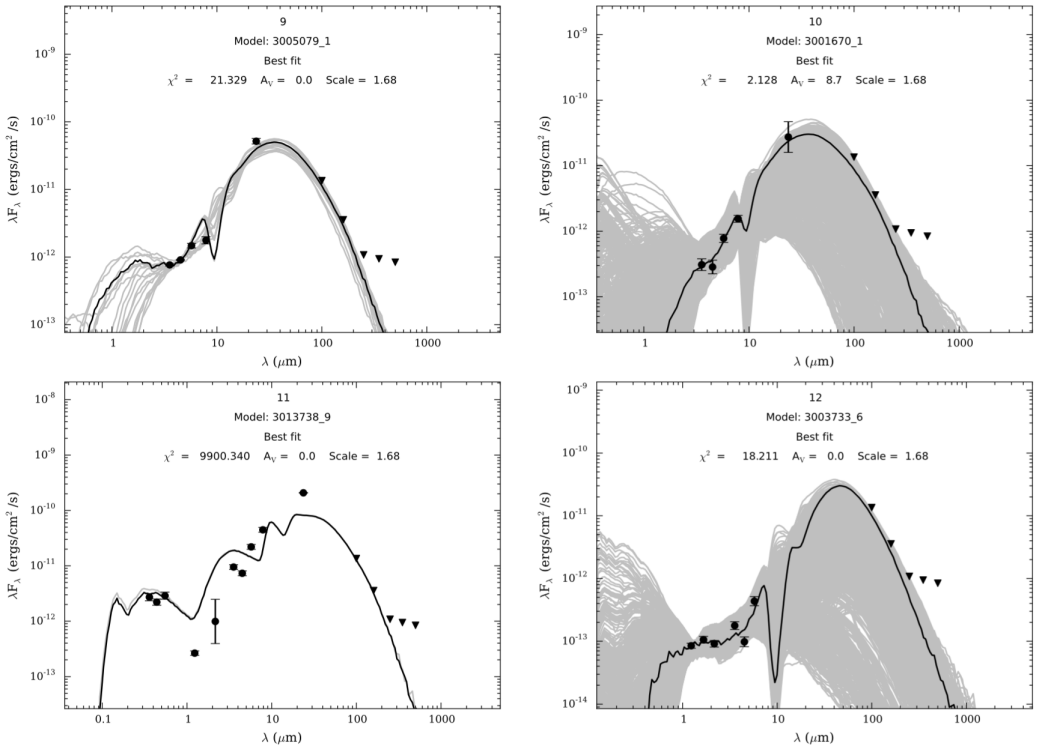

Figure 3.7: SED fits of YSO candidates 9-12 in the ALMA footprint of N159W. They are ordered from top to bottom, left to right in order of highest mass to lowest mass. Black dots are the fitted data points, black triangles are upper limits, the black line is the best fit model, and the grey lines are all models that have χ^2<3 relative to the best fit model. The YSO candidate number corresponds to the same number in Table 3.11.

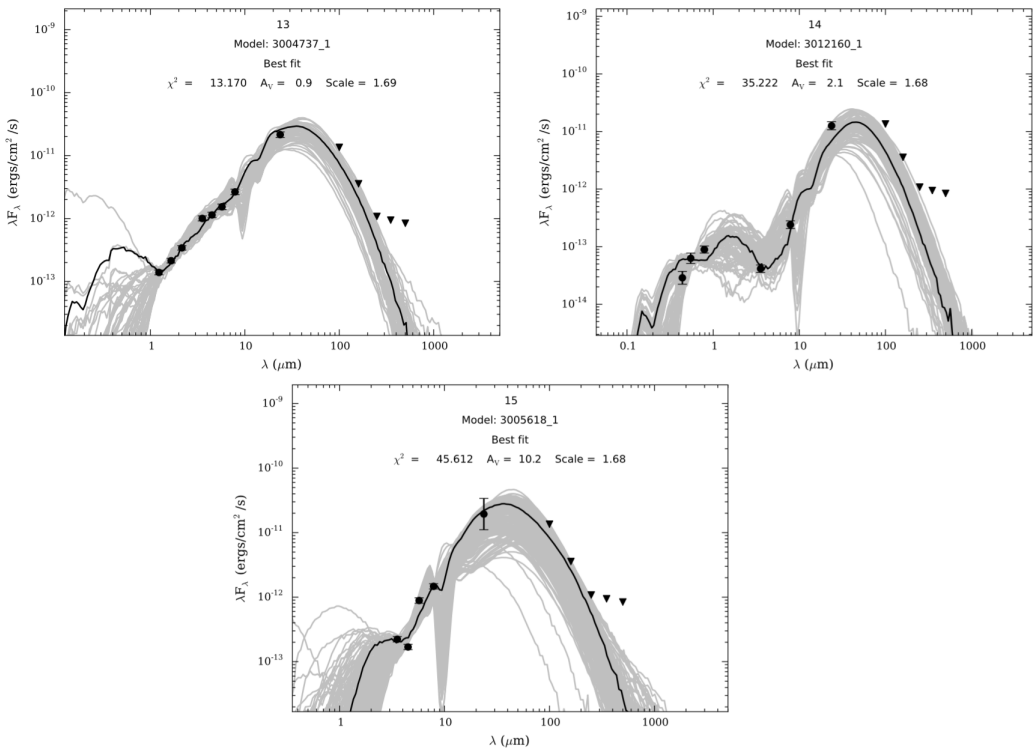

Figure 3.8: SED fits of YSO candidates 13-15 in the ALMA footprint of N159W. They are ordered from top to bottom, left to right in order of highest mass to lowest mass. Black dots are the fitted data points, black triangles are upper limits, the black line is the best fit model, and the grey lines are all models that have χ^2<3 relative to the best fit model. The YSO candidate number corresponds to the same number in Table 3.11.

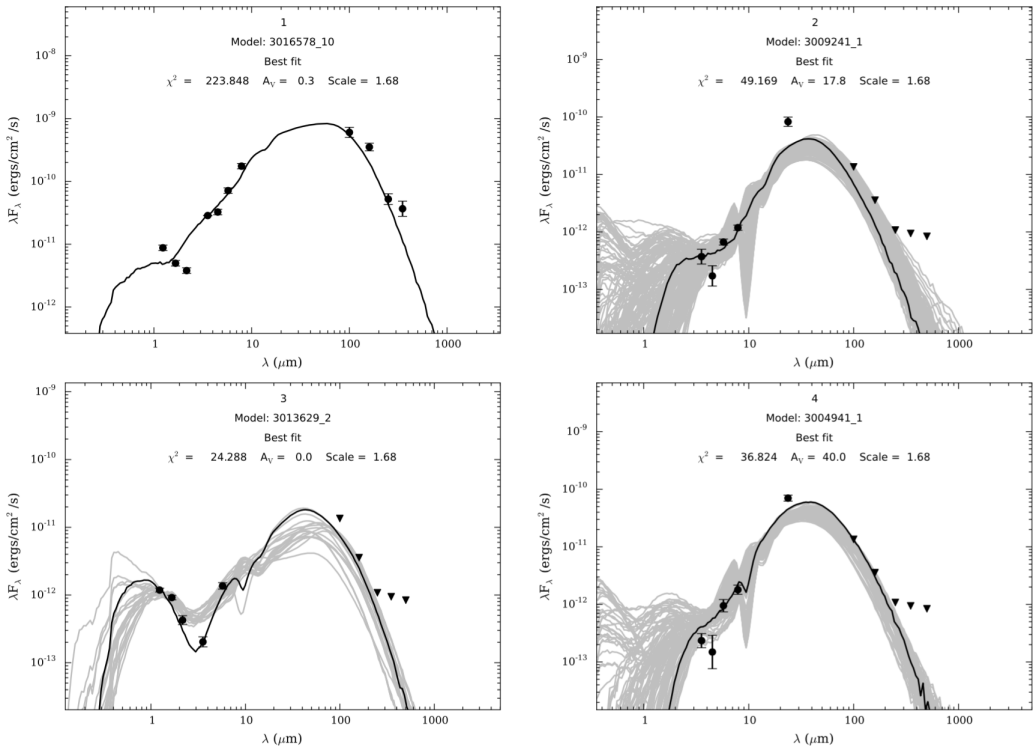

Figure 3.9: SED fits of YSO candidates 1-4 in the ALMA footprint of N159E. They are ordered from top to bottom, left to right in order of highest mass to lowest mass. Black dots are the fitted data points, black triangles are upper limits, the black line is the best fit model, and the grey lines are all models that have χ^2<3 relative to the best fit model. The YSO candidate number corresponds to the same number in Table 3.12.

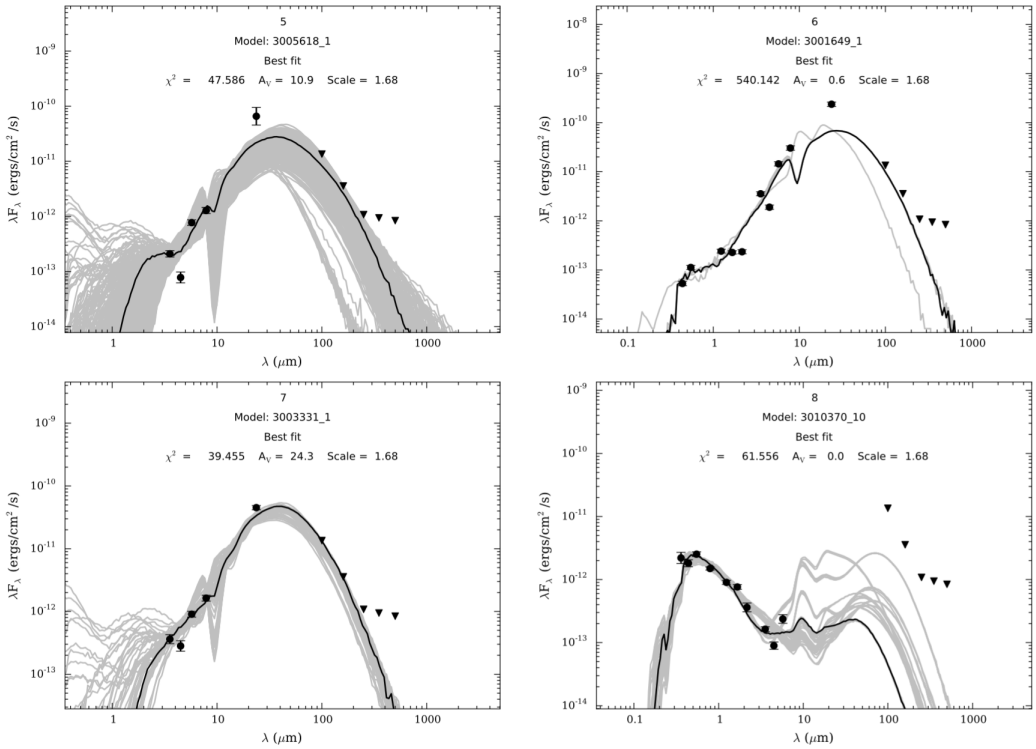

Figure 3.10: SED fits of YSO candidates 5-8 in the ALMA footprint of N159E. They are ordered from top to bottom, left to right in order of highest mass to lowest mass. Black dots are the fitted data points, black triangles are upper limits, the black line is the best fit model, and the grey lines are all models that have χ^2<3 relative to the best fit model. The YSO candidate number corresponds to the same number in Table 3.12.

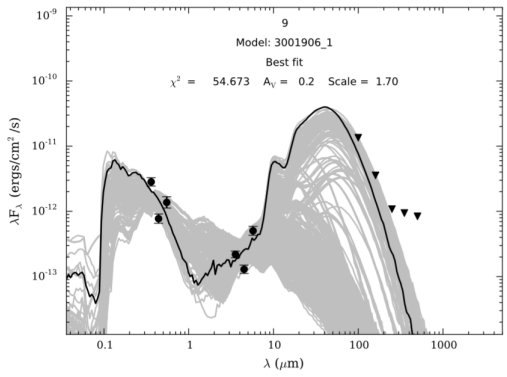

Figure 3.11: SED fits of YSO candidate 9 in the ALMA footprint of N159E. They are ordered from top to bottom, left to right in order of highest mass to lowest mass. Black dots are the fitted data points, black triangles are upper limits, the black line is the best fit model, and the grey lines are all models that have χ^2<3 relative to the best fit model. The YSO candidate number corresponds to the same number in Table 3.12.

Table 3.14: Dendrogram Algorithm Input

Line	Leaf Size [pixels]	Minimum Flux [K]	Flux Separation [K]
^{12}CO	46	7.4	7.4
^{13}CO	46	5.5	5.5
CS	49	1.8	1.8

Column 1: The line we observe with ALMA. Column 2: Minimum size of a structure to consider. Column 3: Minimum flux to consider. Column 4: The flux limit which determines when a single clump should separate into two or more clumps.

Table 3.15: Mass Derived from N159W ^{12}CO (2-1) Clumps

Clump ID	RA	Dec	Radius [pc]	$F_{^{12}CO}$ [K km s^{-1}]	Total Mass [$M_\odot$]	Virial Mass [$M_\odot$]	Linewidth [km/s]
0	84.899215	-69.762008	7.26	59.8 ± 41.1	1.76E+5 ± 1.21E+5	1.08E+5 ± 7.46E+4	3.58
1	84.899442	-69.761883	6.92	61.6 ± 39.2	1.65E+5 ± 1.05E+5	1.02E+5 ± 6.50E+4	3.56
2	84.899488	-69.761849	6.78	62.7 ± 38.4	1.61E+5 ± 9.83E+4	9.91E+4 ± 6.06E+4	3.55
3	84.899456	-69.761877	6.89	61.9 ± 39.0	1.64E+5 ± 1.03E+5	1.02E+5 ± 6.40E+4	3.56
4	84.899313	-69.761960	7.04	61.4 ± 39.9	1.70E+5 ± 1.10E+5	1.04E+5 ± 6.78E+4	3.57
5	84.899301	-69.761968	7.07	61.2 ± 40.0	1.71E+5 ± 1.12E+5	1.05E+5 ± 6.86E+4	3.57
6	84.899546	-69.761830	6.66	63.9 ± 37.7	1.58E+5 ± 9.35E+4	9.71E+4 ± 5.73E+4	3.54
7	84.899471	-69.761850	6.79	62.7 ± 38.4	1.61E+5 ± 9.88E+4	9.92E+4 ± 6.09E+4	3.55
8	84.899420	-69.761893	6.94	61.5 ± 39.3	1.65E+5 ± 1.06E+5	1.02E+5 ± 6.56E+4	3.56
9	84.899528	-69.761838	6.70	63.6 ± 37.9	1.59E+5 ± 9.49E+4	9.77E+4 ± 5.83E+4	3.54

Column 1: The ID we give each clump. Column 4: The radius calculated from the area of the clump. Column 6: The total H_2 mass. We assumed the typical ^{12}CO(2-1)/^{12}CO(1-0) ratio toward HII regions of 0.85 (Nishimura et al., 2015). We use a X_{CO} conversion factor of 7×10^{20} cm^{-2} (Fukui et al., 2008). Column 7: The virial mass calculated by assuming the virial parameter equals 1. Column 8: The measured linewidth. NOTE: This table is available in its entirety in Appendix D. A portion is shown here for guidance.

Table 3.16: Mass Derived from N159E ^{12}CO (2-1) Clumps

Clump ID	RA	Dec	Radius [pc]	$F_{^{12}CO}$ [K km s^{-1}]	Total Mass [$M_\odot$]	Virial Mass [$M_\odot$]	Linewidth [km/s]
0	85.059829	-69.749680	2.96	49.1 ± 25.2	2.41E+4 ± 1.23E+4	2.74E+4 ± 1.41E+4	2.82
1	85.058511	-69.750182	2.59	51.9 ± 22.0	1.94E+4 ± 8.20E+3	1.33E+4 ± 5.63E+3	2.10
2	85.058478	-69.750198	2.54	49.9 ± 21.6	1.79E+4 ± 7.77E+3	1.21E+4 ± 5.25E+3	2.03
3	85.052824	-69.747740	0.265	20.3 ± 2.25	7.95E+1 ± 8.81E+0	4.68E+1 ± 5.19E+0	0.390
4	85.058040	-69.750242	2.40	47.4 ± 20.4	1.52E+4 ± 6.55E+3	9.42E+3 ± 4.05E+3	1.84
5	85.028038	-69.744350	5.29	54.4 ± 45.0	8.49E+4 ± 7.02E+4	3.80E+4 ± 3.14E+4	2.49
6	85.027992	-69.744344	5.26	54.3 ± 44.8	8.39E+4 ± 6.92E+4	3.77E+4 ± 3.11E+4	2.48
7	85.027841	-69.744249	5.13	54.3 ± 43.7	7.97E+4 ± 6.41E+4	3.68E+4 ± 2.96E+4	2.48
8	85.028052	-69.744284	5.21	53.8 ± 44.3	8.16E+4 ± 6.72E+4	3.75E+4 ± 3.08E+4	2.49
9	85.023251	-69.741295	2.99	68.0 ± 25.4	3.39E+4 ± 1.27E+4	2.62E+4 ± 9.81E+3	2.75

Column 1: The ID we give each clump. Column 4: The radius calculated from the area of the clump. Column 6: The total H_2 mass. We assumed the typical ^{12}CO(2-1)/^{12}CO(1-0) ratio toward HII regions of 0.85 (Nishimura et al., 2015). We use a X_{CO} conversion factor of 7×10^{20} cm^{-2} (Fukui et al., 2008). Column 7: The virial mass calculated by assuming the virial parameter equals 1. Column 8: The measured linewidth. NOTE: This table is available in its entirety in Appendix D. A portion is shown here for guidance.

3.5 Results of Dendrogram Analysis

We use ALMA ^{12}CO$(2-1)$, ^{13}CO$(2-1)$, and CS$(2-1)$ data cubes of N159W (Fukui et al., 2015) and N159E (Saigo et al., 2017) for our dendrogram analysis. We chose to exclude all flux less than 10σ of the noise level for the ^{12}CO$(2-1)$ and CS$(2-1)$ molecular gas observations, and all flux less than 5σ of the noise level for the ^{13}CO$(2-1)$ molecular gas observation. We also chose the minimum size of a clump to be the size of the ALMA beam. Details on exact values we chose can be found in Table 3.13. There were a few clumps output from the dendrogram algorithm that were smaller than the minimum number of pixels we specified (and therefore smaller than a beam size) because of rounding errors.We excluded those clumps from our analysis. We list the ^{12}CO clumps and their properties of N159W and N159E in Table 3.14 and Table 3.15, the ^{13}CO clumps and their properties of N159W and N159E in Table 3.16 and Table 3.17, and the CS clumps and their properties of N159W and N159E in Table 3.18 and Table 3.19.

Table 3.17: Column Densities and Mass Derived from N159W ^{13}CO (2-1) Clumps

Clump ID	RA	Dec	Radius [pc]	$N_{^{13}CO}$ [cm^{-2}]	Total H_2 Mass [$M_\odot$]	Virial Mass [$M_\odot$]	Linewidth [km/s]
0	84.904807	-69.769414	0.853	1.38E+16	1.57E+3 ± 7.40E+2	5.31E+2 ± 2.51E+2	0.732
1	84.907429	-69.769590	0.484	1.84E+16	6.70E+2 ± 1.35E+2	2.32E+2 ± 4.68E+1	0.643
2	84.902543	-69.769225	0.665	1.17E+16	8.03E+2 ± 3.50E+2	2.65E+2 ± 1.15E+2	0.586
3	84.908195	-69.772436	0.712	6.95E+15	5.49E+2 ± 4.30E+2	7.70E+2 ± 6.04E+2	0.964
4	84.910940	-69.773204	0.394	9.36E+15	2.26E+2 ± 7.29E+1	1.14E+2 ± 3.66E+1	0.498
5	84.910832	-69.773152	0.291	6.90E+15	9.06E+1 ± 2.92E+1	2.25E+1 ± 7.27E+0	0.258
6	84.903995	-69.769022	0.394	1.09E+16	2.63E+2 ± 7.26E+1	1.58E+2 ± 4.35E+1	0.587
7	84.895716	-69.769467	0.199	4.39E+15	2.71E+1 ± 9.40E+0	1.65E+1 ± 5.73E+0	0.267
8	84.899779	-69.769674	0.326	8.18E+15	1.36E+2 ± 4.14E+1	3.48E+1 ± 1.06E+1	0.303
9	84.901012	-69.759896	2.67	3.89E+16	4.30E+4 ± 2.26E+4	1.58E+4 ± 8.28E+3	2.25

Column 1: The ID we give each clump. Column 4: The radius calculated from the area of the clump. Column 6: The total H_2 mass. We use a $\frac{^{13}CO(2-1)}{H_2}$ conversion factor of 3.2×10^{-7} (Fujii et al., 2014). Column 8: The measured linewidth. NOTE: This table is available in its entirety in Appendix D. A portion is shown here for guidance.

Table 3.18: Column Densities and Mass Derived from N159E ^{13}CO (2-1) Clumps

Clump ID	RA	Dec	Radius [pc]	$N_{^{13}CO}$ [cm^{-2}]	Total H_2 Mass [$M_\odot$]	Virial Mass [$M_\odot$]	Linewidth [km/s]
0	85.038545	-69.757583	0.156	2.27E+15	8.55E+0 ± 2.30E+0	4.46E-1 ± 1.20E-1	0.050
1	85.044310	-69.756562	0.192	2.75E+15	1.57E+1 ± 4.29E+0	1.96E+0 ± 5.35E-1	0.094
2	85.066163	-69.749707	0.147	1.58E+15	5.32E+0 ± 1.95E+0	1.63E-1 ± 5.95E-2	0.031
3	85.029244	-69.732067	0.175	2.59E+15	1.23E+1 ± 3.25E+0	4.18E-2 ± 1.11E-2	0.014
4	85.011350	-69.756320	0.139	1.75E+15	5.31E+0 ± 1.66E+0	1.43E+0 ± 4.46E-1	0.094
5	85.057335	-69.749045	0.220	1.43E+15	1.08E+1 ± 6.51E+0	2.54E+0 ± 1.53E+0	0.100
6	85.066326	-69.738986	0.131	1.87E+15	5.02E+0 ± 1.38E+0	2.31E+0 ± 6.36E-1	0.123
7	85.068687	-69.752008	0.156	1.99E+15	7.50E+0 ± 2.30E+0	1.43E+0 ± 4.38E-1	0.089
8	85.059543	-69.753669	0.183	2.34E+15	1.22E+1 ± 3.73E+0	1.60E+0 ± 4.89E-1	0.087
9	85.031573	-69.740692	0.270	2.41E+15	2.74E+1 ± 1.21E+1	4.25E+1 ± 1.87E+1	0.368

Column 1: The ID we give each clump. Column 4: The radius calculated from the area of the clump. Column 6: The total H_2 mass. We use a $\frac{^{13}CO(2-1)}{H_2}$ conversion factor of 3.2×10^{-7} (Fujii et al., 2014). Column 8: The measured linewidth. NOTE: This table is available in its entirety in Appendix D. A portion is shown here for guidance.

Table 3.19: N159W CS Clump Properties

Clump ID	RA	Dec	F_{CS} [K km s^{-1}]	Radius [pc]	Linewidth [km/s]
0	84.900490	-69.760668	7.03	1.87	1.57
1	84.901670	-69.760488	7.53	1.42	1.50
2	84.924222	-69.769256	4.14	1.07	1.15
3	84.924179	-69.769225	4.03	0.968	1.04
4	84.902862	-69.760181	6.43	0.692	0.818
5	84.893736	-69.761932	4.20	0.695	0.636
6	84.903132	-69.760252	1.28	0.326	0.072
7	84.902832	-69.760261	3.91	0.477	0.378
8	84.899555	-69.757131	1.25	0.789	0.334
9	84.924917	-69.770213	0.885	0.426	0.209
10	84.902966	-69.759894	3.20	0.466	0.331
11	84.901660	-69.757901	1.60	0.978	0.552
12	84.909124	-69.756705	1.00	0.425	0.206

Column 1: The ID we give each clump. Column 4: Total integrated flux of the CS clump. Column 5: The radius calculated from the area of the clump. Column 6: The measured linewidth.

Table 3.20: N159E CS Clump Properties

Clump ID	RA	Dec	F_{CS} [K km s^{-1}]	Radius [pc]	Linewidth [km/s]
0	85.002085	-69.748477	0.685	0.563	0.074
1	85.045296	-69.733553	0.690	0.668	0.020
2	85.009611	-69.736158	0.637	0.367	0.099
3	85.009678	-69.749372	0.726	0.404	0.098
4	85.049712	-69.734107	0.601	0.487	0.087
5	85.022810	-69.733709	0.579	0.385	0.100
6	85.000666	-69.744195	0.608	0.433	0.039
7	85.001176	-69.747212	0.654	0.486	0.043
8	85.035000	-69.744526	1.13	0.793	0.477
9	85.012019	-69.750076	2.68	1.01	0.921
10	85.012619	-69.750668	0.945	0.624	0.220
11	85.039625	-69.744220	0.588	0.464	0.010
12	85.019641	-69.742696	2.97	0.911	0.834
13	85.015413	-69.753279	0.556	0.410	0.142
14	85.019712	-69.742675	2.83	0.894	0.766
15	85.072125	-69.744963	0.666	0.399	0.045
16	85.011860	-69.749921	3.14	0.752	0.594

Continued on next page

Table 3.20 – continued from previous page

Clump ID	RA	Dec	F_{CS} [K km s^{-1}]	Radius [pc]	Linewidth [km/s]
17	85.012093	-69.749964	1.11	0.475	0.182
18	85.020176	-69.742593	2.19	0.378	0.219
19	85.015773	-69.754563	0.683	0.404	0.070
20	85.011605	-69.749873	2.46	0.533	0.306
21	85.022312	-69.746297	1.27	0.526	0.325
22	85.021811	-69.740961	1.72	0.709	0.382
23	85.038764	-69.739443	0.659	0.351	0.067
24	85.034426	-69.740282	1.45	0.597	0.342
25	85.040074	-69.732837	0.940	0.831	0.348
26	85.018950	-69.747129	0.794	0.482	0.083
27	85.027638	-69.745328	0.693	0.379	0.069
28	85.025787	-69.733035	0.749	0.544	0.100
29	85.069060	-69.748944	0.657	0.447	0.060
30	85.000212	-69.745836	0.646	0.326	0.080
31	85.012802	-69.735531	0.587	0.391	0.043

Column 1: The ID we give each clump. Column 4: Total integrated flux of the CS clump. Column 5: The radius calculated from the area of the clump. Column 6: The measured linewidth.

We derive the radius, linewidth, mass from known conversion factors. We calculate the virial mass assuming a virial parameter of 1 for all three gas tracers. The radius of the clumps lets us trace the substructure of the GMCs, from the larger and less dense clumps to the small and compact and high density cores. The linewidth allows us to determine the importance of potential shocks in the vicinity of the massive stars. Comparisons between the molecular mass and the virial mass show that the clumps are gravitationally bound, i.e. gravity is playing a more important role than the kinetic energy of the clumps. For the $^{13}CO(2-1)$ gas we also calculate the column density of the molecular clumps. The column density in N159W ranges from 2.5×10^{15} cm^{-2} to 7.8×10^{16} cm^{-2}. And the column density in N159E ranges from

1.3×10^{15} cm^{-2} to 3.2×10^{16} cm^{-2}. The column density varies by a factor of x31 in N159W and a factor of x24 in N159E.

In order to calculate the total mass from $^{12}CO(2-1)$ we use a typical $^{12}CO(2-1)/^{12}CO(1-0)$ ratio of 0.85 (Nishimura et al., 2015) and a $^{12}CO(1-0)$ intensity to column density ratio of $X_{CO} = 7 \times 10^{20}$ cm^{-2} (Fukui et al., 2008). The total mass derived from $^{12}CO(2-1)$ of N159W is $(2.12 \pm 1.36) \times 10^5$ M$_\odot$. Fukui et al. (2015) calculate the total mass of N159W from $^{12}CO(2-1)$ to be 2.4×10^5 M$_\odot$. The total mass of N159W we calculate in this chapter is consistent with the mass derived from Fukui et al. (2015). The total mass derived from $^{12}CO(2-1)$ of N159E is $(1.23 \pm 0.87) \times 10^5$ M$_\odot$. Saigo et al. (2017) derive the total mass of N159E from $^{12}CO(2-1)$ to be 1.3×10^5 M$_\odot$. The N159E mass estimation in this chapter and in Saigo et al. (2017) are within error.

We calculate the mass from $^{13}CO(2-1)$ using LTE and a $H_2/^{13}CO$ ratio of 3.1×10^6 (Fujii et al., 2014). The total mass derived from $^{13}CO(2-1)$ of N159W is $(0.82 \pm 0.35) \times 10^5$ M$_\odot$. The total mass derived from $^{13}CO(2-1)$ of N159E is $(0.44 \pm 0.25) \times 10^5$ M$_\odot$. Saigo et al. (2017) calculate the total mass of N159E from $^{13}CO(2-1)$ to be 0.9×10^5 M$_\odot$. The total mass of N159E calculated in this chapter is about 1/2 the total mass calculated by Saigo et al. (2017). One reason for a lower mass estimation in this chapter could be because Saigo et al. (2017) assumed a 20K

excitation temperature where the calculated excitation temperature is below 20K. We do not make this assumption, and use excitation temperatures below 20K when the calculated excitation temperature is below 20K. This would give us a lower mass estimation than Saigo et al. (2017). Another reason for this discrepancy is because Saigo et al. (2017) used the whole ^{13}CO$(2-1)$ emission to calculate the mass, whereas we are using emission above 5σ to calculate the mass.

3.6 Results

3.6.1 Size-Linewidth Relation

The size-linewidth relation (r-σ relation) of molecular gas for Galactic and extragalactic sources has been studied for decades. Larson (1981) first proposed this relation after finding r $\propto \sigma^{0.38}$ for several ^{12}CO clumps from literature. This observational result was very close to the turbulent theory of molecular clouds. The r-σ relation originally found by Larson was not that different from the Kolmogoroff law for subsonic turbulence which predicts a power-law index of 0.33. A power-law index between 0.38-0.8 has been observed for both Galactic (Heyer et al., 2009; Larson, 1981; Shetty et al., 2012) and extragalactic environment (Bolatto et al., 2008; Wong et al., 2011). The importance of the measuring sizes and linewidths is that there is a similarity in the r-σ relation of molecular clouds independent of the local environment because of the universality of turbulence (Heyer & Brunt, 2004). My work shows that deviations

from this similarity can be used to quantify local turbulence. The slope and intercept values for all relevant size-linewidth relations are given in Table 3.20.

Table 3.21: Slopes and Intercepts in r - σ Relations

Region	Line	Transition	A	b	citation
30 Doradus	^{12}CO	2-1	1.66	0.65	Nayak et al. (2016)
N159W	^{12}CO	2-1	1.04	0.75	
N159E	^{12}CO	2-1	1.01	0.90	
Dwarf Galaxies	^{12}CO	2-1, 1-0	0.44	0.60	Bolatto et al. (2008)
30 Doradus	^{13}CO	2-1	1.58	0.97	Nayak et al. (2016)
N159W	^{13}CO	2-1	0.97	1.11	
N159E	^{13}CO	2-1	1.03	1.27	
Perseus	^{13}CO	1-0	0.62	0.54	Shetty et al. (2012)
CMZ	HCN, N_2H^+	1-0	3.60	0.50	Shetty et al. (2012)
N159W	CS	2-1	0.83	1.55	
N159E	CS	2-1	0.62	2.37	

We lists slopes and intercepts where A and b are from the general equation of a line: $y = Ax^b$.

We define the radius of the clumps as the following: $R = (A/\pi)^{1/2}$, where A is the total area of the clumps that is output by *astrodendro*. We use the *astrodendro* to identify the molecular clumps in N159W and N159E. As noted in Section 3.4, the dendrogram algorithm eliminates clumps that are less than the beam size and those with fluxes less than 10σ of the noise level. We further remove clumps that have linewidths of 0 km/s (that is noise clumps that spuriously got detected) and clumps that are slightly smaller than the beam size (most likely due to the dendrogram algorithm rounding numbers). We compare our results to a similar study done in 30 Doradus by Nayak et al. (2016). We plot the resulting r-σ relation in Figure 3.12. Black diamonds represent $^{13}CO(2-1)$ clumps in N159W, red squares repre-

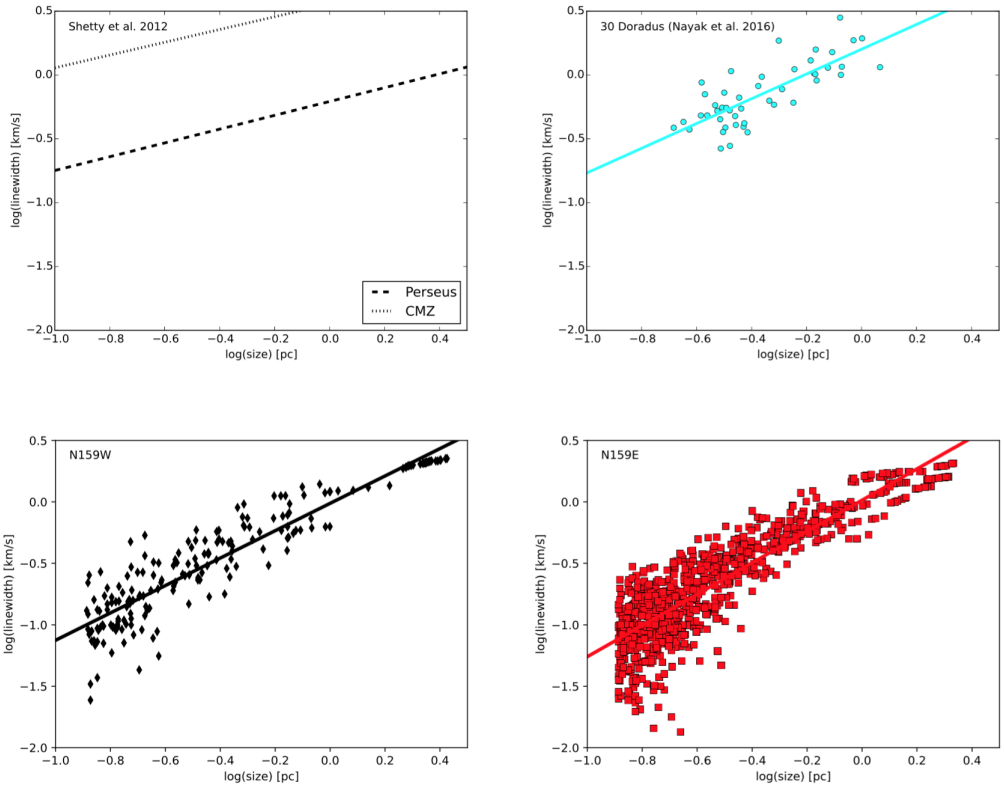

Figure 3.12: Size-linewidth relation of ^{13}CO (2-1) clumps. We only include clumps that are at least as large as a beam size and have emission greater than 10σ of the noise level. Top Left: The dashed black line ($\sigma = 0.62\mathrm{r}^{0.54}$) is the best-fit line for CO molecular clumps in the Perseus analysis by Shetty et al. (2012) using dendrograms. The dotted black line ($\sigma = 3.60\mathrm{r}^{0.50}$) is the best-fit line for N_2H^+ and HCN dendrogram clumps in the CMZ (Shetty et al., 2012). Top Right: Cyan circles are the ^{13}CO (2-1) clumps in 30 Doradus. The best fit line going through the cyan circles is given by $\sigma = (1.58 \pm 0.18)\mathrm{r}^{(0.97\pm0.12)}$. Bottom Left: Black diamonds are the ^{13}CO (2-1) clumps in N159W. The best fit line to the black diamonds is give by $\sigma = (0.97 \pm 0.04)\mathrm{r}^{(1.11\pm0.03)}$. Bottom Right: Red squares are the ^{13}CO (2-1) clumps in N159E. The best fit line to the red squares is given by $\sigma = (1.03 \pm 0.03)\mathrm{r}^{(1.27\pm0.02)}$.

sent ^{13}CO$(2-1)$ clumps in N159E, and cyan circles represent ^{13}CO$(2-1)$ clumps in 30 Doradus. The solid black line represents the best-fit line for the N159W clumps ($\sigma = (0.97 \pm 0.04)\mathrm{r}^{(1.11\pm0.03)}$), the solid red line represents the best-fit line for the N159E clumps ($\sigma = (1.03 \pm 0.03)\mathrm{r}^{(1.27\pm0.02)}$), and the solid cyan line represents the best-fit line for the 30 Doradus clumps ($\sigma = (1.58 \pm 0.18)\mathrm{r}^{(0.97\pm0.12)}$). The dashed black line is the best-fit line for the size-linewidth relation for clumps in the Perseus cloud studied by Shetty et al. (2012), and the dotted line is the best-fit line for the relation for clumps in the Galactic center. The slope in the size-linewidth relation in N159W, N159E, 30 Doradus, and other Galactic clouds traced by various different high density gas tracers are very similar. We conduct a similar analysis of the ^{12}CO$(2-1)$ clumps in N159W and N159E. And once again find that the size-linewidth relation slope of the ^{12}CO$(2-1)$ gas is similar to previous Galactic and extragalactic studies. We list the slope and intercepts in Table 3.20.

We plot the size-linewidth relation of ^{12}CO$(2-1)$, ^{13}CO$(2-1)$, and CS$(2-1)$ in Figures 3.13 (N159W) and 3.14 (N159E) in different symbols and colors. The ^{12}CO$(2-1)$ clumps are in orange triangles, the ^{13}CO$(2-1)$ clumps are in black diamonds, and the CS$(2-1)$ clumps are in green pentagons for N159W. The ^{12}CO$(2-1)$ clumps are in purple stars, the ^{13}CO$(2-1)$ clumps are in red squares, and the CS$(2-1)$ are in blue hexagons for N159E. The best-fit line going through the ^{12}CO$(2-1)$ clumps is $\sigma = (1.04 \pm 0.02)\mathrm{r}^{(0.75\pm0.02)}$ for N159W (Figure 3.13) and $\sigma = (1.01 \pm 0.05)\mathrm{r}^{(0.90\pm0.04)}$

in N159E (Figure 3.14). The best-fit line going through the CS$(2-1)$ clumps is $\sigma = (0.83 \pm 0.11)\mathrm{r}^{(1.55\pm0.22)}$ for N159W and $\sigma = (0.62 \pm 0.22)\mathrm{r}^{(2.37\pm0.47)}$ for N159E.

One similarity in both regions is that the slope of the size-linewidth relation gets steeper when looking at ^{12}CO$(2-1)$ (slope is 0.75 in N159W), ^{13}CO$(2-1)$ (slope is 1.11 in N159W), and CS$(2-1)$ clumps (slope in 1.55 in N159W). What is causing the slope of the size-linewidth relation of the CS$(2-1)$ gas to be significantly steeper than those of the ^{12}CO$(2-1)$ and ^{13}CO$(2-1)$ gas? The answer could be because of shocks from protostellar jets. The average linewidth of ^{12}CO clumps that are near (within 2 clump radii) the CS clumps is 2.7 km/s in N159W and 1.9 km/s in N159E. The average linewidth of ^{12}CO clumps that are not near any CS clumps is 0.75 km/s in N159W and 0.68 km/s in N159E. The average linewidth of the ^{12}CO clumps near CS clumps is x3.6 higher than ^{12}CO clumps not near CS clumps in N159W, and is x2.8 higher than ^{12}CO clumps not near CS clumps in N159E. A similar trend can be seen in the ^{13}CO clumps. Those that are near CS clumps have an average linewidth of 1.2 km/s in N159W and 1.0 km/s in N159E. And those that are not near any CS clumps have an average linewidth of 0.25 km/s in N159W and 0.28 km/s N159E. ^{13}CO clumps that are near CS in N159W have higher linewidths by a factor of x4.8 than ^{13}CO clumps that are not near CS. And in N159E ^{13}CO clumps that are near CS clumps have higher linewidths by a factor of x3.6 than ^{13}CO clumps that are near CS clumps. The CS$(2-1)$ is more compact and lies closer to the central protostar than either ^{12}CO$(2-1)$ or ^{13}CO$(2-1)$. The ^{12}CO$(2-1)$ or ^{13}CO$(2-1)$ clumps that

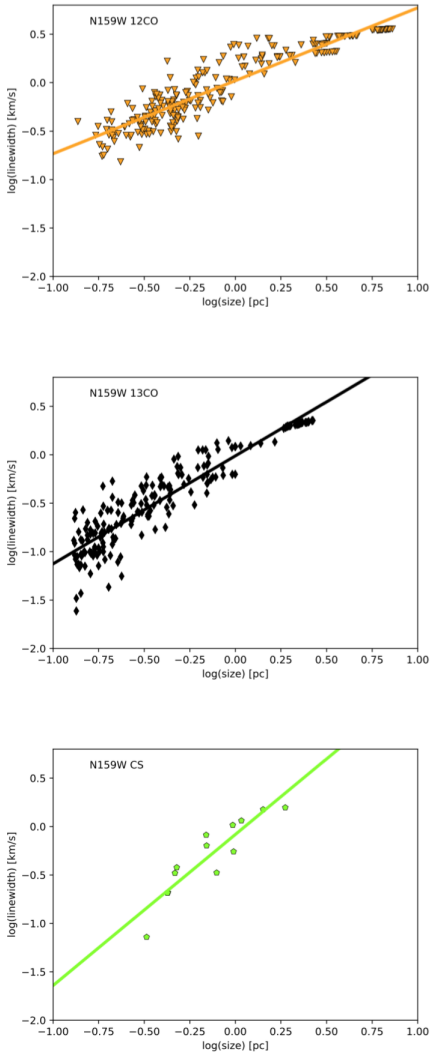

Figure 3.13: Size-linewidth relation of clumps in N159W. Top: The ^{12}CO (2-1) relation. The best-fit line going through the ^{12}CO (2-1) clumps is $\sigma = (1.04 \pm 0.02)\ \mathrm{r}^{(0.75\pm0.02)}$. Middle: The ^{13}CO (2-1) relation. The best-fit line going through the ^{13}CO (2-1) clumps is given by equation $\sigma = (0.97 \pm 0.04)\ \mathrm{r}^{(1.11\pm0.03)}$. Bottom: The CS (2-1) relation. The best-fit line going through the CS (2-1) clumps is $\sigma = (0.83 \pm 0.11)\ \mathrm{r}^{(1.55\pm0.22)}$.

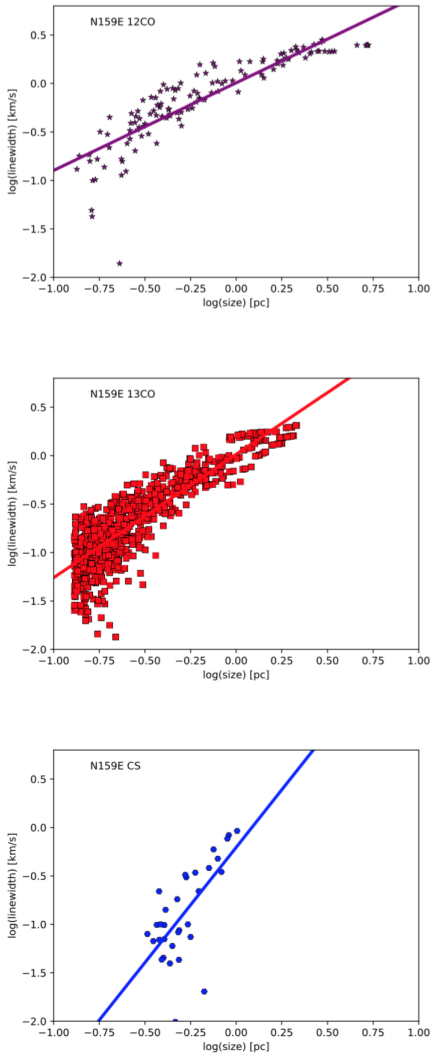

Figure 3.14: Size-linewidth relation of clumps in N159E. Top: The ^{12}CO (2-1) relation. The best-fit line going through the ^{12}CO (2-1) clumps is $\sigma = (1.01 \pm 0.05)\mathrm{r}^{(0.90\pm0.04)}$. Middle: The ^{13}CO (2-1) relation. The best-fit line going through the ^{13}CO (2-1) clumps is given by equation $\sigma = (1.03 \pm 0.03)\mathrm{r}^{(1.27\pm0.02)}$. Bottom: The CS (2-1) relation. The best-fit line going through the CS (2-1) clumps is $\sigma = (0.62 \pm 0.22)\mathrm{r}^{(2.37\pm0.47)}$.

lie closer to the protostar in the same region as the CS$(2-1)$ gas show enhanced linewidths. The CS$(2-1)$ could be interacting with the protostellar jets and winds more so than ^{12}CO$(2-1)$ or ^{13}CO$(2-1)$, and therefore we see the resulting effect in a much steeper slope in the size-linewidth relation of the gas.

3.6.2 Is Larson's Law Applicable to Massive Star Forming Regions?

For decades Larson's laws (Larson, 1981) have been thought to be applicable to all molecular gas clouds. Larson's first law implied that the clump linewidth is only dependent on the size of the clumps: $\sigma \propto \mathrm{r}$. Assuming self-gravitating clumps, which is a fair assumption since all the clumps in N159W and N159E have virial parameters less than 1, and substituting $\Sigma = \frac{\mathrm{M_{obs}}}{\pi \mathrm{r}^2}$ for the molecular gas surface density we can write the following equation for the linewidth (Heyer et al., 2009):

$$\sigma = \left(\frac{\pi G}{5}\right)^{0.5} \Sigma^{0.5} r^{0.5}. \tag{3.1}$$

In the above equation σ is the linewidth, G is the gravitational constant, r is the clumps size and Σ is the mass surface density. You can recover Larson's first law from Equation 1 when if you assume Σ is constant ($\sigma \propto \mathrm{r}^{0.5}$). In other words $\frac{\sigma}{\mathrm{r}^{0.5}} = \left(\frac{\pi \mathrm{G}\Sigma}{5}\right)^{0.5}$, where $\frac{\sigma}{\mathrm{r}^{0.5}}$ is a constant. We define $\frac{\sigma}{\mathrm{r}^{0.5}}$ to be ν. If Larson's first law were to hold, then we would see a flat line with a slope of zero when we plot ν versus Σ

(Heyer et al., 2009; Nayak et al., 2016).

Figure 3.15 shows that Larson's first law is not applicable to N159W, N159E, 30 Doradus, or the clumps studied by Heyer et al. (2009) because ν does have a dependence on Σ in all these regions of massive star formation. We find that $\nu \propto \Sigma^{0.22}$ in N159W (solid black line), $\nu \propto \Sigma^{0.36}$ in N159E (solid red line), $\nu \propto \Sigma^{0.45}$ in 30 Doradus (solid cyan line, Nayak et al. (2016)), and $\nu \propto \Sigma^{0.34}$ in the study done by Heyer et al. (2009). The slope of the line when plotting ν versus Σ is not reported in Heyer et al. (2009). The slope of 0.34 is what we find when we take their reported size, mass, and linewidth values. Table 3.21 lists the slope and linewidth values for the Σ - ν relations we plot in Figure 3.15. Ballesteros-Paredes et al. (2011) discuss the size-linewidth relation of massive star forming regions and show in their paper (Figure 1) that dense massive cores are located above Larson's original size-linewidth relation. Ballesteros-Paredes et al. (2011) theorize that molecular clouds are collapsing as a whole, and clumps within molecular clouds are also locally collapsing at the same time. Larson's law only holds in the case of constant column density. Larson (1981) find the column density is nearly independent of the size of the molecular cloud in their study: column density $\propto R^{-0.1}$. However in massive star forming regions we are probing column densities that span a few orders of magnitude, which leads to the break down of Larson's size-linewidth relation (Ballesteros-Paredes et al., 2011). As mentioned in Section 3.4.3, the $^{13}CO(2-1)$ column density in N159W ranges from

2.5×10^{15} cm^{-2} to 7.8×10^{16} cm^{-2}. And the ^{13}CO$(2-1)$ column density in N159E ranges from 1.3×10^{15} cm^{-2} to 3.2×10^{16} cm^{-2}. The column densities we probe in N159W and N159E have a range that spans over an order of magnitude. The findings from this study on N159, as well as previous studies on 30 Doradus and Milky Way clumps (Ballesteros-Paredes et al., 2011; Heyer et al., 2009), lead to the conclusion that Larson's relationships are not always applicable, especially in regions of high mass star formation.

Table 3.22: Slopes and Intercepts in Σ - ν Relations

Region	Line	Transition	A	b	citation
Milky Way Clouds	^{13}CO	1-0	0.13	0.34	Heyer et al. (2009)
30 Doradus	^{13}CO	2-1	0.04	0.45	Nayak et al. (2016)
N159W	^{13}CO	2-1	0.21	0.22	
N159E	^{13}CO	2-1	0.11	0.36	

We lists slopes and intercepts where A and b are from the general equation of a line: $y = Ax^b$.

3.6.3 Virial Analysis

The dynamics of the ^{13}CO$(2-1)$ clumps can further be analyzed by the virial parameter, α, which is the ratio of the kinetic energy to the gravitational energy. We define α to be equal to $\frac{5\sigma^2_r}{GM}$ (Rosolowsky et al., 2008). Figure 3.16 shows the virial parameter versus the clump mass of the ^{13}CO$(2-1)$ clumps in 30 Doradus (top plot), N159W (middle plot), and N159E (bottom plot). When $\alpha<1$, the clump is self-gravitating. Almost all the ^{13}CO$(2-1)$ clumps in 30 Doradus, N159W, and N159E

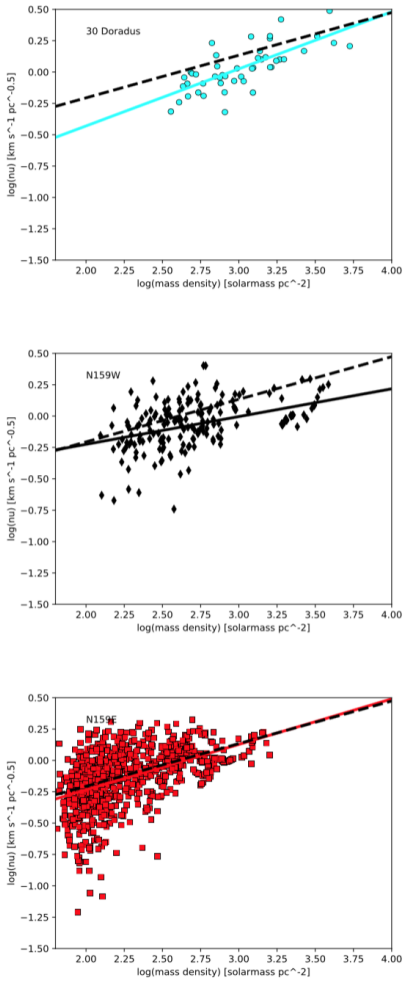

Figure 3.15: The dependence of $\frac{\sigma}{r^{0.5}}$ on Σ. Top: The cyan line given by equation $\nu = (0.04 \pm 0.02)\Sigma^{(0.45\pm0.06)}$ is the best-fit line going through ν versus Σ of clumps in 30 Doradus. Middle: The black line given by equation $\nu = (0.21 \pm 0.04)\Sigma^{(0.22\pm0.03)}$ is the best-fit line going through ν versus Σ of N159W clumps in this study. Bottom: The red line ($\nu = (0.11 \pm 0.01)\Sigma^{(0.36\pm0.02)}$) is the best-fit line going through ν versus Σ of N159E clumps in this study. The dashed line in all plots is the ν-Σ relation found by Heyer et al. (2009): $\nu = 0.13\Sigma^{0.34}$. The dependence of ν on Σ is contradictory to Larson's scaling relation which predicts there should be no dependence (slope = 0).

are self-gravitating. High mass star forming regions analyzed by Pillai et al. (2011), Tan et al. (2013), and Wienen et al. (2012) have virial parameters much smaller than non-high mass star forming regions analyzed by Lada et al. (2008) and Enoch et al. (2006). Kauffmann et al. (2013) analyze virial parameters of molecular gas in a wide range of star forming conditions. Their analytical calculations show that it is possible for molecular gas clouds to not have star formation, even when virial parameters indicate the cloud is self-gravitating. When the velocity dispersions are low for a given mass and size of a clump, a non-magnetized molecular gas cloud can be stable against collapse. Tables 3.16 and 3.17 list the velocity dispersions of $^{13}CO(2-1)$ clumps in N159W and N159E. It is possible the clumps in this study to fall in the range shaded in yellow in Figure 4a in Kauffmann et al. (2013). Therefore several of the $^{13}CO(2-1)$ clumps are not forming stars. Kauffmann et al. (2013) suggest that another possibility is that magnetic forces counteract the gravitational collapse, leading to our observed result of many molecular gas clumps having low virial parameters but are not actively forming stars. An alternate explanation for the clumps with small virial parameters that are not collapsing could be that they are clumps which have short life spans and will soon collapse and form a protostar. Clumps with low virial parameters that do not have other means to support themselves would collapse quickly and rapidly. New protostars could soon form in many of the starless $^{13}CO(2-1)$ molecular gas clumps in N159W and N159E.

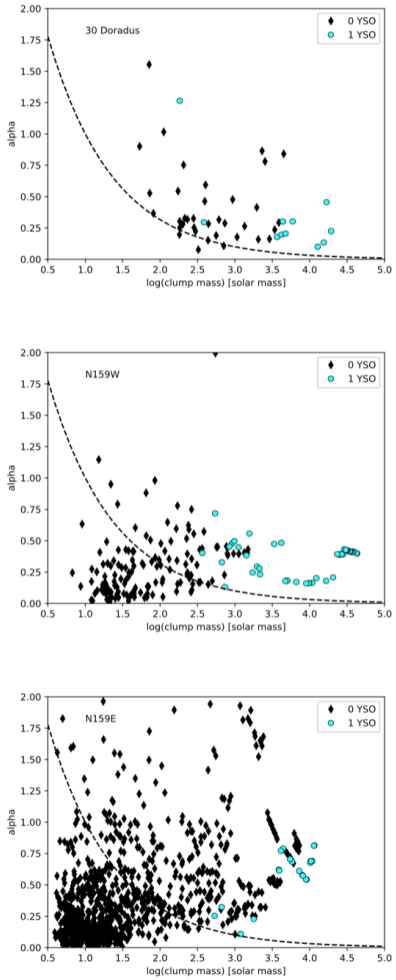

Figure 3.16: Top: Figure showing the relation between the virial parameter versus the mass of the clump in 30 Doradus. We define α to equal to $\frac{5\sigma^2 \mathrm{r}}{\mathrm{G\,M}}$. Middle: Figure showing the relation between the virial parameter versus the mass of the clump in N159W. Bottom: Figure showing the relation between the virial parameter versus the mass of the clump in N159E. Black diamonds are clumps with no YSO candidates and cyan circles are clumps with 1 YSO candidate. Virial parameters for the smallest clumps are underestimated because the size is overestimated (not spatially resolved). We match YSO candidates to ^{13}CO (2-1) clumps. This is to reduce the possibility of a YSO candidate being associated with a spurious noise clump. The dashed line in the plots separates the clumps forming by monolithic collapse (above the line) versus those forming by competitive accretion (below the line) (Krumholz et al., 2005).

3.6.4 The Massive YSO Candidates Greater Than $20M_\odot$

All the YSO candidates greater than $20M_\odot$ are associated with $^{12}CO(2-1)$ molecular gas. We say a YSO is associated with a molecular cloud or a molecular cloud is associated with a YSO if the YSO candidate lies within a distance that is less the radius of the clump, where the radius is defined as $R = (A/\pi)^{1/2}$. The $^{12}CO(2-1)$ clumps associated with YSO candidates 'w1' and 'w3' are located, in the Northern region of N159W, have a complex spatial-velocity structure (Fukui et al., 2015). The interaction of the molecular gas seems to trigger the formation of these massive YSO candidates. YSO candidate 'w1' is associated with a blue-shifted outflow (Fukui et al., 2015). The red-shifted outflow is not observed and could be masked by the complex gas distribution in which this YSO candidate is located. The low abundance of high density gas tracers means that they can easily be photodissociated in star forming regions. The strong stellar winds and turbulence from the chaotic interactions of the gas can cause some molecules to break apart. High mass star formation takes place at much higher densities of that 10^5 cm^{-3}, therefore making the $CS(2-1)$ ALMA observation a better probe of high mass star formation. There is a lot less $CS(2-1)$ than $^{12}CO(2-1)$ or $^{13}CO(2-1)$. And what little of it exists, does so in the vicinity of the more massive YSO candidates in this chapter. Figures 3.3 shows that the 2/5 of the very high mass YSO candidates ($>20M_\odot$) in N159W and the most massive YSO

candidate in N159E ($50M_{\odot}$) are associated with CS$(2-1)$. The 3 very high massive YSO candidates not associated with CS$(2-1)$ in N159W are still located very near (within a few parsecs) of the CS$(2-1)$ molecular gas. YSO candidates 'w1' and 'w3' in the Northern part of N159W as well as YSO candidates 'w5' is the Southern part of N159W are associated with $C^{18}O(2-1)$ gas. The intensity of $C^{18}O(2-1)$ in the Northern part of N159W is the strongest, which indicates the youth of the YSO candidates 'w1' and 'w3'. This is consistent with the existence of an outflow associated with YSO candidates 'w1' (Fukui et al., 2015). $C^{18}O(2-1)$ is detected in N159E, however it is very weak and not associated with the massive YSO candidates in the region. Once again in N159W we see that the high density gas tracer $C^{18}O(2-1)$ is found in the vicinity of YSO candidates $>20M_{\odot}$. A deeper analysis of the $C^{18}O(2-1)$ molecular gas and $C^{18}O(1-0)$ molecular gas and comparison of them to $C^{18}O$ observations in the Milky Way will be presented by Tokuda et al. (in prep).

Is it just a coincidence that 6/6 of the YSO candidates $>20M_{\odot}$ presented in this chapter are associated with $^{12}CO(2-1)$ molecular gas, half of which are also associated with CS$(2-1)$ and the other half of which lie within 5 clump radii to CS$(2-1)$? Tosaki et al. (2016) find that more massive GMCs have higher CS/^{13}CO ratios and smaller CS/^{13}CO ratios are found in less massive GMCs. In this chapter we find the CS$(2-1)$ to be located at the central knots of the massive $^{13}CO(2-1)$ molecular

gas clouds. This correlation between CS and ^{13}CO might exist because more massive GMCs form dense molecular gas more efficiently than the less massive GMCs (Tosaki et al., 2016). In this chapter we find that the more massive YSO candidates are located within or in the vicinity of CS$(2-1)$. It is possible that more massive GMCs are not only more efficient at forming dense clouds, but more massive GMCs are more efficient at forming massive YSOs that are $>20M_{\odot}$. The formation of massive clouds, and the subsequent massive YSOs, is like a runaway effect. The clouds that initially start off a bit larger than the other clouds in the vicinity are able to gravitationally attract even more mass. This in turn leads to more fuel for when the star formation process starts, and for the stars in the more massive clouds accrete more mass than their counterparts in less massive clouds.

3.6.5 YSO Candidates Less Than 20$M_{\odot}$

There are a total of 10 YSO candidates in N159W that are between 7-20$M_{\odot}$. Their Types can be seen in Table 3.11. Only 1/10 of these slightly lower mass (but still considered to be massive) YSO candidates is a Type I object. The majority of these 7-20$M_{\odot}$ have spectral properties that indicate that these objects are more evolved and are starting to clear out the dust around them and the optical star light is becoming more prevalent in their SEDs. More evidence that these objects are later Type objects is given by looking at their association (or lack of association) with molecular gas clumps. There are only 4 YSO candidates that are associated with

^{12}CO$(2-1)$, and none that are associated with ^{13}CO$(2-1)$ or CS$(2-1)$. Perhaps several (or even all) these YSOs initially did have a small amount of ^{12}CO$(2-1)$ and ^{13}CO$(2-1)$ molecular gas surrounding them, but they were able to blow all the gas away from them with the stellar winds. Therefore we find that the majority of the YSO candidates between 7-20M$_\odot$ in N159W are not associated with ^{12}CO$(2-1)$ or ^{13}CO$(2-1)$ molecular gas. It is likely that none of the 7-20M$_\odot$ YSOs in N159W had any correlation with CS$(2-1)$ molecular gas in their lifetime. The initial gas cloud these lower mass (but still massive) YSOs formed in were most likely not large enough to accrete lots of star formation fuel and not efficient enough to form dense molecular gas tracers like CS$(2-1)$.

There is only one very massive YSO in N159E, the Papillon Nebula YSO. All the other 8 YSO candidates in N159E have masses between 7-20M$_\odot$. Table 3.12 lists the Type. There is not a single Type I object in N159E. They are all Type II or Type III objects. The majority of the 8 YSO candidates are not associated with molecular gas: 2/8 are associated with ^{12}CO$(2-1)$, 1/8 is associated with ^{13}CO$(2-1)$, and none are associated with CS$(2-1)$. The lack of any Type I YSO candidate and the majority of the candidates not being associated with any gas is consistent with the N159E GMC being at a later stage than the N159W GMC. There has been more time for the YSOs in N159E to dispel the gas around them than the YSOs in N159W. Also the 7-20M$_\odot$ YSOs could have had less molecular gas surrounding them to being with.

Therefore making it easier to blow away the molecular gas than an embedded YSO $>20M_{\odot}$ in a larger cloud.

3.6.6 CO Clumps With and Without Massive YSO Candidates

We investigate the difference between $^{13}CO(2-1)$ clumps associated with massive YSO candidates, and those not associated with any massive YSO candidates. We look for massive YSO candidates that are within the radius of the clump (where the radius is calculated from the exact clump area). We find a total of 6 candidates that are associated with $^{13}CO(2-1)$: [w1] J84.906560-69.756949, [w2] J84.907135-69.769883, [w3] J84.904533-69.760199, [w5] J84.924542-69.769972, [e1] J85.018920-69.743290, [e8] J85.004318-69.735780. We denote N159W by 'w' and N159E by 'e', and the number that follows is the YSO candidate rank, i.e. 'w1' is the most massive YSO candidate in N159W.

Figure 3.17 shows the difference of clump mass and clump mass surface density distributions between clumps that do not contain YSO candidates and clumps that are associated with YSO candidates in N159W. Figure 3.18 is the same as Figure 3.17, but for clumps in N159E. There is a noticeable difference between clumps that are not associated with massive star formation and those that are, and this difference exists

in both N159W and N159E. The clumps without any massive star formation have a quasi-normal distribution in mass (top left) and mass surface density (top right) in N159W (Figure 3.17) and N159E (Figure 3.18). The mass distribution (bottom left) and mass surface density distribution (bottom right) of clumps associated with YSO candidates in N159W (Figure 3.17) is flat with a noticeable peak ($10^{4.5}$ $M_\odot$ and $10^{3.3}$ $M_\odot$ pc^{-2}). Clumps with YSO candidates are more massive and more dense on average. The average mass of clumps without any massive star formation is $6400M_\odot$ and the average mass surface density of clumps without any massive star formation is $690M_\odot$ pc^{-2} in N159W. The average mass of clumps without any massive star formation is $160M_\odot$ and the average mass surface density of clumps without any massive star formation is $25M_\odot$ pc^{-2} in N159E. In N159W the average mass of clumps associated with YSOs is x2.6 higher and the average mass surface density of clumps associated with YSOs is x2.6 higher than clumps not associated with any YSOs. In N159E the average mass of clumps associated with YSOs is x38 higher and the average mass surface density of clumps associated with YSOs is x39 higher than clumps not associated with any YSOs. There are more $^{13}CO(2-1)$ clumps with smaller sizes and smaller masses in N159E than in N159W. The YSOs in this study tend to be associated with the larger and more massive clumps. Therefore this skews the average mass and average mass density of clumps with YSOs in N159E be higher than clumps without YSOs by almost a factor of 40. Massive YSOs ($M>8M_\odot$) have a preference to form within massive clumps.

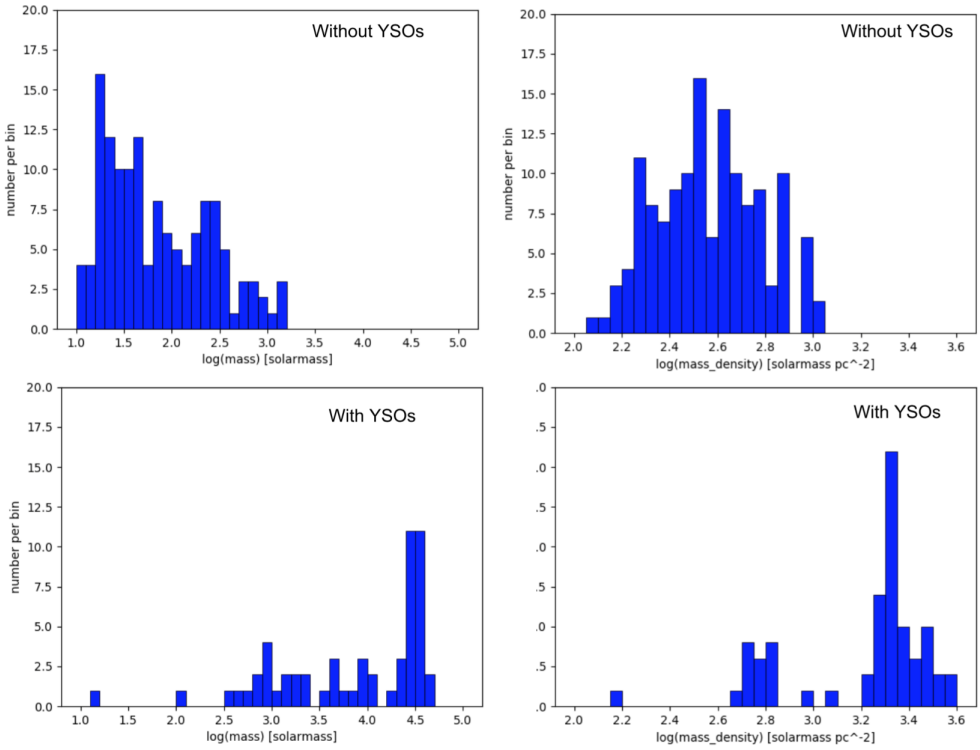

Figure 3.17: Left Column: Mass distribution of clumps in N159W without (top) and with (bottom) YSO candidates. Right Column: Mass surface density distribution of clumps in N159W without (top) and with (bottom) YSO candidates.

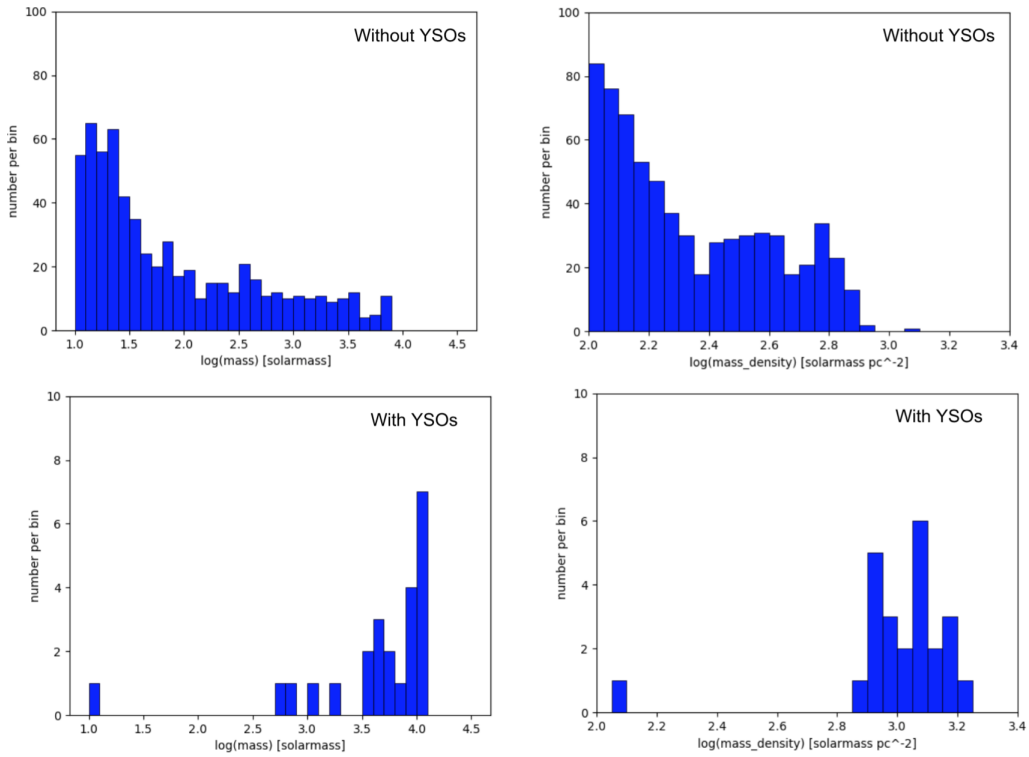

Figure 3.18: Left Column: Mass distribution of clumps in N159E without (top) and with (bottom) YSO candidates. Right Column: Mass surface density distribution of clumps in N159E without (top) and with (bottom) YSO candidates.

3.6.7 Threshold for Massive Star Formation

Star formation in N159W occurs in clumps with M>16$M_\odot$, linewidths greater than σ>0.15km s^{-1}, and mass surface densities greater than 147$M_\odot$ pc^{-2}. This can be seen in the bottom two panels in Figure 3.17. Star formation in N159E occurs in clumps with M>11$M_\odot$, linewidths greater than σ>0.16km s^{-1}, and mass surface densities greater than 125$M_\odot$ pc^{-2}. This can be seen in the bottom two panels in Figure 3.18. In the figure showing the mass distribution of clumps associated with YSOs in N159W (bottom left panel of Figure 3.17), the minimum mass of clump is 16$M_\odot$. However

there is gap of 1.5 dex before the percentage of clumps associated with massive YSOs is rapidly increasing around $10^{2.5}$ $M_\odot$. A similar trend can be seen in the distribution of mass density in N159W (distribution ramps up around $10^{2.7}$ $M_\odot$ pc^{-2}), distribution of mass in N159E (distribution ramps up around $10^{2.7}$ $M_\odot$), and distribution of mass density in N159E (distribution ramps up around $10^{2.9}$ $M_\odot$ pc^{-2}). Therefore we say that massive star formation in N159W occurs in clumps with masses greater than 316 $M_\odot$ and mass densities greater than 501 $M_\odot$ pc^{-2}. And in N159E massive star formation occurs in clumps with masses greater than 501 $M_\odot$ and in clumps with mass densities greater than 794 $M_\odot$ pc^{-2}.

Lada et al. (2010) study low-mass star formation in the Milky Way and find a gas surface density threshold of 116$M_\odot$ pc^{-2} is necessary for low mass star formation to occur in the Galaxy. The mass density thresholds in N159W and N159E are 501 $M_\odot$ pc^{-2} and 794 $M_\odot$ pc^{-2}, respectively. Table 3.22 lists the threshold properties of 30 Doradus (Nayak et al., 2016), N159W, and N159E. The mass density threshold in 30 Doradus is x5.8 than what is observed in the Milky Way. This could be because of extreme turbulence in 30 Doradus due to the proximity of the R136 supercluster. The mass density thresholds in N159W and N159E are x4.3 and x6.8 larger than what is observed in the Milky Way, and consistent with what is observed in 30 Doradus. There are two dozen massive YSO candidates in N159W and N159E in total, several of which have been associated with molecular outflows. These outflows from massive

stars could potentially shock the surrounding gas. There are several factors in the N159 region that could lead to there being higher turbulence than typical Milky Way star forming regions, therefore there is a higher mass density threshold in the N159 region. The higher observed threshold in N159 could be explained by the massive YSOs blowing away their surrounding gas and dust. There are several YSO candidates in this chapter that are not associated with ^{12}CO molecular gas. Perhaps some of these massive YSOs are more evolved and therefore have blown out their surrounding gas. Also stellar winds from some of the massive YSOs could have blown away the gas and dust around a neighboring YSO in the region. An alternative reason we do not find all YSOs associated with ^{12}CO molecular gas could be because we are not observing all the molecular gas at such low surface densities. We are only partially sensitive to surface densities comparable to star formation regions in the Milky Way. Further ALMA observations would be necessary to prove or disprove this idea.

Table 3.23: Clump Properties

Properties	30 Doradus	N159W	N159E
Number of YSOs	10	15	9
Average Mass of Clumps with YSOs [$M_\odot$]	5.7×10^3	1.8×10^4	6.6×10^3
Average Mass of Clumps without YSOs [$M_\odot$]	1.9×10^3	6.9×10^3	1.7×10^2
Average Mass Density of Clumps with YSOs [$M_\odot$ pc^{-2}]	9.6×10^2	1.9×10^3	1.1×10^3
Average Mass Density of Clumps without YSOs [$M_\odot$ pc^{-2}]	9.6×10^2	7.4×10^2	2.8×10^1
Threshold for Star Formation [$M_\odot$ pc^{-2}]	6.7×10^2	5.0×10^2	7.9×10^2

We lists the ALMA ^{13}CO clump properties in 30 Doradus, N159W, and N159E.

3.6.8 Testing Theories of Massive Star Formation

Fukui et al. (2015) show the filamentary structure of the ^{13}CO gas in N159W. The South cloud in N159W (the cloud containing YSO candidates 'w5') is thought to be the collision of two filaments. A red shifted filament and blue shifted filament are colliding, and at the center of the collision is a massive protostar. The massive Stage 0/I YSO candidate at the center of the two colliding filaments has very strong winds and jets. We cannot directly study the winds and jets from this star, due to the distance of the LMC. However we can study the gas that gets entrained in the jets and winds and outflows from the central star. We show the red shifted and blue shifted component in ^{13}CO and CS in Figure 3.2. The central velocity of the colliding filaments in the South cloud of N159W is 237km/s. The red shifted filament is integrated over the velocity range of 237-240 km/s, and the blue shifted filament is integrated over the velocity range of 234-237 km/s. The total ^{12}CO mass of the two colliding filaments (not shown) is $1.3 \times 10^4 M_\odot$ and the total ^{13}CO mass is $4.2 \times 10^3 M_\odot$. The red shifted filaments in CS is about 1.5 pc long and the blue shifted filament in CS is about 1 pc long. The existence of CS and C^{18}O implies that there is high density gas (see Table 3.2 for critical densities).

The Papillon Nebula YSO is at the center of three colliding filaments (Saigo et al., 2017). The total ^{12}CO and ^{13}CO mass of the three filaments are $1.8 \times 10^4 M_\odot$ and $5.1 \times 10^3 M_\odot$, respectively. Two of the filaments are blue shifted and the third filament

is red shifted, as shows in Figure 6b in Saigo et al. (2017). Once again we notice that there is a lot less CS than ^{12}CO or ^{13}CO. But the small presence of CS near this protostar that is nearly 50$M_{\odot}$ is surrounded by high density gas. Each of the three filamentary structure seem very similar (not the exact same, due to there being a lot less CS in the Large Magellanic Cloud) in all three lines. Therefore it is very likely that the ^{12}CO, ^{13}CO, and CS gases are tracing the same physical properties and energetics. The filamentary structure in both the South cloud in N159W as well as the filaments surrounding the Papillon Nebula YSO are not bi-conical. This could be due to the orientation of the molecular cloud with respect to us. Moreover, the strong stellar winds and magnetic fields are affecting the dynamics of the gas, and therefore resulting in an outflow that is not bi-polar.

There are three star formation theories currently being debated: competitive accretion, monolithic collapse, and filamentary collision. It is most likely that YSO candidates 'w5' and 'e1' might be forming via filamentary collision. We detect the YSO candidates at the center of colliding filamentary structures. But what about the other candidates? The majority of the candidates do not have distinctive filaments. Perhaps one of the other two theories can explain the formation of the other massive YSO candidates in N159W and N159E. In both the monolithic collapse theory (Tan & McKee, 2002, 2003; Zinnecker & Yorke, 2007) and competitive accretion theory (Bonnell et al., 1997) you start out with a large cloud and within the cloud are em-

bedded dense cores. The difference is that the cores in the monolithic collapse theory are not interacting with each other, and the cores in the competitive accretion theory are interacting with each other and stealing material away from each other.

Krumholz et al. (2005) model star formation and show that the competitive accretion theory requires that virial parameters be less than 1. Their simulations show that a high gas density and a small relative velocity between the gas and the star is necessary in order for such virial parameters to exist. Also, Krumholz et al. (2005) have the additional constraint that competitive accretion requires $\alpha^2 M < 10 M_{\odot}$. The dashed line in the virial parameter versus clump mass plots in Figure 3.16 represents this limit, below which competitive accretion is the plausible star formation scenario. All but 3 clumps in 30 Doradus lie above the limit separating monolithic collapse and competitive accretion (top panel in Figure 3.16). The majority of the clumps in 30 Doradus are consistent with Krumholz et al. (2005), where they conclude that stars form by monolithic collapse. In N159W and N159E, there are clumps that lie above and below this analytical threshold. All clumps associated with massive YSO candidates lie above the dashed line, perhaps giving more proof to the conclusions made by Krumholz et al. (2005). However this does not rule out competitive accretion. We do not have a consensus of the low-mass YSO candidates in the region which could be associated with many of the clumps that are currently star-less. The simulations by Krumholz et al. (2005) only took into account two geometries (spherical and filamen-

tary). Also Krumholz et al. (2005) assumed the protostars follow the Bondi-Hoyle accretion formula. The physics behind massive star formation is much more complex. Therefore perhaps the dashed lined in Figure 3.16 could shift upwards or downwards for star formation conditions specific to the LMC due to the lower metallicity and very high star formation rate in a region like N159.

3.6.9 Evolutionary State of N159W and N159E

N159E is in a more evolved state than N159W. The evidence for this is seen in the most massive YSO the two different regions host. The most massive YSO in N159W is J84.906560-69.756949 which has a mass of $35.5M_{\odot}$. Fukui et al. (2015) refer to this YSO as YSO-N (the Northern YSO in the N159W region). Fukui et al. (2015) find that YSO-N is associated with a blue-shifted outflow. The age of the outflow is calculated to be 10^4 yrs based on SED fits (Robitaille et al., 2006). This is a Stage 0/I YSO candidate that is still accreting material, therefore has noticeable outflows associated with the protostar forming. The most massive YSO in N159E is J85.018920-69.743290, also known as the 'Papillon Nebula YSO' (Saigo et al., 2017). Meynadier et al. (2004) use evolutionary track models (Lejeune & Schaerer, 2001) to estimate the mass of the Papillon Nebula YSO to be $50M_{\odot}$. Saigo et al. (2017) find that there is a CO-hole surrounding the Papillon Nebula YSO and that the Papillon Nebula YSO is surrounded by a lower density gas in comparison to YSO-N in N159W. The Papillon Nebula YSO seems to be a later YSO than YSO-N in N159W: there

is no clear sign of a single or bi-conical outflow associated with the Papillon Nebula YSO and the YSO seems to have cleared out much of the surrounding gas. These differences suggests that N159E is a more evolved star forming region than N159W.

The second massive candidate in N159E ('e2') has a mass of $13.5M_{\odot}$. There are no other massive YSOs in N159E with masses between 20-$50M_{\odot}$ like there are in N159W. Perhaps the Papillon Nebula YSO accreted the mass necessary to get so big, stealing gas and material from other stars and preventing the other stars to be as massive. Feedback mechanisms such as stellar winds and UV radiation from the Papillon Nebula YSO could be blowing gas and material out of N159E, and therefore there are no other massive stars higher than $20M_{\odot}$. Or the massive HII region located next to N159E, as shown in Figure 2 of Saigo et al. (2017), could be expanding and removing gas necessary to form another massive star greater than $20M_{\odot}$ in the vicinity.

Other evidence that highlights the differences in these two molecular cloud complexes is the $^{13}CO/^{12}CO$ ratio that can be seen in Figure 3.19. The average $^{13}CO/^{12}CO$ ratio in N159W is 0.18, and the average $^{13}CO/^{12}CO$ ratio in N159E is 0.11. The $^{13}CO/^{12}CO$ can be affected by dust UV extinction, gas chemistry, and local star formation. The stellar winds and UV radiation from the local massive YSO candidates in N159W and N159E must have an impact on the CO gas chemistry. A lower $^{13}CO/^{12}CO$ ratio in N159E, in comparison to N159W, could be because the YSO candidates in

N159E have had enough time to preferentially photodissociate ^{13}CO compared to ^{12}CO. N159W has many more YSO candidates (15 YSO candidates) than N159E (9 YSO candidates). The most massive YSO in N159E, which has a depletion of CO seen with a CO-hole around the protostar, is more evolved than the most massive YSO in N159W, which is associated with CO outflow. Therefore it is plausible N159E is a more evolved molecular cloud complex than N159W.

3.7 Conclusion

We study the ^{12}CO$(2-1)$, ^{13}CO$(2-1)$, and CS$(2-1)$ molecular gas observations taken by ALMA. We use dendrograms to identify the clumps in N159W and N159E in a systematic method. We find six new massive YSO candidates in N159W and 4 new massive YSO candidates in N159E. We identify all the high mass stars forming within the ALMA footprint of N159W and N159E and relate the high mass star formation to the sub-parsec size clumps in the region. Star formation exclusively takes place in sub-parsec size clumps. Our studies lead us to several conclusions relating the high mass star formation to very embedded clumps.

1. The size-linewidth relation appears to be dependent on the local environment. The ^{12}CO size-linewidth relation shows the N159 clumps to be offset to lower linewidths by a factor of 0.6 from 30 Doradus clumps. N159 is an extreme star forming envi-

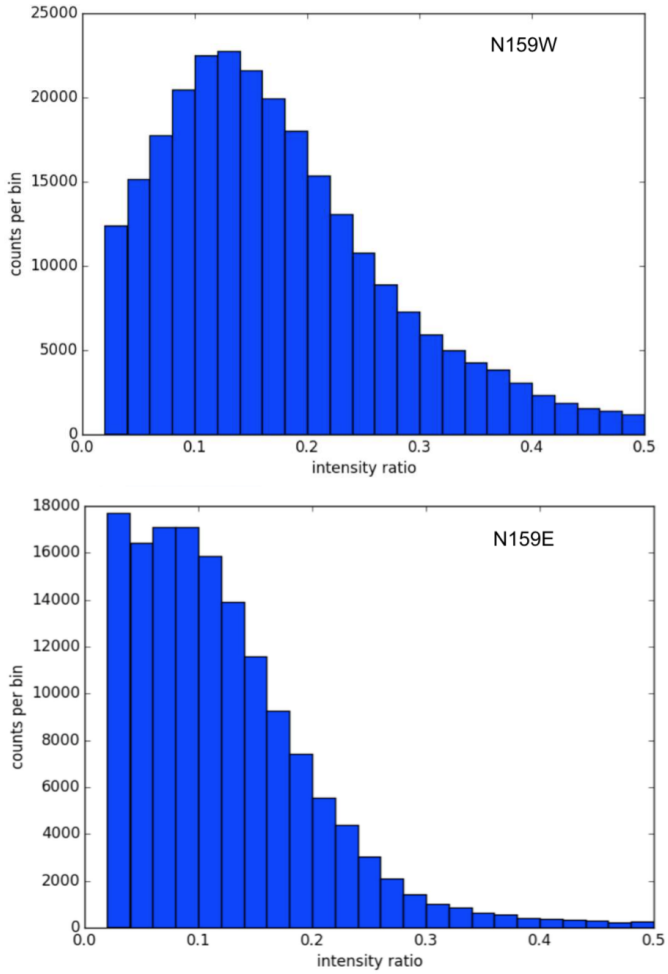

Figure 3.19: Top: The histogram of the ^{13}CO(2-1)/^{12}CO(2-1) flux in N159W. Bottom: The histogram of the ^{13}CO(2-1)/^{12}CO(2-1) flux in N159E.

ronment, however there is possibly more turbulence and chaos in 30 Doradus. The 30 Doradus ALMA footprint (Indebetouw et al., 2013; Nayak et al., 2016) is located 11pc away from the R136 supercluster.

2. The ^{13}CO size-linewidth relation shows N159 clumps to be offset to lower linewidths from 30 Doradus clumps by a factor of 0.6. Shetty et al. (2012) study the Perseus cloud complex and the CMZ (slopes and intercepts are listed in Table 3.20). They find that in quiescent star forming environments, like Perseus, the size-linewidth relation is also offset to lower linewidths in comparison to more extreme regions like CMZ.

3. The steeper size-linewidth relation in CS$(2-1)$ molecular gas could be due to shocks. It is possible that the ^{12}CO and ^{13}CO$(2-1)$ molecular gas in the same region as the CS$(2-1)$ gas are also tracing shocks, as they have a higher average linewidth than clumps that are not in the vicinity of CS$(2-1)$. In N159W the ^{12}CO clumps that are near CS$(2-1)$ clumps have linewidths larger by a factor of x3.6 than those that are not near CS$(2-1)$ clumps, and in N159E ^{12}CO clumps that are near CS$(2-1)$ clumps have linewidths larger by a factor of x2.8 than those that are not near CS$(2-1)$ clumps. In N159W the ^{13}CO clumps that are near CS$(2-1)$ clumps have linewidths larger by a factor of x4.8 than those that are not near CS$(2-1)$ clumps, and in N159E ^{13}CO clumps that are near CS$(2-1)$ clumps have linewidths larger by a factor of x3.6 than those that are not near CS$(2-1)$ clumps.

4. Assuming self-gravitating clumps and σ is only dependent on r means that the slope in the $\Sigma - \nu$ relation should be 0. However we find that in 30 Doradus, N159, and Milky Way clumps studied by Heyer et al. (2009), this does not hold. Therefore we conclude that Larson's first law where σ is only dependent on r might not be applicable to high mass star forming regions.

5. Virial analysis shows that all the clumps in N159 and the majority of clumps in 30 Doradus have virial parameters less than 1, meaning that they should all be gravitationally contracting and forming stars. However the majority of clumps are not associated with massive star formation. This could be because of a strong magnetic field present that is slowing down the gravitational force (Kauffmann et al., 2013).

6. The low-virial parameters (<1) in N159W and N159E could mean that competitive accretion plays a more important role in the LMC that in the Milky Way. Several of the clumps do not have any massive YSO candidates associated with them, however could potentially be associated with low-mass ($<8M_{\odot}$) stars. The clumps that are associated with massive YSO candidates lie above the predicted threshold for monolithic collapse (Krumholz et al., 2005).

7. All YSOs above $20M_{\odot}$ are associated with molecular gas. However the major-

ity of YSO candidates under 20$M_\odot$ are not associated with any molecular gas. The YSO candidates under 20$M_\odot$ could potentially be more evolved and therefore have had enough time to disperse their surrounding gas. Or it could be that our observations are not sensitive enough to detect molecular gas clumps that small.

8. We find that on average clumps associated with massive protostellar candidates have higher masses(>18000$M_\odot$ in N159W, >6600$M_\odot$ in N159E) and higher surface mass densities (>1900$M_\odot$ pc^{-2} in N159W, >1100$M_\odot$ pc^{-2} in N159E) than clumps not associated with any star formation. This is true for 30 Doradus (Nayak et al., 2016), N159W, and N159E.

9. The threshold for massive star formation in N159W is 501$M_\odot$ pc^{-2} and in N159E is 794$M_\odot$ pc^{-2}. This is several times higher than the threshold for massive star formation in the Milky Way which is 116 $M_\odot$ pc^{-2}. But this is more consistent with the threshold for massive star formation in the 30 Doradus region of the LMC which is 670$M_\odot$ pc^{-2}.

10. N159E is in a more evolved state than N159W. The $^{13}CO/^{12}CO$ ratio is on average lower in N159E than N159W. This could be because N159E has had more time to photodissociate the ^{13}CO gas.

3.8 Acknowledgements

This chapter makes use of the following ALMA data:

ADS/JAO.ALMA#2012.1.00554.S. ALMA is a partnership of ESO (representing its member states), NSF (USA) and NINS (Japan), together with NRC (Canada), NSC and ASIAA (Taiwan), and KASI (Republic of Korea), in cooperation with the Republic of Chile. The Joint ALMA Observatory is operated by ESO, AUI/NRAO and NAOJ. The National Radio Astronomy Observatory is a facility of the National Science Foundation operated under cooperative agreement by Associated Universities, Inc. This chapter also makes use of astrodendro, a Python package to compute dendrograms of astronomical data (http://www. dendrograms.org).

M. Meixner and O. Nayak were supported by NSF grant 1312902. This chapter was also supported by JSPS KAKENHI grant numbers 15H05694 and 26247026. We would like to thank Dr. Olivia Jones and Dr. Bram Ochsendorf for helpful discussions about massive star formation.

Chapter 4

ALMA Reveals Kinematics of Potential Super Star Cluster H72.97-69.39 in N79

Abstract

Conditions in super star clusters (SSCs) lead to the formation of dozens of massive stars. However, SSCs are rare in the local Universe. H72.97-69.39, located in the N79 region of the LMC, is a potential embedded SSC. In this chapter we report the ALMA observations of the potential SSC. ALMA reveals colliding filaments, outflows, HII region, and CII region associated with this cluster. The timescale of the outflow is 19,500 yrs which is consistent with this being a young cluster. We also present the

first extragalactic detection of a rotating toroid around this SSC. The radius of the toroid spans 20,000-40,000 AU and the mass infall rate is $\dot{M}_{\rm inf} = 0.06 - 0.12 M_{\odot}$ yr^{-1}. The molecular gas around this potential early-stage SSC is complex in nature on small scales (as seen with ALMA) and large scales (as seen with *Herschel*).

4.1 Introduction

Massive star clusters or super star clusters (SSCs) are rare in the local universe, often found in interacting galaxies (Zhang & Fall, 1999). Weidner et al. (2010) simulate the formation of SSCs and find the presence of shear determines if a GMC is viable for SSCs to form. The shear forces may impede the accumulation of GMCs and the subsequent formation of SSCs. Indeed, one of the most elusive questions in astronomy has been: how do SSCs form?

We have a rare opportunity to study the earliest stage of SSC formation in N79. The N79 region is located in the southwestern corner of the LMC. Figure 4.1 shows the location and density of massive YSOs ($M>8M_{\odot}$) identified across the face of the LMC with the use of sensitive infrared surveys (SAGE & HERITAGE; Meixner et al. (2006) Meixner et al. (2013), Seale et al. (2014)). Strikingly, there are two obvious clusterings: 30 Doradus, and the newly discovered star forming complex surrounding N79 (Ochsendorf et al., 2017b). At the heart of the large-scale N79 complex

lies the potential embedded SSC H72.97-69.39 which has a luminosity of $2.2 \times 10^6 L_\odot$ (Ochsendorf et al., 2017b). As seen in the center panel of Figure 4.1, both N79 and 30 Doradus lie at the 'tips' of the LMC tidal arms. Ochsendorf et al. (2017b) calculate the star formation rate averaged over the last few million years using Hα emission as well as the star formation rate averaged over the last 0.5 million years by counting YSOs in both 30 Doradus and N79. They find that the star formation rate in 30 Doradus is ramping down, while the star formation rate in N79 is ramping up. The luminosity of SSC H72.97-69.39 has the potential to increase by an order of magnitude to be similar to the luminosity of R136 SSC in 30 Doradus ($\sim 1.0 \times 10^7 L_\odot$).

Prior to the study done by Ochsendorf et al. (2017b), SSC H72.97-69.39 was thought to be the most luminous YSO in the entire LMC by fitting SED models to far-infrared HERITAGE observations by Seale et al. (2014). The N79 region is not very notable in optical star formation tracers such as Hα. Indeed, upon first inspection of the Hα map of the LMC, the N79 region pales in comparison to many optically bright star forming regions (most notably 30 Doradus). However, N79 is extremely active: it is the second most densely populated region of YSOs in the LMC after 30 Doradus. The many parallels drawn with R136 shows that this source has the potential to become a super star cluster. The high resolution ALMA observations in this chapter of the potential proto-SSC covers just a $\approx$ 0.5' x 0.5' region (Figures 4.2 and 4.3). In this chapter we characterize the gas kinematics of the immediate vicinity of H72.97-69.39 and lay the foundation for future follow-up observations of

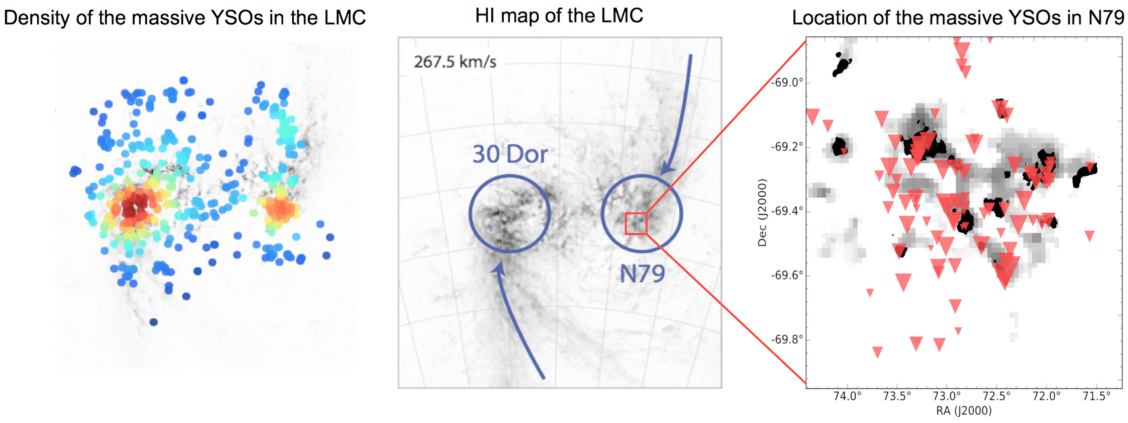

Figure 4.1: Left - An HI map of the LMC (Kim et al., 2001) overlayed with the massive YSO probability density map (the color code shows the probability density function based on the location of the massive YSOs, and thus reveals the intrinsic clustering of these sources). Two obvious massive YSO complexes are found: 30 Doradus, and our newly discovered region of N79. Middle - Same HI map (figure adapted from Kim et al. (2001)). The arrows indicate the location of the spiral arms of the LMC stretched by the fast rotation of the LMC and its interaction with the SMC and Milky Way (D'Onghia & Fox, 2016). Strikingly, both 30 Doradus and N79 are very extended, harbor a massive central source/cluster (for 30 Doradus this is R136, for N79 it is the most luminous massive YSO), and are located at the 'tip' of opposite spiral arms of the LMC. Right - Location of the massive YSOs in N79. The grey color represents dust-based molecular gas (Jameson et al., 2016), the black color is the MAGMA CO (Wong et al., 2011), and the red symbols represent the massive YSOs. The sizes of the symbols represent the mass/luminosity of the YSOs.

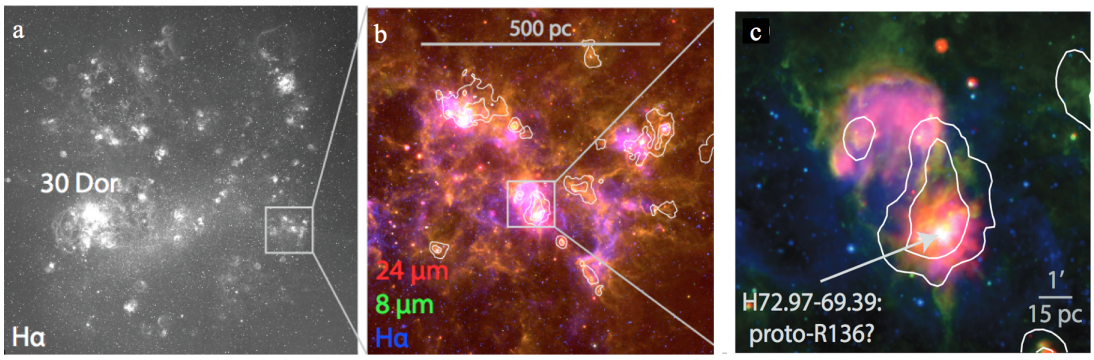

Figure 4.2: Left - Hα image of the LMC. Shown is 30 Doradus and N79 (grey box). Middle - Blow-up of the N79 region in a three color image showing Hα in blue, Spitzer/IRAC 8μm in green, and Spitzer/MIPS 24μm in red (Ochsendorf et al., 2017b). Right - The immediate environment of the most luminous massive YSO in the LMC (same colors as middle panel). In white contours we plot CO clouds from the MAGMA survey (Wong et al., 2011).

this source. Chapter 4.2 discusses our ALMA observations. In Chapter 4.3 we talk about the results of our ALMA observations. In Chapter 4.4 we analyze the molecular gas clumps and in Chapter 4.5 we determine if this source is indeed a proto-SSC. Chapter 4.6 lists our conclusions.

4.2 Description of Data ALMA Observations of the Most Luminous Young Stellar Object

Using ALMA Cycle 2 Band 6 (Project Code: 2013.1.01155.S, PI: M. Meixner) observations, we observed H792.97-69.39 in the following lines: ^{12}CO$(2-1)$, ^{13}CO$(2-1)$,

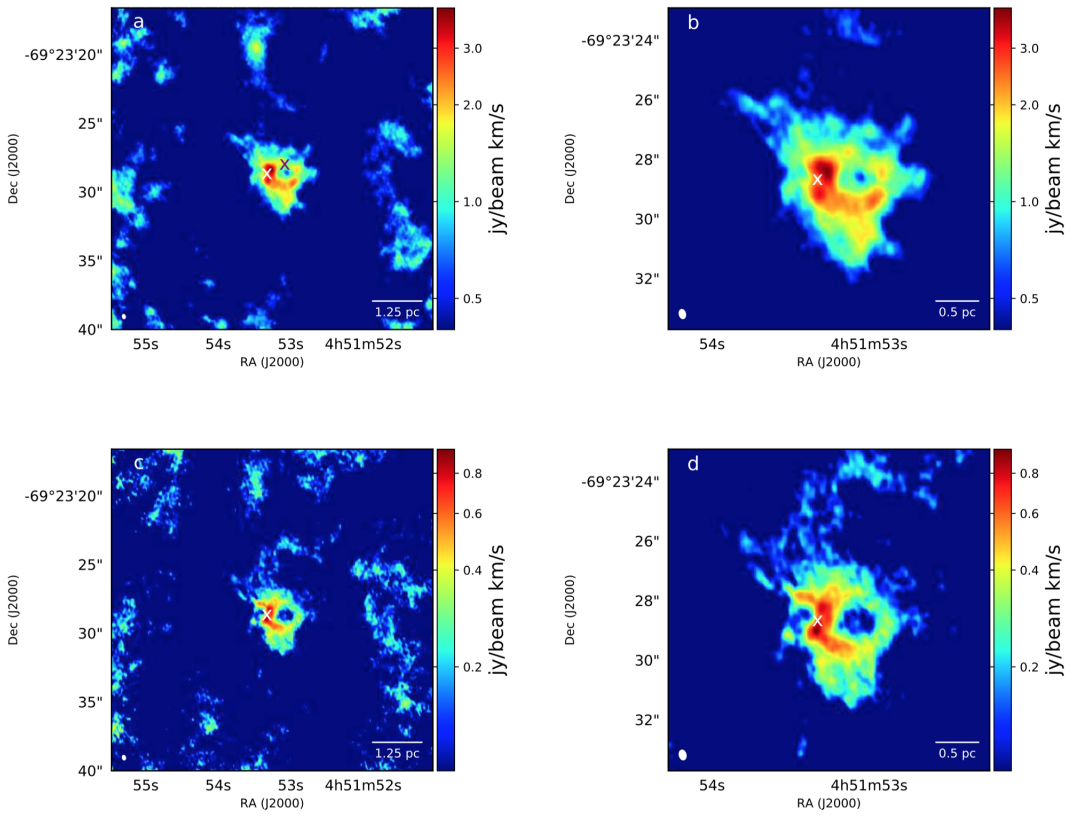

Figure 4.3: **a)** ^{12}CO$(2-1)$ image of H72.97-69.39 and its immediate surrounding. Location of the most luminous YSO marked by white 'x', as determined by the peak C^{18}O emission. *Herschel* coordinates of the most luminous YSO marked by purple 'x'. **b)** Zoom-in view of ^{12}CO$(2-1)$ molecular gas. **c)** ^{13}CO$(2-1)$ image of H72.97-69.39 and its immediate surrounding. **d)** Zoom-in view of ^{13}CO$(2-1)$ molecular gas.

$C^{18}O(2-1)$, $HCN(3-2)$, $HCO+(3-2)$, SO_2, H30α, and C30α. We are only interested in H72.97-69.69 and its immediate surroundings, therefore only a single pointing was used in all observations. The Band 6 (211-275 GHz) observations cover a map size of 26" x 26" (6.3 pc x 6.3 pc at a distance of 50 kpc). We use two different tunings to observe all the molecular lines. The first tuning included four spectral windows with three molecular lines and one continuum observation in a single correlator setup: $^{12}CO(2-1)$, $^{13}CO(2-1)$, and $C^{18}O(2-1)$ were observed in the first tuning. The continuum observation included H30α, and C30α lines. The second tuning included three spectral windows with two molecular lines and one continuum observations in a single correlator setup: $HCN(3-2)$ and $HCO+(3-2)$ were observed in the second tuning, along with SO_2 which was observed in the continuum band. Table 4.1 summarizes all the observed lines and their critical densities. C30α and SO_2, both of which were measured in the continuum bands, were unexpected findings. Table 4.2 lists observation details.

Table 4.1: Critical Densities of Molecular Gas Observed with ALMA

Line	Critical Density [cm^{-3}]
^{12} CO (2-1)	2.7 x 10^3
^{13} CO (2-1)	2.0 x 10^4
$C^{18}O$ (2-1)	3.0 x 10^3
HCN (3-2)	4.1 x 10^6
HCO+ (3-2)	7.8 x 10^5
SO_2	2.0 x 10^6

The ALMA observed line (column 1) and the critical density of the line (column 2).

Table 4.2: ALMA Observation Information

Line	12m Configuration	Observation Date	Number of Pointings	Number of Antennae
^{12}CO (2-1)	Compact	January 28, 2015	1	34
^{12}CO (2-1)	Extended	January 28, 2015	1	38
^{13}CO (2-1)	Compact	August 18, 2015	1	34
^{13}CO (2-1)	Extended	January 28, 2015	1	38
C^{18}O (2-1)	Compact	August 18, 2015	1	34
C^{18}O (2-1)	Extended	January 28, 2015	1	38
HCN (3-2)	Compact	September 29, 2015	1	34
HCN (3-2)	Extended	January 29, 2015	1	38
HCO+ (3-2)	Compact	September 29, 2015	1	41
HCO+ (3-2)	Extended	January 29, 2015	1	33
SO_2	Compact	January 29, 2015	1	41
SO_2	Extended	January 29, 2015	1	33
H30α	Compact	January 28, 2015	1	34
H30α	Extended	January 28, 2015	1	38
C30α	Compact	January 28, 2015	1	34
C30α	Extended	January 28, 2015	1	38

Column 1: The molecular line observed. Column 2: The ALMA 12m array configuration. Column 3: The observation date. Column 4: Number of pointings. Column 5: Number of antennas.

Table 4.3: ALMA Data Properties of Combined 12m and Compact and 12m Extended Array

Line	Frequency [GHz]	Bandwidth	Channel Width	Beam Size	Spectral Resolution [km/s]	Maximum Flux Scale [arcsec/pc]	Resolution [arcsec/pc]
^{12}CO (2-1)	230.550	234.375 MHz	122.070 kHz	0.309" x 0.207"	0.184	17.8" / 4.27 pc	0.170" / 0.041 pc
^{13}CO (2-1)	220.389	117.188 MHz	122.070 kHz	0.331" x 0.224"	0.192	18.6" / 4.46 pc	0.178" / 0.043 pc
C^{18}O (2-1)	219.560	117.188 MHz	122.070 kHz	0.328" x 0.219"	0.192	18.7" / 4.47 pc	0.178" / 0.043 pc
HCN (3-2)	265.886	58.594 MHz	15.258 kHz	0.222" x 0.141"	0.036	15.4" / 3.70 pc	0.087" / 0.021 pc
HCO+ (3-2)	267.557	58.594 MHz	15.258 kHz	0.229" x 0.147"	0.036	15.3" / 3.67 pc	0.087" / 0.021 pc
SO_2	251.428	2.000 GHz	15.625 MHz	0.239" x 0.160"	20.0	16.3" / 3.91 pc	0.092" / 0.022 pc
H30α	231.995	2.000 GHz	15.625 MHz	0.307"x 0.203"	20.0	17.7" / 4.24 pc	0.170" / 0.041 pc
C30α	232.017	2.000 GHz	15.625 MHz	0.303" x 0.201"	20.0	17.7" / 4.24 pc	0.170" / 0.041 pc

Column 1: The molecular line observed. Column 2: Frequency of the line. Column 3: Spectral Window bandwidth. Column 4: Spectral window channel width. Column 5: Beam size of the observation. Column 6: Spectral resolution of the observation. Column 7: The maximum recoverable flux scale calculated using $\frac{\lambda}{B_{min}}$, where B_{min} is the minimum baseline of 15.1 m. Column 8: The resolution of our images calculated using $\frac{\lambda}{B_{max}}$. The maximum baseline for ^{12}CO, ^{13}CO, C^{18}O, H30α, and C30α is 1575 m. The maximum baseline for HCN, HCO+, and SO_2 is 2670 m.

The Band 6 observations of YSO H72.97-69.39 and its immediate surrounding with 12m array and the 7m Atacama Compact Array (ACA) were processed and reduced using the Common Astronomy Software Application (CASA) package (http://casa.nrao.edu) version 4.7.2. The phase calibration was done with observations of 1 quasars (J0635-7516), the band-pass calibration was done with observations of 2 quasars (J0538-4405, J0635-7516), and flux calibration was done with 1 solar system objects and 1 quasar (Ganymede, J0519-454). Butler-JPL-Horizons 2012 model was used for the flux calibration of the solar system objects [1]. We combine the 12m extended and compact array observations using the concat command in CASA and convert the high spectral resolution ALMA data from a position-position-frequency data cube to a position-position-velocity (PPV) cube. The resulting extended and compact combined synthesized beam size is listed in Table 4.3. The channel width of the map where the rms noises were measured is 0.5 km s^{-1}.

The minimum baseline for $^{12}CO(2-1)$ from the 12m compact array was 15.1 m, giving a maximum recoverable flux scale of 17.8" (4.27 pc at a distance of 50 kpc). The maximum baseline of the 12m extended array was 1575 m for $^{12}CO(2-1)$, giving a resolution of 0.170" (0.041 pc at a distance of 50 kpc). Figure 4.3 shows the entire ALMA view of H72.97-69.39 in $^{12}CO(2-1)$ and $^{13}CO(2-1)$, as well as a zoomed-in view of both molecular gas lines. Velocity integrated ALMA images of the concate-

[1] https://science.nrao.edu/facilities/alma/aboutALMA/Technology/ALMAMemoSeries/alma594/abs594

nated 12m compact and extended array of all the lines (^{12}CO$(2-1)$, ^{13}CO$(2-1)$, C^{18}O$(2-1)$, HCN$(3-2)$, HCO$+(3-2)$, SO_2, H30α, and C30α) are given in Figure 4.4. The different molecular lines probe different critical densities and show varying degrees of abundances in the region.

4.3 ALMA Results

Figure 4.4 shows the ^{12}CO$(2-1)$, ^{13}CO$(2-1)$, C^{18}O$(2-1)$, HCN$(3-2)$, HCO$+(3-2)$, SO_2, H30α, and C30α integrated images. The location of YSO H72.97-69.39 is marked by a white 'x' in the panels. The ^{12}CO$(2-1)$, ^{13}CO$(2-1)$, and HCO$+(3-2)$ emission look similar. These three molecular lines are the most abundant out of the eight lines we observe. However, ^{12}CO$(2-1)$ traces diffuse emission and therefore is observed to be the strongest line. HCO$+(3-2)$ traces gas that is 7.8×10^5 cm^{-3}, about 40 times more dense than gas traced by ^{13}CO$(2-1)$. We find HCO$+(3-2)$ to be less abundant than ^{12}CO$(2-1)$ and ^{13}CO$(2-1)$, as well as less contiguous. Figure 4.4e shows the integrated HCO$+(3-2)$ emission to be more porous than either ^{12}CO$(2-1)$ (Figure 4.4a) or ^{13}CO$(2-1)$ (Figure 4.4b). The structure of the gas seen in ^{12}CO$(2-1)$, ^{13}CO$(2-1)$, and HCO$+(3-2)$ are composed of two filaments (Section 4.4.2).

C^{18}O$(2-1)$ is barely visible, however a small clump of C^{18}O$(2-1)$ is spatially coin-

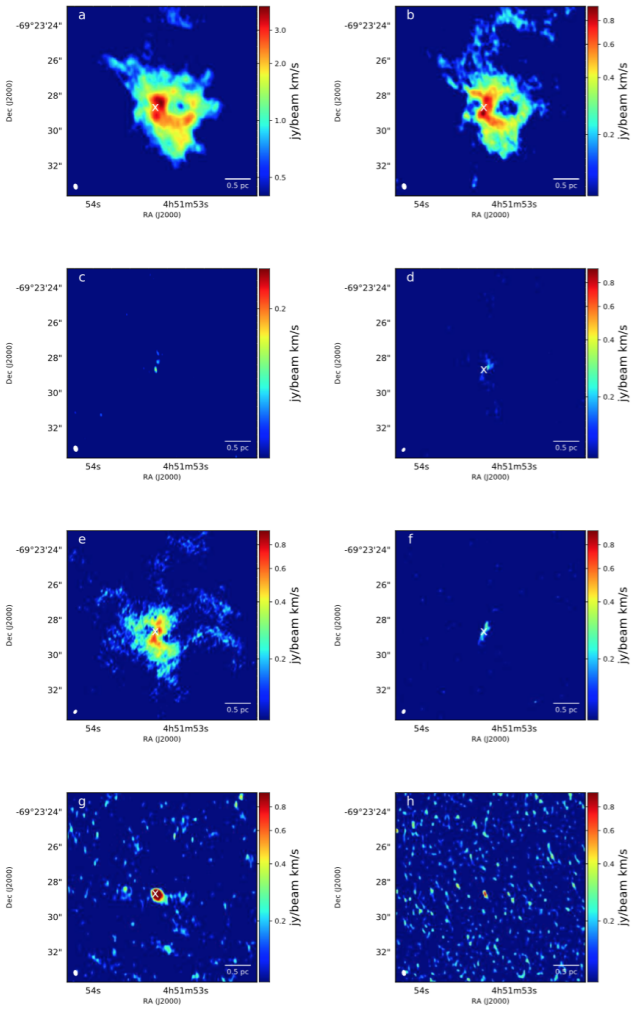

Figure 4.4: **a)** ^{12}CO$(2-1)$ molecular gas. The white 'x' marks the location of SSC H72.97-69.39. **b)** ^{13}CO$(2-1)$ molecular gas. **c)** C^{18}O$(2-1)$ molecular gas. **d)** HCN$(3-2)$ molecular gas. **e)** HCO$+(3-2)$ molecular gas. **f)** SO_2 molecular gas. **g)** H30α recombination line. **h)** C30α recombination line. We do not mark a 'x' on the C^{18}O$(2-1)$ panel or the C30α panel (indicating the location of the SSC) because we do not want to cover up the emission.

cident with the massive YSO or potential cluster. Often times $C^{18}O(2-1)$ cores are found to be more compact and located at the knots of filaments where star formation is taking place (Fukui et al., 2015; Gong et al., 2017; Onishi et al., 1999). We assume the coordinates of this luminous source to be centered on the $C^{18}O(2-1)$ core which gives RA: 72.972201 and Dec: -69.391301. High resolution ALMA observations provide much better astrometry in comparison to previous *Spitzer* or *Herschel* observations. H72.96-69.39 was first detected by Seale et al. (2014) and had coordinates RA: 72.971176 and Dec: -69.391112. The *Herschel* coordinates are shown in purple in Figure 4.3a. Coordinates derived from ALMA are offset by 1.8" (0.43 pc) from *Herschel* coordinates.

We report the third ever detection of a SO_2, a tracer of hot molecular core, outside the Galaxy. The first detection of extragalactic SO_2 was made by Shimonishi et al. (2016). The size of the emission measured by Shimonishi et al. (2016) was similar to the beam size, and therefore considered to be a point source. The second detection of SO_2 was in the N113 region of the LMC, a giant molecular gas cloud whose spectral energy distribution is dominated by 3 massive (30-40$M_\odot$) YSOs (Sewiło et al., 2018). Our observations of SO_2 in the vicinity of H72.97-69.39 show this tracer of hot gas to be extended: 0.076 pc long and 0.027 pc wide. SO_2 and $HCN(3-2)$ are tracing very high density gas (10^6 cm^{-3}). This very high density gas is centered around the YSO or protocluster. SO_2 emission is tracing outflows from the central source (Section

4.4.3).

We resolve H30α which is 0.093 pc x 0.065 pc in size. The H30α provides information on the HII region surrounding H72.97-69.39. Beyond the HII region is the photodissociatied region (PDR). Less energetic photons ($h\nu$<13.6 eV) can dissociate molecules such as carbon. We detect C30α in our observations (Figure 4.4h), which likely arises from the PDR region.

4.4 Analysis

4.4.1 Filaments on Large and Small Scales

N79 region of the LMC consists of three giant molecular clouds: East, West, and South (Ochsendorf et al., 2017b). Figure 4.5a shows the *Herschel* 350 μm map of N79 South which is host to H72.97-69.39. There are five filamentary structures emanating from the center of N79 South (white arrows). Filaments are ubiquitous and commonly associated with star formation (André et al., 2010; Fukui et al., 2015; Molinari et al., 2010). Higher column densities are often found at the intersection of merging filaments, therefore providing more favorable conditions for cluster formation. Peretto et al. (2012) find the B59 core of the Pipe Nebula to contain several filaments, all merging at the location of the only star forming cluster in the entire Pipe Nebula. They theorize that cluster formation was only possible because of the

condensation of filaments which then merged to form a region with enhanced local density. The filaments in Figure 4.5a are situated within a larger molecular cloud, consistent with the formation scenario where filaments form from condensation of diffuse clouds. The filaments seen in 350 μm in N79 South are tens of parsecs in length.

ALMA $^{13}CO(2-1)$ reveals filaments on much smaller scales. The blue-shifted and red-shifted filaments are seen in Figures 4.5b and 4.5c, respectively. The blue-shifted filament is 0.5 pc in length and the red-shifted filament is 1.5 pc in length. These filaments can be seen separately when integrating over 215.0 - 232.5 km/s (blue) and 233.0 - 245.0 km/s (red). ALMA $^{12}CO(2-1)$ observations show similar filamentary structure as the $^{13}CO(2-1)$ observations. We list the properties of the filaments observed with the different molecular gas lines in Tables 4.4 - 4.8. The large scale filament seen in the *Herschel* 350 μm map could be connected to the smaller filaments seen in ALMA, which in turn fragments into a high density core where cluster formation takes place. We do not see the blue-shifted and red-shifted filaments connect to a larger network of filaments. This is likely because we do not have ALMA ACA data or single dish data, therefore we are unable to see the diffuse large-scale gas.

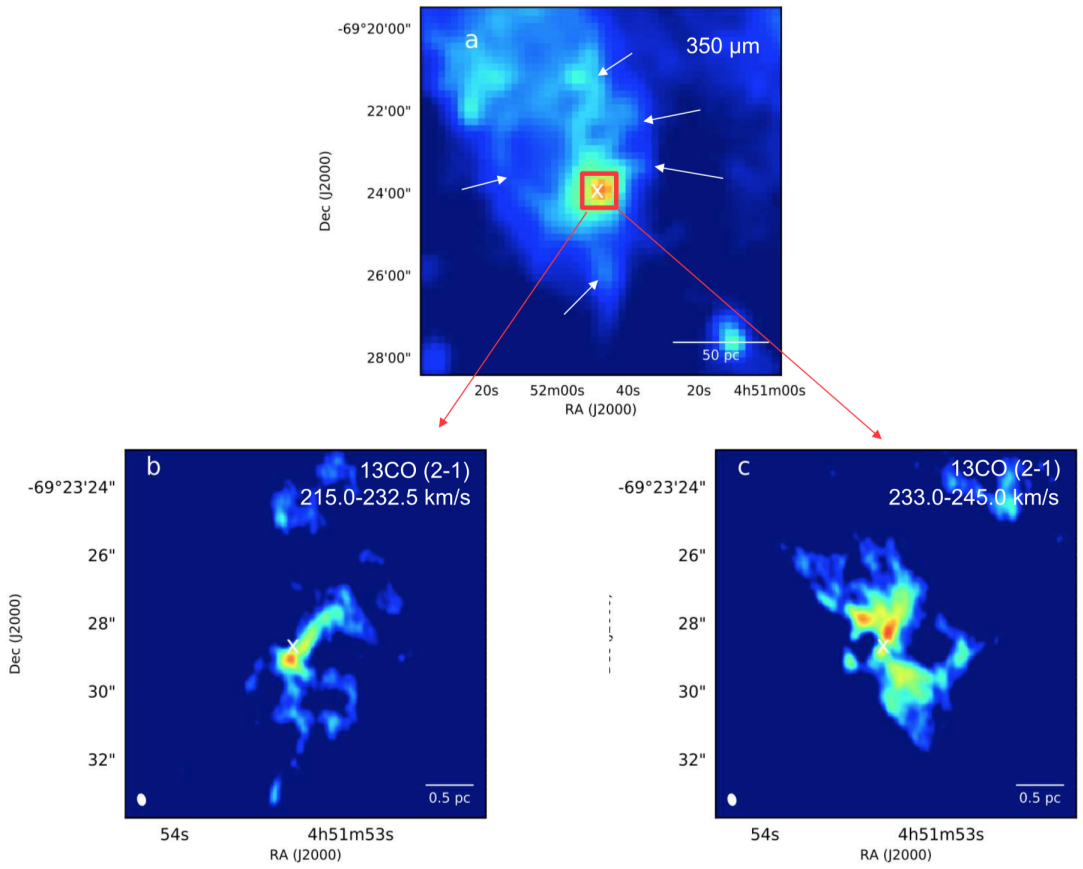

Figure 4.5: **a)** *Herschel* 350 μm image of N79 South. White arrows indicate filaments connected to the central gas cloud where H72.97-69.39 is located. **b)** Blue-shifted filament of ^{13}CO$(2-1)$ molecular gas. **c)** Red-shifted filament of ^{13}CO$(2-1)$ molecular gas.

Table 4.4: ALMA Observation: ^{12}CO (2-1)

Clump ID	RA	Dec	Filament Length [pc]	Filament Width [pc]	Linewidth [km s^{-1}]	Virial Parameter	F_{12CO} [K km s^{-1}]	Mass [$M_\odot$]
0	72.972025	-69.391438	1.184	0.611	2.495	1.563	91.39 ± 73.53	3937 ± 3168
1	72.972087	-69.391574	0.995	0.416	1.768	0.501	150.9 ± 52.41	4663± 1619

Properties of the blue-shifted (0) and red-shifted (1) filaments for ^{12}CO (2-1).

Table 4.5: ALMA Observation: ^{13}CO (2-1)

Clump ID	RA	Dec	Filament Length [pc]	Filament Width [pc]	Linewidth [km s^{-1}]	Virial Parameter	N_{13CO} [cm^{-3}]	$Mass_{H2}$ [$M_\odot$]
0	72.971843	-69.391287	0.412	0.108	1.157	1.307	4.889E16 ± 1.767E16	249.5 ± 90.18
1	72.972243	-69.391205	0.722	0.330	1.574	0.9542	6.623E16 ± 4.418E16	1465 ± 977.3

Properties of the blue-shifted (0) and red-shifted (1) filaments for ^{13}CO (2-1).

Table 4.6: ALMA Observation: $C^{18}O$ (2-1)

Clump ID	RA	Dec	Filament Length [pc]	Filament Width [pc]	Linewidth [km s^{-1}]	F_{C18O} [K km s^{-1}]
0	72.972195	-69.391394	0.245	0.132	1.638	3.401 ± 2.183
1	72.871894	-69.391408	0.476	0.317	1.481	3.516 ± 2.202

Properties of the blue-shifted (0) and red-shifted (1) filaments for $C^{18}O$ (2-1).

Table 4.7: ALMA Observation: HCN (3-2)

Clump ID	RA	Dec	Filament Length [pc]	Filament Width [pc]	Linewidth [km s^{-1}]	F_{HCN} [K km s^{-1}]
0	72.971936	-69.391332	0.413	0.163	1.729	7.833 ± 3.762
1	72.971997	-69.391183	0.151	0.102	2.032	13.87 ± 4.120

Properties of the blue-shifted (0) and red-shifted (1) filaments for HCN (3-2).

Table 4.8: ALMA Observation: HCO+ (3-2)

Clump ID	RA	Dec	Filament Length [pc]	Filament Width [pc]	Linewidth [km s^{-1}]	F_{HCO+} [K km s^{-1}]
0	72.972148	-69.391386	0.416	0.154	1.239	30.88 ± 13.48
1	72.972148	-69.391347	0.681	0.283	1.656	40.86 ± 25.05

Properties of the blue-shifted (0) and red-shifted (1) filaments for HCO+ (3-2).

4.4.2 Molecular Gas Outflows

We report the first extragalactic protocluster outflow from H72.97-69.39. Figure 4.6 (top panel) shows the $^{13}CO(2-1)$ molecular gas. We take a position-velocity (PV) slice across the outflow, as shown in the black dotted line. The resulting PV diagram is shown in Figure 4.6 (bottom panel). There is a red-shifted and blue-shifted components along the outflow axis. High density gas is also entrained in the outflow. PV slice across $HCO+(3-2)$ shows a similar red-shifted and blue-shifted bipolar

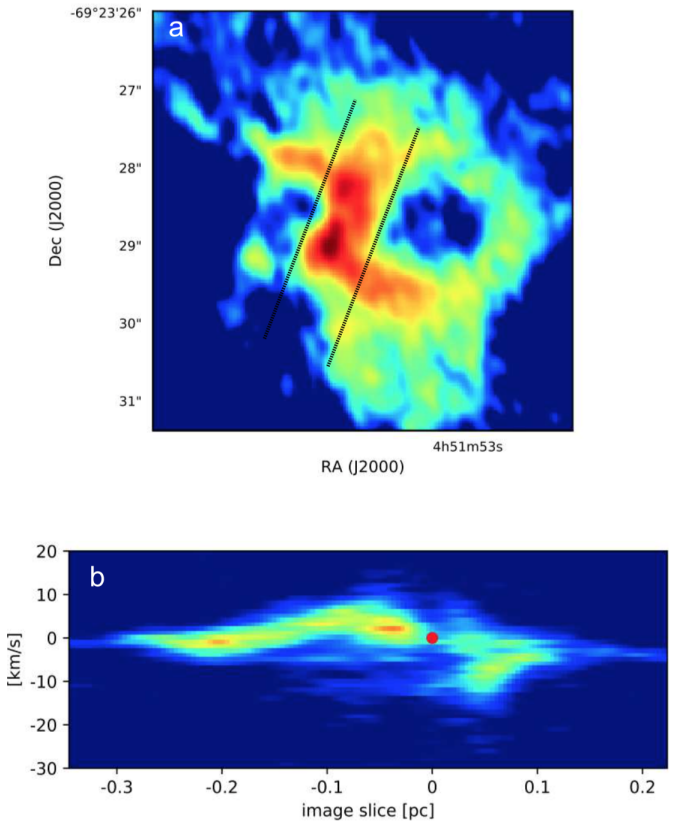

Figure 4.6: Top) The ^{13}CO$(2-1)$ velocity integrated intensity image. We take a position-velocity (PV) slice along the dashed line. Bottom) The resulting PV diagram of ^{13}CO$(2-1)$.

outflow. The outflowing gas is in the northeast to southwest direction. Figure 4.9 shows the blue-shifted (blue contour) and red-shifted (red-contour) gas in ^{12}CO$(2-1)$ molecular gas. The outflows have a velocity span of 10 km s^{-1}. The size of the red-shifted outflow is ≈ 0.25 pc and the size of the blue-shifted outflow is ≈ 0.14 pc. The average size of the outflows is 0.20 pc. Taking into account the velocity span, this gives a timescale of roughly 19,500 yrs.

Sulfur oxide molecules increase their abundance three to four orders of magnitude

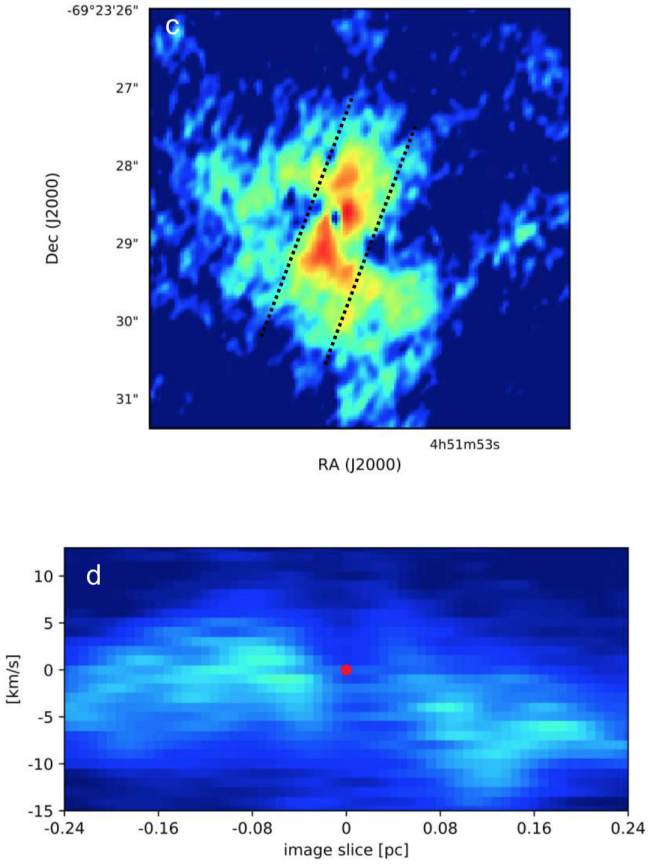

Figure 4.7: Top) HCO + (3 − 2) velocity integrated intensity image. We take a position-velocity (PV) slice along the dashed line. Bottom) The resulting PV diagram of HCO + (3 − 2).

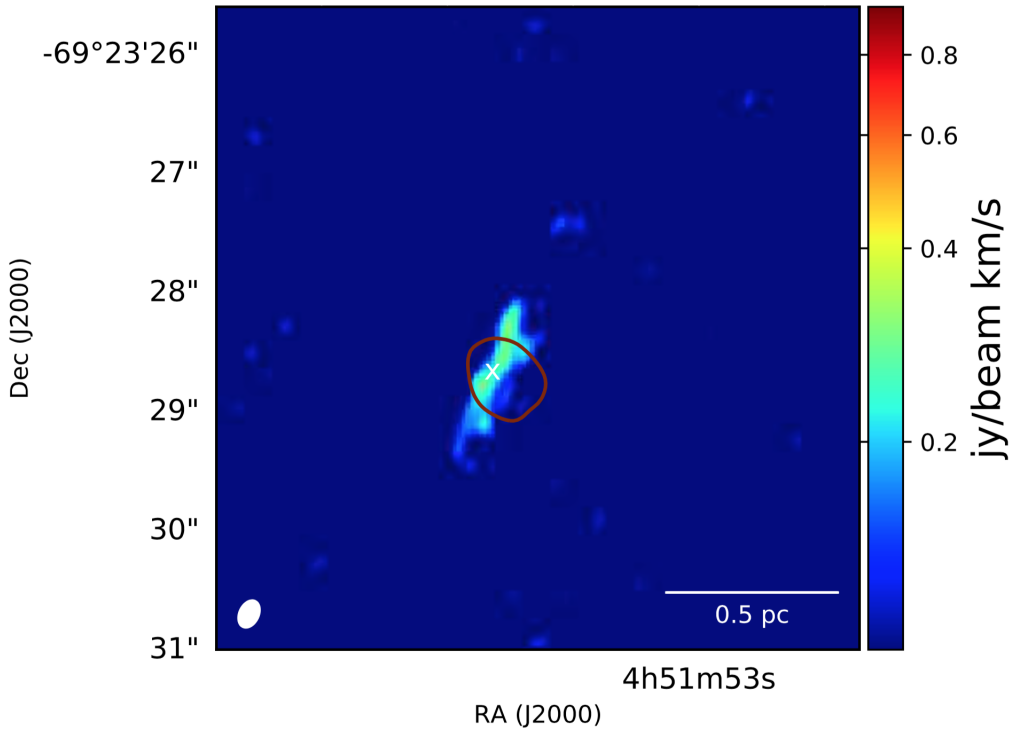

Figure 4.8: Zoomed-in image of the SO_2 observations. The SO_2 outflow aligns with the $^{13}CO(2-1)$ and $HCO+(3-2)$ outflow. We outline the H30α emission in red. The contour signifies 10% of the maximum emission.

in high-mass star formation regions when evolving from infrared luminous massive cores to a hot core phase (Guzmán et al., 2014). SO_2 in particular has become a common tracer of outflows associated with massive YSOs (Kwon et al., 2015; Podio et al., 2015). We find SO_2 to be aligned with the bipolar outflow associated with H72.97.69.39. Figure 4.8 shows the collimated SO_2 outflows with the protocluter (white 'x' located at the center). We also outline the H30α emission in red showing the entire cluster has a surrounding HII region. Table 4.9 gives the properties of the SO_2 molecular gas.

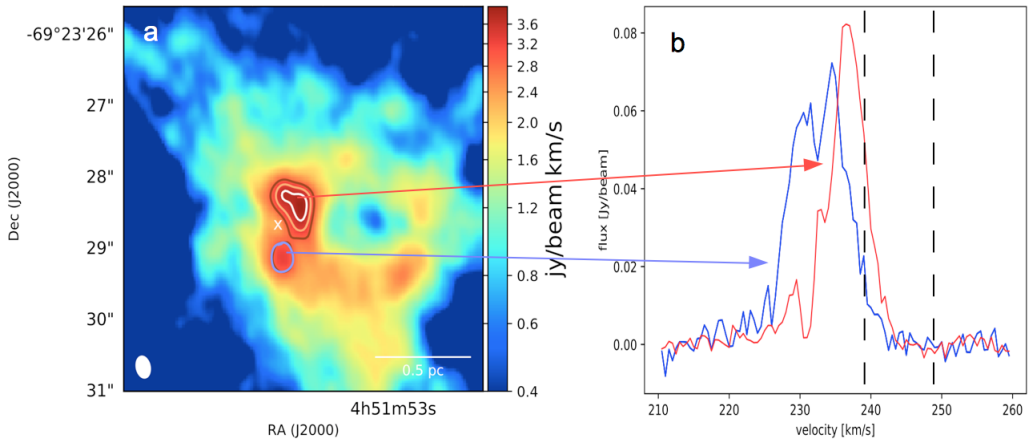

Figure 4.9: a) Image of the $^{12}CO(2-1)$ molecular gas in color. The blue-shifted outflow is shown in blue contour at 2.9 jy/beam km/s. The red-shifted outflow is shown in red/orange/white contour at 2.9, 3.3, and 3.7 jy/beam km/s. b) The spectra of the red and blue contours. The black dashed line marks the outflow wing on the red-shifted side and spans 10 km/s.

Table 4.9: ALMA Observation: SO_2

Clump ID	RA	Dec	Filament Length [pc]	Filament Width [pc]	F_{SO2} [K km s^{-1}]
0	72.972133	-69.391284	0.287	0.069	49.63 ± 11.81

Properties of SO_2 hot core.

4.4.3 Recombination Lines from Ionized Hydrogen and Carbon

Higher-order recombination line emission produced by hydrogen and carbon are optimal star formation tracers. These millimeter and sub-millimeter lines are not affected by dust extinction, unlike star formation tracers in the optical, UV, and infrared wavelengths. Often times these recombination lines are too faint to observe. However, we observe H30α and C30α at the location of the most luminous YSO. Figures 4.4g and 4.4h show the H30α and C30α, respectively. The H30α emission is 0.093 pc long and 0.067 pc wide, and has a total flux of 306 K km s^{-2} (Table 4.10). The C30α emission is 0.076 pc long and 0.027 pc wide, and has a total flux of 56 K km s^{-2} (Table 4.11). The C30α is x6 fainter than the H30α emission, likely due to there being less carbon in comparison to hydrogen.

Table 4.10: ALMA Observation: H30α

Clump ID	RA	Dec	Filament Length [pc]	Filament Width [pc]	$F_{H30\alpha}$ [K km s^{-1}]
0	72.972145	-69.391326	0.093	0.065	305.8 $\pm$ 12.73

Properties of H30α recombination line.

Table 4.11: ALMA Observation: C30α

Clump ID	RA	Dec	Filament Length [pc]	Filament Width [pc]	$F_{C30\alpha}$ [K km s^{-1}]
0	72.972181	-69.391321	0.076	0.027	55.69 $\pm$ 6.862

Properties of C30α recombination line.

We use equations from Mezger & Henderson (1967) to determine the electron

density, ionized mass, emission measure, ionization parameter, and continuum flux of the luminous protostar in N79. These properties are listed in Table 4.12. We also include properties of the Papillon Nebula YSO in N159 East and another massive YSO in N159 West for comparison purposes (Saigo et al., 2017). The electron density surrounding the most luminous YSO is two orders of magnitude higher than the electron density in the vicinity of the two massive YSOs in the N159 region. However the ionized mass is much smaller than that measured in N159 East or N159 West, most likely because this luminous YSO in N79 is just starting to ionize its surrounding. The photon flux is $\log(N_{continuum}) = 51.35\ s^{-1}$, which is about an order of magnitude higher than the photon flux measured using hydrogen recombination near the Papillon Nebula YSO ($\log(N_{continuum}) = 50.04\ s^{-1}$) and N159 West YSO-N ($\log(N_{continuum}) = 50.18\ s^{-1}$). We estimate a lower limit on the spectral type of the central ionizing source in N79 to be a O3 star (Smith et al., 2002).

Table 4.12: Derives and Gas and Stellar Properties from ALMA H30α Emission

Object	n_e [cm^{-3}]	$M_{ionized}$ [$M_\odot$]	EM [pc cm^{-6}]	U [pc cm^{-2}]	log($N_{continuum}$) [s^{-1}]	Type
N79 Most Luminous YSO	3.9×10^5	17.5	1.3×10^{10}	414	51.35	$\geq$ O3
N159E Papillon Nebula YSO	2.2×10^3	65.0	3.9×10^6	153	50.04	$\geq$ O3
N159W YSO-N	2.6×10^3	154	6.3×10^6	168	50.18	$\geq$ O3

Column 1: The name of the object. The Most Luminous YSO is from this work. The Papillon Nebula YSO is discussed in Saigo et al. (2017) and N159W YSO-N is discussion in Fukui et al. (2015). Column 2: The electron density. Column 3: The ionized mass. Column 4: The emission measure. Column 5: The ionization parameter. Properties listed in columns 2-5 are derived using equations from Mezger & Henderson (1967). Column 6: The photon flux. Column 7: Estimate of the spectral type (Smith et al., 2002).

Table 4.13: Properties of ^{13}CO (2-1) Clumps Associated with YSO Candidates

Location	Virial Parameter	Size [pc]	Linewidth [km s^{-1}]	Mass [M$_\odot$]
N159 West	0.558	0.844	0.732	1565.2
N159 West	0.328	0.479	0.643	669.95
N159 West	0.399	2.64	2.25	43032
N159 West	0.402	2.61	2.25	42195
N159 West	0.410	2.40	2.16	36678
N159 West	0.414	2.49	2.19	38059
N159 West	0.413	2.50	2.19	38280
N159 West	0.408	2.44	2.15	36974
N159 West	0.413	2.31	2.16	35364
N159 West	0.418	2.25	2.12	33151
N159 West	0.421	2.23	2.10	32232
N159 West	0.421	2.21	2.09	31815
N159 West	0.415	2.28	2.14	34363
N159 West	0.415	2.28	2.14	34213
N159 West	0.421	2.22	2.09	31938
N159 West	0.422	2.20	2.08	31366
N159 West	0.422	2.19	2.07	31076
N159 West	0.428	2.15	2.06	30301
N159 West	0.432	2.11	2.04	28916
N159 West	0.394	1.95	1.98	26981
N159 West	0.393	1.90	1.96	26268
N159 West	0.389	1.87	1.92	25163
N159 West	0.393	1.99	2.00	27808
N159 West	0.390	1.87	1.92	25096
N159 West	0.392	1.92	1.97	26758
N159 West	0.427	2.16	2.07	30447
N159 West	0.428	2.16	2.07	30387
N159 West	0.208	1.63	1.36	20564
N159 West	0.393	1.82	1.87	23328
N159 West	0.180	1.36	1.31	16576
N159 West	0.202	1.20	1.24	12309
N159 West	0.165	1.06	1.23	10792
N159 West	0.162	0.990	1.21	9812.2
N159 West	0.484	0.907	1.39	4183.2
N159 West	0.162	0.986	1.21	9696.8
N159 West	0.160	0.948	1.19	8993.6
N159 West	0.171	0.795	1.13	6623.0
N159 West	0.475	0.784	1.32	3353.4

Continued on next page

Table 4.13 – continued from previous page

Location	Virial Parameter	Size [pc]	Linewidth [km s^{-1}]	Mass [$M_\odot$]
N159 West	0.182	0.655	1.12	4886.8
N159 West	0.183	0.681	1.12	5040.2
N159 West	0.178	0.619	1.12	4736.0
N159 West	0.232	0.480	0.961	2168.3
N159 West	0.247	0.455	0.900	1726.3
N159 West	0.132	0.347	0.485	736.74
N159 West	0.295	0.952	0.627	1968.9
N159 West	0.280	0.988	0.629	2130.2
N159 West	0.384	0.848	0.614	1420.8
N159 West	0.452	0.692	0.507	829.43
N159 West	0.479	0.727	0.555	916.81
N159 West	0.497	0.743	0.586	985.25
N159 West	0.448	0.772	0.589	1119.7
N159 West	0.719	0.548	0.570	544.32
N159 West	0.455	0.698	0.515	845.97
N159 West	0.403	0.423	0.464	366.53
N159 East	0.815	2.13	2.06	11545
N159 East	0.688	1.96	1.96	10649
N159 East	0.692	2.00	1.97	10807
N159 East	0.812	2.10	2.05	11396
N159 East	0.689	1.89	1.95	10296
N159 East	0.677	1.86	1.94	10169
N159 East	0.543	1.65	1.76	9097.4
N159 East	0.689	1.93	1.95	10419
N159 East	0.545	1.60	1.76	8940.4
N159 East	0.578	1.46	1.76	8000.5
N159 East	0.575	1.47	1.76	8094.4
N159 East	0.611	1.35	1.75	7238.9
N159 East	0.685	1.22	1.71	5813.5
N159 East	0.706	1.18	1.71	5465.3
N159 East	0.774	1.03	1.64	4253.9
N159 East	0.790	1.07	1.67	4420.9
N159 East	0.622	0.912	1.56	3866.1
N159 East	0.228	0.606	0.841	1784.1
N159 East	0.108	0.484	0.541	1195.2
N159 East	0.614	0.923	1.55	3898.1
N159 East	0.772	1.01	1.62	4122.8
N159 East	0.324	0.541	0.699	667.38
N159 East	0.254	0.410	0.616	535.96

Continued on next page

Table 4.13 – continued from previous page

Location	Virial Parameter	Size [pc]	Linewidth [km s^{-1}]	Mass [M$_\odot$]
30 Doradus	0.296	0.352	0.579	384.62
30 Doradus	1.26	0.293	0.873	182.76
30 Doradus	0.302	1.23	1.15	5917.2
30 Doradus	0.302	0.988	1.16	4380.6
30 Doradus	0.178	0.838	0.906	3663.3
30 Doradus	0.197	0.843	1.03	4203.1
30 Doradus	0.205	0.965	1.00	4760.2
30 Doradus	0.162	0.583	0.969	2900.0
30 Doradus	0.456	1.16	2.81	16796
30 Doradus	0.225	1.36	1.94	19352
30 Doradus	0.134	1.07	1.5	15404
30 Doradus	0.100	0.867	1.30	12788
N79	1.31	0.403	1.16	249.52
N79	0.954	0.964	1.57	1465.7

Column 1: Location of the CO clump. Column 2: Virial parameter. Column 3: Size. Column 4: Linewidth. Column 5: Mass.

Indebetouw et al. (2004) calculate the Lyman continuum flux by assuming all the 3 cm emission (measured using the Australian Compact Telescope Array) is from the HII region. They find $\log(N_{\rm continuum}) = 49.6\ {\rm s}^{-1}$. The spectral type of the central ionizing source is a O5V star, assuming a single star is producing all the continuum emission. The continuum measurement we make in this chapter is two orders of magnitude greater than the measurement by Indebetouw et al. (2004). The frequency of H30α emission is 235.995 GHz, which is 0.13 cm. Indebetouw et al. (2004) assume a power-law to relate the flux to the frequency: $F_\nu \propto \nu^\alpha$. They measure the power-law index from 3 cm (9.993 GHz) to 6 cm (4.997 GHz) to be $\alpha = 0.2$. As frequency increases so does the flux since Indebetouw et al. (2004) measure the 6 cm flux to be 138 mJy and the 3cm flux to be 160 mJy. Therefore, it is not surprising we measure

a Lyman continuum flux two orders of magnitude larger than that by Indebetouw et al. (2004) at 235.995 GHz. Our measurement is likely to be more accurate since we measure the cascading of the electrons in the Hydrogen atom directly with the H30α observation.

4.4.4 Virial Analysis

The virial parameter is the ratio of the kinetic energy to the gravitational energy: $\alpha = \frac{5\sigma^2 \mathrm{r}}{\mathrm{GM}}$. We plot the virial parameter of the N79 red-shifted and blue-shifted clumps in Figure 4.10. Clumps above the solid black line (where the kinetic energy is equal to the gravitational energy) are not virialized, i.e. they are considered to not be gravitationally contracting to form a star. However, this is not always true. Figure 4.10 shows the blue-shifted clump in N79 has a virial parameter greater than 1 and the red-shifted clump in N79 has a virial parameter just slightly less than 1. How can there be a proto-cluster at the center of two colliding clumps when the clumps do not seem to be gravitationally contracting? Klassen et al. (2017) analyze the orientation of magnetic field in cluster-forming filaments and track how the virial parameter changes as the filaments evolve. They show that clumps which start out with a higher density (1.2×10^3 cm^{-3}, x3 higher than their low-density simulation) can become magnetically critical: magnetic support can slow-down and stall the star formation process. In such clumps, the virial parameter starts out just below 1 and quickly rises to 1.4 in just 150,000 years. However feedback from just a single 16 $\mathrm{M}_\odot$

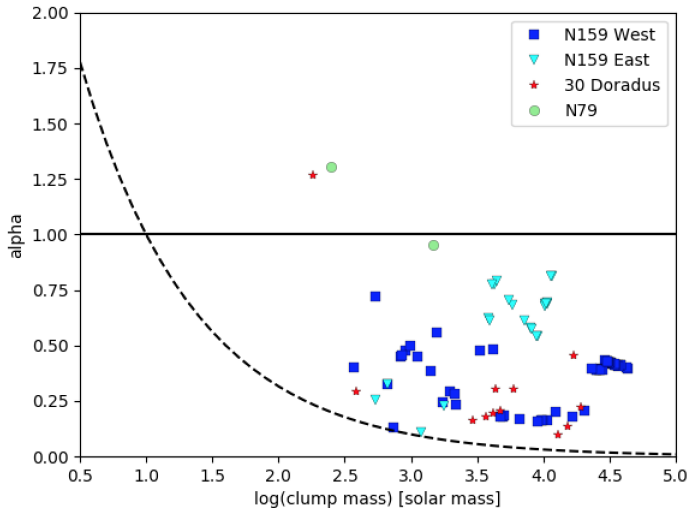

Figure 4.10: Clump mass derived using ^{13}CO$(2-1)$ versus the virial parameter ($\frac{5\sigma^2_r}{GM}$). Points above the solid black line are not virialized, points below the solid black line are virialized (i.e. gravitationally bound). The dashed black line is the boundary between clumps forming stars via monolithic collapse (above the dashed line) and clumps forming star via competitive accretion (below the dashed line).

protostar can disrupt the entire magnetic field structure and therefore change the virial state of a clump. Perhaps we are observing this potentially embedded SSC in N79 at a point in time where star formation has started taking place, however the magnetic field is orientated in such a way that the gravitational contraction of the clump in which the SSC resides is stalling. Instead gravitational energy is being converted to kinetic energy as the collapse is slowing down, and therefore these clumps have a high virial parameter (Klassen et al., 2017). However if a single protostar that is 16 $M_\odot$ can disrupt the entire surrounding filamentary structure, then several high mass protostars at a center of a SSC can change the dynamical state and virial parameter of the molecular gas clump.

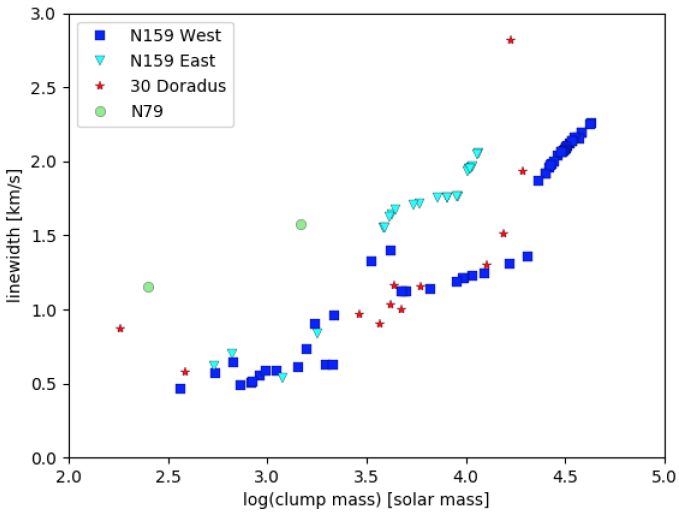

Figure 4.11: Linewidth versus clump mass for $^{13}CO(2-1)$ clumps in N159 East, N159 West, 30 Doradus, and N79.

Alternatively, it could also be the case that strong stellar winds from the massive protostars and outflows from the central cluster are adding kinetic energy to the surrounding gas clumps. And therefore the virial parameters of the red-shifted and blue-shifted clumps are near or greater than 1. Figure 4.11 shows that the $^{13}CO(2-1)$ clumps in N79 have very high linewidths for their given size. The linewidth of the blue-shifted clumps is x1.3 higher than other clumps of a simlilar size, and the linewidth of the red-shifted clumps is x2 higher than other clumps of a similar size. The majority of the star forming $^{13}CO(2-1)$ clumps in N159 East (19/23) have virial parameters greater than 0.5 (but less than 1) as shown in Figure 4.10. The same 19 clumps also have very high linewidths for their given size as shown in Figure 4.11. These clumps in N159 East with high linewidths are part of three different filaments which are colliding to form a massive protostar that is 50 $M_{\odot}$. This shift to higher linewidths

for a given size could be due to the chaotic nature of the central protocluster (in N79) and colliding filaments (in N159 East) injecting energy into the surrounding molecular gas.

4.5 Discussion

4.5.1 Is there a Rotating Toroid Around this Object?

Several instances of rotating disks around high mass YSOs have been reported in the past few years (Beuther & Walsh, 2008; Cesaroni et al., 2007; Zapata et al., 2015, 2008). Rotating structures that are several 10 $M_{\odot}$ and several 1000 AU are called toroids. In Figure 4.12 we plot the velocity field of the $^{13}CO(2-1)$ gas and find there is a gradient, indicative of rotation. The grey arrow points in the direction from blue-shift to red-shift. We further investigate the velocity gradient in Figures 4.13a and 4.13b. Figure 4.13a shows the $^{13}CO(2-1)$ image. We take a PV slice along the dotted lines and the resulting PV structure is shown in Figure 4.13b. The rotating toroid is along the northwest to southeast direction, 62° to the direction of the outflow. The radius of the toroid spans 0.1-0.2 pc (20,000-40,000 AU). Rotating toroids perpendicular to the direction of outflowing jets have been detected in the Milky Way (Beltrán et al., 2011a). With the high resolution interferometry data

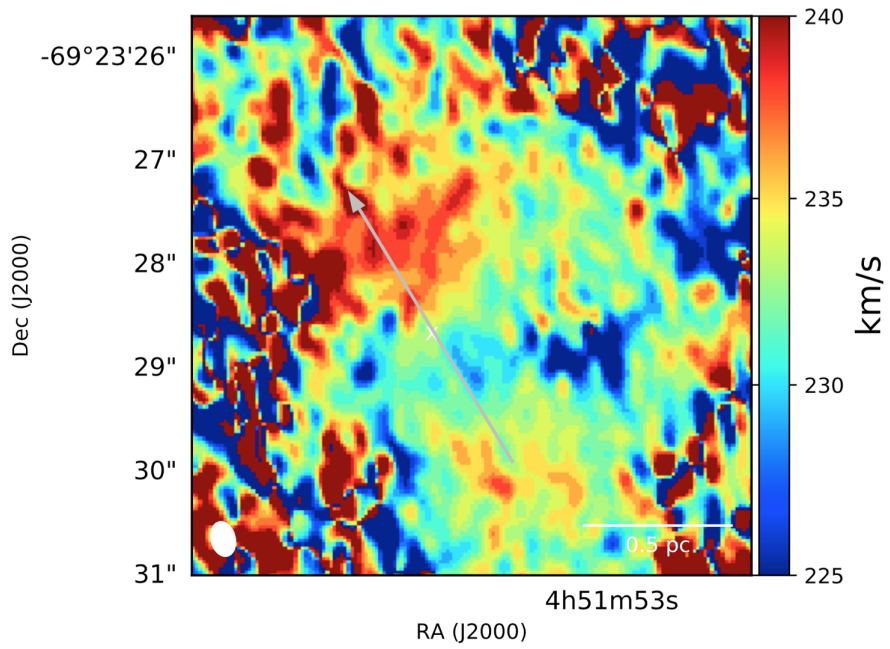

Figure 4.12: The velocity gradient of the $^{13}CO(2-1)$ molecular gas. The grey arrow goes through the location of the central cluster (white 'x') and is pointing in the direction from blue-shift to red-shift.

of ALMA, we report the first extragalactic detection of a rotating toroid around a cluster.

We estimate the rotation velocity to be half the velocity range in the gradient which is 10km/s, this is a similar estimation as done by Beltrán et al. (2011b). The virial mass is calculated from assuming equilibrium between the kinetic energy and the gravitational energy of the toroid: $M_{vir} = r\ v^2/2\ G$, where r is the size of the toroid and v is the linewidth of the molecular gas. The virial mass equals $578M_{\odot}$ because the linewith of both the red-shifted and blue-shifted components of the toroid are about 5km/s. The mass infall rate can then be estimated by the following: $\dot{M}_{inf} = 2M_{vir}V_{inf}/R$. Assuming the infall velocity equals the rotational velocity, the

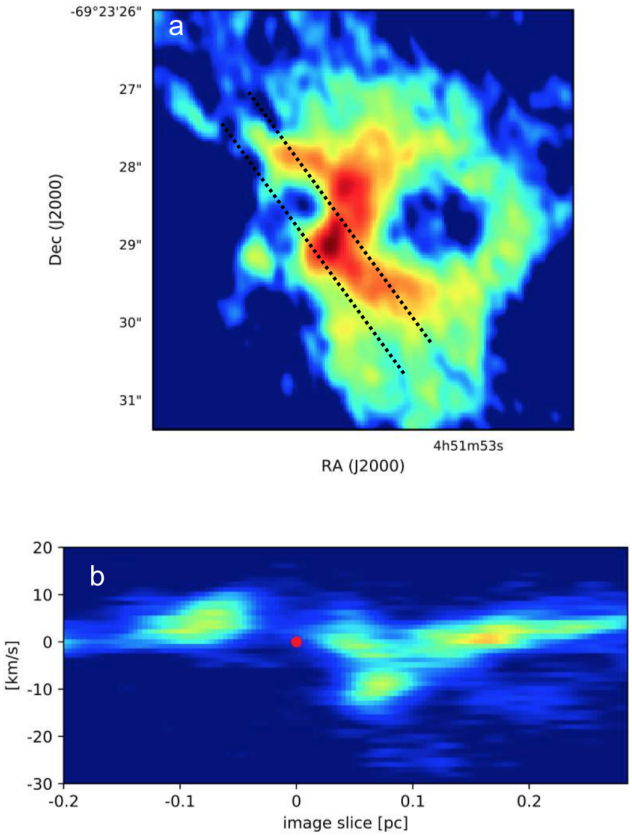

Figure 4.13: Top: ^{13}CO$(2-1)$ image. Bottom: The resulting position-velocity slice taken along the dashed lines.

infall mass is estimated to be 0.06-0.12$M_\odot$ yr^{-1}. The virial mass and infall mass are comparable to those seen in rotating toroids in the Milky way by Beltrán et al. (2011b): $M_{vir} = 149 - 615 M_\odot$ and $\dot{M}_{inf} = 0.008 - 0.03 M_\odot$ yr^{-1}. The mass infall rate in proto-SSC H72.97-69.39 is 3-4 times higher than that observed in Milky Way clusters. This may be due to the fact that proto-SSC H72.97-69.39 might be the next 30 Doradus whereas the Milky Way clusters are smaller and therefore do not have as high of a mass infall rate. This is consistent with the predictions of Ochsendorf et al. (2017b) who find the star formation rate of H72.97-69.39 has been increasing over the past few million years and the luminosity of the region can one day be similar to the R136 SSC in 30 Doradus.

4.5.2 What is this Object?

Rotation around a central source with bipolar collimated jets is seen on several astrophysical scales: from solar-type stars to AGNs. Therefore, it is perhaps not surprising to see such a phenomena around a potential SSC. Figure 4.14 shows a cartoon picture of H72.97-69.39. Two filaments (0.5 pc and 1.5pc in length) collided leading to a formation of a SSC. There is a toroidal structure rotating around this SSC on scales of 20,000-40,000 AU with bipolar jets streaming on scales of 0.076 pc x 0.027 pc flowing out at a directional that is almost perpendicular (62°) to rotation. The high mass protostars in the cluster have started ionizing a HII region. The detection of C30alpha suggests there is a CII region surrounding the HII region: the photons

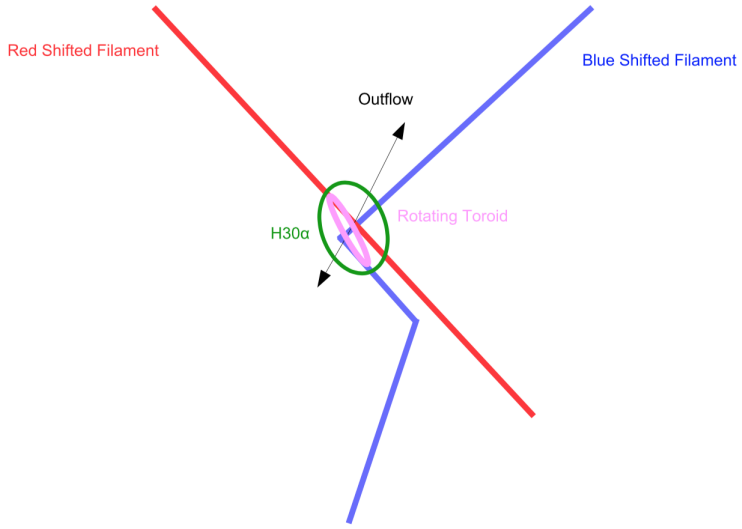

Figure 4.14: Cartoon diagram showing the different components of the potential embedded SSC H72.97-69.39: blue-shifted filament (blue), red-shifted filament (red), outflowing gas (black), HII region (green), rotating toroid (pink).

slightly longer than the Lyman limit streaming out of the HII regions would be able to ionize carbon.

Toroids are different than the Keplerian disks observed around protostars. The toroid, not the central star, is dominating the gravitational potential. Therefore Keplerian rotation is not possible on scales of several 1000 AU for such massive structures. Cesaroni et al. (2006) theorize these toroidal structures seen around massive clusters are transient objects with short lifetimes ($\approx 10^4$ yrs). This is consistent with the results from Ochsendorf et al. (2017b) who report this objects to be a very young

embedded SSC as well the timescale of the $^{13}CO(2-1)$ outflows of 19,500 yrs we calculate in this work.

High resolution ALMA observations indicate it is plausible for a rotating toroid around the potential SSC. We propose a scenario where the large scale *Herschel* filaments seen in Figure 4.5a are connected to the small scale colliding filaments we see with ALMA, as well as accreting material onto the rotating toroid. The dynamics of the gas surrounding individual stars within the SSC would be obscured by the toroid. However, Beltrán et al. (2011a) theorize material from the toroid would infall onto the circumstellar disks of the individual stars in the cluster. This scenario would also explain why we find red-shifted and blue-shifted $^{13}CO(2-1)$ to not be virialized, unlike similar clumps seen in other star forming regions like 30 Doradus (Nayak et al., 2016) and N159 (Fukui et al., 2015; Saigo et al., 2017). We are not observing a singular core or clump gravitationally collapsing. Instead, we are observing a rotating structure which potentially contains several cores collapsing to form stars. However, the kinematic signature of the collapsing cores gets obscured by the stellar winds of the protostars and rotating toroid.

4.6 Conclusion

We report the third extragalactic detection of SO_2, which is tracing the outflow from the potential embedded SSC H72.97-69.39. The outflow is also traced with other molecular gas observed with ALMA: $^{12}CO(2-1)$, $^{13}CO(2-1)$, and $HCO+(3-2)$. In addition, ALMA resolved other kinematic structures surrounding this SSC.

1) The SSC is located at the center of two colliding filaments. The blue-shifted filament is 0.5 pc in length and the red-shifted filament is 1.5 pc in length. Filaments can also be seen on a larger scale with the *Herschel* images. These large-scale filaments are tens of parsecs long.

2) Molecular gas bipolar outflows are 0.2pc in length and the outflow velocity is 10 km/s. We calculate the timescale of the outflows to be roughly 19,500 yrs.

3) H30α detection implies a HII region around this cluster. The Lyα photon flux from this source is 1 dex higher than YSOs in the N159 region of the LMC (Table 4.12). This source is at least an O3 star, assuming all the flux is originating from a single protostar.

4) PV slice taken of $^{13}CO(2-1)$ and $HCO+(3-2)$ shows an increase in velocity closer to the SSC which is a signature of rotation. We interpret the rotation on

scales of 20,000-40,000 AU to be a toroid around the potential embedded SSC.

5) We calculate the mass infall rate to be $\dot{M}_{inf} = 0.06 - 0.12 M_{\odot}\ yr^{-1}$, three to four times higher that clusters in the Milky Way. This higher infall rate is likely due to the formation of a SSC which is much more massive than a regular cluster.

4.7 Acknowledgements

This chapter makes use of the following ALMA data:
ADS/JAO.ALMA#2013.1.01155.S. ALMA is a partnership of ESO (representing its member states), NSF (USA) and NINS (Japan), together with NRC (Canada), NSC and ASIAA (Taiwan), and KASI (Republic of Korea), in cooperation with the Republic of Chile. The Joint ALMA Observatory is operated by ESO, AUI/NRAO and NAOJ. The National Radio Astronomy Observatory is a facility of the National Science Foundation operated under cooperative agreement by Associated Universities, Inc.

M. Meixner and O. Nayak were supported by NSF grant AST-1312902. O. Ochsendorf was supported by grant NNX15AF17G. M. Sewilo was supported by an appointment to the NASA Postdoctoral Program at the Goddard Space Flight Center, administered by Universities Space Research Association under contract with NASA.

Chapter 5

Conclusion

We increase the total number of YSO candidates in the ALMA footprint regions of 30 Doradus, N159W, and N159E to a total of 34, a factor of 1.7 increase from the 20 that have previously been identified (Chen et al., 2010; Gruendl & Chu, 2009; Seale et al., 2014; Whitney et al., 2008). Of the 14 new YSO candidates we found, 13 of them have masses between $7 - 13 M_{\odot}$. Our work identifies the lower mass, but still massive, protostars missed by previous color-color cut studies. The stringent cuts from previous studies were good at identifying thousands of very massive YSO candidates, however a more precise method of looking at individual SEDs is necessary to get the complete sample of YSO candidates $>8 M_{\odot}$.

Massive protostars are associated with high density and turbulent gas, some even found at the center of colliding filaments (Papillon Nebula YSO in N159E, YSO #5

in N159W, and the potential SSC in N79). The turbulent nature of the molecular gas can be quantified by measuring the linewidth of a given cloud. The size-linewidth relation show similar power-law scaling relations across a range of environments, suggesting there are common underlying physical processes in the ISM. Measuring this relation in a variety of star-forming and non-star-forming regions is required to understand the 'universality' of the physical properties such as size and linewidth of molecular gas. Size-linewidth of the ^{13}CO gas in 30 Doradus is elevated (the linewidth for a given clump size is larger than expected) compared to N159 West, N159 East, and other extragalactic environments (Bolatto et al., 2008; Nayak et al., 2016). This elevation in the size-linewidth relation has also been observed in the Galactic Center where ^{13}CO and other high density gas tracers show an elevated size-linewidth relation in comparison to other locations in the Milky Way (Shetty et al., 2012). Our work measures the feedback from turbulence: shock induced turbulence that occurs on a local scale due to the nearby SSC could cause the elevation in the size-linewidth relation in 30 Doradus (similar to that seen in the Galactic Center). The linewidth of a clump is also indicative of its kinetic energy. The ratio of the kinetic energy to the gravitational energy (i.e. virial parameter) of all star forming clumps in 30 Doradus, N159W, N159E, and N79 show that these gas clouds are likely undergoing monolithic collapse. It is not clear if filamentary collision and monolithic collapse are mutually exclusive formation mechanisms or can both happen at the same time. More observations of massive YSOs at the center of filamentary collisions are needed

to determine how to distinguish between the two formation processes.

ALMA ^{13}CO observation of N79 show the molecular gas is very filamentary in nature in the vicinity of the potential SSC. H72.97-69.39 is at the center of two colliding filaments. Molecular gas observations also show a rotating toroid that around the central cluster with bipolar outflows streaming out of the centeral source, the first extragalactic observation of such a phenomena. The toroid is 20,000-40,000 AU in size and the timescale of the outflow is 19,500 yrs. This is a very young source that is only a couple of tens of thousands of years old with a mass infall rate of $\dot{M}_{inf} = 0.06 - 0.12 M_{\odot}$ yr^{-1}. Integrating over the SED for H72.97-69.39 gives a total luminosity of over 2,000,000 $L_{\odot}$. This makes H72.97-69.39 the most luminous compact object known in either the LMC or the Milky Way. We use ALMA H30α observations to calculate the total Lyα photo flux ($\log(N_{continuum}) = 51.35 s^{-1}$), which in turn gives a lower limit on the spectral type of this star (O3, Smith et al. 2002).

The three star forming regions discussed in this thesis provide a good framework on which we will build future observations around.We have Magellan FIRE spectrograph for H72.97-69.39. The lines identified in the spectrum include: H, He, OI, [SII], [FeII], [FeIII], and H_2. The [FeII] and H_2 lines are indicative of the gas being shocked. Further analysis on the SSC and the entire N79 region will be done with ALMA ACA (PI: O. Nayak) and SOFIA/GREAT (PI: M. Meixner) observations. We will use the

new method of identifying YSOs proved to nearly double the number of known protostars as part of selection in identifying candidates to follow-up with JWST MIRI, NIRCam, and NIRSpec observations. How do massive stars form, especially in a low-metallicity environment? More metal content in a galaxy helps with dissipating energy, therefore protostars in a low-metallicity environment should be able to accrete more mass before dissipating the dust and gas they are enshrouded within. However, this has not been observed. Further analysis of current massive protostars and future analysis with JWST will be the key in determining how massive stars form in the local and distant Universe.

Appendix A

Calculating H_2 mass using N_{13CO}

We assume that ^{13}CO is optically thin. The optical depth of ^{13}CO is given by:

$$\tau_{^{13}\mathrm{CO}(2-1)} = -\ln[1 - \frac{\mathrm{T}_{\mathrm{B},^{13}\mathrm{CO}(2-1)}}{10.6}([\mathrm{e}^{10.6/\mathrm{T}_{\mathrm{ex},^{12}\mathrm{CO}(2-1)}} - 1]^{-1} - 0.02)^{-1}], \tag{A.1}$$

where the excitation temperature is given by:

$$\mathrm{T}_{\mathrm{ex},^{12}\mathrm{CO}(2-1)} = \frac{10.6\ \mathrm{K}}{\ln(1 + \frac{10.6\ \mathrm{K}}{\mathrm{T}_{\mathrm{B},^{12}\mathrm{CO}(2-1)} + 0.21\ \mathrm{K}})}. \tag{A.2}$$

The ^{12}CO excitation temperature is only dependent on the ^{12}CO brightness temperature because we assume ^{12}CO to be optically thick. The ^{12}CO is likely to be optically thick if ^{13}CO is present because a larger column of molecular has is needed to see ^{13}CO, as oppose to ^{12}CO. The ^{13}CO map is the mask and we do not impose an artificial mask on the excitation temperature. There are places where the optical depth

(equation A1) does not make sense, and therefore gives a column density value that is not believable, which has been masked out. For example, there are pixels for which the optical depth is negative or infinity because of the natural log and an exponent of -1 in equation A1. This is because of how you clean the ALMA data. These pixels with negative values of values that equal infinity are not real or believable, but rather an artifact of the data cube quality. Further assumptions of the local thermodynamic equilibrium (or LTE) analysis include: ^{13}CO has the same excitation temperature as ^{12}CO, CO is thermalized (level population is described by the Boltzmann equation), and the abundance ratio between ^{12}CO and ^{13}CO is constant. The total ^{13}CO column density is then given by the equation:

$$N_{^{13}CO,tot} = \frac{1.5 \times 10^{14}\ T_{ex}\ e^{5.3/T_{ex}}\ \int \tau dv}{1 - e^{-10.6/T_{ex}}}. \tag{A.3}$$

We assume $\frac{H_2}{^{13}CO} = 5 \times 10^2$ (Indebetouw et al., 2013) to convert the ^{13}CO column density to H_2 column density. The total H_2 mass is then derived by:

$$M = m_{H_2} \int N_{H_2} dA. \tag{A.4}$$

Appendix B

Comparison Between Cprops and Astrodendro

Due to the different algorithm used by Indebetouw et al. (2013) (cprops), it is not possible to have a 1:1 relation between the clumps identified in this work and those published by Indebetouw and collaborators. Therefore we pick three clumps we identify by eye that are similar in the output of both programs to compare to each other. We compare the clump properties listed in Table 2.2 in this work, to the clump properties from Indebetouw et al. (2013). We used the same definition of sizes and linewidths when comparing clump properties by Indebetouw et al. (2013) and the results from this work. We got the size and linewidth values of ^{13}CO clumps output from cprops from our personal correspondence with Remy Indebetouw. Definition of sizes and linewidths is further described in Appendix C. The two algorithms (cprops

and *astrodendro*) work in different ways and therefore not possible to select a clump output from one program, and match it to the same exact clump output from the other program. And we cannot do this for all the leaves and branches output from the dendrogram program. We match the ^{13}CO clumps output from cprops to the same clumps identified by astrodendro, i.e. we search for clumps output from the two different algorithms and find those that are within 1 clump radii of each other. There are a total of 8 such clumps we can match from the two different algorithms and their properties are listed below. The purpose of this comparison is to see if we can find clump mass and size properties output from the two programs that are not different by orders of magnitude.

For the first clump listed in the table below we find that the astrodendro picks out a size that is twice as high as the size calculated from cprops, however the linewidth calculated by astrodendro is about 70% of the linewidth calculated by cprops. The next four clumps listed in the table below are comparable in size output from cprops and astrodendro, however the linewidths calculated by astrodendro are lower by 60-80%. Clumps selected by astrodendro that are larger or comparable in size to clumps selected by cprops tend to have lower linewidths. The next two in the table below are ^{13}CO clumps selected by astrodendro that are smaller in size than the same clumps selected by cprops. The size derived by astrodendro for the two clumps is smaller by a fact of 60-70%, however the linewidths are smaller by a factor of 40-50%. Astro-

dendro systematically calculates smaller linewidths, which explains the offset of the Indebetouw et al. (2013) clumps from the clumps we derived in this chapter. If we assume the clumps selected with astrodendro have lower linewidths than the clumps selected with cprops by a factor of 60-80% (as in the case for comparable size clumps), we can calculate this shift in the cprops clumps shown in cyan in Figure 2.13. The equation of the best fit line going through the cprops clumps in Figure 2.13 is given by $\sigma = (2.39 \pm 0.33)\mathrm{r}^{(0.91\pm0.15)}$. Shifting this line down by 60-80% changes the intercept of 2.39 to be between 1.69 to 1.99. The equation of the best fit line going through the astrodendro clumps in Figure 2.13 is given by $\sigma = (1.58 \pm 0.18)\mathrm{r}^{(0.97\pm0.12)}$. After taking into account the offset to lower linewidths inherent to astrodendro, the best fit-line going through the ^{13}CO cprops clumps and the best-fit line going through the ^{13}CO astrodendro clumps are in agreement within 1σ.

Table B.1: Comparing Cprops and *Astrodendro* Outputs

Size [pc] From Cprops	σ [km/s] From Cprops	^{12}CO ID	^{12}CO Size [pc]	^{12}CO σ [km/s]	Mass Derived From ^{12}CO [$M_\odot$]	^{13}CO ID	^{13}CO Size [pc]	^{13}CO σ [km/s]	Mass Derived From ^{13}CO [$M_\odot$]
0.35	0.57	26	0.34	0.68	259	0	0.73	0.39	297
0.28	0.87	53	0.17	0.94	62	16	0.32	0.55	112
0.32	0.94	69	0.32	0.95	359	22	0.32	0.73	612
0.36	0.78	28	0.31	0.84	271	4	0.35	0.48	281
0.48	1.15	94	0.31	0.98	851	41	0.42	0.82	2050
0.44	1.37	67	0.20	0.65	206	15	0.29	0.58	385
0.39	0.96	80	0.41	1.0	681	27	0.28	0.48	232
0.51	1.36	98	0.19	0.47	125	39	0.34	1.07	934

Column 1: Clump size derived from cprops. Column 2: The linewidth derived from cprops. Column 3: ^{12}CO clump ID as listed in Table 3. Column 4: ^{12}CO clump radius as listed in Table 3. Column 5: The linewidth of ^{12}CO clumps in this study. Column 6: H_2 mass derived using ^{12}CO. Column 7: ^{13}CO clump ID as listed in Table 4. Column 8: ^{13}CO clump radius. Column 9: The linewidth of ^{13}CO clumps in this study. Column 10: H_2 mass derived using ^{13}CO.

Appendix C

Defining Sizes and Linewidths

There are many definitions of clump 'sizes' and many ways to calculate a 'linewidth' of a data cube. These definitions vary significantly in the literature. In Indebetouw et al. (2013), the size was measured by fitting a 2-dimensional ellipse to the half-power contour of each clump. The ellipse was then deconvolved in two dimensions with the beamsize, and the radius quoted in Indebetouw et al. (2013) was 1.91 times the geometric mean of that deconvolved ellipse semimajor and semiminor axes. At time of writing Indebetouw et al. (2013), the ellipse-fitting measure of size was compared to spatial moments and to fitting a two dimensional Gaussian to the spatial distribution of emission, and found to be in agreement within error, but the most robust of the three methods. In this chapter, for both the Indebetouw et al. (2013) clumps and those defined by astrodendro, the size is calculated from the weighted second moment in two spatial directions, specifically the direction of greatest spatial extent and per-

pendicular to that. The radius is then 1.91 times the geometric mean of those two spatial second moments. In particular it should be noted that the current numbers thus include convolution by the $\sim$ 0.5pc beam.

In Indebetouw et al. (2013), the linewidth was calculated for each clump by extracting the 'column' through the cube, i.e. for each pixel in the clump, the pixels covering the full velocity range of the cube. A Gaussian was then fitted to the spectrum of that 'column', and the width, deconvolved by the spectral resolution of 0.35km/s, was reported. The fitted spectrum thus includes velocity line wings which are not explicitly assigned to the clump by the decomposition. At the time of writing Indebetouw et al. (2013), each spectrum was carefully examined, and verified that effects such as two clumps along the same line of sight artificially broadening the linewidth did not occur. That Gaussian fitting linewidth calculation was compared to the weighted second moments in velocity of only the clump-assigned pixels, and of the entire 'column' through the cube. Results were within uncertainties, but fitting a Gaussian to the 'column' was more robust. For the current comparison, we use the weighted velocity second moment of the pixels assigned to the cprops clump or astrodendro structure. The Indebetouw et al. (2013) method could over-estimate the linewidth, if significant emission is along the line of sight, whereas the current method likely underestimates the linewidth of a structure, since PPV and PPP space do not precisely correspond. As with the sizes, the current reported linewidths include the effects of finite spectral

resolution, but that is less than a 2% effect for the linewidths under consideration. The slight difference between the cprops and astrodendro 30 Doradus clumps seen in Figure 2.13 can be attributed to the difference between the two algorithms, how they pick out the structure, and the input thresholds used.

Appendix D

12CO and 13CO Clumps Identified using Astrodendro in the N159 Region of the LMC

Table D.1: Mass Derived from N159W ^{12}CO (2-1) Clumps

Clump ID	RA	Dec	Radius [pc]	$F_{^{12}CO}$ [K km s^{-1}]	Total Mass [$M_\odot$]	Virial Mass [$M_\odot$]	Linewidth [km/s]
0	84.899215	-69.762008	6.54	59.8 ± 41.1	1.76E+5 ± 1.21E+5	9.76E+4 ± 6.71E+4	3.58
1	84.899442	-69.761883	6.42	61.6 ± 39.2	1.65E+5 ± 1.05E+5	9.48E+4 ± 6.03E+4	3.56
2	84.899488	-69.761849	6.36	62.7 ± 38.4	1.61E+5 ± 9.83E+4	9.30E+4 ± 5.69E+4	3.55
3	84.899456	-69.761877	6.41	61.9 ± 39.0	1.64E+5 ± 1.03E+5	9.45E+4 ± 5.96E+4	3.56
4	84.899313	-69.761960	6.44	61.4 ± 39.9	1.70E+5 ± 1.10E+5	9.54E+4 ± 6.20E+4	3.57
5	84.899301	-69.761968	6.45	61.2 ± 40.0	1.71E+5 ± 1.12E+5	9.57E+4 ± 6.26E+4	3.57
6	84.899546	-69.761830	6.32	63.9 ± 37.7	1.58E+5 ± 9.35E+4	9.21E+4 ± 5.44E+4	3.54
7	84.899471	-69.761850	6.37	62.7 ± 38.4	1.61E+5 ± 9.88E+4	9.32E+4 ± 5.72E+4	3.55
8	84.899420	-69.761893	6.43	61.5 ± 39.3	1.65E+5 ± 1.06E+5	9.50E+4 ± 6.08E+4	3.56
9	84.899528	-69.761838	6.33	63.6 ± 37.9	1.59E+5 ± 9.49E+4	9.24E+4 ± 5.51E+4	3.54

Continued on next page

APPENDIX D. 12CO AND 13CO CLUMPS IDENTIFIED USING ASTRODENDRO IN THE N159 REGION OF THE LMC

Table D.1 – continued from previous page

Clump ID	RA	Dec	Radius [pc]	$F_{^{12}CO}$ [K km s^{-1}]	Total Mass [$M_\odot$]	Virial Mass [$M_\odot$]	Linewidth [km/s]
10	84.899539	-69.761836	6.33	63.7 ± 37.8	1.59E+5 ± 9.42E+4	9.22E+4 ± 5.48E+4	3.54
11	84.899575	-69.761819	6.29	64.1 ± 37.4	1.56E+5 ± 9.13E+4	9.13E+4 ± 5.33E+4	3.53
12	84.899682	-69.761775	6.19	64.9 ± 36.4	1.50E+5 ± 8.41E+4	8.92E+4 ± 5.01E+4	3.52
13	84.899714	-69.761760	6.16	65.4 ± 36.1	1.48E+5 ± 8.17E+4	8.85E+4 ± 4.89E+4	3.52
14	84.899790	-69.761749	6.11	65.8 ± 35.5	1.44E+5 ± 7.79E+4	8.72E+4 ± 4.71E+4	3.50
15	84.899755	-69.761759	6.14	65.7 ± 35.8	1.46E+5 ± 7.97E+4	8.78E+4 ± 4.79E+4	3.51
16	84.923197	-69.767047	3.28	46.0 ± 20.3	3.31E+4 ± 1.46E+4	1.68E+4 ± 7.43E+3	2.10
17	84.899831	-69.761737	6.07	66.6 ± 35.0	1.42E+5 ± 7.45E+4	8.63E+4 ± 4.53E+4	3.50
18	84.899904	-69.761724	6.01	67.3 ± 34.4	1.38E+5 ± 7.07E+4	8.51E+4 ± 4.35E+4	3.49
19	84.899878	-69.761727	6.03	67.3 ± 34.5	1.40E+5 ± 7.17E+4	8.55E+4 ± 4.39E+4	3.49
20	84.923213	-69.767067	3.22	47.0 ± 19.9	3.23E+4 ± 1.37E+4	1.63E+4 ± 6.91E+3	2.09
21	84.923529	-69.766962	2.96	49.8 ± 18.6	2.99E+4 ± 1.12E+4	1.46E+4 ± 5.47E+3	2.06
22	84.902668	-69.770069	2.94	46.8 ± 18.0	2.62E+4 ± 1.01E+4	2.21E+4 ± 8.48E+3	2.54
23	84.900633	-69.761855	5.62	71.0 ± 32.5	1.31E+5 ± 6.00E+4	8.13E+4 ± 3.73E+4	3.53
24	84.902679	-69.770034	2.91	46.7 ± 17.6	2.50E+4 ± 9.41E+3	2.16E+4 ± 8.12E+3	2.53
25	84.902697	-69.769994	2.89	46.3 ± 17.2	2.38E+4 ± 8.88E+3	2.12E+4 ± 7.89E+3	2.51
26	84.923612	-69.767032	2.85	51.6 ± 17.9	2.89E+4 ± 1.00E+4	1.41E+4 ± 4.89E+3	2.06
27	84.923239	-69.767096	3.15	48.4 ± 19.3	3.13E+4 ± 1.25E+4	1.57E+4 ± 6.27E+3	2.07
28	84.899931	-69.761708	5.97	67.9 ± 34.0	1.36E+5 ± 6.82E+4	8.43E+4 ± 4.22E+4	3.48
29	84.900558	-69.761781	5.51	72.5 ± 31.9	1.28E+5 ± 5.65E+4	7.90E+4 ± 3.48E+4	3.51
30	84.900552	-69.761785	5.52	72.4 ± 31.9	1.28E+5 ± 5.67E+4	7.91E+4 ± 3.49E+4	3.51
31	84.902708	-69.769962	2.88	46.4 ± 16.9	2.30E+4 ± 8.34E+3	2.01E+4 ± 7.29E+3	2.45
32	84.903010	-69.770164	2.73	48.8 ± 15.8	2.11E+4 ± 6.85E+3	1.99E+4 ± 6.45E+3	2.50
33	84.903063	-69.770140	2.72	49.5 ± 15.5	2.06E+4 ± 6.46E+3	2.00E+4 ± 6.26E+3	2.51
34	84.903067	-69.770105	2.70	50.3 ± 15.1	2.00E+4 ± 6.02E+3	1.96E+4 ± 5.91E+3	2.50
35	84.923588	-69.767073	2.78	52.7 ± 17.4	2.77E+4 ± 9.16E+3	1.34E+4 ± 4.43E+3	2.04
36	84.899927	-69.761709	5.98	67.8 ± 34.0	1.37E+5 ± 6.85E+4	8.43E+4 ± 4.23E+4	3.48
37	84.903203	-69.769903	2.47	55.9 ± 13.0	1.65E+4 ± 3.84E+3	1.74E+4 ± 4.05E+3	2.46
38	84.905939	-69.770352	1.70	51.8 ± 9.26	7.73E+3 ± 1.38E+3	1.14E+4 ± 2.04E+3	2.40
39	84.906086	-69.770352	1.62	52.8 ± 8.99	7.42E+3 ± 1.26E+3	1.10E+4 ± 1.87E+3	2.41
40	84.903803	-69.769843	2.33	53.2 ± 10.7	1.07E+4 ± 2.15E+3	1.26E+4 ± 2.55E+3	2.16
41	84.906375	-69.769974	1.49	47.4 ± 8.16	5.48E+3 ± 9.44E+2	2.60E+3 ± 4.47E+2	1.23
42	84.896572	-69.768733	0.417	24.2 ± 2.91	3.57E+2 ± 4.30E+1	1.62E+2 ± 1.96E+1	0.579
43	84.900019	-69.759636	3.78	84.2 ± 26.3	1.01E+5 ± 3.17E+4	4.11E+4 ± 1.29E+4	3.06
44	84.900075	-69.759631	3.76	85.1 ± 26.0	9.99E+4 ± 3.05E+4	4.08E+4 ± 1.25E+4	3.06
45	84.900172	-69.759707	3.66	86.1 ± 25.0	9.33E+4 ± 2.71E+4	3.94E+4 ± 1.14E+4	3.04
46	84.900208	-69.759706	3.64	85.9 ± 24.8	9.19E+4 ± 2.66E+4	3.91E+4 ± 1.13E+4	3.04
47	84.900155	-69.759710	3.66	86.1 ± 25.1	9.40E+4 ± 2.73E+4	3.95E+4 ± 1.15E+4	3.04

Continued on next page

Table D.1 – continued from previous page

Clump ID	RA	Dec	Radius [pc]	$F_{^{12}CO}$ [K km s^{-1}]	Total Mass [$M_\odot$]	Virial Mass [$M_\odot$]	Linewidth [km/s]
48	84.906084	-69.769837	1.36	59.0 ± 6.78	4.72E+3 ± 5.42E+2	2.39E+3 ± 2.74E+2	1.23
49	84.923511	-69.767159	2.62	54.7 ± 16.8	2.69E+4 ± 8.30E+3	1.27E+4 ± 3.90E+3	2.04
50	84.923534	-69.767277	2.52	57.7 ± 15.9	2.53E+4 ± 6.95E+3	1.19E+4 ± 3.26E+3	2.01
51	84.923547	-69.767319	2.49	58.1 ± 15.5	2.44E+4 ± 6.53E+3	1.16E+4 ± 3.10E+3	2.00
52	84.909347	-69.766296	0.523	20.5 ± 3.39	4.09E+2 ± 6.75E+1	5.88E+2 ± 9.71E+1	0.984
53	84.906157	-69.769639	1.15	66.5 ± 5.24	3.17E+3 ± 2.50E+2	1.56E+3 ± 1.23E+2	1.08
54	84.906268	-69.769375	0.913	76.5 ± 4.49	2.68E+3 ± 1.57E+2	8.13E+2 ± 4.77E+1	0.875
55	84.908746	-69.766303	0.316	22.4 ± 2.27	2.01E+2 ± 2.04E+1	1.20E+2 ± 1.22E+1	0.571
56	84.900341	-69.759725	3.55	87.3 ± 24.0	8.70E+4 ± 2.39E+4	3.80E+4 ± 1.04E+4	3.04
57	84.900312	-69.759723	3.57	87.2 ± 24.1	8.83E+4 ± 2.44E+4	3.83E+4 ± 1.06E+4	3.04
58	84.903075	-69.771215	0.309	18.4 ± 2.08	1.38E+2 ± 1.56E+1	1.82E+2 ± 2.05E+1	0.712
59	84.903179	-69.771108	0.222	17.4 ± 1.55	7.25E+1 ± 6.43E+0	7.60E+1 ± 6.75E+0	0.543
60	84.906798	-69.769329	0.591	71.8 ± 3.23	1.30E+3 ± 5.84E+1	2.88E+2 ± 1.30E+1	0.648
61	84.907214	-69.770654	0.109	37.3 ± 0.775	3.90E+1 ± 8.10E-1	2.01E+1 ± 4.17E-1	0.397
62	84.909486	-69.764054	0.267	8.58 ± 1.89	5.34E+1 ± 1.18E+1	3.16E+1 ± 6.96E+0	0.319
63	84.906796	-69.769275	0.522	72.5 ± 3.01	1.14E+3 ± 4.73E+1	2.13E+2 ± 8.85E+0	0.593
64	84.900637	-69.759752	3.39	86.4 ± 22.4	7.56E+4 ± 1.97E+4	3.59E+4 ± 9.34E+3	3.02
65	84.900605	-69.759747	3.41	86.5 ± 22.6	7.70E+4 ± 2.01E+4	3.61E+4 ± 9.45E+3	3.02
66	84.900803	-69.759769	3.29	84.2 ± 21.6	6.85E+4 ± 1.76E+4	3.47E+4 ± 8.92E+3	3.01
67	84.917417	-69.771908	0.732	21.1 ± 4.27	6.69E+2 ± 1.35E+2	3.26E+2 ± 6.59E+1	0.619
68	84.917077	-69.771995	0.921	19.7 ± 4.76	7.74E+2 ± 1.87E+2	4.51E+2 ± 1.09E+2	0.649
69	84.897711	-69.768348	0.954	56.2 ± 5.27	2.71E+3 ± 2.54E+2	1.23E+3 ± 1.15E+2	1.05
70	84.897460	-69.765991	0.814	31.6 ± 4.82	1.28E+3 ± 1.95E+2	6.42E+2 ± 9.80E+1	0.824
71	84.900882	-69.759790	3.27	84.3 ± 21.4	6.69E+4 ± 1.70E+4	3.44E+4 ± 8.72E+3	3.01
72	84.907172	-69.774231	0.257	13.5 ± 1.82	7.76E+1 ± 1.05E+1	6.12E+1 ± 8.25E+0	0.452
73	84.923833	-69.768374	1.82	62.2 ± 11.6	1.46E+4 ± 2.72E+3	7.78E+3 ± 1.45E+3	1.92
74	84.901073	-69.759704	3.16	85.6 ± 20.6	6.33E+4 ± 1.53E+4	3.33E+4 ± 8.04E+3	3.01
75	84.900939	-69.759788	3.23	84.0 ± 21.0	6.44E+4 ± 1.61E+4	3.38E+4 ± 8.46E+3	3.00
76	84.907225	-69.769490	0.264	48.0 ± 1.71	2.45E+2 ± 8.74E+0	4.22E+1 ± 1.51E+0	0.371
77	84.905689	-69.768812	0.142	44.5 ± 1.00	7.75E+1 ± 1.74E+0	2.07E+1 ± 4.66E-1	0.354
78	84.912704	-69.766325	0.176	13.2 ± 1.23	3.46E+1 ± 3.22E+0	1.86E+1 ± 1.73E+0	0.302
79	84.901399	-69.759884	2.79	82.7 ± 18.7	5.02E+4 ± 1.14E+4	2.90E+4 ± 6.56E+3	2.99
80	84.901422	-69.759905	2.77	81.6 ± 18.5	4.84E+4 ± 1.10E+4	2.86E+4 ± 6.47E+3	2.98
81	84.901531	-69.759974	2.62	81.5 ± 17.8	4.50E+4 ± 9.86E+3	2.70E+4 ± 5.90E+3	2.97
82	84.924136	-69.768754	1.40	77.0 ± 9.85	1.30E+4 ± 1.66E+3	5.57E+3 ± 7.13E+2	1.85
83	84.924132	-69.768748	1.38	78.9 ± 9.63	1.27E+4 ± 1.55E+3	5.53E+3 ± 6.75E+2	1.86
84	84.924152	-69.768750	1.41	76.3 ± 9.96	1.32E+4 ± 1.72E+3	5.64E+3 ± 7.36E+2	1.85
85	84.923916	-69.768454	1.71	64.3 ± 11.2	1.41E+4 ± 2.47E+3	7.15E+3 ± 1.25E+3	1.90

Continued on next page

APPENDIX D. 12CO AND 13CO CLUMPS IDENTIFIED USING ASTRODENDRO IN THE N159 REGION OF THE LMC

Table D.1 – continued from previous page

Clump ID	RA	Dec	Radius [pc]	$F_{^{12}CO}$ [K km s^{-1}]	Total Mass [$M_\odot$]	Virial Mass [$M_\odot$]	Linewidth [km/s]
86	84.901546	-69.760207	2.39	77.9 ± 15.2	3.12E+4 ± 6.09E+3	2.09E+4 ± 4.07E+3	2.74
87	84.902779	-69.771532	0.137	13.0 ± 0.971	2.13E+1 ± 1.59E+0	1.32E+1 ± 9.87E-1	0.288
88	84.902957	-69.769210	0.168	23.6 ± 1.12	5.18E+1 ± 2.46E+0	3.30E+1 ± 1.57E+0	0.411
89	84.901879	-69.765511	0.266	18.8 ± 1.75	1.00E+2 ± 9.37E+0	2.30E+2 ± 2.15E+1	0.863
90	84.899983	-69.761273	1.79	87.9 ± 12.1	2.24E+4 ± 3.08E+3	5.43E+3 ± 7.47E+2	1.61
91	84.899189	-69.769815	0.265	26.8 ± 1.81	1.53E+2 ± 1.03E+1	5.98E+1 ± 4.03E+0	0.440
92	84.913830	-69.769140	0.397	15.2 ± 2.56	1.73E+2 ± 2.91E+1	1.69E+2 ± 2.84E+1	0.605
93	84.901757	-69.761057	1.33	79.6 ± 8.68	1.04E+4 ± 1.14E+3	3.83E+3 ± 4.18E+2	1.57
94	84.914479	-69.772659	0.282	12.3 ± 1.97	8.36E+1 ± 1.34E+1	1.35E+2 ± 2.16E+1	0.642
95	84.899295	-69.771433	0.516	15.6 ± 3.01	2.46E+2 ± 4.75E+1	1.78E+2 ± 3.45E+1	0.545
96	84.902296	-69.760867	1.16	78.9 ± 7.89	8.53E+3 ± 8.53E+2	3.27E+3 ± 3.27E+2	1.56
97	84.886900	-69.772291	0.354	9.02 ± 2.60	1.06E+2 ± 3.07E+1	1.81E+2 ± 5.22E+1	0.662
98	84.924090	-69.769099	1.13	88.3 ± 7.96	9.72E+3 ± 8.76E+2	4.49E+3 ± 4.05E+2	1.85
99	84.904382	-69.760200	0.595	113 ± 4.62	4.19E+3 ± 1.71E+2	1.79E+3 ± 7.33E+1	1.61
100	84.894562	-69.767205	0.152	7.72 ± 1.06	1.50E+1 ± 2.06E+0	8.37E+0 ± 1.15E+0	0.218
101	84.890217	-69.771945	0.317	8.96 ± 2.25	7.85E+1 ± 1.97E+1	7.81E+1 ± 1.96E+1	0.460
102	84.910270	-69.771237	0.596	15.1 ± 3.55	3.32E+2 ± 7.80E+1	5.48E+1 ± 1.29E+1	0.281
103	84.910449	-69.771083	0.489	15.2 ± 2.75	2.01E+2 ± 3.63E+1	3.90E+1 ± 7.05E+0	0.262
104	84.903863	-69.766666	0.420	5.21 ± 2.61	6.16E+1 ± 3.08E+1	6.37E+1 ± 3.19E+1	0.361
105	84.900213	-69.766295	0.155	3.97 ± 1.05	7.65E+0 ± 2.03E+0	5.46E+0 ± 1.45E+0	0.174
106	84.896834	-69.766041	0.587	36.4 ± 3.64	8.40E+2 ± 8.39E+1	2.10E+2 ± 2.10E+1	0.555
107	84.903985	-69.775229	0.414	17.9 ± 2.69	2.25E+2 ± 3.37E+1	1.01E+2 ± 1.51E+1	0.458
108	84.904161	-69.774685	0.789	16.0 ± 3.50	3.40E+2 ± 7.42E+1	1.67E+2 ± 3.65E+1	0.427
109	84.905490	-69.771204	0.463	32.9 ± 2.74	4.31E+2 ± 3.59E+1	1.07E+2 ± 8.90E+0	0.445
110	84.924104	-69.769447	0.845	102 ± 6.31	7.04E+3 ± 4.37E+2	3.34E+3 ± 2.07E+2	1.84
111	84.924175	-69.769528	0.794	104 ± 5.90	6.28E+3 ± 3.58E+2	2.97E+3 ± 1.69E+2	1.79
112	84.898869	-69.762096	0.969	39.7 ± 5.62	2.18E+3 ± 3.08E+2	1.29E+3 ± 1.83E+2	1.07
113	84.879946	-69.768098	0.414	7.76 ± 2.91	1.14E+2 ± 4.27E+1	1.70E+2 ± 6.36E+1	0.594
114	84.924791	-69.773331	0.284	10.5 ± 1.99	7.26E+1 ± 1.38E+1	6.10E+1 ± 1.16E+1	0.430
115	84.910083	-69.772074	0.167	11.5 ± 1.07	2.31E+1 ± 2.16E+0	6.19E+0 ± 5.77E-1	0.179
116	84.907413	-69.770828	0.150	24.1 ± 1.02	4.35E+1 ± 1.84E+0	9.20E+0 ± 3.88E-1	0.230
117	84.883081	-69.770049	0.322	6.97 ± 2.04	5.04E+1 ± 1.47E+1	2.33E+2 ± 6.83E+1	0.789
118	84.924547	-69.769949	0.513	149 ± 3.79	3.73E+3 ± 9.46E+1	1.79E+3 ± 4.54E+1	1.73
119	84.913103	-69.765738	0.191	6.75 ± 1.40	2.30E+1 ± 4.75E+0	2.71E+1 ± 5.62E+0	0.350
120	84.906335	-69.757105	1.27	57.7 ± 8.58	7.38E+3 ± 1.10E+3	1.21E+4 ± 1.81E+3	2.87
121	84.904507	-69.773565	0.392	13.1 ± 2.21	1.10E+2 ± 1.87E+1	4.17E+1 ± 7.05E+0	0.303
122	84.904880	-69.771267	0.278	30.0 ± 1.84	1.77E+2 ± 1.09E+1	2.78E+1 ± 1.71E+0	0.294
123	84.888456	-69.769953	0.236	8.37 ± 1.50	3.29E+1 ± 5.91E+0	2.08E+1 ± 3.73E+0	0.275

Continued on next page

Table D.1 – continued from previous page

Clump ID	RA	Dec	Radius [pc]	$F_{^{12}CO}$ [K km s^{-1}]	Total Mass [M$_\odot$]	Virial Mass [M$_\odot$]	Linewidth [km/s]
124	84.903757	-69.772251	0.184	24.7 ± 1.21	6.32E+1 ± 3.11E+0	1.57E+1 ± 7.70E-1	0.271
125	84.881636	-69.766682	0.298	11.2 ± 2.24	9.70E+1 ± 1.94E+1	1.50E+2 ± 3.01E+1	0.659
126	84.885575	-69.764346	0.371	16.5 ± 2.72	2.11E+2 ± 3.48E+1	6.99E+1 ± 1.15E+1	0.403
127	84.894010	-69.762465	0.781	42.5 ± 4.76	1.67E+3 ± 1.87E+2	5.74E+2 ± 6.43E+1	0.795
128	84.906923	-69.757090	1.10	56.4 ± 6.65	4.33E+3 ± 5.11E+2	7.24E+3 ± 8.54E+2	2.38
129	84.905152	-69.757586	0.666	59.6 ± 3.86	1.54E+3 ± 9.99E+1	1.24E+3 ± 8.04E+1	1.27
130	84.906637	-69.757100	1.13	57.1 ± 7.43	5.48E+3 ± 7.13E+2	1.09E+4 ± 1.42E+3	2.87
131	84.906703	-69.757119	1.02	48.8 ± 5.92	2.98E+3 ± 3.61E+2	7.08E+3 ± 8.58E+2	2.44
132	84.894774	-69.761762	0.377	32.0 ± 2.42	3.25E+2 ± 2.46E+1	3.03E+2 ± 2.29E+1	0.832
133	84.906633	-69.757234	0.894	52.7 ± 5.34	2.61E+3 ± 2.65E+2	5.61E+3 ± 5.68E+2	2.32
134	84.902801	-69.764146	0.179	8.01 ± 1.29	2.33E+1 ± 3.76E+0	1.86E+1 ± 3.01E+0	0.299
135	84.906282	-69.757099	1.30	56.5 ± 8.72	7.47E+3 ± 1.15E+3	1.24E+4 ± 1.91E+3	2.86
136	84.881908	-69.757874	1.45	31.3 ± 9.62	5.04E+3 ± 1.55E+3	5.57E+3 ± 1.71E+3	1.82
137	84.896895	-69.773404	0.358	8.57 ± 2.44	8.88E+1 ± 2.53E+1	1.45E+2 ± 4.12E+1	0.590
138	84.891850	-69.769039	0.258	18.1 ± 1.80	1.02E+2 ± 1.02E+1	3.32E+1 ± 3.30E+0	0.332
139	84.889633	-69.767663	0.577	30.0 ± 3.64	6.92E+2 ± 8.41E+1	2.87E+2 ± 3.49E+1	0.654
140	84.893111	-69.763369	0.462	37.8 ± 2.55	4.29E+2 ± 2.90E+1	1.79E+2 ± 1.21E+1	0.578
141	84.882702	-69.757507	1.28	28.1 ± 7.87	3.02E+3 ± 8.46E+2	4.63E+3 ± 1.30E+3	1.77
142	84.892855	-69.773277	0.356	17.6 ± 2.54	1.98E+2 ± 2.86E+1	1.67E+2 ± 2.42E+1	0.636
143	84.887365	-69.769343	0.242	5.15 ± 1.69	2.54E+1 ± 8.32E+0	1.29E+1 ± 4.24E+0	0.215
144	84.893571	-69.765008	1.30	23.2 ± 7.96	2.56E+3 ± 8.77E+2	5.62E+3 ± 1.93E+3	1.93
145	84.896767	-69.756864	0.477	32.4 ± 3.43	6.62E+2 ± 7.02E+1	4.99E+2 ± 5.29E+1	0.949
146	84.881643	-69.754565	0.278	8.14 ± 1.94	5.32E+1 ± 1.27E+1	7.98E+1 ± 1.90E+1	0.497
147	84.885080	-69.753394	0.484	16.5 ± 3.53	3.57E+2 ± 7.64E+1	3.03E+2 ± 6.50E+1	0.735
148	84.899607	-69.766600	0.182	10.6 ± 1.23	2.78E+1 ± 3.22E+0	1.30E+1 ± 1.51E+0	0.248
149	84.900296	-69.764601	0.278	10.6 ± 1.98	7.19E+1 ± 1.34E+1	5.04E+1 ± 9.43E+0	0.395
150	84.883350	-69.757546	0.807	26.7 ± 4.87	1.10E+3 ± 2.00E+2	3.30E+3 ± 6.03E+2	1.88
151	84.889137	-69.770089	0.174	10.1 ± 1.15	2.32E+1 ± 2.64E+0	1.69E+1 ± 1.92E+0	0.288
152	84.892672	-69.764929	0.495	32.5 ± 2.74	4.25E+2 ± 3.59E+1	1.09E+2 ± 9.23E+0	0.436
153	84.904765	-69.771898	0.616	42.6 ± 3.75	1.04E+3 ± 9.17E+1	1.15E+3 ± 1.01E+2	1.27
154	84.904884	-69.771780	0.486	43.4 ± 3.09	7.19E+2 ± 5.13E+1	3.74E+2 ± 2.66E+1	0.813
155	84.882920	-69.763696	0.221	10.4 ± 1.58	4.54E+1 ± 6.91E+0	4.43E+1 ± 6.74E+0	0.415
156	84.893292	-69.765021	1.17	24.2 ± 7.34	2.27E+3 ± 6.87E+2	3.93E+3 ± 1.19E+3	1.70
157	84.898802	-69.759000	0.294	11.0 ± 1.74	5.75E+1 ± 9.11E+0	2.94E+1 ± 4.65E+0	0.293
158	84.884288	-69.755807	0.469	17.1 ± 2.98	2.63E+2 ± 4.58E+1	1.48E+2 ± 2.58E+1	0.521
159	84.901548	-69.754394	0.896	21.7 ± 5.55	1.16E+3 ± 2.98E+2	6.38E+3 ± 1.64E+3	2.48
160	84.903822	-69.753683	0.506	22.6 ± 3.17	3.95E+2 ± 5.55E+1	2.54E+2 ± 3.56E+1	0.657
161	84.924531	-69.771510	0.253	18.0 ± 1.70	9.09E+1 ± 8.58E+0	3.86E+1 ± 3.64E+0	0.362

Continued on next page

APPENDIX D. 12CO AND 13CO CLUMPS IDENTIFIED USING ASTRODENDRO IN THE N159 REGION OF THE LMC

Table D.1 – continued from previous page

Clump ID	RA	Dec	Radius [pc]	$F_{^{12}CO}$ [K km s^{-1}]	Total Mass [$M_\odot$]	Virial Mass [$M_\odot$]	Linewidth [km/s]
162	84.897151	-69.766432	0.567	10.6 ± 2.79	1.43E+2 ± 3.80E+1	2.31E+2 ± 6.11E+1	0.592
163	84.900267	-69.751214	0.462	6.56 ± 2.93	9.79E+1 ± 4.38E+1	9.47E+1 ± 4.23E+1	0.420
164	84.883093	-69.764460	0.444	13.5 ± 2.69	1.70E+2 ± 3.40E+1	2.78E+2 ± 5.54E+1	0.733
165	84.874176	-69.760093	0.393	6.40 ± 2.69	8.05E+1 ± 3.38E+1	4.50E+1 ± 1.89E+1	0.314
166	84.913677	-69.763757	0.629	13.8 ± 3.42	2.81E+2 ± 6.98E+1	2.21E+2 ± 5.48E+1	0.550
167	84.896390	-69.754441	0.700	27.2 ± 4.12	8.02E+2 ± 1.21E+2	3.93E+2 ± 5.95E+1	0.695
168	84.886012	-69.763044	0.188	8.52 ± 1.41	2.93E+1 ± 4.84E+0	2.74E+1 ± 4.52E+0	0.354
169	84.897244	-69.754916	0.375	29.7 ± 2.49	3.19E+2 ± 2.67E+1	1.00E+2 ± 8.41E+0	0.480
170	84.895711	-69.753764	0.371	12.2 ± 2.20	1.03E+2 ± 1.85E+1	1.63E+2 ± 2.92E+1	0.614
171	84.935598	-69.765138	0.289	7.74 ± 2.07	5.79E+1 ± 1.55E+1	4.65E+1 ± 1.25E+1	0.372
172	84.896577	-69.764089	0.303	14.8 ± 2.04	1.07E+2 ± 1.47E+1	7.54E+1 ± 1.04E+1	0.463
173	84.892942	-69.764899	1.01	26.4 ± 6.41	1.89E+3 ± 4.58E+2	2.55E+3 ± 6.19E+2	1.48
174	84.892865	-69.764933	0.937	27.3 ± 6.18	1.81E+3 ± 4.10E+2	2.31E+3 ± 5.23E+2	1.46
175	84.908071	-69.760517	0.153	13.9 ± 1.11	2.98E+1 ± 2.39E+0	1.93E+1 ± 1.55E+0	0.329
176	84.908043	-69.758131	0.157	29.7 ± 1.18	7.18E+1 ± 2.85E+0	4.59E+1 ± 1.82E+0	0.501
177	84.914154	-69.751624	0.714	11.9 ± 4.42	4.05E+2 ± 1.50E+2	1.05E+3 ± 3.90E+2	1.13
178	84.905138	-69.750862	0.286	11.4 ± 2.18	9.45E+1 ± 1.81E+1	1.83E+2 ± 3.50E+1	0.743
179	84.929828	-69.768904	0.239	6.34 ± 1.75	3.39E+1 ± 9.37E+0	2.95E+1 ± 8.18E+0	0.326
180	84.895478	-69.765556	0.425	27.8 ± 2.95	4.20E+2 ± 4.46E+1	1.94E+2 ± 2.06E+1	0.626
181	84.905621	-69.752296	0.499	13.6 ± 3.45	2.82E+2 ± 7.14E+1	7.19E+2 ± 1.82E+2	1.11
182	84.910169	-69.764663	0.624	11.5 ± 3.96	3.12E+2 ± 1.08E+2	1.29E+3 ± 4.46E+2	1.33
183	84.907435	-69.764352	0.330	8.19 ± 2.06	6.04E+1 ± 1.52E+1	6.38E+1 ± 1.61E+1	0.408
184	84.906341	-69.752637	0.279	9.35 ± 1.82	5.40E+1 ± 1.05E+1	5.04E+1 ± 9.83E+0	0.395
185	84.916754	-69.770172	0.830	30.0 ± 5.06	1.34E+3 ± 2.25E+2	1.14E+3 ± 1.93E+2	1.09
186	84.922816	-69.768486	0.431	33.9 ± 2.63	4.09E+2 ± 3.18E+1	1.37E+2 ± 1.06E+1	0.523
187	84.925142	-69.767226	0.336	32.4 ± 2.42	3.29E+2 ± 2.46E+1	1.60E+2 ± 1.20E+1	0.640
188	84.931243	-69.761027	0.536	10.7 ± 3.53	2.33E+2 ± 7.67E+1	2.36E+2 ± 7.80E+1	0.616
189	84.923893	-69.765557	0.470	13.3 ± 2.59	1.54E+2 ± 3.01E+1	1.15E+2 ± 2.25E+1	0.460
190	84.882941	-69.763504	0.413	12.9 ± 2.77	1.71E+2 ± 3.68E+1	1.35E+2 ± 2.90E+1	0.530
191	84.900515	-69.756932	0.325	21.1 ± 2.11	1.63E+2 ± 1.63E+1	1.01E+2 ± 1.01E+1	0.516
192	84.902975	-69.771095	0.291	26.5 ± 2.06	1.95E+2 ± 1.51E+1	8.90E+1 ± 6.91E+0	0.512
193	84.917535	-69.769543	0.217	15.6 ± 1.52	6.28E+1 ± 6.10E+0	2.07E+1 ± 2.01E+0	0.287
194	84.911097	-69.767154	0.501	10.6 ± 3.13	1.80E+2 ± 5.32E+1	3.18E+2 ± 9.37E+1	0.739
195	84.917925	-69.762260	0.659	15.1 ± 3.94	4.07E+2 ± 1.06E+2	5.44E+2 ± 1.42E+2	0.843
196	84.878951	-69.759935	0.361	11.9 ± 2.50	1.29E+2 ± 2.70E+1	1.10E+2 ± 2.32E+1	0.512
197	84.904771	-69.772500	0.198	35.4 ± 1.45	1.30E+2 ± 5.32E+0	8.55E+1 ± 3.51E+0	0.609
198	84.928739	-69.770465	0.172	15.5 ± 1.19	3.81E+1 ± 2.92E+0	2.11E+1 ± 1.62E+0	0.325
199	84.916964	-69.770429	0.429	30.3 ± 2.63	3.63E+2 ± 3.15E+1	3.58E+2 ± 3.10E+1	0.847

Continued on next page

Table D.1 – continued from previous page

Clump ID	RA	Dec	Radius [pc]	$F_{^{12}CO}$ [K km s^{-1}]	Total Mass [$M_\odot$]	Virial Mass [$M_\odot$]	Linewidth [km/s]
200	84.912709	-69.769066	0.299	9.43 ± 2.15	7.57E+1 ± 1.73E+1	1.02E+2 ± 2.32E+1	0.541
201	84.912211	-69.767119	0.218	9.70 ± 1.57	4.17E+1 ± 6.77E+0	4.36E+1 ± 7.07E+0	0.415
202	84.910949	-69.764751	0.453	11.2 ± 3.33	2.17E+2 ± 6.45E+1	5.39E+2 ± 1.60E+2	1.01
203	84.929837	-69.765203	0.169	5.63 ± 1.13	1.25E+1 ± 2.50E+0	8.40E+0 ± 1.68E+0	0.207
204	84.921635	-69.763803	0.422	11.0 ± 2.49	1.18E+2 ± 2.69E+1	6.26E+1 ± 1.42E+1	0.357
205	84.918758	-69.762608	0.865	14.0 ± 4.66	5.28E+2 ± 1.76E+2	6.20E+2 ± 2.07E+2	0.785
206	84.909035	-69.756641	0.484	40.0 ± 3.57	8.87E+2 ± 7.91E+1	7.43E+2 ± 6.63E+1	1.15
207	84.905314	-69.752129	0.297	15.2 ± 2.14	1.21E+2 ± 1.71E+1	1.65E+2 ± 2.32E+1	0.691
208	84.885047	-69.760976	0.416	20.8 ± 2.69	2.62E+2 ± 3.38E+1	2.69E+2 ± 3.48E+1	0.746
209	84.907207	-69.755980	0.431	24.8 ± 2.40	2.48E+2 ± 2.40E+1	1.39E+3 ± 1.34E+2	1.67
210	84.916941	-69.763631	0.288	18.5 ± 2.10	1.41E+2 ± 1.60E+1	1.93E+2 ± 2.19E+1	0.760
211	84.919313	-69.761065	0.380	16.4 ± 2.51	1.80E+2 ± 2.76E+1	4.31E+1 ± 6.60E+0	0.313
212	84.897220	-69.756132	0.208	12.0 ± 1.43	4.25E+1 ± 5.06E+0	1.99E+1 ± 2.36E+0	0.286
213	84.914498	-69.755158	0.474	26.9 ± 2.90	3.93E+2 ± 4.25E+1	1.72E+2 ± 1.86E+1	0.559
214	84.900097	-69.754780	0.557	20.5 ± 3.53	4.42E+2 ± 7.63E+1	1.18E+3 ± 2.03E+2	1.35
215	84.914055	-69.771409	0.238	11.8 ± 1.84	6.92E+1 ± 1.08E+1	8.52E+1 ± 1.33E+1	0.555
216	84.892045	-69.764734	0.776	25.8 ± 5.39	1.30E+3 ± 2.72E+2	4.59E+2 ± 9.58E+1	0.714
217	84.889174	-69.764910	0.201	10.4 ± 1.48	3.97E+1 ± 5.69E+0	3.35E+1 ± 4.80E+0	0.378
218	84.895942	-69.758298	0.540	29.7 ± 4.02	8.37E+2 ± 1.13E+2	3.64E+2 ± 4.92E+1	0.761
219	84.909815	-69.767274	0.211	11.4 ± 1.54	4.71E+1 ± 6.38E+0	4.07E+1 ± 5.51E+0	0.407
220	84.881006	-69.762237	0.408	10.6 ± 2.57	1.21E+2 ± 2.95E+1	7.17E+1 ± 1.74E+1	0.389
221	84.892225	-69.764739	0.714	26.5 ± 4.85	1.08E+3 ± 1.98E+2	3.37E+2 ± 6.16E+1	0.637
222	84.913119	-69.761418	0.277	16.9 ± 1.90	1.06E+2 ± 1.19E+1	6.63E+1 ± 7.46E+0	0.454
223	84.900586	-69.754653	0.380	19.1 ± 2.49	2.05E+2 ± 2.68E+1	5.61E+2 ± 7.33E+1	1.13
224	84.920546	-69.769121	0.168	9.06 ± 1.19	2.25E+1 ± 2.96E+0	1.62E+1 ± 2.13E+0	0.288
225	84.908054	-69.752847	0.257	10.8 ± 1.99	7.38E+1 ± 1.36E+1	9.71E+1 ± 1.79E+1	0.570
226	84.922705	-69.769488	0.177	26.7 ± 1.19	6.56E+1 ± 2.92E+0	3.21E+1 ± 1.43E+0	0.395
227	84.895915	-69.763102	0.202	4.64 ± 1.33	1.43E+1 ± 4.08E+0	5.48E+0 ± 1.57E+0	0.153
228	84.912541	-69.754547	0.241	12.1 ± 1.65	5.76E+1 ± 7.86E+0	2.66E+1 ± 3.63E+0	0.308
229	84.888054	-69.759456	0.487	13.5 ± 3.028	2.15E+2 ± 4.82E+1	3.54E+2 ± 7.95E+1	0.790
230	84.892191	-69.762758	0.299	11.3 ± 2.01	7.89E+1 ± 1.41E+1	3.41E+1 ± 6.08E+0	0.313
231	84.890139	-69.766512	0.373	8.52 ± 2.53	9.48E+1 ± 2.81E+1	5.13E+1 ± 1.52E+1	0.344
232	84.883445	-69.765426	0.282	7.92 ± 1.91	5.03E+1 ± 1.21E+1	2.85E+1 ± 6.87E+0	0.295
233	84.879068	-69.761305	0.242	8.85 ± 1.72	4.53E+1 ± 8.79E+0	3.49E+1 ± 6.76E+0	0.352
234	84.890327	-69.767668	0.365	5.09 ± 2.11	3.93E+1 ± 1.63E+1	6.38E+1 ± 2.64E+1	0.388
235	84.895435	-69.763829	0.236	11.4 ± 1.69	5.67E+1 ± 8.37E+0	4.43E+1 ± 6.53E+0	0.401
236	84.898096	-69.755278	0.277	10.5 ± 1.64	4.91E+1 ± 7.70E+0	6.24E+1 ± 9.77E+0	0.440
237	84.904953	-69.757224	0.741	23.2 ± 4.03	6.54E+2 ± 1.14E+2	2.36E+2 ± 4.10E+1	0.524

Continued on next page

APPENDIX D. 12CO AND 13CO CLUMPS IDENTIFIED USING ASTRODENDRO IN THE N159 REGION OF THE LMC

Table D.1 – continued from previous page

Clump ID	RA	Dec	Radius	$F_{^{12}CO}$	Total Mass	Virial Mass	Linewidth
			[pc]	[K km s^{-1}]	[$M_\odot$]	[$M_\odot$]	[km/s]

Column 1: The ID we give each clump. Column 4: The radius calculated from the area of the clump. Column 6: The total H_2 mass. We assumed the typical ^{12}CO(2-1)/^{12}CO(1-0) ratio toward HII regions of 0.85 (Nishimura et al., 2015). We use a X_{CO} conversion factor of 7×10^{20} cm^{-2} (Fukui et al., 2008). Column 7: The virial mass calculated by assuming the virial parameter equals 1. Column 8: The measured linewidth.

APPENDIX D. 12CO AND 13CO CLUMPS IDENTIFIED USING ASTRODENDRO IN THE N159 REGION OF THE LMC

Table D.2: Mass Derived from N159E ^{12}CO (2-1) Clumps

Clump ID	RA	Dec	Radius	$F_{^{12}CO}$	Total Mass	Virial Mass	Linewidth
			[pc]	[K km s^{-1}]	[$M_\odot$]	[$M_\odot$]	[km/s]
0	85.059829	-69.749680	2.64	49.1 ± 25.2	2.41E+4 ± 1.23E+4	2.45E+4 ± 1.25E+4	2.82
1	85.058511	-69.750182	2.27	51.9 ± 22.0	1.94E+4 ± 8.20E+3	1.17E+4 ± 4.94E+3	2.10
2	85.058478	-69.750198	2.24	49.9 ± 21.6	1.79E+4 ± 7.77E+3	1.07E+4 ± 4.63E+3	2.03
3	85.052824	-69.747740	0.206	20.3 ± 2.25	7.95E+1 ± 8.81E+0	3.65E+1 ± 4.05E+0	0.390
4	85.058040	-69.750242	2.12	47.4 ± 20.4	1.52E+4 ± 6.55E+3	8.35E+3 ± 3.59E+3	1.84
5	85.028038	-69.744350	6.78	54.4 ± 45.0	8.49E+4 ± 7.02E+4	4.88E+4 ± 4.03E+4	2.49
6	85.027992	-69.744344	6.77	54.3 ± 44.8	8.39E+4 ± 6.92E+4	4.86E+4 ± 4.01E+4	2.48
7	85.027841	-69.744249	6.68	54.3 ± 43.7	7.97E+4 ± 6.41E+4	4.79E+4 ± 3.85E+4	2.48
8	85.028052	-69.744284	6.71	53.8 ± 44.3	8.16E+4 ± 6.72E+4	4.82E+4 ± 3.97E+4	2.49
9	85.023251	-69.741295	3.64	68.0 ± 25.4	3.39E+4 ± 1.27E+4	3.19E+4 ± 1.19E+4	2.75
10	85.023726	-69.744563	5.76	56.5 ± 39.0	6.63E+4 ± 4.57E+4	4.12E+4 ± 2.85E+4	2.48
11	85.023131	-69.741396	3.54	68.4 ± 24.7	3.22E+4 ± 1.16E+4	2.89E+4 ± 1.05E+4	2.65
12	85.057545	-69.750466	1.74	42.7 ± 16.5	8.93E+3 ± 3.44E+3	6.37E+3 ± 2.45E+3	1.77
13	85.022382	-69.741438	3.40	66.2 ± 22.7	2.64E+4 ± 9.06E+3	2.51E+4 ± 8.62E+3	2.52
14	85.024244	-69.748032	4.17	47.6 ± 29.4	3.17E+4 ± 1.96E+4	2.23E+4 ± 1.38E+4	2.14
15	85.024744	-69.747939	4.09	46.9 ± 28.4	2.92E+4 ± 1.77E+4	2.17E+4 ± 1.32E+4	2.14
16	85.025724	-69.747589	3.81	51.1 ± 26.0	2.66E+4 ± 1.36E+4	2.03E+4 ± 1.04E+4	2.14
17	85.025192	-69.747845	4.02	48.3 ± 27.5	2.81E+4 ± 1.60E+4	2.11E+4 ± 1.20E+4	2.13
18	85.033943	-69.741796	1.67	37.6 ± 9.5	2.63E+3 ± 6.65E+2	2.91E+3 ± 7.37E+2	1.23
19	85.025415	-69.747472	3.70	51.0 ± 24.2	2.30E+4 ± 1.09E+4	2.01E+4 ± 9.54E+3	2.16
20	85.025455	-69.747436	3.69	51.0 ± 23.7	2.21E+4 ± 1.03E+4	1.98E+4 ± 9.19E+3	2.15
21	85.030736	-69.746348	2.91	44.8 ± 18.8	1.22E+4 ± 5.12E+3	1.45E+4 ± 6.07E+3	2.07
22	85.028993	-69.745930	2.03	43.7 ± 17.1	9.82E+3 ± 3.83E+3	1.13E+4 ± 4.42E+3	2.19
23	85.033485	-69.743753	0.31	31.1 ± 3.27	2.56E+2 ± 2.69E+1	2.48E+2 ± 2.61E+1	0.830
24	85.015082	-69.749503	1.26	51.1 ± 12.0	5.68E+3 ± 1.33E+3	4.68E+3 ± 1.10E+3	1.78
25	84.996467	-69.750066	0.143	6.2 ± 1.34	8.59E+0 ± 1.87E+0	4.15E+0 ± 9.05E-1	0.158
26	85.019834	-69.741658	2.04	70.1 ± 18.3	1.81E+4 ± 4.71E+3	1.19E+4 ± 3.09E+3	2.23
27	85.020769	-69.749786	0.323	34.5 ± 3.40	3.08E+2 ± 3.03E+1	3.55E+2 ± 3.50E+1	0.973
28	85.014685	-69.749417	1.03	50.3 ± 10.1	3.97E+3 ± 7.99E+2	3.40E+3 ± 6.85E+2	1.68
29	85.019148	-69.742185	1.71	72.8 ± 16.1	1.45E+4 ± 3.19E+3	6.72E+3 ± 1.48E+3	1.84
30	85.019089	-69.742285	1.63	74.3 ± 15.5	1.37E+4 ± 2.85E+3	5.86E+3 ± 1.22E+3	1.76
31	85.019104	-69.742439	1.45	79.6 ± 14.3	1.25E+4 ± 2.25E+3	5.02E+3 ± 9.01E+2	1.72
32	85.030160	-69.742863	0.497	64.9 ± 5.17	1.34E+3 ± 1.07E+2	8.69E+2 ± 6.92E+1	1.23
33	85.019071	-69.742667	1.22	93.6 ± 11.9	1.02E+4 ± 1.29E+3	3.99E+3 ± 5.07E+2	1.68
34	85.049734	-69.742497	2.44	40.1 ± 19.9	1.22E+4 ± 6.07E+3	1.59E+4 ± 7.88E+3	2.37
35	85.049144	-69.742767	2.32	37.3 ± 18.0	9.37E+3 ± 4.53E+3	1.53E+4 ± 7.41E+3	2.39
36	85.054567	-69.754787	0.144	7.24 ± 1.39	1.08E+1 ± 2.08E+0	1.66E+0 ± 3.20E-1	0.100

Continued on next page

Table D.2 – continued from previous page

Clump ID	RA	Dec	Radius [pc]	$F_{^{12}CO}$ [K km s^{-1}]	Total Mass [$M_\odot$]	Virial Mass [$M_\odot$]	Linewidth [km/s]
37	85.005565	-69.754189	0.344	8.37 ± 2.81	5.11E+1 ± 1.72E+1	3.65E+1 ± 1.23E+1	0.302
38	85.024242	-69.750042	0.449	21.9 ± 3.87	2.52E+2 ± 4.46E+1	2.49E+2 ± 4.41E+1	0.691
39	84.996677	-69.749979	0.220	11.6 ± 2.27	4.59E+1 ± 9.02E+0	6.20E+1 ± 1.22E+1	0.492
40	85.028424	-69.745990	1.81	40.7 ± 15.5	7.57E+3 ± 2.89E+3	8.91E+3 ± 3.40E+3	2.06
41	85.003958	-69.751910	0.732	16.6 ± 6.76	5.86E+2 ± 2.38E+2	5.82E+2 ± 2.37E+2	0.827
42	85.003146	-69.752504	0.317	16.3 ± 3.24	1.32E+2 ± 2.63E+1	1.19E+2 ± 2.36E+1	0.568
43	85.047753	-69.749607	0.461	27.5 ± 4.25	3.84E+2 ± 5.93E+1	1.37E+2 ± 2.11E+1	0.505
44	85.042881	-69.747078	0.669	24.7 ± 6.36	7.72E+2 ± 1.98E+2	2.06E+3 ± 5.30E+2	1.63
45	85.043212	-69.747150	0.703	19.8 ± 5.34	4.36E+2 ± 1.18E+2	4.06E+2 ± 1.10E+2	0.705
46	85.034603	-69.745209	1.16	25.2 ± 8.14	1.29E+3 ± 4.15E+2	1.53E+3 ± 4.95E+2	1.07
47	85.028158	-69.746031	1.77	39.1 ± 15.0	6.75E+3 ± 2.59E+3	8.33E+3 ± 3.19E+3	2.01
48	85.035119	-69.748905	0.753	28.6 ± 6.73	9.99E+2 ± 2.35E+2	9.64E+2 ± 2.27E+2	1.05
49	85.076186	-69.745138	0.640	17.3 ± 5.80	4.49E+2 ± 1.50E+2	1.21E+3 ± 4.07E+2	1.28
50	85.036263	-69.739471	2.01	44.8 ± 15.4	8.15E+3 ± 2.80E+3	5.57E+3 ± 1.91E+3	1.54
51	85.076122	-69.744674	0.499	15.4 ± 4.89	2.85E+2 ± 9.03E+1	1.81E+2 ± 5.72E+1	0.558
52	85.076147	-69.744813	0.554	16.0 ± 5.14	3.25E+2 ± 1.05E+2	2.66E+2 ± 8.57E+1	0.643
53	85.076200	-69.744401	0.380	16.8 ± 3.64	1.71E+2 ± 3.72E+1	1.30E+2 ± 2.82E+1	0.542
54	85.014936	-69.752789	1.10	22.6 ± 8.88	1.37E+3 ± 5.40E+2	3.62E+3 ± 1.43E+3	1.68
55	85.004217	-69.751533	0.428	11.7 ± 4.04	1.47E+2 ± 5.08E+1	1.24E+2 ± 4.28E+1	0.499
56	85.039434	-69.744335	0.248	30.5 ± 2.62	1.62E+2 ± 1.39E+1	1.30E+2 ± 1.12E+1	0.671
57	85.018043	-69.745824	0.529	34.0 ± 5.00	6.56E+2 ± 9.65E+1	4.29E+2 ± 6.32E+1	0.836
58	84.999535	-69.751290	0.121	6.92 ± 1.18	7.37E+0 ± 1.25E+0	4.51E+0 ± 7.65E-1	0.179
59	85.026300	-69.743696	0.311	54.7 ± 3.56	5.35E+2 ± 3.48E+1	2.76E+2 ± 1.80E+1	0.874
60	85.076038	-69.745424	0.386	6.84 ± 3.12	5.13E+1 ± 2.34E+1	2.61E+1 ± 1.19E+1	0.241
61	85.006107	-69.753501	0.443	16.8 ± 4.62	2.77E+2 ± 7.62E+1	1.51E+2 ± 4.16E+1	0.542
62	84.997268	-69.750242	0.378	36.8 ± 3.94	4.40E+2 ± 4.71E+1	3.18E+2 ± 3.40E+1	0.850
63	85.004291	-69.754250	0.122	6.77 ± 1.14	6.79E+0 ± 1.15E+0	2.42E+0 ± 4.07E-1	0.131
64	85.028626	-69.749165	0.362	17.7 ± 3.67	1.84E+2 ± 3.80E+1	9.79E+1 ± 2.03E+1	0.482
65	85.001218	-69.751230	0.689	15.1 ± 6.50	4.92E+2 ± 2.12E+2	1.80E+3 ± 7.77E+2	1.50
66	85.076426	-69.746042	0.215	8.51 ± 2.15	3.03E+1 ± 7.66E+0	1.45E+1 ± 3.66E+0	0.241
67	85.026212	-69.746283	1.50	37.8 ± 12.07	4.24E+3 ± 1.35E+3	2.26E+3 ± 7.23E+2	1.14
68	85.051750	-69.740209	0.550	31.4 ± 5.38	7.01E+2 ± 1.20E+2	1.56E+3 ± 2.68E+2	1.56
69	85.039677	-69.748564	0.700	44.6 ± 7.41	1.89E+3 ± 3.14E+2	9.15E+2 ± 1.52E+2	1.06
70	85.065804	-69.747385	1.75	25.4 ± 14.40	4.06E+3 ± 2.30E+3	5.21E+3 ± 2.95E+3	1.60
71	84.997317	-69.750192	0.225	7.66 ± 2.12	2.65E+1 ± 7.33E+0	4.03E+0 ± 1.11E+0	0.124
72	85.072239	-69.748055	0.501	9.61 ± 4.13	1.26E+2 ± 5.43E+1	1.08E+2 ± 4.64E+1	0.431
73	85.016667	-69.738583	0.394	22.5 ± 3.62	2.27E+2 ± 3.65E+1	1.38E+2 ± 2.22E+1	0.548
74	85.002488	-69.752422	0.246	4.52 ± 1.96	1.33E+1 ± 5.77E+0	5.50E-2 ± 2.38E-2	0.014

Continued on next page

Table D.2 – continued from previous page

Clump ID	RA	Dec	Radius [pc]	$F_{^{12}CO}$ [K km s^{-1}]	Total Mass [$M_\odot$]	Virial Mass [$M_\odot$]	Linewidth [km/s]
75	85.042346	-69.747103	0.269	22.9 ± 2.92	1.50E+2 ± 1.91E+1	1.62E+2 ± 2.06E+1	0.720
76	85.052068	-69.755212	0.159	5.49 ± 1.44	8.78E+0 ± 2.30E+0	1.93E+0 ± 5.05E-1	0.102
77	85.003273	-69.736315	0.261	7.15 ± 2.50	3.45E+1 ± 1.21E+1	3.79E+1 ± 1.33E+1	0.353
78	84.996991	-69.750182	0.313	24.8 ± 3.11	1.84E+2 ± 2.31E+1	8.06E+1 ± 1.01E+1	0.470
79	85.076362	-69.746357	0.336	12.6 ± 3.00	8.73E+1 ± 2.08E+1	1.07E+2 ± 2.56E+1	0.524
80	85.017547	-69.740547	0.461	28.8 ± 4.27	4.04E+2 ± 5.99E+1	7.20E+1 ± 1.07E+1	0.366
81	85.003610	-69.752480	0.446	23.2 ± 4.75	4.04E+2 ± 8.29E+1	2.87E+2 ± 5.90E+1	0.744
82	84.997161	-69.750208	0.230	12.2 ± 2.00	3.77E+1 ± 6.19E+0	3.44E+0 ± 5.65E-1	0.113
83	85.013257	-69.756078	1.12	14.1 ± 9.04	8.89E+2 ± 5.70E+2	2.39E+3 ± 1.53E+3	1.35
84	84.996552	-69.750057	0.165	21.5 ± 1.68	4.67E+1 ± 3.64E+0	1.71E+1 ± 1.34E+0	0.299
85	85.045507	-69.749166	0.346	38.2 ± 3.70	4.02E+2 ± 3.89E+1	8.67E+1 ± 8.39E+0	0.464
86	85.076585	-69.746539	0.279	7.97 ± 2.40	3.54E+1 ± 1.07E+1	6.82E+1 ± 2.06E+1	0.459
87	85.070465	-69.740294	0.145	5.09 ± 1.37	7.40E+0 ± 2.00E+0	4.09E-1 ± 1.10E-1	0.049
88	85.009882	-69.756295	0.407	7.47 ± 3.53	7.19E+1 ± 3.40E+1	9.23E+1 ± 4.37E+1	0.441
89	85.009882	-69.756335	0.420	6.65 ± 3.36	5.77E+1 ± 2.91E+1	1.00E+2 ± 5.06E+1	0.453
90	85.015248	-69.755502	0.797	11.52 ± 5.39	2.58E+2 ± 1.21E+2	4.38E+2 ± 2.05E+2	0.687
91	85.065503	-69.747375	1.68	25.5 ± 13.6	3.66E+3 ± 1.95E+3	3.82E+3 ± 2.04E+3	1.40
92	85.072930	-69.747148	0.762	11.3 ± 5.70	2.84E+2 ± 1.43E+2	4.04E+2 ± 2.03E+2	0.675
93	85.034818	-69.740053	1.05	39.1 ± 8.73	2.30E+3 ± 5.14E+2	8.11E+2 ± 1.81E+2	0.816
94	85.001091	-69.737230	0.203	16.4 ± 2.37	7.14E+1 ± 1.03E+1	3.70E+1 ± 5.34E+0	0.396
95	85.011928	-69.756415	0.700	14.2 ± 7.11	5.53E+2 ± 2.77E+2	8.09E+2 ± 4.05E+2	0.997
96	85.009567	-69.756503	0.240	6.03 ± 2.02	1.90E+1 ± 6.38E+0	6.93E+0 ± 2.32E+0	0.157
97	85.064653	-69.747455	1.34	26.7 ± 11.7	2.82E+3 ± 1.24E+3	2.38E+3 ± 1.04E+3	1.24
98	85.025480	-69.737981	0.759	41.6 ± 6.30	1.28E+3 ± 1.93E+2	9.04E+2 ± 1.37E+2	1.01
99	85.052817	-69.751100	0.306	26.0 ± 3.30	2.19E+2 ± 2.77E+1	1.35E+2 ± 1.71E+1	0.616
100	85.076700	-69.746531	0.186	6.02 ± 1.72	1.37E+1 ± 3.90E+0	1.03E+1 ± 2.94E+0	0.218
101	85.002953	-69.737966	0.144	7.49 ± 1.48	1.26E+1 ± 2.48E+0	4.59E+0 ± 9.05E-1	0.166
102	85.017547	-69.737507	0.269	21.2 ± 2.87	1.35E+2 ± 1.83E+1	7.37E+1 ± 1.00E+1	0.486
103	85.011704	-69.734970	0.264	10.0 ± 2.69	5.59E+1 ± 1.51E+1	4.49E+1 ± 1.21E+1	0.383
104	85.068243	-69.751014	0.402	20.7 ± 4.23	2.85E+2 ± 5.83E+1	4.75E+2 ± 9.71E+1	1.01
105	85.012063	-69.756453	0.670	11.9 ± 6.24	3.58E+2 ± 1.87E+2	4.99E+2 ± 2.61E+2	0.800
106	85.032150	-69.737499	0.421	34.2 ± 3.83	3.86E+2 ± 4.32E+1	3.88E+2 ± 4.35E+1	0.891
107	85.016745	-69.735281	0.234	16.8 ± 2.65	9.11E+1 ± 1.43E+1	3.61E+1 ± 5.67E+0	0.364
108	85.076634	-69.747365	0.140	7.42 ± 1.33	1.02E+1 ± 1.83E+0	5.52E+0 ± 9.93E-1	0.184
109	85.012035	-69.756412	0.562	12.1 ± 5.22	2.55E+2 ± 1.10E+2	4.09E+2 ± 1.76E+2	0.791
110	85.042728	-69.752071	0.153	24.2 ± 1.72	5.55E+1 ± 3.96E+0	3.59E+1 ± 2.56E+0	0.449
111	85.048114	-69.755548	0.139	13.3 ± 1.53	2.40E+1 ± 2.76E+0	1.63E+1 ± 1.87E+0	0.317
112	85.008565	-69.756096	0.266	6.13 ± 2.23	2.35E+1 ± 8.54E+0	3.33E+1 ± 1.21E+1	0.328

Continued on next page

APPENDIX D. 12CO AND 13CO CLUMPS IDENTIFIED USING ASTRODENDRO IN THE N159 REGION OF THE LMC

Table D.2 – continued from previous page

Clump ID	RA	Dec	Radius [pc]	$F_{^{12}CO}$ [K km s^{-1}]	Total Mass [$M_\odot$]	Virial Mass [$M_\odot$]	Linewidth [km/s]
113	85.021673	-69.737511	0.240	24.9 ± 2.51	1.21E+2 ± 1.23E+1	5.28E+1 ± 5.34E+0	0.436
114	85.011322	-69.756953	0.274	5.75 ± 2.38	2.51E+1 ± 1.04E+1	1.30E+1 ± 5.39E+0	0.202
115	85.043305	-69.755487	0.220	21.0 ± 2.45	9.72E+1 ± 1.13E+1	2.83E+1 ± 3.30E+0	0.333
116	85.025682	-69.735951	0.382	32.1 ± 4.09	4.15E+2 ± 5.28E+1	3.48E+2 ± 4.43E+1	0.886
117	85.044056	-69.756383	0.258	9.90 ± 2.58	5.07E+1 ± 1.32E+1	2.47E+1 ± 6.42E+0	0.287
118	84.999686	-69.751209	0.213	7.41 ± 2.00	2.29E+1 ± 6.19E+0	6.85E+0 ± 1.85E+0	0.166
119	85.075133	-69.749400	0.284	9.45 ± 2.46	4.41E+1 ± 1.15E+1	8.91E+1 ± 2.32E+1	0.519
120	85.025265	-69.731896	0.207	5.74 ± 1.61	1.15E+1 ± 3.24E+0	4.53E+0 ± 1.27E+0	0.137
121	85.041726	-69.754449	0.281	25.3 ± 3.15	1.94E+2 ± 2.40E+1	1.17E+2 ± 1.45E+1	0.597
122	85.072220	-69.749588	0.326	16.1 ± 3.34	1.38E+2 ± 2.86E+1	7.85E+1 ± 1.62E+1	0.455
123	85.070166	-69.747871	0.276	26.8 ± 3.08	1.96E+2 ± 2.25E+1	1.63E+2 ± 1.86E+1	0.712
124	85.025658	-69.731884	0.146	4.81 ± 1.38	7.10E+0 ± 2.04E+0	3.04E-1 ± 8.75E-2	0.042
125	85.006931	-69.755881	0.258	7.67 ± 2.23	2.94E+1 ± 8.54E+0	2.16E+1 ± 6.28E+0	0.268

Column 1: The ID we give each clump. Column 4: The radius calculated from the area of the clump. Column 6: The total H_2 mass. We assumed the typical ^{12}CO(2-1)/^{12}CO(1-0) ratio toward HII regions of 0.85 (Nishimura et al., 2015). We use a X_{CO} conversion factor of 7×10^{20} cm^{-2} (Fukui et al., 2008). Column 7: The virial mass calculated by assuming the virial parameter equals 1. Column 8: The measured linewidth.

APPENDIX D. 12CO AND 13CO CLUMPS IDENTIFIED USING ASTRODENDRO IN THE N159 REGION OF THE LMC

Table D.3: Column Densities and Mass Derived from N159W ^{13}CO (2-1) Clumps

Clump ID	RA	Dec	Radius [pc]	$N_{^{13}CO}$ [cm^{-2}]	Total H_2 Mass [$M_\odot$]	Virial Mass [$M_\odot$]	Linewidth [km/s]
0	84.904807	-69.769414	1.12	1.38E+16	1.57E+3 ± 7.40E+2	8.73E+2 ± 4.13E+2	0.732
1	84.907429	-69.769590	0.366	1.84E+16	6.70E+2 ± 1.35E+2	2.20E+2 ± 4.43E+1	0.643
2	84.902543	-69.769225	0.619	1.17E+16	8.03E+2 ± 3.50E+2	3.09E+2 ± 1.35E+2	0.586
3	84.908195	-69.772436	0.810	6.95E+15	5.49E+2 ± 4.30E+2	1.10E+3 ± 8.59E+2	0.964
4	84.910940	-69.773204	0.325	9.36E+15	2.26E+2 ± 7.29E+1	1.17E+2 ± 3.77E+1	0.498
5	84.910832	-69.773152	0.275	6.90E+15	9.06E+1 ± 2.92E+1	2.67E+1 ± 8.62E+0	0.258
6	84.903995	-69.769022	0.394	1.09E+16	2.63E+2 ± 7.26E+1	1.98E+2 ± 5.45E+1	0.587
7	84.895716	-69.769467	0.207	4.39E+15	2.71E+1 ± 9.40E+0	2.15E+1 ± 7.45E+0	0.267
8	84.899779	-69.769674	0.274	8.18E+15	1.36E+2 ± 4.14E+1	3.65E+1 ± 1.11E+1	0.303
9	84.901012	-69.759896	2.32	3.89E+16	4.30E+4 ± 2.26E+4	1.72E+4 ± 9.01E+3	2.25
10	84.901015	-69.759914	2.31	3.91E+16	4.22E+4 ± 2.18E+4	1.70E+4 ± 8.76E+3	2.25
11	84.901183	-69.759937	2.22	4.01E+16	3.67E+4 ± 1.70E+4	1.50E+4 ± 6.98E+3	2.16
12	84.901108	-69.759946	2.26	3.86E+16	3.81E+4 ± 1.90E+4	1.58E+4 ± 7.86E+3	2.19
13	84.901096	-69.759945	2.26	3.84E+16	3.83E+4 ± 1.93E+4	1.58E+4 ± 7.97E+3	2.19
14	84.911360	-69.773346	0.156	4.98E+15	1.99E+1 ± 4.91E+0	6.36E+0 ± 1.57E+0	0.168
15	84.893356	-69.769155	0.15	3.05E+15	8.70E+0 ± 2.96E+0	1.19E+0 ± 4.04E-1	0.074
16	84.901150	-69.759949	2.24	3.91E+16	3.70E+4 ± 1.79E+4	1.51E+4 ± 7.30E+3	2.15
17	84.901265	-69.759995	2.16	4.16E+16	3.54E+4 ± 1.52E+4	1.46E+4 ± 6.30E+3	2.16
18	84.901307	-69.760022	2.13	4.11E+16	3.32E+4 ± 1.41E+4	1.39E+4 ± 5.89E+3	2.12
19	84.901328	-69.760031	2.11	4.10E+16	3.22E+4 ± 1.36E+4	1.36E+4 ± 5.70E+3	2.10
20	84.901349	-69.760034	2.11	4.10E+16	3.18E+4 ± 1.33E+4	1.34E+4 ± 5.58E+3	2.09
21	84.901286	-69.760008	2.14	4.14E+16	3.44E+4 ± 1.47E+4	1.43E+4 ± 6.08E+3	2.14
22	84.901288	-69.760010	2.14	4.13E+16	3.42E+4 ± 1.46E+4	1.42E+4 ± 6.07E+3	2.14
23	84.913881	-69.773824	0.196	3.78E+15	2.40E+1 ± 9.80E+0	8.19E+0 ± 3.34E+0	0.17
24	84.905990	-69.771815	0.632	5.57E+15	2.82E+2 ± 2.21E+2	1.57E+2 ± 1.23E+2	0.413
25	84.917861	-69.772754	0.134	2.51E+15	6.73E+0 ± 2.70E+0	1.65E+0 ± 6.61E-1	0.092
26	84.909906	-69.772186	0.187	4.49E+15	3.46E+1 ± 1.31E+1	9.87E+0 ± 3.74E+0	0.19
27	84.901342	-69.760033	2.11	4.09E+16	3.19E+4 ± 1.34E+4	1.34E+4 ± 5.63E+3	2.09
28	84.901357	-69.760040	2.10	4.09E+16	3.14E+4 ± 1.31E+4	1.32E+4 ± 5.50E+3	2.08
29	84.901362	-69.760044	2.10	4.08E+16	3.11E+4 ± 1.29E+4	1.31E+4 ± 5.44E+3	2.07
30	84.901380	-69.760058	2.09	4.11E+16	3.03E+4 ± 1.23E+4	1.30E+4 ± 5.26E+3	2.06
31	84.901413	-69.760074	2.07	4.09E+16	2.89E+4 ± 1.15E+4	1.25E+4 ± 4.98E+3	2.04
32	84.901723	-69.760112	1.87	4.45E+16	2.70E+4 ± 9.16E+3	1.06E+4 ± 3.61E+3	1.98
33	84.901759	-69.760116	1.85	4.57E+16	2.63E+4 ± 8.45E+3	1.03E+4 ± 3.32E+3	1.96
34	84.901777	-69.760130	1.83	4.52E+16	2.52E+4 ± 8.06E+3	9.79E+3 ± 3.14E+3	1.92
35	84.901701	-69.760104	1.88	4.44E+16	2.78E+4 ± 9.63E+3	1.09E+4 ± 3.78E+3	2.00
36	84.901780	-69.760132	1.83	4.52E+16	2.51E+4 ± 8.03E+3	9.78E+3 ± 3.13E+3	1.92

Continued on next page

Table D.3 – continued from previous page

Clump ID	RA	Dec	Radius [pc]	$N_{^{13}CO}$ [cm^{-2}]	Total H_2 Mass [$M_\odot$]	Virial Mass [$M_\odot$]	Linewidth [km/s]
37	84.901747	-69.760110	1.86	4.57E+16	2.68E+4 ± 8.69E+3	1.05E+4 ± 3.41E+3	1.97
38	84.901374	-69.760056	2.09	4.10E+16	3.04E+4 ± 1.24E+4	1.30E+4 ± 5.31E+3	2.07
39	84.901376	-69.760057	2.09	4.10E+16	3.04E+4 ± 1.24E+4	1.30E+4 ± 5.29E+3	2.07
40	84.910561	-69.771155	0.345	6.26E+15	1.66E+2 ± 8.40E+1	1.59E+1 ± 8.06E+0	0.178
41	84.897479	-69.768246	0.623	9.09E+15	3.86E+2 ± 1.70E+2	2.21E+2 ± 9.73E+1	0.494
42	84.896325	-69.768587	0.432	8.24E+15	2.43E+2 ± 9.82E+1	1.44E+2 ± 5.80E+1	0.478
43	84.901549	-69.760436	1.60	4.87E+16	2.06E+4 ± 5.32E+3	4.27E+3 ± 1.11E+3	1.36
44	84.901821	-69.760151	1.80	4.41E+16	2.33E+4 ± 7.47E+3	9.18E+3 ± 2.94E+3	1.87
45	84.901525	-69.760670	1.20	5.61E+16	1.66E+4 ± 3.12E+3	2.99E+3 ± 5.62E+2	1.31
46	84.901928	-69.760591	1.11	5.37E+16	1.23E+4 ± 2.13E+3	2.49E+3 ± 4.30E+2	1.24
47	84.899787	-69.767571	0.226	9.43E+15	1.16E+2 ± 2.64E+1	4.84E+1 ± 1.10E+1	0.384
48	84.902659	-69.760460	0.808	6.07E+16	1.08E+4 ± 1.46E+3	1.78E+3 ± 2.40E+2	1.23
49	84.902839	-69.760408	0.741	6.30E+16	9.81E+3 ± 1.19E+3	1.59E+3 ± 1.93E+2	1.21
50	84.924396	-69.769416	0.717	3.20E+16	4.18E+3 ± 9.17E+2	2.02E+3 ± 4.44E+2	1.39
51	84.896529	-69.766134	0.446	8.36E+15	2.30E+2 ± 8.84E+1	5.35E+1 ± 2.06E+1	0.287
52	84.902852	-69.760407	0.735	6.27E+16	9.70E+3 ± 1.18E+3	1.57E+3 ± 1.91E+2	1.21
53	84.902934	-69.760391	0.704	6.30E+16	8.99E+3 ± 1.05E+3	1.44E+3 ± 1.67E+2	1.19
54	84.903153	-69.760335	0.607	6.60E+16	6.62E+3 ± 6.17E+2	1.13E+3 ± 1.06E+2	1.13
55	84.924404	-69.769556	0.624	3.43E+16	3.35E+3 ± 5.92E+2	1.59E+3 ± 2.81E+2	1.32
56	84.903447	-69.760224	0.487	7.17E+16	4.89E+3 ± 3.45E+2	8.88E+2 ± 6.27E+1	1.12
57	84.903416	-69.760230	0.503	6.84E+16	5.04E+3 ± 3.88E+2	9.22E+2 ± 7.10E+1	1.12
58	84.903486	-69.760208	0.463	7.78E+16	4.74E+3 ± 2.92E+2	8.43E+2 ± 5.19E+1	1.12
59	84.903540	-69.760229	0.375	5.91E+16	2.17E+3 ± 1.36E+2	5.03E+2 ± 3.16E+1	0.961
60	84.903554	-69.760236	0.362	5.24E+16	1.73E+3 ± 1.16E+2	4.26E+2 ± 2.87E+1	0.900
61	84.903618	-69.760311	0.284	3.85E+16	7.37E+2 ± 5.14E+1	9.72E+1 ± 6.77E+0	0.485
62	84.897237	-69.762321	0.281	1.17E+16	1.72E+2 ± 3.45E+1	2.67E+1 ± 5.36E+0	0.255
63	84.888938	-69.765083	0.237	6.76E+15	9.72E+1 ± 3.35E+1	3.38E+1 ± 1.16E+1	0.313
64	84.893446	-69.762044	0.400	2.03E+16	7.92E+2 ± 1.49E+2	3.16E+2 ± 5.96E+1	0.738
65	84.903562	-69.757760	0.667	1.92E+16	1.47E+3 ± 4.10E+2	5.94E+2 ± 1.65E+2	0.783
66	84.903567	-69.757752	0.636	1.90E+16	1.33E+3 ± 3.62E+2	5.42E+2 ± 1.47E+2	0.766
67	84.903507	-69.757730	0.567	1.87E+16	1.13E+3 ± 2.87E+2	4.47E+2 ± 1.14E+2	0.736
68	84.903657	-69.757482	0.426	2.16E+16	7.72E+2 ± 1.32E+2	3.52E+2 ± 5.99E+1	0.754
69	84.903537	-69.757764	0.668	1.91E+16	1.50E+3 ± 4.27E+2	6.48E+2 ± 1.84E+2	0.816
70	84.900824	-69.761440	0.301	1.48E+16	2.59E+2 ± 4.51E+1	2.37E+1 ± 4.12E+0	0.232
71	84.900035	-69.761631	0.148	9.47E+15	3.79E+1 ± 4.91E+0	7.56E-1 ± 9.80E-2	0.059
72	84.901282	-69.761388	0.164	1.25E+16	6.76E+1 ± 7.76E+0	5.30E+0 ± 6.08E-1	0.149
73	84.903425	-69.760089	0.324	2.33E+16	4.40E+2 ± 5.05E+1	6.69E+1 ± 7.67E+0	0.377
74	84.900054	-69.760139	0.133	7.24E+15	2.52E+1 ± 3.99E+0	9.71E-1 ± 1.54E-1	0.071

Continued on next page

Table D.3 – continued from previous page

Clump ID	RA	Dec	Radius [pc]	$N_{^{13}CO}$ [cm^{-2}]	Total H_2 Mass [$M_\odot$]	Virial Mass [$M_\odot$]	Linewidth [km/s]
75	84.903666	-69.759885	0.198	1.54E+16	1.09E+2 ± 1.16E+1	5.73E+0 ± 6.08E-1	0.141
76	84.902932	-69.758548	0.316	1.09E+16	2.20E+2 ± 5.58E+1	6.89E+1 ± 1.74E+1	0.387
77	84.893066	-69.762126	0.286	1.53E+16	2.47E+2 ± 3.99E+1	4.96E+1 ± 8.02E+0	0.345
78	84.893131	-69.762096	0.356	1.49E+16	3.45E+2 ± 6.83E+1	5.87E+1 ± 1.16E+1	0.337
79	84.902888	-69.758522	0.308	1.03E+16	1.88E+2 ± 4.75E+1	3.15E+1 ± 7.97E+0	0.265
80	84.903607	-69.757284	0.279	1.91E+16	3.11E+2 ± 4.05E+1	9.56E+1 ± 1.24E+1	0.485
81	84.893978	-69.762088	0.143	1.37E+16	5.49E+1 ± 4.91E+0	4.78E+0 ± 4.27E-1	0.152
82	84.903274	-69.760165	0.313	1.95E+16	2.66E+2 ± 3.10E+1	2.86E+1 ± 3.32E+0	0.251
83	84.898127	-69.759195	0.193	5.36E+15	4.32E+1 ± 1.40E+1	1.80E+1 ± 5.84E+0	0.253
84	84.897950	-69.759001	0.329	4.56E+15	7.73E+1 ± 4.29E+1	2.58E+1 ± 1.43E+1	0.232
85	84.897219	-69.754856	0.295	1.13E+16	2.64E+2 ± 6.96E+1	9.42E+1 ± 2.48E+1	0.469
86	84.897295	-69.754868	0.277	1.16E+16	2.33E+2 ± 5.53E+1	5.73E+1 ± 1.36E+1	0.377
87	84.892556	-69.762157	0.253	1.17E+16	1.07E+2 ± 1.70E+1	1.80E+1 ± 2.85E+0	0.221
88	84.891958	-69.762235	0.116	1.42E+16	3.80E+1 ± 2.70E+0	8.17E+0 ± 5.81E-1	0.220
89	84.894722	-69.761718	0.138	7.59E+15	2.13E+1 ± 2.87E+0	1.20E-1 ± 1.62E-2	0.024
90	84.900423	-69.761532	0.209	8.51E+15	4.04E+1 ± 6.33E+0	2.56E+0 ± 4.02E-1	0.092
91	84.900903	-69.761323	0.381	8.37E+15	6.69E+1 ± 1.39E+1	3.38E+0 ± 7.01E-1	0.078
92	84.902833	-69.760304	0.207	1.53E+16	6.20E+1 ± 5.01E+0	2.77E+0 ± 2.24E-1	0.096
93	84.903509	-69.760003	0.189	1.55E+16	7.96E+1 ± 7.15E+0	5.44E+0 ± 4.89E-1	0.141
94	84.892996	-69.762098	0.173	1.03E+16	4.53E+1 ± 5.66E+0	2.30E+0 ± 2.88E-1	0.096
95	84.897716	-69.758746	0.225	3.83E+15	3.28E+1 ± 1.54E+1	2.55E+0 ± 1.20E+0	0.088
96	84.897810	-69.757456	0.701	9.58E+15	7.25E+2 ± 4.04E+2	1.65E+2 ± 9.18E+1	0.402
97	84.894488	-69.753817	0.346	8.80E+15	2.60E+2 ± 9.88E+1	5.87E+1 ± 2.23E+1	0.342
98	84.924278	-69.766765	0.186	5.80E+15	4.67E+1 ± 1.40E+1	2.82E+1 ± 8.48E+0	0.323
99	84.899850	-69.758645	0.153	6.21E+15	2.76E+1 ± 5.77E+0	2.55E+0 ± 5.33E-1	0.107
100	84.897945	-69.757429	0.666	8.98E+15	4.98E+2 ± 2.53E+2	8.94E+1 ± 4.55E+1	0.304
101	84.898394	-69.757250	0.428	1.02E+16	3.29E+2 ± 1.13E+2	5.53E+1 ± 1.89E+1	0.298
102	84.891227	-69.761486	0.180	3.84E+15	2.19E+1 ± 8.38E+0	6.58E+0 ± 2.51E+0	0.158
103	84.901741	-69.758393	0.117	7.18E+15	1.89E+1 ± 2.61E+0	2.91E+0 ± 4.03E-1	0.130
104	84.894747	-69.761548	0.148	6.28E+15	2.08E+1 ± 3.70E+0	1.97E+0 ± 3.51E-1	0.096
105	84.903210	-69.760041	0.193	1.01E+16	4.50E+1 ± 5.77E+0	3.50E+0 ± 4.48E-1	0.112
106	84.893192	-69.759255	0.667	1.26E+16	9.61E+2 ± 4.09E+2	3.82E+2 ± 1.63E+2	0.628
107	84.893263	-69.759129	0.450	1.54E+16	5.69E+2 ± 1.38E+2	2.56E+2 ± 6.22E+1	0.625
108	84.903037	-69.758405	0.150	6.12E+15	2.62E+1 ± 5.44E+0	1.79E+0 ± 3.71E-1	0.090
109	84.896433	-69.758016	0.366	6.01E+15	1.02E+2 ± 4.31E+1	3.11E+1 ± 1.31E+1	0.242
110	84.902493	-69.758400	0.234	6.50E+15	4.53E+1 ± 1.13E+1	4.80E+0 ± 1.20E+0	0.119
111	84.892928	-69.761993	0.142	1.05E+16	3.49E+1 ± 3.70E+0	1.50E+1 ± 1.59E+0	0.270
112	84.931447	-69.761520	0.215	3.30E+15	1.83E+1 ± 8.00E+0	3.94E+0 ± 1.73E+0	0.112

Continued on next page

Table D.3 – continued from previous page

Clump ID	RA	Dec	Radius [pc]	$N_{^{13}CO}$ [cm^{-2}]	Total H_2 Mass [$M_\odot$]	Virial Mass [$M_\odot$]	Linewidth [km/s]
113	84.901103	-69.758956	0.394	7.67E+15	2.31E+2 ± 1.02E+2	9.14E+1 ± 4.02E+1	0.400
114	84.893730	-69.759074	0.335	1.57E+16	3.66E+2 ± 6.88E+1	1.60E+2 ± 3.01E+1	0.573
115	84.893743	-69.759125	0.294	1.45E+16	2.39E+2 ± 4.12E+1	1.49E+2 ± 2.57E+1	0.590
116	84.893848	-69.759181	0.175	1.19E+16	6.50E+1 ± 7.88E+0	5.73E+1 ± 6.95E+0	0.474
117	84.898918	-69.758756	0.186	5.53E+15	1.52E+1 ± 2.79E+0	1.74E+1 ± 3.20E+0	0.253
118	84.906722	-69.757947	0.247	8.71E+15	1.26E+2 ± 3.37E+1	8.16E+1 ± 2.18E+1	0.476
119	84.879797	-69.764679	0.154	3.06E+15	9.08E+0 ± 3.14E+0	5.75E+0 ± 1.99E+0	0.160
120	84.932152	-69.761039	0.184	2.98E+15	1.57E+1 ± 7.39E+0	6.39E+0 ± 3.02E+0	0.155
121	84.899818	-69.758080	0.154	3.48E+15	1.21E+1 ± 3.99E+0	2.13E+0 ± 7.00E-1	0.098
122	84.903413	-69.757721	0.214	9.97E+15	6.78E+1 ± 1.09E+1	9.20E+0 ± 1.48E+0	0.172
123	84.896607	-69.757325	0.152	8.25E+15	3.06E+1 ± 4.39E+0	8.77E+0 ± 1.26E+0	0.200
124	84.897993	-69.757186	0.153	7.84E+15	3.36E+1 ± 5.44E+0	5.31E+0 ± 8.61E-1	0.154
125	84.882366	-69.764708	0.180	3.68E+15	1.87E+1 ± 7.03E+0	2.69E+0 ± 1.01E+0	0.101
126	84.921779	-69.761425	0.353	4.27E+15	8.75E+1 ± 5.70E+1	1.47E+1 ± 9.57E+0	0.169
127	84.901120	-69.758981	0.240	6.53E+15	4.18E+1 ± 9.93E+0	1.06E+1 ± 2.51E+0	0.174
128	84.900667	-69.758941	0.281	6.62E+15	7.45E+1 ± 2.32E+1	3.76E+1 ± 1.17E+1	0.303
129	84.898321	-69.756206	0.481	5.66E+15	1.71E+2 ± 1.02E+2	1.33E+2 ± 7.95E+1	0.437
130	84.926654	-69.764550	0.253	3.99E+15	4.47E+1 ± 2.30E+1	1.33E+1 ± 6.86E+0	0.190
131	84.926878	-69.764306	0.155	4.29E+15	1.93E+1 ± 5.88E+0	9.54E+0 ± 2.90E+0	0.206
132	84.921821	-69.761740	0.160	4.75E+15	1.87E+1 ± 4.80E+0	2.32E+0 ± 5.94E-1	0.100
133	84.894095	-69.761443	0.131	7.02E+15	2.49E+1 ± 4.09E+0	5.64E+0 ± 9.28E-1	0.172
134	84.921466	-69.761372	0.168	3.73E+15	1.83E+1 ± 6.68E+0	2.91E+0 ± 1.06E+0	0.109
135	84.902218	-69.757998	0.243	5.77E+15	2.77E+1 ± 6.45E+0	1.18E+1 ± 2.75E+0	0.183
136	84.883452	-69.763192	0.334	6.86E+15	1.39E+2 ± 5.63E+1	6.92E+1 ± 2.79E+1	0.377
137	84.893281	-69.759143	0.471	1.46E+16	5.87E+2 ± 1.57E+2	2.65E+2 ± 7.10E+1	0.623
138	84.893939	-69.758744	0.135	8.45E+15	2.66E+1 ± 3.42E+0	3.47E+0 ± 4.46E-1	0.133
139	84.896830	-69.758539	0.138	3.75E+15	1.22E+1 ± 3.61E+0	3.35E+0 ± 9.90E-1	0.129
140	84.895745	-69.757704	0.286	4.37E+15	3.80E+1 ± 1.57E+1	1.60E+1 ± 6.60E+0	0.196
141	84.926438	-69.764800	0.173	3.56E+15	1.97E+1 ± 8.00E+0	2.50E+0 ± 1.01E+0	0.100
142	84.883468	-69.763621	0.227	3.45E+15	1.99E+1 ± 8.50E+0	2.26E+0 ± 9.65E-1	0.083
143	84.883523	-69.762995	0.183	9.38E+15	6.53E+1 ± 1.13E+1	3.53E+1 ± 6.09E+0	0.364
144	84.883517	-69.763019	0.163	8.20E+15	4.26E+1 ± 7.27E+0	1.47E+1 ± 2.51E+0	0.25
145	84.891213	-69.759397	0.215	9.79E+15	8.61E+1 ± 1.60E+1	3.16E+1 ± 5.87E+0	0.318
146	84.904677	-69.757483	1.02	1.37E+16	1.97E+3 ± 1.06E+3	5.81E+2 ± 3.13E+2	0.627
147	84.904592	-69.757493	1.04	1.37E+16	2.13E+3 ± 1.19E+3	5.96E+2 ± 3.32E+2	0.629
148	84.888570	-69.761794	0.161	4.52E+15	2.48E+1 ± 7.88E+0	3.56E+0 ± 1.13E+0	0.124
149	84.899976	-69.758884	0.182	5.68E+15	2.79E+1 ± 6.68E+0	1.35E+0 ± 3.22E-1	0.071
150	84.901644	-69.758825	0.144	5.27E+15	1.65E+1 ± 3.42E+0	1.83E+0 ± 3.79E-1	0.094

Continued on next page

Table D.3 – continued from previous page

Clump ID	RA	Dec	Radius [pc]	$N_{^{13}CO}$ [cm^{-2}]	Total H_2 Mass [$M_\odot$]	Virial Mass [$M_\odot$]	Linewidth [km/s]
151	84.899167	-69.758458	0.214	4.19E+15	1.84E+1 ± 5.66E+0	3.09E+0 ± 9.50E-1	0.100
152	84.894855	-69.758315	0.126	4.54E+15	1.45E+1 ± 3.51E+0	1.50E+0 ± 3.63E-1	0.090
153	84.904715	-69.757497	0.997	1.24E+16	1.42E+3 ± 7.51E+2	5.46E+2 ± 2.89E+2	0.614
154	84.903521	-69.757651	0.157	6.33E+15	1.74E+1 ± 2.79E+0	1.60E+0 ± 2.58E-1	0.084
155	84.904947	-69.757497	1.00	1.09E+16	8.29E+2 ± 4.08E+2	3.75E+2 ± 1.84E+2	0.507
156	84.908109	-69.756857	0.443	1.33E+16	3.40E+2 ± 7.97E+1	1.46E+2 ± 3.42E+1	0.476
157	84.904890	-69.757501	0.980	1.09E+16	9.17E+2 ± 4.73E+2	4.39E+2 ± 2.27E+2	0.555
158	84.904881	-69.757489	0.981	1.12E+16	9.85E+2 ± 5.04E+2	4.90E+2 ± 2.50E+2	0.586
159	84.904739	-69.757499	0.993	1.18E+16	1.12E+3 ± 5.66E+2	5.02E+2 ± 2.54E+2	0.589
160	84.906788	-69.757247	0.828	1.14E+16	5.44E+2 ± 2.02E+2	3.91E+2 ± 1.45E+2	0.570
161	84.921561	-69.761767	0.242	2.55E+15	2.25E+1 ± 1.60E+1	1.10E+0 ± 7.81E-1	0.056
162	84.893990	-69.761219	0.175	3.88E+15	1.71E+1 ± 5.66E+0	2.55E+0 ± 8.45E-1	0.100
163	84.893249	-69.760099	0.294	5.30E+15	5.99E+1 ± 2.33E+1	1.83E+1 ± 7.14E+0	0.207
164	84.893076	-69.759986	0.229	5.18E+15	2.78E+1 ± 7.63E+0	8.57E+0 ± 2.35E+0	0.161
165	84.893825	-69.759146	0.201	1.22E+16	8.52E+1 ± 1.13E+1	8.35E+1 ± 1.11E+1	0.534
166	84.904911	-69.757500	0.998	1.09E+16	8.46E+2 ± 4.19E+2	3.85E+2 ± 1.90E+2	0.515
167	84.893864	-69.759574	0.171	4.68E+15	1.74E+1 ± 4.39E+0	5.43E+0 ± 1.37E+0	0.148
168	84.893746	-69.759031	0.206	7.00E+15	2.00E+1 ± 2.96E+0	2.37E+0 ± 3.51E-1	0.089
169	84.901284	-69.757992	0.487	9.44E+15	2.73E+2 ± 9.56E+1	4.26E+1 ± 1.49E+1	0.245
170	84.908444	-69.756822	0.373	1.08E+16	1.65E+2 ± 3.66E+1	9.82E+1 ± 2.18E+1	0.426
171	84.908773	-69.756807	0.281	1.14E+16	1.32E+2 ± 2.42E+1	4.68E+1 ± 8.60E+0	0.338
172	84.907934	-69.756880	0.471	1.29E+16	3.67E+2 ± 9.28E+1	1.48E+2 ± 3.74E+1	0.464
173	84.883583	-69.762907	0.166	5.31E+15	1.43E+1 ± 2.70E+0	3.59E+0 ± 6.81E-1	0.122
174	84.884230	-69.762534	0.177	6.60E+15	4.45E+1 ± 1.07E+1	1.84E+1 ± 4.45E+0	0.267
175	84.893438	-69.760231	0.139	4.30E+15	1.35E+1 ± 3.42E+0	1.07E+0 ± 2.72E-1	0.073
176	84.897109	-69.758472	0.237	6.25E+15	5.78E+1 ± 1.73E+1	1.85E+1 ± 5.52E+0	0.232
177	84.900778	-69.757987	0.294	9.37E+15	1.09E+2 ± 2.42E+1	2.11E+1 ± 4.70E+0	0.222
178	84.883066	-69.760892	0.165	3.97E+15	2.20E+1 ± 8.00E+0	2.09E+1 ± 7.60E+0	0.295
179	84.893122	-69.760338	0.216	3.97E+15	3.00E+1 ± 1.27E+1	5.86E+0 ± 2.48E+0	0.137
180	84.902853	-69.757958	0.179	8.73E+15	3.59E+1 ± 5.12E+0	2.40E+0 ± 3.42E-1	0.096
181	84.904389	-69.758074	0.329	8.59E+15	1.03E+2 ± 2.53E+1	4.90E+1 ± 1.21E+1	0.320
182	84.904249	-69.758055	0.434	8.49E+15	1.68E+2 ± 5.42E+1	5.76E+1 ± 1.85E+1	0.302
183	84.905138	-69.757159	0.169	7.15E+15	2.17E+1 ± 3.23E+0	1.15E+0 ± 1.71E-1	0.068
184	84.904303	-69.758245	0.181	7.71E+15	3.48E+1 ± 5.88E+0	6.38E+0 ± 1.08E+0	0.156
185	84.903128	-69.758189	0.176	6.38E+15	1.90E+1 ± 3.14E+0	1.41E+0 ± 2.34E-1	0.074
186	84.901021	-69.757820	0.261	6.35E+15	4.20E+1 ± 1.05E+1	3.16E+0 ± 7.88E-1	0.091
187	84.898523	-69.757659	0.164	4.48E+15	1.25E+1 ± 2.87E+0	2.60E-1 ± 5.95E-2	0.033
188	84.899064	-69.758195	0.163	3.83E+15	1.20E+1 ± 3.42E+0	3.26E-1 ± 9.25E-2	0.037

Continued on next page

Table D.3 – continued from previous page

Clump ID	RA	Dec	Radius [pc]	$N_{^{13}CO}$ [cm^{-2}]	Total H_2 Mass [$M_\odot$]	Virial Mass [$M_\odot$]	Linewidth [km/s]
189	84.900772	-69.757769	0.176	6.85E+15	3.83E+1 ± 8.13E+0	9.41E+0 ± 2.00E+0	0.192
190	84.904747	-69.757489	0.232	6.45E+15	4.68E+1 ± 1.20E+1	5.87E+0 ± 1.50E+0	0.132
191	84.905009	-69.758223	0.137	6.46E+15	2.22E+1 ± 3.89E+0	2.00E+0 ± 3.51E-1	0.100
192	84.904547	-69.757128	0.166	6.57E+15	2.44E+1 ± 4.39E+0	4.27E+0 ± 7.69E-1	0.133
193	84.884826	-69.760975	0.223	3.07E+15	1.95E+1 ± 9.80E+0	6.00E-1 ± 3.02E-1	0.043
194	84.904725	-69.758253	0.299	4.83E+15	7.04E+1 ± 3.41E+1	9.51E+0 ± 4.61E+0	0.148

Column 1: The ID we give each clump. Column 4: The radius calculated from the area of the clump. Column 6: The total H_2 mass. We use a $\frac{^{13}CO(2-1)}{H_2}$ conversion factor of 3.2×10^{-7} (Fujii et al., 2014). Column 8: The measured linewidth.

APPENDIX D. 12CO AND 13CO CLUMPS IDENTIFIED USING ASTRODENDRO IN THE N159 REGION OF THE LMC

Table D.4: Column Densities and Mass Derived from N159E ^{13}CO (2-1) Clumps

Clump ID	RA	Dec	Radius [pc]	$N_{^{13}CO}$ [cm^{-2}]	Total H_2 Mass [$M_\odot$]	Virial Mass [$M_\odot$]	Linewidth [km/s]
0	85.038545	-69.757583	0.149	2.27E+15	8.55E+0 ± 2.30E+0	4.27E-1 ± 1.15E-1	0.050
1	85.044310	-69.756562	0.193	2.75E+15	1.57E+1 ± 4.29E+0	1.97E+0 ± 5.38E-1	0.094
2	85.066163	-69.749707	0.160	1.58E+15	5.32E+0 ± 1.95E+0	1.77E-1 ± 6.48E-2	0.031
3	85.029244	-69.732067	0.172	2.59E+15	1.23E+1 ± 3.25E+0	4.13E-2 ± 1.09E-2	0.014
4	85.011350	-69.756320	0.189	1.75E+15	5.31E+0 ± 1.66E+0	1.93E+0 ± 6.04E-1	0.094
5	85.057335	-69.749045	0.219	1.43E+15	1.08E+1 ± 6.51E+0	2.53E+0 ± 1.53E+0	0.100
6	85.066326	-69.738986	0.128	1.87E+15	5.02E+0 ± 1.38E+0	2.26E+0 ± 6.22E-1	0.123
7	85.068687	-69.752008	0.179	1.99E+15	7.50E+0 ± 2.30E+0	1.64E+0 ± 5.03E-1	0.089
8	85.059543	-69.753669	0.184	2.34E+15	1.22E+1 ± 3.73E+0	1.60E+0 ± 4.91E-1	0.087
9	85.031573	-69.740692	0.241	2.41E+15	2.74E+1 ± 1.21E+1	3.78E+1 ± 1.66E+1	0.368
10	85.061496	-69.740372	0.154	1.82E+15	6.88E+0 ± 2.30E+0	7.51E-2 ± 2.51E-2	0.02
11	85.060891	-69.749754	1.99	1.10E+16	7.30E+3 ± 5.39E+3	5.93E+3 ± 4.38E+3	1.60
12	85.060987	-69.749737	1.97	1.08E+16	6.65E+3 ± 4.83E+3	5.75E+3 ± 4.17E+3	1.58
13	85.060967	-69.749742	1.97	1.09E+16	6.79E+3 ± 4.92E+3	5.77E+3 ± 4.18E+3	1.59
14	85.060932	-69.749750	1.98	1.10E+16	7.13E+3 ± 5.21E+3	5.87E+3 ± 4.29E+3	1.60
15	85.060950	-69.749746	1.98	1.09E+16	6.90E+3 ± 5.00E+3	5.84E+3 ± 4.23E+3	1.59
16	85.061022	-69.749729	1.97	1.05E+16	6.21E+3 ± 4.55E+3	5.66E+3 ± 4.14E+3	1.57
17	85.057701	-69.749230	0.227	3.66E+15	4.47E+1 ± 1.34E+1	2.73E+1 ± 8.20E+0	0.321
18	85.056864	-69.750768	1.18	8.83E+15	2.41E+3 ± 1.42E+3	4.05E+3 ± 2.38E+3	1.72
19	85.056201	-69.750453	0.190	1.74E+15	9.33E+0 ± 3.91E+0	1.08E+0 ± 4.55E-1	0.07
20	85.053660	-69.749286	0.289	4.15E+15	6.92E+1 ± 2.14E+1	3.85E+1 ± 1.19E+1	0.338
21	85.056847	-69.750800	1.15	8.95E+15	2.31E+3 ± 1.30E+3	3.71E+3 ± 2.09E+3	1.67
22	85.056841	-69.750806	1.13	8.94E+15	2.19E+3 ± 1.20E+3	3.61E+3 ± 1.99E+3	1.66
23	85.056942	-69.750857	1.06	9.28E+15	2.07E+3 ± 1.05E+3	3.16E+3 ± 1.60E+3	1.60
24	85.056844	-69.750812	1.13	8.89E+15	2.23E+3 ± 1.25E+3	3.65E+3 ± 2.04E+3	1.66
25	85.063782	-69.749040	1.33	1.12E+16	3.67E+3 ± 1.86E+3	3.17E+3 ± 1.61E+3	1.43
26	85.054431	-69.754805	0.151	1.74E+15	5.17E+0 ± 1.61E+0	2.83E+0 ± 8.80E-1	0.127
27	85.005962	-69.754632	0.175	2.95E+15	1.55E+1 ± 3.79E+0	3.61E+0 ± 8.83E-1	0.133
28	85.060950	-69.749747	1.98	1.09E+16	6.90E+3 ± 5.01E+3	5.83E+3 ± 4.23E+3	1.59
29	85.056921	-69.750867	1.06	8.93E+15	1.92E+3 ± 9.94E+2	3.10E+3 ± 1.60E+3	1.59
30	85.056885	-69.750863	1.06	8.74E+15	1.83E+3 ± 9.55E+2	3.14E+3 ± 1.64E+3	1.60
31	85.056614	-69.750844	1.01	9.03E+15	1.60E+3 ± 7.44E+2	2.88E+3 ± 1.33E+3	1.56
32	85.056541	-69.750830	0.989	8.95E+15	1.50E+3 ± 6.81E+2	2.74E+3 ± 1.24E+3	1.54
33	85.056905	-69.750863	1.06	8.78E+15	1.86E+3 ± 9.73E+2	3.14E+3 ± 1.64E+3	1.60
34	85.020854	-69.749881	0.254	7.32E+15	1.31E+2 ± 2.39E+1	3.38E+1 ± 6.16E+0	0.339
35	85.053401	-69.749308	0.199	4.27E+15	3.76E+1 ± 8.21E+0	1.40E+1 ± 3.06E+0	0.246
36	85.063755	-69.749039	1.32	1.14E+16	3.60E+3 ± 1.76E+3	3.16E+3 ± 1.55E+3	1.43

Continued on next page

Table D.4 – continued from previous page

Clump ID	RA	Dec	Radius [pc]	$N_{^{13}CO}$ [cm^{-2}]	Total H_2 Mass [$M_\odot$]	Virial Mass [$M_\odot$]	Linewidth [km/s]
37	85.063751	-69.749042	1.31	1.14E+16	3.45E+3 ± 1.65E+3	3.14E+3 ± 1.50E+3	1.43
38	85.063721	-69.749049	1.29	1.16E+16	3.37E+3 ± 1.55E+3	3.09E+3 ± 1.42E+3	1.44
39	85.063726	-69.749045	1.29	1.15E+16	3.23E+3 ± 1.47E+3	3.05E+3 ± 1.39E+3	1.43
40	85.063733	-69.749036	1.27	1.13E+16	3.02E+3 ± 1.38E+3	2.97E+3 ± 1.36E+3	1.42
41	85.063686	-69.748250	0.827	1.18E+16	1.61E+3 ± 4.99E+2	7.90E+2 ± 2.45E+2	0.906
42	85.063732	-69.749042	1.28	1.13E+16	3.10E+3 ± 1.43E+3	3.03E+3 ± 1.40E+3	1.43
43	85.063736	-69.749037	1.27	1.11E+16	2.90E+3 ± 1.33E+3	2.94E+3 ± 1.35E+3	1.41
44	85.020264	-69.741803	1.91	1.61E+16	1.15E+4 ± 6.05E+3	9.40E+3 ± 4.93E+3	2.06
45	85.019923	-69.741857	1.64	1.74E+16	1.06E+4 ± 4.76E+3	7.33E+3 ± 3.27E+3	1.96
46	85.019936	-69.741832	1.66	1.70E+16	1.08E+4 ± 5.04E+3	7.48E+3 ± 3.49E+3	1.97
47	85.034938	-69.745817	1.96	1.23E+16	6.08E+3 ± 3.47E+3	4.09E+3 ± 2.33E+3	1.34
48	85.056906	-69.750084	0.352	3.79E+15	9.05E+1 ± 3.67E+1	3.49E+1 ± 1.42E+1	0.292
49	85.063745	-69.749031	1.27	1.11E+16	2.85E+3 ± 1.28E+3	2.91E+3 ± 1.31E+3	1.41
50	85.063692	-69.748240	0.817	1.15E+16	1.53E+3 ± 4.79E+2	7.55E+2 ± 2.37E+2	0.892
51	85.063793	-69.749018	1.26	1.13E+16	2.73E+3 ± 1.19E+3	2.94E+3 ± 1.28E+3	1.41
52	85.020250	-69.741819	1.90	1.63E+16	1.14E+4 ± 5.84E+3	9.26E+3 ± 4.75E+3	2.05
53	85.056503	-69.750881	0.95	9.20E+15	1.28E+3 ± 5.16E+2	2.32E+3 ± 9.37E+2	1.45
54	85.056767	-69.750883	0.911	8.99E+15	1.17E+3 ± 4.70E+2	2.27E+3 ± 9.06E+2	1.46
55	85.056054	-69.750548	0.648	8.16E+15	5.48E+2 ± 1.73E+2	2.84E+2 ± 8.97E+1	0.614
56	85.063733	-69.749038	1.27	1.12E+16	2.92E+3 ± 1.33E+3	2.96E+3 ± 1.35E+3	1.42
57	85.063674	-69.748246	0.822	1.16E+16	1.54E+3 ± 4.81E+2	7.56E+2 ± 2.36E+2	0.89
58	85.034915	-69.745816	1.95	1.22E+16	5.69E+3 ± 3.15E+3	4.00E+3 ± 2.21E+3	1.33
59	85.034915	-69.745814	1.95	1.24E+16	5.47E+3 ± 2.92E+3	3.94E+3 ± 2.10E+3	1.32
60	85.034917	-69.745814	1.95	1.23E+16	5.50E+3 ± 2.99E+3	3.95E+3 ± 2.15E+3	1.32
61	85.005138	-69.753911	0.161	1.84E+15	7.23E+0 ± 2.46E+0	1.87E+0 ± 6.36E-1	0.1
62	85.055962	-69.750554	0.649	8.82E+15	4.67E+2 ± 1.21E+2	2.79E+2 ± 7.25E+1	0.609
63	85.058673	-69.750644	0.333	7.94E+15	1.76E+2 ± 3.29E+1	5.94E+1 ± 1.11E+1	0.392
64	85.058861	-69.750600	0.283	6.27E+15	9.28E+1 ± 1.79E+1	3.73E+1 ± 7.19E+0	0.336
65	85.056138	-69.750546	0.631	8.75E+15	3.91E+2 ± 9.41E+1	1.73E+2 ± 4.17E+1	0.486
66	85.025331	-69.750384	0.154	2.50E+15	1.28E+1 ± 3.67E+0	2.84E+0 ± 8.11E-1	0.126
67	85.049864	-69.749400	0.166	1.66E+15	7.22E+0 ± 2.84E+0	1.36E+0 ± 5.34E-1	0.084
68	85.019866	-69.741895	1.61	1.80E+16	1.03E+4 ± 4.29E+3	7.10E+3 ± 2.95E+3	1.95
69	85.019859	-69.741921	1.58	1.85E+16	1.02E+4 ± 4.05E+3	6.89E+3 ± 2.74E+3	1.94
70	85.019440	-69.742233	1.37	2.11E+16	9.10E+3 ± 2.82E+3	4.94E+3 ± 1.53E+3	1.76
71	85.019896	-69.741879	1.62	1.76E+16	1.04E+4 ± 4.51E+3	7.18E+3 ± 3.11E+3	1.95
72	85.019407	-69.742260	1.35	2.19E+16	8.94E+3 ± 2.60E+3	4.87E+3 ± 1.42E+3	1.76
73	85.019416	-69.742303	1.29	2.37E+16	8.00E+3 ± 1.95E+3	4.62E+3 ± 1.13E+3	1.76
74	85.067858	-69.741265	0.203	1.79E+15	6.04E+0 ± 1.95E+0	1.38E+0 ± 4.43E-1	0.076

Continued on next page

Table D.4 – continued from previous page

Clump ID	RA	Dec	Radius [pc]	$N_{^{13}CO}$ [cm^{-2}]	Total H_2 Mass [$M_\odot$]	Virial Mass [$M_\odot$]	Linewidth [km/s]
75	85.053868	-69.750455	0.269	9.86E+15	1.95E+2 ± 2.76E+1	6.03E+1 ± 8.56E+0	0.440
76	85.051422	-69.750102	0.190	2.11E+15	1.53E+1 ± 6.14E+0	5.28E+0 ± 2.12E+0	0.155
77	85.056253	-69.749529	0.203	2.41E+15	1.91E+1 ± 7.04E+0	3.89E+0 ± 1.43E+0	0.128
78	85.063849	-69.748190	0.765	1.18E+16	1.30E+3 ± 3.62E+2	6.30E+2 ± 1.75E+2	0.841
79	85.063842	-69.748180	0.742	1.16E+16	1.14E+3 ± 3.06E+2	6.05E+2 ± 1.63E+2	0.837
80	85.063837	-69.748176	0.744	1.20E+16	1.22E+3 ± 3.24E+2	6.07E+2 ± 1.61E+2	0.837
81	85.064376	-69.748024	0.658	9.25E+15	4.87E+2 ± 1.20E+2	3.99E+2 ± 9.85E+1	0.723
82	85.061786	-69.748129	0.141	6.55E+15	2.77E+1 ± 2.73E+0	6.27E+0 ± 6.18E-1	0.196
83	85.063981	-69.748122	0.721	8.72E+15	6.22E+2 ± 1.89E+2	5.52E+2 ± 1.68E+2	0.811
84	85.034984	-69.745801	1.94	1.28E+16	4.89E+3 ± 2.36E+3	3.71E+3 ± 1.79E+3	1.28
85	85.034216	-69.745364	1.55	1.25E+16	4.01E+3 ± 1.80E+3	2.09E+3 ± 9.38E+2	1.08
86	85.019419	-69.742298	1.29	2.35E+16	8.09E+3 ± 2.00E+3	4.65E+3 ± 1.15E+3	1.76
87	85.019417	-69.742345	1.24	2.48E+16	7.24E+3 ± 1.57E+3	4.42E+3 ± 9.58E+2	1.75
88	85.019339	-69.742415	1.17	2.45E+16	5.81E+3 ± 1.15E+3	3.98E+3 ± 7.89E+2	1.71
89	85.027266	-69.742009	0.548	8.19E+15	4.53E+2 ± 1.29E+2	1.75E+2 ± 5.00E+1	0.524
90	85.051468	-69.754540	0.152	2.04E+15	5.47E+0 ± 1.38E+0	1.77E+0 ± 4.46E-1	0.1
91	85.005756	-69.754587	0.166	3.02E+15	1.62E+1 ± 3.91E+0	3.11E+0 ± 7.49E-1	0.127
92	85.002994	-69.751464	0.196	2.31E+15	1.00E+1 ± 2.84E+0	1.41E+0 ± 4.00E-1	0.079
93	84.999927	-69.751307	0.157	2.46E+15	9.83E+0 ± 2.51E+0	4.16E+0 ± 1.06E+0	0.151
94	85.056514	-69.750437	0.240	3.35E+15	3.37E+1 ± 1.00E+1	8.82E+0 ± 2.63E+0	0.178
95	84.998327	-69.749050	0.159	1.57E+15	5.48E+0 ± 2.05E+0	2.56E-1 ± 9.56E-2	0.037
96	85.017017	-69.748383	1.93	1.31E+16	7.02E+3 ± 3.92E+3	5.45E+3 ± 3.04E+3	1.56
97	85.017007	-69.748374	1.92	1.31E+16	6.70E+3 ± 3.64E+3	5.28E+3 ± 2.86E+3	1.54
98	85.016988	-69.748396	1.93	1.27E+16	7.15E+3 ± 4.20E+3	5.50E+3 ± 3.23E+3	1.56
99	85.016979	-69.748370	1.90	1.37E+16	6.33E+3 ± 3.13E+3	5.14E+3 ± 2.54E+3	1.53
100	85.016990	-69.748370	1.90	1.37E+16	6.47E+3 ± 3.24E+3	5.20E+3 ± 2.60E+3	1.53
101	85.013163	-69.749704	1.07	1.59E+16	3.71E+3 ± 1.12E+3	1.87E+3 ± 5.62E+2	1.22
102	85.013147	-69.749703	1.07	1.58E+16	3.58E+3 ± 1.07E+3	1.79E+3 ± 5.38E+2	1.20
103	85.013087	-69.749705	1.05	1.58E+16	3.35E+3 ± 9.71E+2	1.70E+3 ± 4.94E+2	1.18
104	85.013101	-69.749707	1.05	1.59E+16	3.37E+3 ± 9.75E+2	1.72E+3 ± 4.96E+2	1.18
105	85.064032	-69.748124	0.713	9.09E+15	6.52E+2 ± 1.91E+2	5.35E+2 ± 1.57E+2	0.804
106	85.061840	-69.748703	0.303	5.45E+15	8.03E+1 ± 1.78E+1	3.19E+1 ± 7.06E+0	0.301
107	85.076274	-69.744558	0.202	4.06E+15	3.29E+1 ± 7.27E+0	2.50E+1 ± 5.51E+0	0.326
108	85.076309	-69.744563	0.16	2.88E+15	1.20E+1 ± 2.68E+0	4.48E+0 ± 9.97E-1	0.155
109	85.034192	-69.745359	1.52	1.23E+16	3.72E+3 ± 1.66E+3	1.96E+3 ± 8.78E+2	1.05
110	85.034215	-69.745356	1.50	1.17E+16	3.29E+3 ± 1.49E+3	1.82E+3 ± 8.18E+2	1.02
111	85.034228	-69.745349	1.49	1.17E+16	3.17E+3 ± 1.41E+3	1.73E+3 ± 7.69E+2	0.999
112	85.019342	-69.742433	1.14	2.49E+16	5.47E+3 ± 1.02E+3	3.86E+3 ± 7.24E+2	1.71

Continued on next page

Table D.4 – continued from previous page

Clump ID	RA	Dec	Radius [pc]	$N_{^{13}CO}$ [cm^{-2}]	Total H_2 Mass [$M_\odot$]	Virial Mass [$M_\odot$]	Linewidth [km/s]
113	85.034226	-69.745361	1.55	1.24E+16	4.05E+3 ± 1.85E+3	2.13E+3 ± 9.76E+2	1.09
114	85.030541	-69.743050	0.396	8.26E+15	3.17E+2 ± 7.50E+1	1.64E+2 ± 3.87E+1	0.597
115	85.030513	-69.743050	0.396	8.29E+15	3.33E+2 ± 8.00E+1	2.03E+2 ± 4.89E+1	0.665
116	85.026615	-69.742128	0.343	1.05E+16	2.83E+2 ± 4.40E+1	8.19E+1 ± 1.27E+1	0.453
117	85.004817	-69.751934	0.809	6.10E+15	6.90E+2 ± 3.78E+2	3.60E+2 ± 1.97E+2	0.618
118	85.004755	-69.752025	0.726	6.55E+15	6.09E+2 ± 2.82E+2	2.46E+2 ± 1.14E+2	0.540
119	85.010013	-69.752317	1.51	6.57E+15	1.63E+3 ± 1.23E+3	3.09E+3 ± 2.33E+3	1.33
120	84.996838	-69.750232	0.140	2.63E+15	7.82E+0 ± 1.61E+0	1.93E+0 ± 3.98E-1	0.109
121	85.064876	-69.749374	0.152	1.78E+15	6.70E+0 ± 2.30E+0	1.75E+0 ± 6.03E-1	0.100
122	85.013037	-69.749699	1.02	1.56E+16	2.99E+3 ± 8.32E+2	1.56E+3 ± 4.36E+2	1.15
123	85.013000	-69.749704	1.02	1.54E+16	2.86E+3 ± 7.99E+2	1.54E+3 ± 4.30E+2	1.14
124	85.016125	-69.749142	0.588	1.22E+16	8.78E+2 ± 1.93E+2	7.99E+2 ± 1.76E+2	1.08
125	85.016150	-69.749156	0.561	1.15E+16	7.02E+2 ± 1.50E+2	6.63E+2 ± 1.42E+2	1.01
126	85.076229	-69.744636	0.300	3.19E+15	4.02E+1 ± 1.41E+1	3.93E+1 ± 1.38E+1	0.336
127	85.034705	-69.741687	0.400	4.55E+15	1.87E+2 ± 8.28E+1	1.05E+2 ± 4.66E+1	0.476
128	85.030019	-69.741432	0.189	3.75E+15	3.17E+1 ± 7.73E+0	1.55E+1 ± 3.78E+0	0.265
129	85.051311	-69.755283	0.187	3.29E+15	2.50E+1 ± 6.59E+0	2.45E+1 ± 6.46E+0	0.336
130	85.004782	-69.752098	0.670	6.00E+15	4.29E+2 ± 1.90E+2	1.70E+2 ± 7.55E+1	0.467
131	85.004710	-69.752028	0.712	6.53E+15	5.65E+2 ± 2.53E+2	2.12E+2 ± 9.51E+1	0.506
132	85.004798	-69.752087	0.678	6.17E+15	4.80E+2 ± 2.16E+2	1.94E+2 ± 8.74E+1	0.496
133	85.004824	-69.752097	0.671	6.10E+15	4.50E+2 ± 1.99E+2	1.87E+2 ± 8.28E+1	0.490
134	85.003494	-69.752152	0.220	3.82E+15	2.20E+1 ± 4.36E+0	2.56E+0 ± 5.07E-1	0.100
135	85.005348	-69.752004	0.568	5.38E+15	2.81E+2 ± 1.19E+2	1.56E+2 ± 6.59E+1	0.486
136	85.005605	-69.751994	0.484	5.61E+15	2.27E+2 ± 8.11E+1	1.27E+2 ± 4.53E+1	0.475
137	85.016078	-69.749203	0.530	9.51E+15	4.45E+2 ± 1.01E+2	4.13E+2 ± 9.34E+1	0.818
138	85.064459	-69.748064	0.613	8.25E+15	3.62E+2 ± 9.16E+1	2.16E+2 ± 5.46E+1	0.551
139	85.062396	-69.748071	0.188	9.22E+15	6.11E+1 ± 5.36E+0	2.30E+1 ± 2.02E+0	0.324
140	85.064229	-69.748117	0.597	8.34E+15	3.04E+2 ± 6.94E+1	1.35E+2 ± 3.07E+1	0.441
141	85.064529	-69.748025	0.631	8.78E+15	4.26E+2 ± 1.06E+2	2.59E+2 ± 6.46E+1	0.594
142	85.032805	-69.745123	0.770	1.40E+16	1.86E+3 ± 4.83E+2	7.84E+2 ± 2.03E+2	0.936
143	85.032730	-69.745151	0.737	1.35E+16	1.59E+3 ± 4.01E+2	7.05E+2 ± 1.78E+2	0.907
144	85.034177	-69.745309	1.43	1.19E+16	3.01E+3 ± 1.26E+3	1.61E+3 ± 6.72E+2	0.985
145	85.032973	-69.745119	0.673	1.35E+16	1.34E+3 ± 3.11E+2	4.16E+2 ± 9.68E+1	0.730
146	85.032925	-69.745133	0.698	1.33E+16	1.46E+3 ± 3.63E+2	4.90E+2 ± 1.21E+2	0.777
147	85.033324	-69.745051	0.947	1.35E+16	2.29E+3 ± 6.93E+2	1.01E+3 ± 3.05E+2	0.957
148	85.016878	-69.744460	0.133	9.63E+15	4.29E+1 ± 2.96E+0	1.27E+1 ± 8.73E-1	0.286
149	85.019160	-69.742582	1.05	2.54E+16	4.25E+3 ± 6.80E+2	3.29E+3 ± 5.26E+2	1.64
150	85.019214	-69.742533	1.07	2.43E+16	4.42E+3 ± 7.71E+2	3.49E+3 ± 6.09E+2	1.67

Continued on next page

Table D.4 – continued from previous page

Clump ID	RA	Dec	Radius [pc]	$N_{^{13}CO}$ [cm^{-2}]	Total H_2 Mass [$M_\odot$]	Virial Mass [$M_\odot$]	Linewidth [km/s]
151	85.038197	-69.743894	0.214	2.01E+15	1.26E+1 ± 4.95E+0	2.35E+0 ± 9.21E-1	0.097
152	85.076163	-69.743875	0.196	2.31E+15	1.51E+1 ± 5.29E+0	1.53E+0 ± 5.33E-1	0.082
153	85.033313	-69.745061	0.923	1.32E+16	2.08E+3 ± 6.20E+2	9.26E+2 ± 2.76E+2	0.929
154	85.019125	-69.742709	0.855	2.93E+16	3.87E+3 ± 4.78E+2	2.41E+3 ± 2.97E+2	1.56
155	85.004805	-69.751950	0.801	5.97E+15	6.56E+2 ± 3.62E+2	3.18E+2 ± 1.76E+2	0.585
156	85.002766	-69.752550	0.206	2.78E+15	1.33E+1 ± 3.31E+0	2.20E+0 ± 5.46E-1	0.096
157	85.005842	-69.751976	0.443	5.76E+15	1.98E+2 ± 6.34E+1	9.30E+1 ± 2.98E+1	0.425
158	85.005933	-69.751990	0.423	5.67E+15	1.37E+2 ± 3.74E+1	6.69E+1 ± 1.83E+1	0.369
159	85.005561	-69.751990	0.477	5.78E+15	2.41E+2 ± 8.45E+1	1.28E+2 ± 4.51E+1	0.481
160	85.056708	-69.750053	0.248	1.95E+15	2.01E+1 ± 1.05E+1	2.89E+0 ± 1.50E+0	0.100
161	85.047009	-69.749880	0.257	2.95E+15	4.14E+1 ± 1.66E+1	2.49E+1 ± 9.97E+0	0.289
162	85.060246	-69.749505	0.267	3.33E+15	3.78E+1 ± 1.21E+1	5.33E+0 ± 1.70E+0	0.131
163	85.048355	-69.749300	0.306	1.79E+15	2.18E+1 ± 1.34E+1	1.94E+1 ± 1.19E+1	0.233
164	85.014717	-69.749070	0.146	5.11E+15	2.25E+1 ± 2.90E+0	7.81E+0 ± 1.01E+0	0.214
165	85.032914	-69.745132	0.631	1.35E+16	1.13E+3 ± 2.42E+2	3.41E+2 ± 7.31E+1	0.682
166	85.034546	-69.744525	0.122	4.91E+15	1.57E+1 ± 1.80E+0	2.15E+0 ± 2.46E-1	0.123
167	85.032748	-69.745160	0.568	1.39E+16	1.05E+3 ± 2.05E+2	2.86E+2 ± 5.60E+1	0.659
168	85.039140	-69.744649	0.189	2.21E+15	1.25E+1 ± 4.23E+0	5.29E+0 ± 1.79E+0	0.155
169	85.018043	-69.743266	0.495	3.06E+16	1.78E+3 ± 1.40E+2	4.07E+2 ± 3.20E+1	0.841
170	85.017555	-69.743368	0.381	3.21E+16	1.20E+3 ± 7.15E+1	1.30E+2 ± 7.75E+0	0.541
171	85.019123	-69.742707	0.855	2.88E+16	3.90E+3 ± 4.96E+2	2.39E+3 ± 3.05E+2	1.55
172	85.006433	-69.752012	0.199	8.01E+15	6.68E+1 ± 7.57E+0	1.39E+1 ± 1.57E+0	0.245
173	85.052916	-69.751634	0.251	2.12E+15	1.14E+1 ± 3.91E+0	3.14E+0 ± 1.08E+0	0.104
174	85.057943	-69.750851	0.168	3.16E+15	1.57E+1 ± 3.48E+0	1.93E+0 ± 4.28E-1	0.099
175	85.011310	-69.750659	0.155	1.85E+15	8.02E+0 ± 2.84E+0	5.94E-1 ± 2.11E-1	0.058
176	85.011413	-69.750661	0.228	2.76E+15	2.85E+1 ± 1.05E+1	2.54E+1 ± 9.31E+0	0.310
177	85.008474	-69.749881	0.220	1.64E+15	1.13E+1 ± 5.71E+0	7.57E+0 ± 3.81E+0	0.172
178	85.068230	-69.749960	0.153	1.53E+15	5.16E+0 ± 1.95E+0	2.44E-1 ± 9.19E-2	0.037
179	85.065117	-69.748154	0.162	5.82E+15	2.89E+1 ± 3.48E+0	5.82E+0 ± 7.02E-1	0.176
180	85.033029	-69.746417	0.339	3.82E+15	8.42E+1 ± 3.26E+1	3.04E+1 ± 1.18E+1	0.278
181	85.032983	-69.746461	0.291	3.42E+15	4.92E+1 ± 1.72E+1	2.25E+1 ± 7.84E+0	0.258
182	85.033188	-69.746461	0.239	3.31E+15	2.95E+1 ± 8.37E+0	1.93E+1 ± 5.46E+0	0.263
183	85.033269	-69.746468	0.163	2.48E+15	1.19E+1 ± 3.31E+0	4.36E+0 ± 1.21E+0	0.152
184	85.076050	-69.745019	0.155	1.62E+15	6.02E+0 ± 2.25E+0	1.72E+0 ± 6.43E-1	0.098
185	85.076201	-69.744528	0.194	2.55E+15	1.75E+1 ± 5.64E+0	2.67E+0 ± 8.62E-1	0.109
186	85.032952	-69.745128	0.676	1.34E+16	1.36E+3 ± 3.20E+2	4.48E+2 ± 1.06E+2	0.755
187	85.019178	-69.742569	1.04	2.55E+16	4.12E+3 ± 6.47E+2	3.18E+3 ± 4.99E+2	1.62
188	85.044689	-69.742312	0.328	6.97E+15	1.96E+2 ± 4.67E+1	1.96E+2 ± 4.69E+1	0.717

Continued on next page

Table D.4 – continued from previous page

Clump ID	RA	Dec	Radius [pc]	$N_{^{13}CO}$ [cm^{-2}]	Total H_2 Mass [$M_\odot$]	Virial Mass [$M_\odot$]	Linewidth [km/s]
189	85.026761	-69.741972	0.14	7.91E+15	3.21E+1 ± 2.57E+0	5.11E+0 ± 4.09E-1	0.177
190	85.061933	-69.735215	0.191	2.55E+15	9.18E+0 ± 2.15E+0	4.43E+0 ± 1.04E+0	0.141
191	85.051219	-69.755330	0.151	3.11E+15	9.24E+0 ± 1.61E+0	3.01E+0 ± 5.25E-1	0.131
192	85.014047	-69.752615	0.922	6.71E+15	8.46E+2 ± 4.46E+2	9.91E+2 ± 5.22E+2	0.961
193	85.014042	-69.752615	0.915	6.84E+15	8.82E+2 ± 4.61E+2	1.06E+3 ± 5.56E+2	1.00
194	85.002683	-69.752474	0.307	5.95E+15	7.78E+1 ± 1.49E+1	2.36E+1 ± 4.51E+0	0.257
195	85.065522	-69.749506	0.215	1.78E+15	1.32E+1 ± 6.36E+0	4.51E-2 ± 2.17E-2	0.013
196	85.032064	-69.746468	0.132	2.36E+15	7.02E+0 ± 1.61E+0	2.85E+0 ± 6.55E-1	0.137
197	85.048859	-69.744513	0.145	1.38E+15	4.80E+0 ± 2.05E+0	1.52E+0 ± 6.50E-1	0.095
198	85.038464	-69.744285	0.119	5.19E+15	1.63E+1 ± 1.75E+0	7.40E+0 ± 7.95E-1	0.232
199	85.039136	-69.744368	0.320	7.43E+15	1.61E+2 ± 3.18E+1	4.27E+1 ± 8.42E+0	0.339
200	85.045312	-69.742449	0.179	3.35E+15	2.24E+1 ± 5.43E+0	3.41E+0 ± 8.27E-1	0.128
201	85.041188	-69.742549	0.286	2.35E+15	2.98E+1 ± 1.42E+1	2.30E+1 ± 1.09E+1	0.263
202	85.026172	-69.742399	0.126	3.90E+15	1.09E+1 ± 1.47E+0	2.72E-1 ± 3.67E-2	0.043
203	85.010438	-69.753301	0.172	1.89E+15	8.43E+0 ± 2.96E+0	2.37E+0 ± 8.30E-1	0.109
204	85.047390	-69.753197	0.157	1.90E+15	6.52E+0 ± 2.00E+0	8.91E-1 ± 2.73E-1	0.070
205	85.014122	-69.752603	0.909	6.91E+15	8.09E+2 ± 3.99E+2	9.01E+2 ± 4.44E+2	0.923
206	85.002708	-69.751758	0.141	1.97E+15	5.40E+0 ± 1.43E+0	1.62E+0 ± 4.27E-1	0.099
207	85.057588	-69.751242	0.243	2.00E+15	2.00E+1 ± 9.94E+0	2.69E+0 ± 1.34E+0	0.098
208	85.011454	-69.750663	0.247	2.08E+15	2.03E+1 ± 9.60E+0	7.21E+0 ± 3.41E+0	0.158
209	85.024249	-69.749848	0.158	2.29E+15	1.13E+1 ± 3.42E+0	4.82E+0 ± 1.46E+0	0.162
210	85.016124	-69.749248	0.501	8.04E+15	2.87E+2 ± 6.71E+1	2.44E+2 ± 5.71E+1	0.647
211	85.016172	-69.749220	0.523	8.71E+15	3.52E+2 ± 8.07E+1	2.95E+2 ± 6.78E+1	0.697
212	85.062408	-69.748658	0.141	5.48E+15	2.10E+1 ± 2.35E+0	6.80E+0 ± 7.64E-1	0.204
213	85.033175	-69.746593	0.177	2.04E+15	8.14E+0 ± 2.51E+0	1.29E+0 ± 3.99E-1	0.079
214	85.034950	-69.745811	1.94	1.24E+16	4.98E+3 ± 2.54E+3	3.75E+3 ± 1.91E+3	1.29
215	85.035220	-69.745699	0.198	1.84E+15	1.13E+1 ± 4.82E+0	3.20E+0 ± 1.36E+0	0.118
216	85.076120	-69.745458	0.173	2.70E+15	1.74E+1 ± 5.16E+0	1.62E+0 ± 4.79E-1	0.090
217	85.032724	-69.745170	0.561	1.40E+16	1.02E+3 ± 1.96E+2	2.53E+2 ± 4.87E+1	0.623
218	85.032732	-69.745178	0.491	1.56E+16	9.07E+2 ± 1.40E+2	2.08E+2 ± 3.20E+1	0.603
219	85.032688	-69.745191	0.414	1.65E+16	6.91E+2 ± 8.54E+1	1.25E+2 ± 1.55E+1	0.511
220	85.032766	-69.745141	0.463	1.60E+16	8.07E+2 ± 1.13E+2	1.66E+2 ± 2.33E+1	0.556
221	85.035924	-69.744675	0.237	4.77E+15	5.23E+1 ± 1.14E+1	1.15E+1 ± 2.52E+0	0.205
222	85.033429	-69.744392	0.173	6.06E+15	2.94E+1 ± 3.36E+0	4.83E+0 ± 5.52E-1	0.155
223	85.006855	-69.753549	0.111	2.02E+15	5.29E+0 ± 1.34E+0	2.72E+0 ± 6.89E-1	0.145
224	85.014327	-69.752593	0.870	6.75E+15	6.73E+2 ± 3.13E+2	8.03E+2 ± 3.74E+2	0.891
225	85.010002	-69.752838	0.306	4.62E+15	8.26E+1 ± 2.38E+1	2.42E+1 ± 6.96E+0	0.261
226	85.010227	-69.752882	0.227	5.23E+15	6.63E+1 ± 1.42E+1	1.75E+1 ± 3.76E+0	0.258

Continued on next page

Table D.4 – continued from previous page

Clump ID	RA	Dec	Radius [pc]	$N_{^{13}CO}$ [cm^{-2}]	Total H_2 Mass [$M_\odot$]	Virial Mass [$M_\odot$]	Linewidth [km/s]
227	85.014278	-69.752602	0.895	6.75E+15	7.19E+2 ± 3.46E+2	8.52E+2 ± 4.10E+2	0.905
228	85.004044	-69.751613	0.362	2.95E+15	5.77E+1 ± 2.72E+1	2.04E+1 ± 9.60E+0	0.220
229	85.001649	-69.751013	0.152	2.54E+15	1.12E+1 ± 2.90E+0	5.22E+0 ± 1.36E+0	0.172
230	85.001969	-69.751008	0.199	3.06E+15	2.36E+1 ± 6.73E+0	2.74E+1 ± 7.83E+0	0.344
231	85.057438	-69.751202	0.650	6.52E+15	5.74E+2 ± 2.60E+2	5.68E+2 ± 2.58E+2	0.867
232	85.057346	-69.751100	0.549	6.76E+15	3.92E+2 ± 1.39E+2	3.48E+2 ± 1.23E+2	0.739
233	85.057405	-69.751103	0.517	6.72E+15	3.53E+2 ± 1.20E+2	3.11E+2 ± 1.06E+2	0.719
234	85.055700	-69.750739	0.179	3.16E+15	1.91E+1 ± 4.69E+0	2.08E+0 ± 5.11E-1	0.100
235	85.061689	-69.749416	0.299	2.82E+15	4.03E+1 ± 1.70E+1	8.04E+0 ± 3.39E+0	0.152
236	85.016080	-69.749249	0.498	7.30E+15	2.47E+2 ± 6.20E+1	1.74E+2 ± 4.37E+1	0.548
237	85.064711	-69.748134	0.503	7.76E+15	2.31E+2 ± 5.12E+1	3.34E+1 ± 7.41E+0	0.239
238	85.034372	-69.747920	0.206	1.46E+15	8.52E+0 ± 4.42E+0	1.63E+0 ± 8.44E-1	0.082
239	85.037453	-69.746252	0.607	7.85E+15	5.60E+2 ± 1.90E+2	3.33E+2 ± 1.13E+2	0.687
240	85.037500	-69.746232	0.589	7.53E+15	4.99E+2 ± 1.70E+2	3.04E+2 ± 1.03E+2	0.666
241	85.038331	-69.745080	0.164	3.10E+15	1.57E+1 ± 3.60E+0	7.88E-1 ± 1.80E-1	0.064
242	85.037434	-69.746293	0.623	7.77E+15	5.92E+2 ± 2.09E+2	3.43E+2 ± 1.21E+2	0.689
243	85.044422	-69.742274	0.231	5.43E+15	7.41E+1 ± 1.59E+1	7.15E+1 ± 1.53E+1	0.516
244	85.057222	-69.740491	0.393	2.35E+15	6.35E+1 ± 4.42E+1	3.12E+1 ± 2.17E+1	0.261
245	85.057842	-69.740878	0.185	1.97E+15	1.41E+1 ± 6.00E+0	6.91E+0 ± 2.94E+0	0.179
246	85.057066	-69.740304	0.268	2.48E+15	3.45E+1 ± 1.64E+1	1.19E+1 ± 5.65E+0	0.195
247	85.055232	-69.739636	0.275	2.74E+15	4.42E+1 ± 2.03E+1	2.07E+1 ± 9.52E+0	0.254
248	85.019164	-69.738607	0.183	2.09E+15	6.44E+0 ± 1.70E+0	1.03E+1 ± 2.71E+0	0.220
249	85.004731	-69.754313	0.184	2.73E+15	1.31E+1 ± 3.31E+0	2.60E+0 ± 6.58E-1	0.110
250	85.006568	-69.752928	0.229	1.87E+15	1.08E+1 ± 4.36E+0	1.34E+1 ± 5.40E+0	0.224
251	85.008489	-69.752569	0.169	2.55E+15	9.91E+0 ± 2.41E+0	5.55E+0 ± 1.35E+0	0.168
252	85.004779	-69.751943	0.186	3.17E+15	1.21E+1 ± 2.35E+0	6.96E+0 ± 1.35E+0	0.179
253	85.003524	-69.751694	0.259	2.89E+15	2.69E+1 ± 8.94E+0	2.83E+0 ± 9.41E-1	0.097
254	85.049565	-69.751134	0.212	4.45E+15	5.26E+1 ± 1.28E+1	6.45E+1 ± 1.57E+1	0.512
255	85.005798	-69.750757	0.184	1.96E+15	6.93E+0 ± 2.10E+0	2.14E+0 ± 6.48E-1	0.100
256	85.063966	-69.750155	0.718	1.00E+16	1.08E+3 ± 3.52E+2	7.69E+2 ± 2.51E+2	0.960
257	85.063946	-69.750171	0.691	1.03E+16	1.02E+3 ± 3.12E+2	7.28E+2 ± 2.22E+2	0.953
258	85.063687	-69.750040	0.170	5.13E+15	3.37E+1 ± 5.29E+0	1.88E+1 ± 2.96E+0	0.309
259	85.014311	-69.749417	0.265	5.43E+15	6.57E+1 ± 1.33E+1	4.32E+1 ± 8.71E+0	0.374
260	85.013966	-69.749409	0.190	5.18E+15	3.20E+1 ± 4.82E+0	1.22E+1 ± 1.84E+0	0.235
261	85.064677	-69.748211	0.416	8.00E+15	1.36E+2 ± 2.20E+1	2.45E+1 ± 3.97E+0	0.225
262	85.044108	-69.747106	0.329	3.85E+15	8.23E+1 ± 3.11E+1	6.96E+1 ± 2.63E+1	0.427
263	85.044421	-69.747106	0.183	4.13E+15	2.71E+1 ± 5.29E+0	6.70E+0 ± 1.31E+0	0.178
264	85.032623	-69.745226	0.308	1.60E+16	3.35E+2 ± 2.99E+1	7.10E+1 ± 6.35E+0	0.445

Continued on next page

Table D.4 – continued from previous page

Clump ID	RA	Dec	Radius [pc]	$N_{^{13}CO}$ [cm^{-2}]	Total H_2 Mass [$M_\odot$]	Virial Mass [$M_\odot$]	Linewidth [km/s]
265	85.075661	-69.745077	0.207	1.97E+15	9.70E+0 ± 3.42E+0	1.52E+0 ± 5.39E-1	0.080
266	85.075617	-69.744956	0.235	2.37E+15	1.71E+1 ± 6.07E+0	9.44E+0 ± 3.36E+0	0.186
267	85.039379	-69.744370	0.281	6.32E+15	1.04E+2 ± 2.10E+1	1.49E+1 ± 3.02E+0	0.214
268	85.015699	-69.742714	0.172	6.33E+15	4.19E+1 ± 5.36E+0	1.45E+1 ± 1.85E+0	0.269
269	85.037232	-69.742232	0.219	2.55E+15	2.34E+1 ± 8.77E+0	1.01E+1 ± 3.78E+0	0.199
270	85.055632	-69.739674	0.181	1.97E+15	1.21E+1 ± 4.75E+0	1.19E+0 ± 4.71E-1	0.075
271	85.060133	-69.734410	0.173	2.33E+15	7.45E+0 ± 1.80E+0	3.97E+0 ± 9.59E-1	0.141
272	85.030510	-69.758467	0.215	2.17E+15	1.19E+1 ± 4.04E+0	1.41E+0 ± 4.81E-1	0.075
273	85.004792	-69.753173	0.593	4.04E+15	1.96E+2 ± 1.06E+2	6.03E+2 ± 3.27E+2	0.935
274	85.005608	-69.753481	0.338	4.05E+15	7.86E+1 ± 2.69E+1	3.12E+1 ± 1.07E+1	0.282
275	85.005101	-69.753294	0.519	4.02E+15	1.54E+2 ± 7.48E+1	2.93E+2 ± 1.42E+2	0.696
276	85.004829	-69.753177	0.596	4.13E+15	2.02E+2 ± 1.08E+2	5.92E+2 ± 3.16E+2	0.924
277	85.005343	-69.753361	0.423	4.28E+15	1.28E+2 ± 5.16E+1	1.31E+2 ± 5.25E+1	0.516
278	85.018929	-69.752904	0.227	1.53E+15	1.31E+1 ± 7.89E+0	1.14E+0 ± 6.84E-1	0.066
279	85.009891	-69.752850	0.158	4.63E+15	2.04E+1 ± 2.90E+0	2.32E+0 ± 3.30E-1	0.112
280	85.014028	-69.751157	0.185	3.73E+15	3.30E+1 ± 8.29E+0	3.39E+1 ± 8.52E+0	0.397
281	85.057314	-69.751207	0.377	7.59E+15	2.58E+2 ± 6.25E+1	1.44E+2 ± 3.49E+1	0.573
282	85.057526	-69.751131	0.465	6.97E+15	3.19E+2 ± 9.75E+1	1.91E+2 ± 5.82E+1	0.594
283	85.011275	-69.750008	0.696	1.58E+16	1.69E+3 ± 3.48E+2	5.73E+2 ± 1.18E+2	0.842
284	85.011217	-69.750007	0.683	1.50E+16	1.50E+3 ± 3.12E+2	5.21E+2 ± 1.09E+2	0.810
285	85.036146	-69.749831	0.470	3.35E+15	1.05E+2 ± 5.54E+1	1.53E+2 ± 8.03E+1	0.528
286	85.016231	-69.748835	0.170	3.61E+15	1.96E+1 ± 3.98E+0	1.09E+0 ± 2.21E-1	0.074
287	85.064394	-69.748081	0.609	8.13E+15	3.41E+2 ± 8.56E+1	1.55E+2 ± 3.89E+1	0.468
288	85.035057	-69.748344	0.199	2.31E+15	1.76E+1 ± 6.59E+0	2.91E+1 ± 1.09E+1	0.355
289	85.035485	-69.747363	0.154	2.14E+15	6.61E+0 ± 1.70E+0	1.76E+0 ± 4.54E-1	0.099
290	85.042795	-69.747079	0.159	2.06E+15	8.81E+0 ± 2.79E+0	7.81E+0 ± 2.47E+0	0.206
291	85.043980	-69.747103	0.360	3.76E+15	9.16E+1 ± 3.78E+1	7.26E+1 ± 2.99E+1	0.417
292	85.035405	-69.745520	0.140	2.22E+15	9.02E+0 ± 2.57E+0	1.34E+0 ± 3.81E-1	0.091
293	85.032672	-69.745174	0.257	1.58E+16	2.03E+2 ± 1.45E+1	5.05E+1 ± 3.61E+0	0.411
294	85.032770	-69.745117	0.214	1.38E+16	1.04E+2 ± 6.51E+0	3.37E+1 ± 2.11E+0	0.369
295	85.037545	-69.745995	0.448	7.76E+15	3.42E+2 ± 9.21E+1	1.54E+2 ± 4.15E+1	0.544
296	85.037473	-69.746270	0.576	7.83E+15	4.81E+2 ± 1.52E+2	2.17E+2 ± 6.83E+1	0.569
297	85.032737	-69.745217	0.153	1.22E+16	4.32E+1 ± 2.10E+0	1.13E+1 ± 5.46E-1	0.252
298	85.076755	-69.745318	0.151	1.87E+15	5.44E+0 ± 1.56E+0	6.55E-1 ± 1.88E-1	0.061
299	84.994195	-69.744753	0.141	1.99E+15	6.37E+0 ± 1.80E+0	2.72E+0 ± 7.68E-1	0.129
300	85.033775	-69.744674	0.158	7.13E+15	2.00E+1 ± 1.47E+0	2.16E+0 ± 1.59E-1	0.108
301	85.026362	-69.743707	0.253	1.33E+16	2.60E+2 ± 2.73E+1	7.41E+1 ± 7.77E+0	0.502
302	85.055744	-69.741696	0.184	1.85E+15	1.14E+1 ± 4.82E+0	3.23E+0 ± 1.37E+0	0.123

Continued on next page

Table D.4 – continued from previous page

Clump ID	RA	Dec	Radius [pc]	$N_{^{13}CO}$ [cm^{-2}]	Total H_2 Mass [$M_\odot$]	Virial Mass [$M_\odot$]	Linewidth [km/s]
303	85.064145	-69.740374	0.151	1.35E+15	4.23E+0 ± 1.75E+0	6.58E+0 ± 2.72E+0	0.193
304	85.064247	-69.738458	0.166	2.21E+15	7.71E+0 ± 2.05E+0	4.85E-1 ± 1.29E-1	0.050
305	85.005844	-69.753584	0.202	2.72E+15	1.76E+1 ± 5.16E+0	4.88E-1 ± 1.43E-1	0.046
306	85.053992	-69.752168	0.136	2.08E+15	6.65E+0 ± 1.80E+0	2.73E-1 ± 7.40E-2	0.042
307	85.005460	-69.750952	0.322	2.72E+15	4.57E+1 ± 2.16E+1	1.75E+1 ± 8.28E+0	0.216
308	85.002315	-69.751000	0.181	2.57E+15	8.82E+0 ± 2.00E+0	3.27E+0 ± 7.40E-1	0.125
309	85.003718	-69.750668	0.205	2.39E+15	8.88E+0 ± 2.25E+0	1.90E+0 ± 4.81E-1	0.089
310	85.052852	-69.750646	0.164	3.75E+15	2.12E+1 ± 4.23E+0	3.02E+0 ± 6.02E-1	0.126
311	85.011119	-69.750566	0.169	3.83E+15	1.69E+1 ± 2.90E+0	1.96E+0 ± 3.38E-1	0.100
312	84.997837	-69.750261	0.331	2.14E+15	3.04E+1 ± 1.68E+1	4.90E+0 ± 2.70E+0	0.113
313	84.997690	-69.750232	0.367	2.03E+15	3.70E+1 ± 2.46E+1	8.98E+0 ± 5.96E+0	0.145
314	85.063997	-69.750171	0.637	1.00E+16	7.75E+2 ± 2.14E+2	6.29E+2 ± 1.74E+2	0.922
315	85.036327	-69.749872	0.404	3.34E+15	7.12E+1 ± 3.09E+1	1.06E+2 ± 4.63E+1	0.476
316	85.036417	-69.749715	0.295	2.90E+15	4.63E+1 ± 2.01E+1	4.65E+1 ± 2.02E+1	0.368
317	84.998009	-69.750107	0.236	2.20E+15	1.64E+1 ± 6.44E+0	1.22E+0 ± 4.79E-1	0.067
318	85.025914	-69.746367	0.155	1.46E+15	4.01E+0 ± 1.43E+0	3.26E-1 ± 1.16E-1	0.043
319	85.010722	-69.743928	0.151	1.45E+15	4.48E+0 ± 1.70E+0	1.75E+0 ± 6.65E-1	0.100
320	85.060286	-69.740993	0.247	3.10E+15	3.95E+1 ± 1.43E+1	1.34E+1 ± 4.85E+0	0.216
321	85.062076	-69.740515	0.227	1.31E+15	5.89E+0 ± 3.01E+0	6.19E-1 ± 3.17E-1	0.048
322	85.054864	-69.739620	0.149	3.11E+15	1.53E+1 ± 3.42E+0	1.73E+0 ± 3.89E-1	0.100
323	85.061587	-69.739470	0.298	1.81E+15	2.09E+1 ± 1.23E+1	2.94E+0 ± 1.73E+0	0.092
324	85.022473	-69.758403	0.194	2.15E+15	6.75E+0 ± 1.75E+0	1.67E-1 ± 4.33E-2	0.027
325	85.012706	-69.752893	0.543	4.36E+15	1.93E+2 ± 9.23E+1	6.07E+1 ± 2.91E+1	0.310
326	85.006357	-69.752203	0.165	2.46E+15	7.59E+0 ± 1.70E+0	1.33E+0 ± 3.00E-1	0.083
327	85.001650	-69.751983	0.161	2.03E+15	7.54E+0 ± 2.25E+0	3.63E-1 ± 1.08E-1	0.044
328	85.057161	-69.750986	0.275	2.89E+15	2.47E+1 ± 7.89E+0	3.16E+0 ± 1.01E+0	0.099
329	85.011068	-69.749978	0.603	1.41E+16	9.73E+2 ± 1.80E+2	3.42E+2 ± 6.32E+1	0.699
330	85.064012	-69.750177	0.649	9.57E+15	7.39E+2 ± 2.14E+2	5.79E+2 ± 1.67E+2	0.876
331	85.063876	-69.749935	0.518	9.16E+15	4.49E+2 ± 1.08E+2	2.31E+2 ± 5.56E+1	0.620
332	85.063560	-69.749727	0.343	9.72E+15	2.60E+2 ± 4.36E+1	6.90E+1 ± 1.15E+1	0.416
333	85.063921	-69.749924	0.516	8.40E+15	3.73E+2 ± 9.32E+1	2.25E+2 ± 5.61E+1	0.612
334	85.063684	-69.749743	0.160	4.77E+15	2.26E+1 ± 3.25E+0	6.70E+0 ± 9.62E-1	0.190
335	85.064952	-69.748959	0.167	2.99E+15	1.33E+1 ± 2.96E+0	7.07E+0 ± 1.57E+0	0.191
336	85.029152	-69.749078	0.193	1.36E+15	5.81E+0 ± 2.79E+0	1.95E+0 ± 9.35E-1	0.093
337	85.017019	-69.749170	0.312	7.31E+15	1.31E+2 ± 2.38E+1	5.53E+1 ± 1.01E+1	0.391
338	85.065765	-69.747776	0.247	5.27E+15	3.61E+1 ± 5.64E+0	2.18E+0 ± 3.41E-1	0.087
339	85.035920	-69.746776	0.157	3.20E+15	8.96E+0 ± 1.47E+0	2.60E+0 ± 4.27E-1	0.119
340	85.076180	-69.744151	0.153	2.35E+15	8.46E+0 ± 2.15E+0	1.23E+0 ± 3.12E-1	0.083

Continued on next page

Table D.4 – continued from previous page

Clump ID	RA	Dec	Radius [pc]	$N_{^{13}CO}$ [cm^{-2}]	Total H_2 Mass [$M_\odot$]	Virial Mass [$M_\odot$]	Linewidth [km/s]
341	85.032239	-69.744039	0.187	3.14E+15	1.93E+1 ± 4.82E+0	4.60E+0 ± 1.15E+0	0.145
342	85.070366	-69.740223	0.179	2.35E+15	7.52E+0 ± 1.80E+0	2.06E+0 ± 4.93E-1	0.100
343	85.065624	-69.738752	0.274	1.88E+15	8.79E+0 ± 3.19E+0	8.18E-1 ± 2.97E-1	0.051
344	85.005589	-69.753554	0.231	2.89E+15	1.98E+1 ± 5.64E+0	1.17E+0 ± 3.33E-1	0.066
345	85.005455	-69.753416	0.334	3.10E+15	4.08E+1 ± 1.50E+1	6.30E+0 ± 2.31E+0	0.127
346	85.015058	-69.753188	0.183	1.92E+15	1.08E+1 ± 4.17E+0	2.12E+0 ± 8.19E-1	0.100
347	85.002857	-69.752609	0.174	2.52E+15	1.24E+1 ± 3.42E+0	8.33E+0 ± 2.31E+0	0.203
348	85.009556	-69.752556	0.149	2.66E+15	9.26E+0 ± 2.05E+0	8.22E-1 ± 1.82E-1	0.069
349	85.017865	-69.752549	0.149	1.61E+15	5.42E+0 ± 1.95E+0	1.73E+0 ± 6.22E-1	0.100
350	85.010026	-69.752655	0.244	3.68E+15	4.10E+1 ± 1.17E+1	3.53E+1 ± 1.01E+1	0.353
351	85.016364	-69.752378	0.437	7.80E+15	3.35E+2 ± 8.87E+1	9.61E+1 ± 2.54E+1	0.435
352	85.007040	-69.752150	0.194	1.93E+15	6.18E+0 ± 1.80E+0	1.10E+0 ± 3.19E-1	0.070
353	85.059141	-69.750605	0.224	3.73E+15	3.34E+1 ± 8.45E+0	2.93E+0 ± 7.40E-1	0.106
354	85.036127	-69.750261	0.146	3.40E+15	1.63E+1 ± 3.31E+0	1.47E+1 ± 2.97E+0	0.294
355	85.011010	-69.749964	0.568	1.24E+16	6.85E+2 ± 1.30E+2	3.07E+2 ± 5.81E+1	0.682
356	85.010271	-69.749957	0.386	1.21E+16	3.79E+2 ± 5.52E+1	2.43E+2 ± 3.55E+1	0.736
357	85.010245	-69.749977	0.371	1.12E+16	3.03E+2 ± 4.42E+1	2.44E+2 ± 3.55E+1	0.752
358	85.010230	-69.750138	0.191	4.36E+15	2.44E+1 ± 4.17E+0	1.96E+0 ± 3.34E-1	0.094
359	85.010263	-69.750087	0.320	1.02E+16	2.00E+2 ± 2.73E+1	1.37E+2 ± 1.87E+1	0.607
360	85.063593	-69.749716	0.333	6.82E+15	1.32E+2 ± 2.69E+1	4.17E+1 ± 8.48E+0	0.329
361	85.063636	-69.749656	0.313	6.46E+15	1.09E+2 ± 2.19E+1	2.34E+1 ± 4.68E+0	0.254
362	85.016833	-69.749145	0.204	7.79E+15	6.28E+1 ± 7.19E+0	2.02E+1 ± 2.32E+0	0.292
363	85.073165	-69.747785	0.176	1.80E+15	6.26E+0 ± 2.05E+0	1.90E+0 ± 6.21E-1	0.096
364	85.068867	-69.747499	0.198	2.96E+15	2.13E+1 ± 6.07E+0	2.80E+0 ± 7.99E-1	0.110
365	85.043249	-69.744790	0.518	6.86E+15	4.68E+2 ± 1.77E+2	9.09E+2 ± 3.45E+2	1.23
366	85.013124	-69.744344	0.194	1.43E+15	3.91E+0 ± 1.43E+0	4.71E-1 ± 1.72E-1	0.046
367	85.035413	-69.744260	0.244	4.50E+15	5.11E+1 ± 1.21E+1	6.18E+0 ± 1.46E+0	0.148
368	85.011482	-69.743925	0.231	2.40E+15	2.15E+1 ± 8.45E+0	6.82E+0 ± 2.68E+0	0.159
369	85.041888	-69.742425	0.188	2.48E+15	2.00E+1 ± 7.19E+0	2.02E+1 ± 7.28E+0	0.304
370	85.017241	-69.739056	0.521	4.61E+15	2.57E+2 ± 1.31E+2	1.08E+2 ± 5.51E+1	0.423
371	84.998770	-69.737014	0.131	2.11E+15	5.66E+0 ± 1.38E+0	1.43E+0 ± 3.50E-1	0.097
372	85.007300	-69.753728	0.216	1.75E+15	8.59E+0 ± 3.42E+0	4.77E+0 ± 1.90E+0	0.138
373	85.014318	-69.753056	0.271	5.09E+15	8.20E+1 ± 2.03E+1	1.77E+1 ± 4.39E+0	0.237
374	85.015000	-69.752556	0.801	6.46E+15	5.65E+2 ± 2.57E+2	4.08E+2 ± 1.86E+2	0.662
375	85.011465	-69.752841	0.206	2.48E+15	1.90E+1 ± 6.66E+0	2.31E+0 ± 8.11E-1	0.098
376	85.010483	-69.752714	0.308	3.65E+15	6.12E+1 ± 2.16E+1	4.04E+1 ± 1.43E+1	0.336
377	85.016211	-69.752379	0.484	7.71E+15	3.67E+2 ± 1.03E+2	1.32E+2 ± 3.71E+1	0.484
378	85.006349	-69.751651	0.142	1.65E+15	4.54E+0 ± 1.43E+0	3.70E-1 ± 1.16E-1	0.047

Continued on next page

Table D.4 – continued from previous page

Clump ID	RA	Dec	Radius [pc]	$N_{^{13}CO}$ [cm^{-2}]	Total H_2 Mass [$M_\odot$]	Virial Mass [$M_\odot$]	Linewidth [km/s]
379	85.052243	-69.750831	0.208	7.28E+15	7.78E+1 ± 1.10E+1	3.40E+1 ± 4.80E+0	0.375
380	85.062014	-69.750930	0.137	1.46E+15	4.25E+0 ± 1.56E+0	4.39E-1 ± 1.61E-1	0.053
381	84.997420	-69.750376	0.329	8.94E+15	2.02E+2 ± 3.38E+1	5.98E+1 ± 1.00E+1	0.395
382	84.997414	-69.750366	0.329	9.59E+15	2.33E+2 ± 3.78E+1	8.83E+1 ± 1.43E+1	0.480
383	85.010952	-69.750552	0.153	3.79E+15	1.36E+1 ± 2.15E+0	1.34E+0 ± 2.12E-1	0.087
384	85.011059	-69.749988	0.616	1.40E+16	9.87E+2 ± 1.87E+2	3.50E+2 ± 6.64E+1	0.700
385	85.063984	-69.750183	0.653	9.79E+15	7.84E+2 ± 2.25E+2	6.49E+2 ± 1.87E+2	0.925
386	85.065620	-69.747463	0.167	6.31E+15	2.16E+1 ± 2.00E+0	6.78E+0 ± 6.26E-1	0.187
387	85.043840	-69.746990	0.252	2.20E+15	1.85E+1 ± 7.65E+0	7.25E+0 ± 3.00E+0	0.157
388	85.072930	-69.745933	0.168	2.09E+15	6.93E+0 ± 1.90E+0	1.11E+1 ± 3.04E+0	0.239
389	85.037611	-69.745612	0.252	5.14E+15	5.67E+1 ± 1.15E+1	2.20E+1 ± 4.46E+0	0.274
390	85.043207	-69.744774	0.481	5.88E+15	3.27E+2 ± 1.31E+2	7.83E+2 ± 3.12E+2	1.18
391	85.032800	-69.744926	0.134	1.21E+16	3.18E+1 ± 1.34E+0	2.81E+0 ± 1.19E-1	0.134
392	85.029830	-69.743054	0.195	1.86E+15	1.26E+1 ± 5.57E+0	1.89E+1 ± 8.34E+0	0.289
393	85.061614	-69.740157	0.282	1.74E+15	1.85E+1 ± 1.09E+1	1.14E+1 ± 6.72E+0	0.187
394	85.014579	-69.753035	0.187	2.56E+15	1.33E+1 ± 3.73E+0	3.07E-1 ± 8.61E-2	0.038
395	85.014011	-69.753016	0.359	4.27E+15	1.02E+2 ± 3.67E+1	2.80E+1 ± 1.01E+1	0.259
396	85.009672	-69.752580	0.131	2.73E+15	7.49E+0 ± 1.43E+0	4.24E-1 ± 8.07E-2	0.053
397	85.016330	-69.752367	0.448	7.76E+15	3.46E+2 ± 9.37E+1	1.15E+2 ± 3.12E+1	0.470
398	85.017399	-69.752275	0.145	3.36E+15	1.38E+1 ± 2.62E+0	4.09E+0 ± 7.76E-1	0.156
399	85.004325	-69.752287	0.183	1.81E+15	7.86E+0 ± 2.84E+0	8.04E+0 ± 2.91E+0	0.195
400	85.008220	-69.751766	0.245	1.67E+15	1.15E+1 ± 5.71E+0	1.53E+0 ± 7.58E-1	0.073
401	85.002734	-69.750884	0.237	1.81E+15	1.21E+1 ± 5.43E+0	4.81E+0 ± 2.16E+0	0.132
402	85.057306	-69.751241	0.323	7.36E+15	1.80E+2 ± 3.80E+1	5.20E+1 ± 1.10E+1	0.372
403	84.997543	-69.750447	0.270	8.64E+15	1.22E+2 ± 1.67E+1	2.96E+1 ± 4.05E+0	0.307
404	85.071501	-69.750505	0.143	2.28E+15	7.03E+0 ± 1.70E+0	1.94E+0 ± 4.70E-1	0.108
405	85.010218	-69.750082	0.318	8.66E+15	1.58E+2 ± 2.46E+1	9.01E+1 ± 1.40E+1	0.494
406	85.010035	-69.750080	0.267	8.14E+15	1.15E+2 ± 1.67E+1	3.99E+1 ± 5.79E+0	0.358
407	85.014136	-69.749908	0.160	2.28E+15	1.00E+1 ± 2.90E+0	1.40E+0 ± 4.05E-1	0.087
408	85.063483	-69.749861	0.161	5.22E+15	2.03E+1 ± 2.41E+0	2.85E+0 ± 3.39E-1	0.124
409	85.009661	-69.749775	0.210	5.51E+15	2.80E+1 ± 3.60E+0	2.41E+0 ± 3.10E-1	0.099
410	85.010291	-69.749966	0.381	1.10E+16	3.21E+2 ± 4.99E+1	2.43E+2 ± 3.78E+1	0.741
411	85.065714	-69.749065	0.193	2.40E+15	1.43E+1 ± 4.55E+0	5.30E+0 ± 1.69E+0	0.154
412	85.064898	-69.748477	0.210	2.67E+15	2.12E+1 ± 7.04E+0	1.21E+0 ± 4.03E-1	0.071
413	85.043637	-69.746878	0.112	2.98E+15	8.16E+0 ± 1.43E+0	1.30E+0 ± 2.28E-1	0.100
414	85.076413	-69.746182	0.206	4.36E+15	3.51E+1 ± 7.19E+0	1.78E+1 ± 3.65E+0	0.273
415	85.076361	-69.746211	0.143	4.29E+15	1.84E+1 ± 2.79E+0	2.56E+0 ± 3.89E-1	0.124
416	85.037343	-69.745570	0.153	4.76E+15	1.77E+1 ± 2.25E+0	8.51E+0 ± 1.08E+0	0.218

Continued on next page

Table D.4 – continued from previous page

Clump ID	RA	Dec	Radius [pc]	$N_{^{13}CO}$ [cm^{-2}]	Total H_2 Mass [$M_\odot$]	Virial Mass [$M_\odot$]	Linewidth [km/s]
417	85.003159	-69.744711	0.146	1.65E+15	4.53E+0 ± 1.43E+0	1.64E+0 ± 5.18E-1	0.098
418	85.020006	-69.742878	0.255	1.35E+16	1.97E+2 ± 1.75E+1	5.32E+1 ± 4.72E+0	0.424
419	85.016060	-69.742032	0.266	3.87E+15	4.20E+1 ± 1.12E+1	2.36E+1 ± 6.32E+0	0.276
420	85.043587	-69.741443	0.189	1.71E+15	9.38E+0 ± 4.04E+0	4.29E+0 ± 1.85E+0	0.140
421	85.017386	-69.739184	0.438	5.01E+15	1.92E+2 ± 7.48E+1	7.73E+1 ± 3.01E+1	0.389
422	85.017457	-69.739316	0.392	5.36E+15	1.57E+2 ± 4.96E+1	4.89E+1 ± 1.55E+1	0.328
423	85.017190	-69.738874	0.185	5.60E+15	5.15E+1 ± 8.77E+0	2.90E+1 ± 4.94E+0	0.367
424	85.015819	-69.738714	0.136	1.52E+15	5.45E+0 ± 2.15E+0	8.14E-1 ± 3.21E-1	0.072
425	85.014109	-69.753096	0.255	3.15E+15	3.03E+1 ± 9.35E+0	3.43E+0 ± 1.06E+0	0.108
426	85.005371	-69.752715	0.207	2.14E+15	1.37E+1 ± 5.09E+0	7.58E-2 ± 2.82E-2	0.018
427	85.059752	-69.751813	0.179	1.90E+15	9.21E+0 ± 3.36E+0	8.56E-1 ± 3.13E-1	0.064
428	85.002333	-69.751439	0.234	2.24E+15	1.73E+1 ± 6.73E+0	7.04E+0 ± 2.74E+0	0.161
429	85.007559	-69.751619	0.395	1.87E+15	2.89E+1 ± 1.92E+1	2.85E+1 ± 1.89E+1	0.249
430	85.016513	-69.750662	0.143	1.58E+15	4.24E+0 ± 1.38E+0	1.02E+0 ± 3.33E-1	0.078
431	85.010384	-69.750332	0.152	5.35E+15	2.05E+1 ± 2.35E+0	1.36E+0 ± 1.57E-1	0.088
432	85.010154	-69.750193	0.211	7.76E+15	7.09E+1 ± 8.69E+0	2.66E+1 ± 3.27E+0	0.329
433	85.061915	-69.749334	0.117	2.40E+15	6.43E+0 ± 1.38E+0	3.50E-1 ± 7.52E-2	0.051
434	85.073297	-69.747757	0.121	1.83E+15	5.75E+0 ± 1.75E+0	5.50E-1 ± 1.67E-1	0.062
435	85.041153	-69.746064	0.181	2.17E+15	1.10E+1 ± 3.60E+0	1.06E+1 ± 3.46E+0	0.224
436	85.040934	-69.746060	0.202	2.36E+15	1.74E+1 ± 6.29E+0	3.42E+1 ± 1.24E+1	0.381
437	85.038201	-69.745063	0.175	3.47E+15	2.76E+1 ± 7.04E+0	1.26E+1 ± 3.21E+0	0.248
438	85.051084	-69.743040	0.550	7.25E+15	4.10E+2 ± 1.34E+2	3.99E+2 ± 1.30E+2	0.790
439	85.019699	-69.742966	0.213	7.88E+15	7.06E+1 ± 8.45E+0	6.50E+0 ± 7.77E-1	0.162
440	85.004992	-69.753101	0.361	2.88E+15	4.41E+1 ± 1.88E+1	1.90E+1 ± 8.10E+0	0.213
441	85.005145	-69.752985	0.196	3.63E+15	1.93E+1 ± 3.85E+0	2.54E+0 ± 5.07E-1	0.106
442	85.010331	-69.752723	0.219	2.96E+15	2.23E+1 ± 6.51E+0	1.61E+0 ± 4.69E-1	0.079
443	85.012580	-69.752846	0.209	2.35E+15	1.66E+1 ± 5.93E+0	5.20E+0 ± 1.85E+0	0.146
444	85.010164	-69.752687	0.229	3.27E+15	2.99E+1 ± 8.69E+0	9.67E+0 ± 2.81E+0	0.191
445	85.006379	-69.751926	0.174	1.84E+15	5.46E+0 ± 1.61E+0	2.21E+0 ± 6.51E-1	0.105
446	85.003221	-69.751493	0.130	1.91E+15	6.12E+0 ± 1.80E+0	8.36E-1 ± 2.46E-1	0.074
447	85.057191	-69.751298	0.265	6.97E+15	1.07E+2 ± 1.89E+1	3.19E+1 ± 5.64E+0	0.321
448	85.061886	-69.751126	0.384	3.60E+15	7.61E+1 ± 3.06E+1	4.41E+1 ± 1.77E+1	0.314
449	85.062957	-69.750933	0.171	3.86E+15	2.58E+1 ± 5.43E+0	1.31E+1 ± 2.76E+0	0.257
450	85.035025	-69.749613	0.192	1.71E+15	9.86E+0 ± 4.36E+0	4.48E+0 ± 1.98E+0	0.142
451	85.039647	-69.748498	0.380	1.44E+16	6.67E+2 ± 9.95E+1	2.16E+2 ± 3.22E+1	0.699
452	85.070396	-69.748150	0.363	1.83E+15	2.68E+1 ± 1.77E+1	9.23E-1 ± 6.08E-1	0.047
453	85.069333	-69.748139	0.204	2.04E+15	1.07E+1 ± 3.79E+0	7.44E-1 ± 2.64E-1	0.056
454	85.071024	-69.748172	0.489	1.83E+15	3.73E+1 ± 2.91E+1	4.92E+0 ± 3.83E+0	0.093

Continued on next page

Table D.4 – continued from previous page

Clump ID	RA	Dec	Radius [pc]	$N_{^{13}CO}$ [cm^{-2}]	Total H_2 Mass [$M_\odot$]	Virial Mass [$M_\odot$]	Linewidth [km/s]
455	85.070059	-69.748061	0.506	2.63E+15	8.75E+1 ± 6.03E+1	1.15E+2 ± 7.94E+1	0.443
456	85.033938	-69.748034	0.189	2.10E+15	1.43E+1 ± 5.57E+0	8.28E+0 ± 3.23E+0	0.194
457	85.015963	-69.746573	0.211	2.50E+15	2.19E+1 ± 8.13E+0	2.20E+1 ± 8.15E+0	0.299
458	85.037559	-69.746152	0.274	7.35E+15	1.10E+2 ± 1.82E+1	2.26E+1 ± 3.75E+0	0.267
459	85.016322	-69.746535	0.226	1.35E+15	7.07E+0 ± 3.79E+0	2.87E+0 ± 1.53E+0	0.104
460	85.071724	-69.746367	0.244	1.70E+15	7.01E+0 ± 2.62E+0	7.24E-1 ± 2.71E-1	0.051
461	85.031722	-69.746029	0.167	5.76E+15	3.45E+1 ± 4.62E+0	6.14E+0 ± 8.22E-1	0.178
462	85.043584	-69.745028	0.313	4.96E+15	1.16E+2 ± 3.55E+1	1.43E+2 ± 4.39E+1	0.627
463	85.050256	-69.743425	0.294	1.00E+16	2.47E+2 ± 3.87E+1	2.43E+2 ± 3.80E+1	0.843
464	85.013700	-69.743020	0.152	2.87E+15	1.54E+1 ± 3.91E+0	6.21E+0 ± 1.57E+0	0.188
465	85.022262	-69.741974	0.156	9.20E+15	4.57E+1 ± 3.48E+0	9.19E+0 ± 7.01E-1	0.225
466	85.060415	-69.740807	0.257	2.00E+15	2.11E+1 ± 1.08E+1	2.26E+1 ± 1.16E+1	0.275
467	85.056431	-69.740751	0.146	1.57E+15	6.53E+0 ± 2.68E+0	1.15E+0 ± 4.73E-1	0.082
468	85.017644	-69.739627	0.280	4.54E+15	7.07E+1 ± 1.94E+1	2.12E+1 ± 5.81E+0	0.255
469	85.061728	-69.739291	0.152	2.06E+15	8.00E+0 ± 2.41E+0	1.66E+0 ± 5.00E-1	0.097
470	85.003600	-69.736624	0.126	1.94E+15	5.10E+0 ± 1.34E+0	1.10E-1 ± 2.89E-2	0.027
471	85.010035	-69.756785	0.218	2.91E+15	1.93E+1 ± 5.36E+0	1.23E+1 ± 3.43E+0	0.220
472	85.005726	-69.753604	0.149	2.42E+15	7.88E+0 ± 1.85E+0	3.11E+0 ± 7.28E-1	0.134
473	85.020115	-69.753116	0.313	2.69E+15	3.81E+1 ± 1.68E+1	3.49E+1 ± 1.54E+1	0.310
474	85.020045	-69.753024	0.24	2.81E+15	2.47E+1 ± 8.21E+0	2.58E+1 ± 8.58E+0	0.304
475	85.008182	-69.751682	0.138	1.66E+15	5.40E+0 ± 1.85E+0	3.20E+0 ± 1.09E+0	0.141
476	85.023060	-69.750575	0.192	1.60E+15	4.28E+0 ± 1.38E+0	1.73E+0 ± 5.57E-1	0.088
477	85.010088	-69.750157	0.142	6.33E+15	2.10E+1 ± 1.90E+0	1.38E+0 ± 1.24E-1	0.091
478	85.073142	-69.750278	0.155	2.01E+15	5.61E+0 ± 1.47E+0	2.24E+0 ± 5.87E-1	0.111
479	85.013114	-69.750066	0.313	5.96E+15	7.08E+1 ± 1.29E+1	7.20E+0 ± 1.31E+0	0.141
480	85.013368	-69.750044	0.322	6.68E+15	1.14E+2 ± 2.22E+1	4.03E+1 ± 7.84E+0	0.328
481	85.063340	-69.750051	0.168	4.71E+15	1.99E+1 ± 2.73E+0	2.15E-1 ± 2.95E-2	0.033
482	85.019908	-69.748947	0.177	2.09E+15	1.22E+1 ± 4.42E+0	2.04E+0 ± 7.40E-1	0.099
483	85.066341	-69.749137	0.356	2.27E+15	3.79E+1 ± 2.15E+1	8.69E+0 ± 4.94E+0	0.145
484	85.039676	-69.748468	0.308	2.01E+16	5.36E+2 ± 4.35E+1	1.36E+2 ± 1.10E+1	0.616
485	85.070241	-69.748055	0.527	2.30E+15	7.17E+1 ± 5.49E+1	5.06E+1 ± 3.87E+1	0.287
486	85.037576	-69.748111	0.283	2.97E+15	4.02E+1 ± 1.57E+1	4.10E+0 ± 1.60E+0	0.112
487	85.036946	-69.747637	0.153	3.49E+15	1.79E+1 ± 3.67E+0	9.55E+0 ± 1.95E+0	0.231
488	85.073442	-69.747680	0.236	2.53E+15	2.40E+1 ± 9.18E+0	2.06E+1 ± 7.90E+0	0.274
489	85.037344	-69.747125	0.236	7.74E+15	1.05E+2 ± 1.58E+1	2.29E+1 ± 3.43E+0	0.289
490	85.041422	-69.746918	0.198	2.15E+15	1.50E+1 ± 5.79E+0	6.66E+0 ± 2.57E+0	0.170
491	85.076408	-69.746051	0.143	2.74E+15	7.21E+0 ± 1.34E+0	2.45E-1 ± 4.55E-2	0.038
492	85.043715	-69.745098	0.202	6.12E+15	6.57E+1 ± 1.11E+1	1.73E+1 ± 2.92E+0	0.271

Continued on next page

Table D.4 – continued from previous page

Clump ID	RA	Dec	Radius [pc]	$N_{^{13}CO}$ [cm^{-2}]	Total H_2 Mass [$M_\odot$]	Virial Mass [$M_\odot$]	Linewidth [km/s]
493	85.018583	-69.742348	0.175	4.21E+15	1.88E+1 ± 2.96E+0	2.77E+0 ± 4.36E-1	0.117
494	85.017424	-69.741087	0.207	5.74E+15	5.77E+1 ± 1.00E+1	1.03E+1 ± 1.79E+0	0.207
495	85.046811	-69.739932	0.144	1.63E+15	5.38E+0 ± 1.90E+0	1.14E+0 ± 4.02E-1	0.083
496	85.062422	-69.739081	0.205	1.64E+15	7.97E+0 ± 3.36E+0	1.73E+0 ± 7.30E-1	0.085
497	85.016609	-69.738083	0.203	2.43E+15	2.13E+1 ± 8.13E+0	2.73E+0 ± 1.04E+0	0.108
498	85.016346	-69.752409	0.409	7.19E+15	2.42E+2 ± 6.15E+1	3.53E+1 ± 8.96E+0	0.272
499	85.001726	-69.751401	0.169	2.43E+15	1.01E+1 ± 2.68E+0	7.88E-1 ± 2.08E-1	0.063
500	85.008643	-69.751164	0.187	2.10E+15	1.04E+1 ± 3.48E+0	2.02E+0 ± 6.73E-1	0.096
501	85.007939	-69.750935	0.329	2.37E+15	3.26E+1 ± 1.61E+1	4.69E+1 ± 2.31E+1	0.350
502	85.061294	-69.751234	0.277	3.38E+15	4.70E+1 ± 1.63E+1	1.98E+1 ± 6.86E+0	0.248
503	85.016791	-69.748705	0.235	2.91E+15	2.03E+1 ± 5.79E+0	3.53E+0 ± 1.01E+0	0.114
504	85.069394	-69.747929	0.359	2.08E+15	3.40E+1 ± 2.09E+1	2.14E+1 ± 1.31E+1	0.226
505	85.068228	-69.747929	0.136	2.00E+15	6.98E+0 ± 2.05E+0	1.76E-1 ± 5.15E-2	0.033
506	85.069821	-69.748030	0.139	2.04E+15	6.65E+0 ± 1.85E+0	3.05E-1 ± 8.48E-2	0.043
507	85.069649	-69.747992	0.225	2.13E+15	1.65E+1 ± 6.81E+0	6.63E+0 ± 2.73E+0	0.159
508	85.069630	-69.747911	0.312	2.08E+15	2.26E+1 ± 1.12E+1	1.45E+1 ± 7.20E+0	0.200
509	85.015774	-69.746596	0.166	2.34E+15	1.36E+1 ± 4.42E+0	6.97E+0 ± 2.26E+0	0.190
510	85.022497	-69.746437	1.21	1.13E+16	2.56E+3 ± 1.07E+3	8.24E+2 ± 3.44E+2	0.765
511	85.022281	-69.746260	0.814	1.31E+16	1.72E+3 ± 4.72E+2	4.37E+2 ± 1.20E+2	0.679
512	85.023030	-69.746054	0.667	1.45E+16	1.06E+3 ± 1.97E+2	2.66E+2 ± 4.95E+1	0.586
513	85.037511	-69.746123	0.229	6.16E+15	5.20E+1 ± 7.73E+0	6.63E+0 ± 9.84E-1	0.158
514	85.022238	-69.746282	0.847	1.29E+16	1.87E+3 ± 5.52E+2	4.70E+2 ± 1.38E+2	0.691
515	85.060529	-69.740783	0.275	1.59E+15	1.30E+1 ± 7.34E+0	6.41E+0 ± 3.62E+0	0.142
516	85.013719	-69.752611	0.191	1.87E+15	1.06E+1 ± 4.23E+0	3.53E-1 ± 1.41E-1	0.040
517	85.016287	-69.752607	0.185	7.42E+15	2.88E+1 ± 2.41E+0	6.44E+0 ± 5.38E-1	0.173
518	85.058142	-69.751807	0.347	3.77E+15	7.68E+1 ± 2.90E+1	3.64E+1 ± 1.37E+1	0.301
519	85.002057	-69.751004	0.240	2.27E+15	1.31E+1 ± 4.36E+0	5.69E+0 ± 1.90E+0	0.143
520	85.002410	-69.750985	0.160	2.56E+15	7.59E+0 ± 1.61E+0	1.16E+0 ± 2.47E-1	0.079
521	85.001097	-69.751066	0.463	3.16E+15	1.21E+2 ± 7.45E+1	8.37E+1 ± 5.16E+1	0.394
522	85.064638	-69.750370	0.267	5.37E+15	5.86E+1 ± 1.13E+1	6.20E+0 ± 1.20E+0	0.141
523	84.996650	-69.750209	0.137	4.41E+15	1.39E+1 ± 1.75E+0	6.39E-1 ± 8.08E-2	0.063
524	85.064954	-69.750485	0.366	5.51E+15	9.46E+1 ± 2.24E+1	1.27E+1 ± 3.01E+0	0.173
525	85.062750	-69.749464	0.115	4.79E+15	1.31E+1 ± 1.43E+0	4.04E+0 ± 4.40E-1	0.174
526	85.017675	-69.749171	0.137	3.84E+15	1.34E+1 ± 2.05E+0	2.39E+0 ± 3.65E-1	0.122
527	85.003295	-69.748899	0.148	1.46E+15	5.09E+0 ± 2.05E+0	1.19E-1 ± 4.79E-2	0.026
528	85.073242	-69.746933	0.174	2.10E+15	9.72E+0 ± 3.13E+0	1.26E+0 ± 4.06E-1	0.079
529	85.022464	-69.746393	1.14	1.18E+16	2.16E+3 ± 7.79E+2	6.93E+2 ± 2.50E+2	0.723
530	85.022425	-69.746218	0.746	1.32E+16	1.38E+3 ± 3.36E+2	3.77E+2 ± 9.15E+1	0.659

Continued on next page

Table D.4 – continued from previous page

Clump ID	RA	Dec	Radius [pc]	$N_{^{13}CO}$ [cm^{-2}]	Total H_2 Mass [$M_\odot$]	Virial Mass [$M_\odot$]	Linewidth [km/s]
531	85.022462	-69.746405	1.16	1.15E+16	2.24E+3 ± 8.58E+2	7.22E+2 ± 2.76E+2	0.732
532	85.007938	-69.743596	0.229	1.62E+15	7.97E+0 ± 3.42E+0	9.80E-1 ± 4.21E-1	0.061
533	85.020230	-69.742810	0.204	1.16E+16	9.27E+1 ± 7.11E+0	1.16E+1 ± 8.90E-1	0.221
534	85.071561	-69.741211	0.145	2.10E+15	7.66E+0 ± 2.20E+0	8.30E+0 ± 2.38E+0	0.222
535	85.028335	-69.739816	0.158	1.84E+15	5.99E+0 ± 1.85E+0	2.48E+0 ± 7.64E-1	0.116
536	85.060891	-69.739207	0.133	2.06E+15	5.52E+0 ± 1.38E+0	8.47E-1 ± 2.12E-1	0.074
537	85.007278	-69.735800	0.167	2.48E+15	9.21E+0 ± 2.25E+0	3.78E+0 ± 9.24E-1	0.140
538	85.013128	-69.756584	0.191	1.70E+15	5.63E+0 ± 1.90E+0	8.83E-1 ± 2.98E-1	0.063
539	85.004867	-69.752992	0.133	2.62E+15	8.09E+0 ± 1.70E+0	5.46E+0 ± 1.15E+0	0.188
540	85.003289	-69.752689	0.263	3.08E+15	1.86E+1 ± 4.69E+0	3.44E+0 ± 8.64E-1	0.106
541	85.004696	-69.752380	0.251	2.05E+15	1.76E+1 ± 7.89E+0	6.98E+0 ± 3.13E+0	0.154
542	85.000149	-69.751468	0.165	2.28E+15	1.08E+1 ± 3.25E+0	8.72E-1 ± 2.62E-1	0.067
543	85.061339	-69.751350	0.163	3.13E+15	1.52E+1 ± 3.36E+0	2.81E+0 ± 6.22E-1	0.122
544	85.021937	-69.750079	0.439	3.55E+15	1.07E+2 ± 5.18E+1	8.58E+1 ± 4.17E+1	0.410
545	85.007793	-69.750806	0.183	2.61E+15	1.43E+1 ± 4.04E+0	4.96E+0 ± 1.40E+0	0.153
546	85.065598	-69.750710	0.196	5.07E+15	2.81E+1 ± 4.10E+0	2.57E+0 ± 3.75E-1	0.106
547	85.063330	-69.749997	0.161	4.02E+15	2.02E+1 ± 3.54E+0	1.88E+0 ± 3.29E-1	0.100
548	85.040908	-69.750095	0.125	1.90E+15	6.29E+0 ± 1.90E+0	1.41E+0 ± 4.26E-1	0.098
549	85.010736	-69.750087	0.239	5.26E+15	3.76E+1 ± 6.00E+0	2.83E+0 ± 4.52E-1	0.101
550	85.010180	-69.749684	0.226	6.88E+15	6.05E+1 ± 8.21E+0	1.42E+1 ± 1.93E+0	0.233
551	85.010126	-69.749703	0.232	7.85E+15	7.85E+1 ± 9.94E+0	6.66E+1 ± 8.44E+0	0.497
552	85.045121	-69.749182	0.295	8.31E+15	2.11E+2 ± 4.02E+1	3.40E+1 ± 6.49E+0	0.315
553	85.070974	-69.748359	0.229	2.00E+15	1.13E+1 ± 4.23E+0	2.33E-1 ± 8.72E-2	0.030
554	85.071823	-69.748319	0.385	2.15E+15	2.97E+1 ± 1.62E+1	1.67E+0 ± 9.10E-1	0.061
555	85.072440	-69.748301	0.244	2.46E+15	1.58E+1 ± 5.09E+0	1.09E+0 ± 3.51E-1	0.062
556	85.070109	-69.747882	0.135	1.73E+15	4.54E+0 ± 1.34E+0	1.51E+0 ± 4.46E-1	0.098
557	85.040488	-69.746050	0.152	1.58E+15	5.13E+0 ± 1.85E+0	1.69E+0 ± 6.08E-1	0.098
558	85.030098	-69.745341	0.278	6.28E+15	1.01E+2 ± 2.03E+1	3.80E+1 ± 7.64E+0	0.343
559	85.030413	-69.745169	0.163	5.85E+15	3.27E+1 ± 4.17E+0	5.05E+0 ± 6.43E-1	0.163
560	85.035156	-69.740106	0.980	6.22E+15	1.08E+3 ± 7.23E+2	3.30E+2 ± 2.20E+2	0.538
561	85.034914	-69.740168	0.898	6.31E+15	9.01E+2 ± 5.38E+2	2.63E+2 ± 1.57E+2	0.502
562	85.034788	-69.740203	0.817	6.81E+15	8.51E+2 ± 4.40E+2	2.36E+2 ± 1.22E+2	0.499
563	85.016952	-69.738323	0.198	3.06E+15	2.39E+1 ± 6.88E+0	6.33E+0 ± 1.82E+0	0.166
564	85.066529	-69.737957	0.147	2.69E+15	7.06E+0 ± 1.34E+0	1.56E+0 ± 2.96E-1	0.096
565	85.003271	-69.736566	0.179	2.01E+15	5.29E+0 ± 1.34E+0	4.47E+0 ± 1.13E+0	0.147
566	85.013685	-69.755611	0.233	2.62E+15	2.16E+1 ± 7.42E+0	1.41E+1 ± 4.84E+0	0.228
567	85.013440	-69.755698	0.408	3.00E+15	6.88E+1 ± 3.45E+1	4.11E+1 ± 2.06E+1	0.294
568	85.013560	-69.756095	0.606	3.62E+15	2.32E+2 ± 1.61E+2	2.12E+2 ± 1.48E+2	0.549

Continued on next page

Table D.4 – continued from previous page

Clump ID	RA	Dec	Radius [pc]	$N_{^{13}CO}$ [cm^{-2}]	Total H_2 Mass [$M_\odot$]	Virial Mass [$M_\odot$]	Linewidth [km/s]
569	85.013447	-69.755734	0.389	3.70E+15	1.01E+2 ± 4.46E+1	8.15E+1 ± 3.61E+1	0.425
570	85.013612	-69.756172	0.646	3.61E+15	2.59E+2 ± 1.92E+2	2.41E+2 ± 1.78E+2	0.566
571	85.016638	-69.752327	0.136	4.93E+15	1.38E+1 ± 1.47E+0	4.33E-1 ± 4.62E-2	0.052
572	85.055866	-69.752109	0.137	1.78E+15	4.68E+0 ± 1.34E+0	3.22E-1 ± 9.22E-2	0.045
573	85.058998	-69.751865	0.203	3.38E+15	1.64E+1 ± 3.36E+0	5.06E+0 ± 1.04E+0	0.147
574	85.010482	-69.750675	0.128	3.85E+15	1.28E+1 ± 1.90E+0	2.08E+0 ± 3.09E-1	0.118
575	84.997309	-69.750298	0.252	2.31E+15	1.70E+1 ± 6.29E+0	4.68E+0 ± 1.73E+0	0.127
576	85.013644	-69.750002	0.163	4.50E+15	2.08E+1 ± 3.13E+0	2.29E+0 ± 3.44E-1	0.110
577	85.066301	-69.749024	0.267	1.95E+15	1.66E+1 ± 7.81E+0	4.06E+0 ± 1.91E+0	0.114
578	85.058639	-69.748466	0.148	1.79E+15	4.70E+0 ± 1.34E+0	9.08E-1 ± 2.59E-1	0.073
579	85.033960	-69.748225	0.135	2.35E+15	8.06E+0 ± 2.00E+0	3.49E+0 ± 8.64E-1	0.149
580	85.018577	-69.747932	0.173	2.19E+15	1.09E+1 ± 3.48E+0	2.00E+0 ± 6.41E-1	0.100
581	85.022717	-69.746107	0.612	1.27E+16	6.51E+2 ± 1.16E+2	1.99E+2 ± 3.53E+1	0.528
582	85.022196	-69.746204	0.516	1.26E+16	4.47E+2 ± 6.68E+1	1.33E+2 ± 1.99E+1	0.471
583	85.021301	-69.746381	0.294	1.57E+16	3.27E+2 ± 2.99E+1	4.93E+1 ± 4.51E+0	0.380
584	85.076483	-69.746384	0.244	2.67E+15	1.54E+1 ± 4.36E+0	9.52E+0 ± 2.69E+0	0.183
585	85.030883	-69.745995	0.153	3.64E+15	1.31E+1 ± 2.15E+0	7.22E+0 ± 1.18E+0	0.201
586	85.007803	-69.743549	0.144	1.86E+15	4.98E+0 ± 1.38E+0	9.10E+0 ± 2.53E+0	0.233
587	85.020840	-69.741785	0.392	2.43E+16	1.01E+3 ± 8.38E+1	1.07E+2 ± 8.89E+0	0.484
588	85.053179	-69.742070	0.306	3.75E+15	8.08E+1 ± 3.14E+1	7.22E+1 ± 2.81E+1	0.451
589	85.024897	-69.740579	0.261	2.59E+15	3.43E+1 ± 1.52E+1	1.31E+1 ± 5.78E+0	0.208
590	85.061354	-69.739916	0.158	1.60E+15	7.70E+0 ± 3.31E+0	7.43E-1 ± 3.19E-1	0.064
591	85.061850	-69.739934	0.215	2.20E+15	1.96E+1 ± 8.37E+0	1.30E+1 ± 5.53E+0	0.228
592	85.010874	-69.756521	0.194	1.55E+15	6.64E+0 ± 2.79E+0	3.09E+0 ± 1.30E+0	0.117
593	85.013456	-69.755755	0.371	2.88E+15	5.30E+1 ± 2.48E+1	4.23E+1 ± 1.98E+1	0.313
594	85.064168	-69.750837	0.407	6.49E+15	1.68E+2 ± 4.15E+1	3.00E+1 ± 7.41E+0	0.252
595	85.064024	-69.750797	0.309	6.70E+15	1.17E+2 ± 2.29E+1	2.25E+1 ± 4.41E+0	0.250
596	85.000919	-69.751036	0.409	3.15E+15	9.66E+1 ± 5.34E+1	3.26E+1 ± 1.80E+1	0.262
597	85.000686	-69.751021	0.319	3.25E+15	5.20E+1 ± 2.01E+1	1.03E+1 ± 4.00E+0	0.167
598	84.997625	-69.750441	0.155	2.67E+15	7.16E+0 ± 1.38E+0	1.32E+0 ± 2.55E-1	0.086
599	84.996998	-69.750149	0.167	2.12E+15	7.99E+0 ± 2.30E+0	4.24E+0 ± 1.22E+0	0.148
600	85.016579	-69.748762	0.195	2.55E+15	1.38E+1 ± 3.98E+0	1.18E+0 ± 3.39E-1	0.072
601	85.069080	-69.748091	0.201	1.91E+15	1.32E+1 ± 5.71E+0	8.16E+0 ± 3.53E+0	0.187
602	85.073723	-69.747438	0.131	2.17E+15	7.95E+0 ± 2.20E+0	1.52E+0 ± 4.21E-1	0.100
603	85.064361	-69.747128	0.138	1.74E+15	6.55E+0 ± 2.30E+0	2.89E+0 ± 1.01E+0	0.134
604	85.055155	-69.740471	0.166	1.43E+15	6.71E+0 ± 3.19E+0	6.71E-1 ± 3.19E-1	0.059
605	85.038392	-69.739661	0.376	3.52E+15	6.88E+1 ± 2.72E+1	2.82E+1 ± 1.11E+1	0.254
606	85.062900	-69.739249	0.179	1.47E+15	6.64E+0 ± 3.01E+0	5.71E-1 ± 2.59E-1	0.052

Continued on next page

Table D.4 – continued from previous page

Clump ID	RA	Dec	Radius [pc]	$N_{^{13}CO}$ [cm^{-2}]	Total H_2 Mass [$M_\odot$]	Virial Mass [$M_\odot$]	Linewidth [km/s]
607	85.013887	-69.752606	0.180	3.17E+15	1.72E+1 ± 3.98E+0	1.04E+1 ± 2.40E+0	0.223
608	85.011487	-69.752386	0.184	1.60E+15	5.22E+0 ± 1.85E+0	4.43E-1 ± 1.57E-1	0.045
609	85.002754	-69.752453	0.257	2.61E+15	2.49E+1 ± 9.27E+0	8.45E+0 ± 3.14E+0	0.168
610	85.059961	-69.752233	0.185	3.24E+15	1.92E+1 ± 4.55E+0	1.66E+1 ± 3.93E+0	0.278
611	85.000974	-69.751075	0.463	2.89E+15	1.07E+2 ± 7.07E+1	3.46E+1 ± 2.28E+1	0.254
612	85.001666	-69.751015	0.273	2.43E+15	2.49E+1 ± 1.04E+1	8.13E-1 ± 3.38E-1	0.051
613	85.064041	-69.751006	0.163	5.84E+15	2.54E+1 ± 2.84E+0	3.75E+0 ± 4.21E-1	0.141
614	85.069080	-69.748082	0.167	2.04E+15	5.48E+0 ± 1.38E+0	6.03E-1 ± 1.52E-1	0.056
615	85.074539	-69.747822	0.162	1.92E+15	5.03E+0 ± 1.34E+0	6.33E-1 ± 1.68E-1	0.058
616	85.019044	-69.747711	0.170	2.61E+15	1.28E+1 ± 3.42E+0	3.47E+0 ± 9.27E-1	0.133
617	85.072136	-69.747102	0.170	1.88E+15	7.32E+0 ± 2.41E+0	1.87E+0 ± 6.15E-1	0.097
618	85.024194	-69.747140	0.408	6.99E+15	2.68E+2 ± 7.48E+1	1.95E+2 ± 5.43E+1	0.640
619	85.021345	-69.746396	0.209	1.25E+16	1.20E+2 ± 9.35E+0	9.56E+0 ± 7.47E-1	0.198
620	85.031076	-69.746395	0.159	2.69E+15	1.28E+1 ± 3.25E+0	2.04E+0 ± 5.19E-1	0.105
621	85.029626	-69.745562	0.153	3.55E+15	1.28E+1 ± 2.15E+0	5.35E-1 ± 9.00E-2	0.055
622	85.042390	-69.744275	0.266	4.54E+15	7.19E+1 ± 1.98E+1	1.24E+2 ± 3.42E+1	0.633
623	85.014843	-69.742534	0.165	1.75E+15	7.09E+0 ± 2.57E+0	4.31E+0 ± 1.56E+0	0.150
624	85.062222	-69.739953	0.161	2.11E+15	1.10E+1 ± 3.73E+0	1.53E+0 ± 5.21E-1	0.091
625	85.037997	-69.739937	0.238	3.57E+15	3.48E+1 ± 9.60E+0	1.40E+1 ± 3.85E+0	0.224
626	85.031251	-69.739835	0.257	1.91E+15	1.83E+1 ± 9.35E+0	8.28E+0 ± 4.23E+0	0.167
627	85.065929	-69.738257	0.134	2.05E+15	6.09E+0 ± 1.61E+0	1.98E+0 ± 5.25E-1	0.113
628	85.013660	-69.755964	0.205	3.19E+15	2.00E+1 ± 4.95E+0	2.61E+0 ± 6.46E-1	0.105
629	85.062728	-69.751424	0.133	2.76E+15	7.40E+0 ± 1.38E+0	1.09E+0 ± 2.03E-1	0.084
630	85.065590	-69.750969	0.199	5.02E+15	1.75E+1 ± 2.05E+0	9.10E-1 ± 1.06E-1	0.063
631	85.063970	-69.750593	0.200	5.92E+15	3.14E+1 ± 3.85E+0	2.33E-1 ± 2.86E-2	0.032
632	85.062921	-69.749324	0.155	3.12E+15	1.02E+1 ± 1.85E+0	5.91E+0 ± 1.07E+0	0.181
633	85.073732	-69.747245	0.186	1.53E+15	8.39E+0 ± 4.04E+0	2.16E+0 ± 1.04E+0	0.100
634	85.025345	-69.745570	0.286	6.71E+15	7.40E+1 ± 1.15E+1	3.96E+1 ± 6.17E+0	0.345
635	85.024956	-69.745718	0.182	7.54E+15	5.21E+1 ± 5.71E+0	2.31E+1 ± 2.53E+0	0.330
636	85.043238	-69.744829	0.145	2.63E+15	1.08E+1 ± 2.62E+0	1.04E+0 ± 2.51E-1	0.078
637	85.011407	-69.741463	0.193	1.65E+15	7.05E+0 ± 2.79E+0	5.51E-1 ± 2.18E-1	0.049
638	85.070794	-69.740755	0.237	2.03E+15	1.51E+1 ± 6.36E+0	2.75E+0 ± 1.16E+0	0.100
639	85.025817	-69.740100	0.166	1.79E+15	9.00E+0 ± 3.54E+0	7.69E-1 ± 3.03E-1	0.063
640	85.038933	-69.739308	0.207	3.34E+15	2.88E+1 ± 7.97E+0	9.40E+0 ± 2.60E+0	0.197
641	85.001021	-69.737178	0.164	2.15E+15	9.57E+0 ± 2.96E+0	1.34E+0 ± 4.12E-1	0.084
642	85.013840	-69.756416	0.436	3.16E+15	8.47E+1 ± 4.36E+1	5.34E+1 ± 2.75E+1	0.324
643	85.013709	-69.756410	0.436	3.35E+15	9.79E+1 ± 4.97E+1	5.21E+1 ± 2.64E+1	0.321
644	85.013578	-69.756068	0.594	3.56E+15	2.00E+2 ± 1.32E+2	2.09E+2 ± 1.38E+2	0.550

Continued on next page

Table D.4 – continued from previous page

Clump ID	RA	Dec	Radius [pc]	$N_{^{13}CO}$ [cm^{-2}]	Total H_2 Mass [$M_\odot$]	Virial Mass [$M_\odot$]	Linewidth [km/s]
645	85.004622	-69.752757	0.234	1.90E+15	1.46E+1 ± 6.66E+0	2.31E+0 ± 1.06E+0	0.092
646	85.005313	-69.751330	0.179	1.95E+15	5.79E+0 ± 1.61E+0	1.32E+0 ± 3.68E-1	0.080
647	85.013496	-69.749898	0.126	3.21E+15	9.89E+0 ± 1.70E+0	1.45E+0 ± 2.49E-1	0.100
648	85.009912	-69.749775	0.173	4.95E+15	1.64E+1 ± 1.90E+0	3.25E+0 ± 3.76E-1	0.127
649	85.018797	-69.747143	0.320	7.09E+15	1.51E+2 ± 3.09E+1	1.01E+2 ± 2.07E+1	0.521
650	85.018426	-69.747190	0.218	4.75E+15	3.72E+1 ± 6.88E+0	5.79E+0 ± 1.07E+0	0.151
651	85.042445	-69.747172	0.123	2.32E+15	7.96E+0 ± 2.00E+0	1.32E+0 ± 3.30E-1	0.096
652	85.018865	-69.747131	0.336	7.48E+15	1.82E+2 ± 3.78E+1	1.33E+2 ± 2.75E+1	0.583
653	85.065110	-69.747168	0.466	2.02E+15	4.88E+1 ± 3.75E+1	4.24E+1 ± 3.25E+1	0.280
654	85.064297	-69.747382	0.906	4.29E+15	5.55E+2 ± 4.63E+2	8.49E+2 ± 7.09E+2	0.898
655	85.064198	-69.747394	0.877	4.28E+15	5.22E+2 ± 4.23E+2	8.22E+2 ± 6.66E+2	0.898
656	85.074036	-69.746598	0.154	1.93E+15	8.39E+0 ± 2.84E+0	1.60E+0 ± 5.42E-1	0.095
657	85.070914	-69.746162	0.139	1.58E+15	5.87E+0 ± 2.25E+0	1.18E+0 ± 4.54E-1	0.086
658	85.043013	-69.744184	0.143	2.02E+15	7.03E+0 ± 2.05E+0	9.00E-2 ± 2.62E-2	0.023
659	85.033783	-69.740429	0.494	8.53E+15	4.31E+2 ± 1.13E+2	8.90E+1 ± 2.34E+1	0.394
660	85.033421	-69.740534	0.396	1.01E+16	3.55E+2 ± 6.50E+1	7.41E+1 ± 1.36E+1	0.401
661	85.027462	-69.740012	0.154	1.52E+15	5.29E+0 ± 2.05E+0	1.85E+0 ± 7.17E-1	0.102
662	85.023394	-69.739200	0.258	4.30E+15	6.70E+1 ± 1.94E+1	2.47E+1 ± 7.13E+0	0.287
663	85.023619	-69.739293	0.157	3.36E+15	1.48E+1 ± 2.90E+0	1.34E+0 ± 2.63E-1	0.086
664	85.025247	-69.759418	0.155	2.28E+15	6.65E+0 ± 1.56E+0	1.66E+0 ± 3.91E-1	0.096
665	85.013276	-69.755867	0.366	2.56E+15	2.95E+1 ± 1.23E+1	6.26E+0 ± 2.61E+0	0.121
666	85.045662	-69.752733	0.139	1.81E+15	4.97E+0 ± 1.43E+0	1.04E+0 ± 2.98E-1	0.080
667	85.015095	-69.751991	0.175	2.53E+15	9.69E+0 ± 2.35E+0	1.54E+0 ± 3.73E-1	0.087
668	85.002913	-69.751382	0.160	2.13E+15	1.12E+1 ± 3.79E+0	6.09E+0 ± 2.07E+0	0.181
669	85.074450	-69.747862	0.242	2.45E+15	1.85E+1 ± 6.51E+0	2.48E+0 ± 8.73E-1	0.094
670	85.074571	-69.747865	0.244	2.83E+15	2.82E+1 ± 9.94E+0	8.84E+0 ± 3.11E+0	0.177
671	85.066300	-69.747562	0.148	2.12E+15	6.55E+0 ± 1.70E+0	1.71E+0 ± 4.44E-1	0.100
672	85.016653	-69.747062	0.144	4.19E+15	1.89E+1 ± 3.01E+0	5.69E+0 ± 9.06E-1	0.184
673	85.065079	-69.747142	0.359	1.96E+15	2.22E+1 ± 1.21E+1	6.18E+0 ± 3.35E+0	0.122
674	85.063872	-69.747125	0.122	2.01E+15	6.41E+0 ± 1.80E+0	7.13E-1 ± 2.00E-1	0.071
675	85.069566	-69.746630	0.355	3.20E+15	7.04E+1 ± 3.24E+1	3.07E+1 ± 1.42E+1	0.273
676	85.069535	-69.746621	0.352	3.55E+15	8.24E+1 ± 3.51E+1	6.15E+1 ± 2.62E+1	0.388
677	85.023462	-69.746300	0.181	3.69E+15	1.58E+1 ± 2.79E+0	2.05E+0 ± 3.61E-1	0.099
678	85.013146	-69.742449	0.163	1.53E+15	5.85E+0 ± 2.35E+0	4.81E+0 ± 1.94E+0	0.159
679	85.017948	-69.741858	0.187	2.01E+15	1.24E+1 ± 4.82E+0	5.58E+0 ± 2.17E+0	0.160
680	85.032734	-69.740780	0.176	4.08E+15	2.26E+1 ± 4.10E+0	3.01E+0 ± 5.46E-1	0.121
681	85.035867	-69.739851	0.232	4.46E+15	4.89E+1 ± 1.14E+1	1.56E+1 ± 3.65E+0	0.241
682	85.066691	-69.738184	0.174	1.86E+15	8.81E+0 ± 3.25E+0	8.17E-1 ± 3.01E-1	0.064

Continued on next page

Table D.4 – continued from previous page

Clump ID	RA	Dec	Radius [pc]	$N_{^{13}CO}$ [cm^{-2}]	Total H_2 Mass [$M_\odot$]	Virial Mass [$M_\odot$]	Linewidth [km/s]
683	85.011833	-69.734732	0.193	2.10E+15	1.19E+1 ± 4.23E+0	7.18E+0 ± 2.56E+0	0.179
684	85.021279	-69.734068	0.131	1.71E+15	4.59E+0 ± 1.38E+0	3.89E+0 ± 1.17E+0	0.160
685	85.013685	-69.756866	0.187	2.03E+15	8.13E+0 ± 2.51E+0	3.79E+0 ± 1.17E+0	0.132
686	85.012954	-69.756517	0.244	2.60E+15	2.24E+1 ± 7.97E+0	5.43E+0 ± 1.93E+0	0.138
687	85.009806	-69.756295	0.191	3.57E+15	2.22E+1 ± 4.89E+0	7.86E+0 ± 1.73E+0	0.188
688	85.008215	-69.756225	0.188	2.18E+15	8.84E+0 ± 2.57E+0	1.75E+0 ± 5.09E-1	0.089
689	85.013447	-69.755825	0.288	2.31E+15	2.88E+1 ± 1.38E+1	6.74E+0 ± 3.23E+0	0.142
690	85.013235	-69.755946	0.209	2.54E+15	1.55E+1 ± 4.75E+0	2.22E+0 ± 6.79E-1	0.096
691	85.018482	-69.755445	0.160	2.05E+15	9.24E+0 ± 3.01E+0	4.71E-1 ± 1.54E-1	0.050
692	85.014871	-69.755051	0.199	1.94E+15	1.36E+1 ± 5.86E+0	8.20E+0 ± 3.53E+0	0.188
693	85.014263	-69.752534	0.233	1.86E+15	1.73E+1 ± 8.94E+0	1.28E+0 ± 6.59E-1	0.069
694	85.002410	-69.752134	0.225	2.95E+15	2.45E+1 ± 7.50E+0	2.56E+0 ± 7.85E-1	0.099
695	85.061444	-69.752095	0.149	1.80E+15	7.29E+0 ± 2.57E+0	1.69E+0 ± 5.97E-1	0.099
696	85.068477	-69.750797	0.181	1.80E+15	9.48E+0 ± 3.79E+0	3.96E+0 ± 1.58E+0	0.137
697	85.066048	-69.747316	0.165	1.90E+15	6.75E+0 ± 2.10E+0	1.59E+0 ± 4.93E-1	0.091
698	85.065142	-69.746999	0.164	2.06E+15	7.06E+0 ± 2.00E+0	5.52E-1 ± 1.56E-1	0.054
699	85.065583	-69.747155	0.280	1.92E+15	1.55E+1 ± 7.19E+0	2.25E+0 ± 1.05E+0	0.083
700	85.069265	-69.746604	0.282	3.33E+15	5.08E+1 ± 1.87E+1	2.05E+1 ± 7.56E+0	0.250
701	85.069153	-69.746674	0.179	3.04E+15	1.86E+1 ± 4.75E+0	3.00E+0 ± 7.68E-1	0.120
702	85.026347	-69.745189	0.164	5.18E+15	2.07E+1 ± 2.51E+0	1.34E+1 ± 1.63E+0	0.265
703	85.047851	-69.742818	0.252	1.86E+15	2.28E+1 ± 1.35E+1	2.68E+1 ± 1.59E+1	0.303
704	85.020175	-69.740040	0.377	8.24E+15	2.10E+2 ± 4.04E+1	3.76E+1 ± 7.24E+0	0.293
705	85.025310	-69.738086	0.737	6.77E+15	6.16E+2 ± 2.73E+2	4.13E+2 ± 1.83E+2	0.694
706	85.011480	-69.734975	0.283	3.58E+15	4.66E+1 ± 1.48E+1	6.29E+1 ± 1.99E+1	0.438
707	85.014725	-69.756307	0.243	3.27E+15	3.75E+1 ± 1.22E+1	1.65E+1 ± 5.38E+0	0.241
708	85.014663	-69.756370	0.194	3.43E+15	2.16E+1 ± 4.95E+0	9.32E+0 ± 2.14E+0	0.203
709	85.013816	-69.755612	0.145	2.17E+15	6.93E+0 ± 1.80E+0	8.93E-1 ± 2.32E-1	0.073
710	85.058455	-69.751958	0.264	1.46E+15	1.49E+1 ± 1.02E+1	2.64E+0 ± 1.81E+0	0.093
711	85.065931	-69.750895	0.291	3.48E+15	6.04E+1 ± 2.28E+1	6.86E+1 ± 2.58E+1	0.450
712	85.065469	-69.750874	0.256	2.55E+15	2.47E+1 ± 9.52E+0	2.29E+0 ± 8.79E-1	0.088
713	85.024994	-69.748589	0.158	1.99E+15	8.98E+0 ± 3.01E+0	3.95E+0 ± 1.32E+0	0.146
714	85.074282	-69.748375	0.236	2.46E+15	2.15E+1 ± 8.13E+0	4.31E+0 ± 1.63E+0	0.125
715	85.068481	-69.748163	0.149	2.59E+15	1.05E+1 ± 2.57E+0	8.88E+0 ± 2.17E+0	0.227
716	85.074859	-69.747878	0.157	1.82E+15	8.65E+0 ± 3.25E+0	1.57E-1 ± 5.90E-2	0.029
717	85.072850	-69.747377	0.359	2.32E+15	3.08E+1 ± 1.52E+1	1.15E+1 ± 5.69E+0	0.166
718	85.073673	-69.747598	0.136	1.97E+15	6.63E+0 ± 1.95E+0	9.58E-1 ± 2.81E-1	0.078
719	85.072577	-69.747287	0.248	2.60E+15	1.86E+1 ± 6.00E+0	6.46E+0 ± 2.09E+0	0.150
720	85.063615	-69.746481	0.288	3.94E+15	7.89E+1 ± 2.82E+1	5.45E+1 ± 1.95E+1	0.404

Continued on next page

Table D.4 – continued from previous page

Clump ID	RA	Dec	Radius [pc]	$N_{^{13}CO}$ [cm^{-2}]	Total H_2 Mass [$M_\odot$]	Virial Mass [$M_\odot$]	Linewidth [km/s]
721	85.076618	-69.746453	0.119	2.32E+15	6.36E+0 ± 1.43E+0	1.22E+0 ± 2.74E-1	0.094
722	85.064081	-69.747414	0.889	4.23E+15	4.39E+2 ± 3.33E+2	6.22E+2 ± 4.71E+2	0.775
723	85.042105	-69.744249	0.198	3.29E+15	2.59E+1 ± 6.96E+0	1.42E+1 ± 3.82E+0	0.248
724	85.042944	-69.742880	0.195	1.99E+15	1.44E+1 ± 6.14E+0	7.73E+0 ± 3.29E+0	0.185
725	85.023112	-69.739110	0.149	2.75E+15	9.11E+0 ± 1.90E+0	1.70E+0 ± 3.54E-1	0.099
726	85.014731	-69.757006	0.128	2.93E+15	9.72E+0 ± 1.90E+0	1.31E+1 ± 2.55E+0	0.296
727	85.014238	-69.756993	0.250	2.66E+15	2.10E+1 ± 6.96E+0	1.58E+1 ± 5.25E+0	0.234
728	85.010455	-69.750988	0.275	2.00E+15	2.75E+1 ± 1.61E+1	6.53E+0 ± 3.81E+0	0.143
729	85.018835	-69.747261	0.227	3.44E+15	2.71E+1 ± 6.96E+0	1.80E+0 ± 4.61E-1	0.082
730	85.019104	-69.747129	0.262	4.47E+15	4.97E+1 ± 1.17E+1	3.98E+1 ± 9.36E+0	0.362
731	85.063804	-69.746407	0.210	2.29E+15	1.74E+1 ± 6.59E+0	6.31E-1 ± 2.39E-1	0.051
732	85.063852	-69.746404	0.195	3.27E+15	2.67E+1 ± 7.34E+0	7.98E+0 ± 2.20E+0	0.188
733	85.027690	-69.739926	0.267	1.62E+15	5.91E+0 ± 2.20E+0	4.60E+0 ± 1.71E+0	0.122
734	85.028114	-69.739331	0.185	2.19E+15	7.14E+0 ± 1.85E+0	4.16E+0 ± 1.08E+0	0.139
735	85.020474	-69.738403	0.260	2.73E+15	3.63E+1 ± 1.53E+1	6.99E+0 ± 2.94E+0	0.152
736	85.017313	-69.733579	0.156	1.96E+15	7.50E+0 ± 2.35E+0	1.74E+0 ± 5.47E-1	0.098
737	85.012638	-69.756340	0.188	1.90E+15	9.88E+0 ± 3.73E+0	1.66E+0 ± 6.26E-1	0.087
738	85.066733	-69.750845	0.157	2.19E+15	6.26E+0 ± 1.52E+0	9.00E-1 ± 2.18E-1	0.070
739	85.066345	-69.750906	0.190	3.63E+15	2.59E+1 ± 6.00E+0	2.39E+1 ± 5.53E+0	0.329
740	85.013378	-69.750061	0.168	2.25E+15	1.25E+1 ± 4.10E+0	6.71E+0 ± 2.20E+0	0.185
741	85.015506	-69.748715	0.172	1.36E+15	4.20E+0 ± 1.70E+0	2.40E+0 ± 9.73E-1	0.110
742	85.072662	-69.747459	0.138	2.77E+15	7.74E+0 ± 1.47E+0	1.33E+0 ± 2.53E-1	0.091
743	85.071365	-69.746826	0.109	2.62E+15	7.18E+0 ± 1.43E+0	1.24E+0 ± 2.47E-1	0.099
744	85.069166	-69.746529	0.184	2.72E+15	1.65E+1 ± 4.69E+0	1.93E+0 ± 5.48E-1	0.095
745	85.070183	-69.740493	0.190	2.23E+15	1.30E+1 ± 4.42E+0	2.13E+0 ± 7.25E-1	0.098
746	85.020143	-69.739882	0.208	6.86E+15	5.72E+1 ± 7.57E+0	1.70E+1 ± 2.25E+0	0.265
747	85.020117	-69.739989	0.163	5.93E+15	2.91E+1 ± 3.42E+0	9.25E-1 ± 1.09E-1	0.070
748	85.030580	-69.738884	0.201	2.70E+15	2.45E+1 ± 8.61E+0	3.81E+1 ± 1.34E+1	0.404
749	85.066201	-69.738687	0.154	2.15E+15	6.26E+0 ± 1.56E+0	1.89E+0 ± 4.72E-1	0.103
750	85.017948	-69.737566	0.149	2.15E+15	1.04E+1 ± 3.36E+0	5.18E+0 ± 1.67E+0	0.173
751	85.006556	-69.736764	0.247	2.21E+15	1.32E+1 ± 4.62E+0	3.13E+0 ± 1.09E+0	0.105
752	85.011661	-69.735042	0.185	3.20E+15	1.43E+1 ± 2.96E+0	5.28E+0 ± 1.10E+0	0.157
753	85.004329	-69.752433	0.347	1.92E+15	2.54E+1 ± 1.52E+1	7.45E+0 ± 4.44E+0	0.136
754	85.004144	-69.752723	0.156	2.47E+15	8.90E+0 ± 2.15E+0	7.63E-1 ± 1.84E-1	0.065
755	85.059454	-69.752011	0.220	2.14E+15	1.65E+1 ± 6.73E+0	2.55E+0 ± 1.04E+0	0.100
756	85.067573	-69.751053	0.209	1.60E+15	1.11E+1 ± 5.79E+0	2.29E+0 ± 1.19E+0	0.097
757	85.001938	-69.751018	0.244	2.58E+15	2.24E+1 ± 8.05E+0	6.54E+0 ± 2.35E+0	0.152
758	85.064187	-69.747627	0.687	4.18E+15	3.51E+2 ± 2.41E+2	3.53E+2 ± 2.43E+2	0.664

Continued on next page

Table D.4 – continued from previous page

Clump ID	RA	Dec	Radius [pc]	$N_{^{13}CO}$ [cm^{-2}]	Total H_2 Mass [$M_\odot$]	Virial Mass [$M_\odot$]	Linewidth [km/s]
759	85.074908	-69.747971	0.230	2.14E+15	1.57E+1 ± 6.22E+0	3.86E+0 ± 1.53E+0	0.120
760	85.063811	-69.747656	0.568	4.32E+15	2.71E+2 ± 1.56E+2	2.51E+2 ± 1.45E+2	0.617
761	85.063381	-69.747622	0.491	4.28E+15	1.97E+2 ± 9.81E+1	1.31E+2 ± 6.53E+1	0.479
762	85.063384	-69.747645	0.478	3.86E+15	1.63E+2 ± 8.66E+1	9.87E+1 ± 5.23E+1	0.421
763	85.074788	-69.747786	0.373	2.01E+15	2.66E+1 ± 1.52E+1	8.35E+0 ± 4.76E+0	0.139
764	85.019471	-69.746959	0.188	3.75E+15	2.03E+1 ± 3.98E+0	4.73E+0 ± 9.24E-1	0.147
765	85.021621	-69.740409	0.303	5.39E+15	8.46E+1 ± 1.96E+1	4.02E+0 ± 9.30E-1	0.107
766	85.062493	-69.740059	0.206	2.18E+15	1.20E+1 ± 4.04E+0	5.91E-1 ± 1.99E-1	0.050
767	85.014186	-69.739594	0.158	1.57E+15	5.83E+0 ± 2.25E+0	1.00E+0 ± 3.87E-1	0.074
768	85.035355	-69.739157	0.216	2.08E+15	1.60E+1 ± 6.73E+0	8.73E+0 ± 3.68E+0	0.187
769	85.004516	-69.738007	0.153	1.90E+15	5.75E+0 ± 1.66E+0	1.43E+0 ± 4.11E-1	0.090
770	85.002759	-69.737925	0.145	1.76E+15	5.31E+0 ± 1.66E+0	1.25E+0 ± 3.90E-1	0.086
771	85.009193	-69.756500	0.177	2.71E+15	1.35E+1 ± 3.48E+0	8.72E-1 ± 2.26E-1	0.065
772	85.011016	-69.756039	0.163	1.83E+15	6.28E+0 ± 2.00E+0	1.23E+0 ± 3.90E-1	0.081
773	85.006403	-69.751247	0.216	1.83E+15	7.40E+0 ± 2.57E+0	7.33E+0 ± 2.54E+0	0.171
774	85.052047	-69.751032	0.193	1.65E+15	9.61E+0 ± 4.42E+0	1.52E+0 ± 7.01E-1	0.082
775	85.066215	-69.750928	0.165	3.34E+15	1.80E+1 ± 3.91E+0	2.55E+0 ± 5.56E-1	0.116
776	85.070995	-69.751017	0.115	2.65E+15	7.27E+0 ± 1.43E+0	3.16E-1 ± 6.21E-2	0.049
777	85.074282	-69.748244	0.246	2.77E+15	2.31E+1 ± 7.57E+0	1.14E+1 ± 3.74E+0	0.200
778	85.074553	-69.748000	0.422	2.43E+15	5.00E+1 ± 2.93E+1	4.91E+1 ± 2.88E+1	0.316
779	85.063587	-69.746351	0.160	2.83E+15	1.48E+1 ± 3.79E+0	1.53E+0 ± 3.91E-1	0.091
780	85.027363	-69.739925	0.217	1.90E+15	6.41E+0 ± 1.95E+0	5.39E+0 ± 1.64E+0	0.146
781	85.020195	-69.739729	0.139	5.96E+15	2.04E+1 ± 2.00E+0	9.43E-1 ± 9.22E-2	0.076
782	85.029672	-69.758584	0.168	1.89E+15	4.97E+0 ± 1.34E+0	1.23E-1 ± 3.33E-2	0.025
783	85.013288	-69.756823	0.318	2.10E+15	2.12E+1 ± 1.01E+1	7.15E+0 ± 3.41E+0	0.139
784	85.014672	-69.755612	0.267	1.90E+15	1.08E+1 ± 4.29E+0	3.10E+0 ± 1.23E+0	0.100
785	85.069268	-69.746553	0.217	1.65E+15	1.02E+1 ± 4.82E+0	2.10E+0 ± 9.91E-1	0.091
786	85.030624	-69.738859	0.160	1.95E+15	9.34E+0 ± 3.31E+0	1.79E+0 ± 6.32E-1	0.098
787	85.018651	-69.738624	0.226	2.78E+15	3.36E+1 ± 1.33E+1	2.91E+1 ± 1.15E+1	0.333
788	85.025209	-69.738319	0.234	5.40E+15	6.32E+1 ± 1.26E+1	2.72E+1 ± 5.43E+0	0.316
789	85.007634	-69.735983	0.158	1.83E+15	5.85E+0 ± 1.80E+0	1.58E+0 ± 4.85E-1	0.093
790	85.011175	-69.734810	0.143	3.78E+15	1.32E+1 ± 2.05E+0	2.69E+0 ± 4.18E-1	0.127
791	85.027985	-69.732494	0.186	1.57E+15	8.17E+0 ± 3.73E+0	1.47E+0 ± 6.69E-1	0.082
792	85.010902	-69.757210	0.162	2.41E+15	7.71E+0 ± 1.80E+0	1.87E+0 ± 4.38E-1	0.100
793	85.009952	-69.756081	0.295	2.22E+15	2.04E+1 ± 8.77E+0	6.17E+0 ± 2.65E+0	0.134
794	84.999869	-69.751434	0.137	2.37E+15	8.00E+0 ± 1.95E+0	1.00E+0 ± 2.43E-1	0.079
795	84.998849	-69.750890	0.135	2.83E+15	1.13E+1 ± 2.51E+0	1.18E+1 ± 2.61E+0	0.274
796	85.072170	-69.747454	0.170	2.15E+15	6.51E+0 ± 1.66E+0	2.52E+0 ± 6.40E-1	0.113

Continued on next page

Table D.4 – continued from previous page

Clump ID	RA	Dec	Radius [pc]	$N_{^{13}CO}$ [cm^{-2}]	Total H_2 Mass [$M_\odot$]	Virial Mass [$M_\odot$]	Linewidth [km/s]
797	85.069911	-69.740016	0.127	2.65E+15	7.12E+0 ± 1.38E+0	2.40E-1 ± 4.67E-2	0.040
798	85.019406	-69.734330	0.182	2.00E+15	6.40E+0 ± 1.80E+0	2.11E+0 ± 5.92E-1	0.100
799	85.011265	-69.756579	0.378	2.60E+15	6.43E+1 ± 3.87E+1	1.55E+1 ± 9.33E+0	0.188
800	85.067550	-69.751010	0.25	3.23E+15	4.23E+1 ± 1.49E+1	2.12E+1 ± 7.46E+0	0.270
801	85.067618	-69.751036	0.224	3.30E+15	3.68E+1 ± 1.17E+1	1.42E+1 ± 4.51E+0	0.233
802	85.067518	-69.750986	0.190	2.71E+15	1.93E+1 ± 6.00E+0	1.99E+0 ± 6.16E-1	0.095
803	85.002201	-69.750811	0.158	1.61E+15	6.25E+0 ± 2.41E+0	1.81E+0 ± 6.97E-1	0.099
804	85.019554	-69.746855	0.119	3.57E+15	1.06E+1 ± 1.61E+0	1.38E+0 ± 2.09E-1	0.100
805	85.018815	-69.738680	0.187	2.17E+15	1.48E+1 ± 5.57E+0	1.95E+0 ± 7.37E-1	0.095
806	85.032486	-69.735461	0.152	1.58E+15	4.15E+0 ± 1.34E+0	1.06E+0 ± 3.42E-1	0.078
807	85.020703	-69.733716	0.193	1.92E+15	9.34E+0 ± 3.36E+0	2.42E+0 ± 8.70E-1	0.104
808	85.011129	-69.756969	0.139	3.16E+15	8.85E+0 ± 1.47E+0	1.72E+0 ± 2.86E-1	0.103
809	85.011063	-69.756682	0.285	3.10E+15	3.03E+1 ± 9.60E+0	1.21E+1 ± 3.84E+0	0.191
810	85.000326	-69.751503	0.154	2.52E+15	1.08E+1 ± 2.79E+0	7.58E+0 ± 1.96E+0	0.206
811	85.066889	-69.740296	0.173	1.58E+15	6.12E+0 ± 2.41E+0	2.67E-1 ± 1.05E-1	0.036
812	85.013900	-69.756968	0.164	2.13E+15	6.58E+0 ± 1.70E+0	1.55E+0 ± 4.02E-1	0.090
813	85.011032	-69.756554	0.233	3.04E+15	2.05E+1 ± 5.50E+0	8.08E+0 ± 2.17E+0	0.173
814	85.014094	-69.756292	0.185	1.73E+15	1.07E+1 ± 4.82E+0	1.26E+0 ± 5.68E-1	0.077
815	84.998920	-69.750457	0.191	2.53E+15	1.30E+1 ± 3.67E+0	1.01E-1 ± 2.85E-2	0.021
816	85.070416	-69.745050	0.163	1.51E+15	4.13E+0 ± 1.43E+0	1.80E+0 ± 6.22E-1	0.097
817	85.018409	-69.738511	0.184	1.62E+15	7.98E+0 ± 3.42E+0	2.45E+0 ± 1.05E+0	0.107
818	85.024980	-69.732621	0.232	1.95E+15	1.34E+1 ± 5.64E+0	4.01E+0 ± 1.69E+0	0.122
819	85.017474	-69.755314	0.206	1.80E+15	6.68E+0 ± 2.25E+0	1.43E-1 ± 4.82E-2	0.024
820	85.065843	-69.747781	0.266	2.45E+15	3.24E+1 ± 1.52E+1	2.73E+1 ± 1.28E+1	0.297
821	85.066817	-69.746044	0.323	2.90E+15	5.90E+1 ± 2.88E+1	4.50E+1 ± 2.20E+1	0.346
822	85.064118	-69.744800	0.242	3.08E+15	3.76E+1 ± 1.34E+1	2.30E+1 ± 8.23E+0	0.286
823	85.063414	-69.747327	0.200	2.06E+15	1.36E+1 ± 5.36E+0	1.81E+0 ± 7.12E-1	0.088
824	85.067254	-69.747189	0.223	2.70E+15	2.98E+1 ± 1.15E+1	1.80E+1 ± 6.94E+0	0.263
825	85.021914	-69.733352	0.177	2.52E+15	1.08E+1 ± 2.79E+0	5.10E+0 ± 1.31E+0	0.157
826	85.046645	-69.729195	0.168	1.77E+15	5.44E+0 ± 1.70E+0	1.15E-1 ± 3.60E-2	0.024
827	85.008414	-69.756511	0.178	1.74E+15	7.04E+0 ± 2.57E+0	1.22E+0 ± 4.44E-1	0.077
828	85.037465	-69.756535	0.140	2.08E+15	6.77E+0 ± 1.85E+0	3.33E+0 ± 9.10E-1	0.143
829	85.043417	-69.755506	0.203	3.32E+15	3.06E+1 ± 8.77E+0	8.84E+0 ± 2.54E+0	0.193
830	84.999976	-69.750635	0.160	1.64E+15	6.94E+0 ± 2.73E+0	1.69E+0 ± 6.68E-1	0.096
831	85.073517	-69.749258	0.194	1.70E+15	6.11E+0 ± 2.15E+0	2.43E+0 ± 8.52E-1	0.104
832	85.066968	-69.746074	0.246	2.57E+15	2.97E+1 ± 1.23E+1	2.63E+1 ± 1.09E+1	0.303
833	85.003495	-69.738077	0.164	1.71E+15	7.03E+0 ± 2.62E+0	4.81E-1 ± 1.79E-1	0.050
834	85.009012	-69.755798	0.207	1.95E+15	7.36E+0 ± 2.30E+0	1.06E+0 ± 3.32E-1	0.066

Continued on next page

Table D.4 – continued from previous page

Clump ID	RA	Dec	Radius [pc]	$N_{^{13}CO}$ [cm^{-2}]	Total H_2 Mass [$M_\odot$]	Virial Mass [$M_\odot$]	Linewidth [km/s]
835	85.007846	-69.755483	0.186	1.93E+15	6.74E+0 ± 2.05E+0	5.40E+0 ± 1.64E+0	0.158
836	85.002322	-69.752296	0.130	2.13E+15	6.57E+0 ± 1.70E+0	2.53E+0 ± 6.55E-1	0.129
837	85.068613	-69.750748	0.292	1.76E+15	1.61E+1 ± 8.69E+0	9.08E+0 ± 4.91E+0	0.164
838	85.070597	-69.740392	0.170	2.53E+15	7.81E+0 ± 1.70E+0	1.14E+0 ± 2.50E-1	0.076
839	85.020148	-69.733461	0.161	2.38E+15	7.89E+0 ± 1.90E+0	2.25E-1 ± 5.41E-2	0.035
840	85.009273	-69.755894	0.127	1.70E+15	4.65E+0 ± 1.43E+0	6.22E-1 ± 1.91E-1	0.065
841	84.999990	-69.751139	0.175	2.26E+15	6.06E+0 ± 1.38E+0	2.50E-1 ± 5.70E-2	0.035
842	85.075293	-69.749420	0.159	2.50E+15	1.09E+1 ± 2.84E+0	5.45E+0 ± 1.43E+0	0.172
843	85.071885	-69.749190	0.167	1.63E+15	6.34E+0 ± 2.41E+0	2.74E+0 ± 1.04E+0	0.119
844	85.066150	-69.745736	0.146	1.76E+15	6.55E+0 ± 2.25E+0	1.68E+0 ± 5.76E-1	0.100
845	85.066142	-69.745492	0.197	2.25E+15	1.15E+1 ± 3.60E+0	5.53E+0 ± 1.74E+0	0.155
846	85.028279	-69.731154	0.115	2.61E+15	7.02E+0 ± 1.38E+0	5.27E+0 ± 1.04E+0	0.198
847	85.008808	-69.756511	0.130	3.27E+15	8.77E+0 ± 1.38E+0	1.50E+0 ± 2.37E-1	0.100
848	85.009175	-69.756308	0.382	2.50E+15	3.67E+1 ± 1.77E+1	1.24E+1 ± 5.99E+0	0.167
849	85.043886	-69.756306	0.175	1.56E+15	6.96E+0 ± 2.96E+0	1.86E+0 ± 7.88E-1	0.096
850	85.068070	-69.751110	0.182	2.23E+15	9.81E+0 ± 2.90E+0	9.64E+0 ± 2.85E+0	0.213
851	85.008435	-69.736221	0.147	1.93E+15	5.73E+0 ± 1.61E+0	3.00E-1 ± 8.42E-2	0.042
852	85.012137	-69.756648	0.327	2.21E+15	2.91E+1 ± 1.51E+1	4.49E+1 ± 2.32E+1	0.344
853	85.009199	-69.756172	0.134	3.44E+15	1.06E+1 ± 1.70E+0	2.87E-1 ± 4.61E-2	0.043
854	85.002696	-69.752539	0.155	5.09E+15	2.15E+1 ± 2.73E+0	7.82E-1 ± 9.94E-2	0.066
855	85.002608	-69.752482	0.184	4.18E+15	2.82E+1 ± 5.50E+0	1.94E+1 ± 3.78E+0	0.301
856	85.012168	-69.756520	0.204	1.94E+15	1.05E+1 ± 3.98E+0	1.90E+0 ± 7.15E-1	0.089
857	85.012349	-69.756543	0.219	2.36E+15	1.90E+1 ± 7.19E+0	2.02E+1 ± 7.62E+0	0.281
858	85.010108	-69.756538	0.175	2.33E+15	1.03E+1 ± 2.90E+0	2.08E+0 ± 5.88E-1	0.101
859	85.006737	-69.752411	0.141	2.12E+15	7.37E+0 ± 2.05E+0	6.37E-2 ± 1.77E-2	0.020
860	85.069988	-69.751314	0.148	2.56E+15	9.78E+0 ± 2.35E+0	1.74E+0 ± 4.19E-1	0.101
861	85.067033	-69.745875	0.168	1.89E+15	9.17E+0 ± 3.36E+0	1.94E+0 ± 7.14E-1	0.100
862	85.008592	-69.755831	0.293	2.37E+15	2.63E+1 ± 1.17E+1	6.40E+0 ± 2.84E+0	0.137
863	85.075040	-69.749045	0.145	1.70E+15	4.87E+0 ± 1.52E+0	6.09E-1 ± 1.90E-1	0.060
864	85.043148	-69.743094	0.166	2.70E+15	1.79E+1 ± 5.36E+0	1.93E+1 ± 5.78E+0	0.316
865	85.012647	-69.756576	0.138	1.87E+15	5.55E+0 ± 1.61E+0	1.63E+0 ± 4.74E-1	0.101
866	85.071823	-69.749334	0.173	2.37E+15	1.36E+1 ± 4.36E+0	1.69E+0 ± 5.41E-1	0.092
867	85.028428	-69.737124	0.194	1.44E+15	8.98E+0 ± 4.89E+0	1.96E+0 ± 1.07E+0	0.093
868	84.999985	-69.751372	0.118	2.12E+15	5.81E+0 ± 1.43E+0	9.62E-2 ± 2.36E-2	0.026
869	85.065663	-69.749177	0.207	2.49E+15	2.08E+1 ± 7.57E+0	1.22E+1 ± 4.44E+0	0.225
870	85.071236	-69.747679	0.142	1.78E+15	4.88E+0 ± 1.43E+0	1.65E+0 ± 4.83E-1	0.100
871	85.076351	-69.743901	0.129	1.94E+15	5.54E+0 ± 1.52E+0	6.27E-1 ± 1.72E-1	0.065
872	85.026121	-69.732061	0.168	2.30E+15	7.61E+0 ± 1.90E+0	9.40E-1 ± 2.34E-1	0.069

Continued on next page

APPENDIX D. 12CO AND 13CO CLUMPS IDENTIFIED USING ASTRODENDRO IN THE N159 REGION OF THE LMC

Table D.4 – continued from previous page

Clump ID	RA	Dec	Radius [pc]	$N_{^{13}CO}$ [cm^{-2}]	Total H_2 Mass [$M_\odot$]	Virial Mass [$M_\odot$]	Linewidth [km/s]
873	85.042753	-69.754963	0.166	2.01E+15	5.74E+0 ± 1.52E+0	1.51E+0 ± 4.00E-1	0.088
874	85.070241	-69.751238	0.130	2.44E+15	8.64E+0 ± 2.10E+0	1.86E-1 ± 4.50E-2	0.035
875	85.072803	-69.749417	0.229	1.66E+15	1.01E+1 ± 4.75E+0	1.19E+0 ± 5.60E-1	0.067
876	85.025612	-69.732838	0.194	2.02E+15	7.40E+0 ± 2.20E+0	6.36E+0 ± 1.89E+0	0.168
877	85.007869	-69.755725	0.220	3.12E+15	3.28E+1 ± 1.07E+1	1.99E+1 ± 6.50E+0	0.279
878	85.007915	-69.755787	0.172	3.25E+15	2.23E+1 ± 5.64E+0	5.76E+0 ± 1.46E+0	0.170
879	85.071613	-69.749648	0.254	2.36E+15	2.28E+1 ± 9.43E+0	5.11E+0 ± 2.11E+0	0.132
880	85.025432	-69.731847	0.129	1.91E+15	5.24E+0 ± 1.43E+0	1.03E+0 ± 2.80E-1	0.083
881	85.006937	-69.755933	0.151	3.93E+15	1.73E+1 ± 2.90E+0	3.69E+0 ± 6.20E-1	0.145
882	85.075511	-69.745991	0.147	1.70E+15	5.24E+0 ± 1.70E+0	1.41E-1 ± 4.59E-2	0.029
883	85.047372	-69.756053	0.130	3.10E+15	8.84E+0 ± 1.52E+0	3.10E-1 ± 5.33E-2	0.045
884	85.057571	-69.731816	0.147	3.19E+15	1.53E+1 ± 3.31E+0	1.75E-1 ± 3.79E-2	0.032
885	85.037129	-69.757456	0.140	1.94E+15	5.08E+0 ± 1.34E+0	2.07E-1 ± 5.46E-2	0.036
886	85.026680	-69.731662	0.143	1.59E+15	4.46E+0 ± 1.47E+0	1.17E+0 ± 3.88E-1	0.084
887	84.996624	-69.749989	0.121	2.67E+15	7.02E+0 ± 1.34E+0	1.15E-1 ± 2.19E-2	0.029
888	85.020635	-69.733523	0.132	1.82E+15	5.09E+0 ± 1.47E+0	2.39E-1 ± 6.91E-2	0.040
889	85.025620	-69.732452	0.156	2.21E+15	6.96E+0 ± 1.75E+0	3.62E+0 ± 9.12E-1	0.141

Column 1: The ID we give each clump. Column 4: The radius calculated from the area of the clump. Column 6: The total H_2 mass. We use a $\frac{^{13}CO(2-1)}{H_2}$ conversion factor of 3.2×10^{-7} (Fujii et al., 2014). Column 8: The measured linewidth.

Bibliography

Alencar, S. H. P., Basri, G., Hartmann, L., & Calvet, N. 2005, aap, 440, 595

Alencar, S. H. P., Johns-Krull, C. M., & Basri, G. 2001, aj, 122, 3335

Anderson, C. N., Meier, D. S., Ott, J., Hughes, A., & Wong, T. 2013, in IAU Symposium, Vol. 292, Molecular Gas, Dust, and Star Formation in Galaxies, ed. T. Wong & J. Ott, 95–95

André, P., Men'shchikov, A., Bontemps, S., et al. 2010, aap, 518, L102

Bachiller, R., Martin-Pintado, J., & Bujarrabal, V. 1990, aap, 227, 188

Ballesteros-Paredes, J., Hartmann, L. W., Vázquez-Semadeni, E., Heitsch, F., & Zamora-Avilés, M. A. 2011, mnras, 411, 65

Beltrán, M. T., Cesaroni, R., Neri, R., & Codella, C. 2011a, aap, 525, A151

—. 2011b, aap, 525, A151

Beuther, H., & Walsh, A. J. 2008, apjl, 673, L55

BIBLIOGRAPHY

Bolatto, A. D., Leroy, A. K., Rosolowsky, E., Walter, F., & Blitz, L. 2008, apj, 686, 948

Bonnell, I. A., Bate, M. R., Clarke, C. J., & Pringle, J. E. 1997, mnras, 285, 201

Bonnell, I. A., Vine, S. G., & Bate, M. R. 2004, mnras, 349, 735

Bontemps, S., Motte, F., Csengeri, T., & Schneider, N. 2010, aap, 524, A18

Bressan, A., Marigo, P., Girardi, L., et al. 2012, mnras, 427, 127

Carlson, L. R., Sewilo, M., Meixner, M., Romita, K. A., & Lawton, B. 2012, VizieR Online Data Catalog, 354, 29066

Cesaroni, R., Galli, D., Lodato, G., Walmsley, C. M., & Zhang, Q. 2007, Protostars and Planets V, 197

Cesaroni, R., Galli, D., Lodato, G., Walmsley, M., & Zhang, Q. 2006, nat, 444, 703

Chen, C.-H. R., Indebetouw, R., Chu, Y.-H., et al. 2010, apj, 721, 1206

Chen, Y., Bressan, A., Girardi, L., et al. 2015, mnras, 452, 1068

Chevance, M., Madden, S. C., Lebouteiller, V., et al. 2016, aap, 590, A36

Cohen, R. S., Dame, T. M., Garay, G., et al. 1988, apjl, 331, L95

Cooke, J., Sullivan, M., Gal-Yam, A., et al. 2012, nat, 491, 228

Crowther, P. A., Schnurr, O., Hirschi, R., et al. 2010, mnras, 408, 731

BIBLIOGRAPHY

De Buizer, J. M., Liu, M., Tan, J. C., et al. 2017, apj, 843, 33

De Marchi, G., Panagia, N., Romaniello, M., et al. 2011a, apj, 740, 11

De Marchi, G., Panagia, N., & Sabbi, E. 2011b, apj, 740, 10

De Marchi, G., Paresce, F., Panagia, N., et al. 2011c, apj, 739, 27

De Marchi, G., Panagia, N., Sabbi, E., et al. 2016, mnras, 455, 4373

Dhabal, A., Mundy, L. G., Rizzo, M., et al. 2016, in American Astronomical Society Meeting Abstracts, Vol. 227, American Astronomical Society Meeting Abstracts, 347.09

Dobbs, C. L., Pringle, J. E., & Duarte-Cabral, A. 2015, mnras, 446, 3608

D'Onghia, E., & Fox, A. J. 2016, araa, 54, 363

Dunham, M. K., Rosolowsky, E., Evans, II, N. J., Cyganowski, C., & Urquhart, J. S. 2011, apj, 741, 110

Enoch, M. L., Young, K. E., Glenn, J., et al. 2006, apj, 638, 293

Epchtein, N., Braz, M. A., & Sevre, F. 1984, aap, 140, 67

Federrath, C., & Klessen, R. S. 2012, apj, 761, 156

Fernandez, M., Ortiz, E., Eiroa, C., & Miranda, L. F. 1995, aaps, 114, 439

Fujii, K., Minamidani, T., Mizuno, N., et al. 2014, apj, 796, 123

BIBLIOGRAPHY

Fukui, Y., Kawamura, A., Minamidani, T., et al. 2008, apjs, 178, 56

Fukui, Y., Ohama, A., Hanaoka, N., et al. 2014, apj, 780, 36

Fukui, Y., Harada, R., Tokuda, K., et al. 2015, apjl, 807, L4

Furukawa, N., Dawson, J. R., Ohama, A., et al. 2009, apjl, 696, L115

Gatley, I., Becklin, E. E., Hyland, A. R., & Jones, T. J. 1981, mnras, 197, 17P

Gibson, D., Plume, R., Bergin, E., Ragan, S., & Evans, N. 2009, apj, 705, 123

Goldbaum, N. J., Krumholz, M. R., Matzner, C. D., & McKee, C. F. 2011, apj, 738, 101

Gong, Y., Fang, M., Mao, R., et al. 2017, apjl, 835, L14

Gordon, K. D., Roman-Duval, J., Bot, C., et al. 2014, apj, 797, 85

Gruendl, R. A., & Chu, Y.-H. 2009, apjs, 184, 172

Guzmán, A. E., Garay, G., Rodríguez, L. F., et al. 2014, apj, 796, 117

Heger, A., Fryer, C. L., Woosley, S. E., Langer, N., & Hartmann, D. H. 2003, apj, 591, 288

Heiderman, A., Evans, II, N. J., Allen, L. E., Huard, T., & Heyer, M. 2010, apj, 723, 1019

BIBLIOGRAPHY

Heydari-Malayeri, M., Charmandaris, V., Deharveng, L., Rosa, M. R., & Zinnecker, H. 1999, VizieR Online Data Catalog, 334

Heyer, M., Krawczyk, C., Duval, J., & Jackson, J. M. 2009, apj, 699, 1092

Heyer, M. H., & Brunt, C. M. 2004, apjl, 615, L45

Hopkins, P. F., Quataert, E., & Murray, N. 2012, mnras, 421, 3522

Hyland, A. R., & Jones, T. J. 1991, in IAU Symposium, Vol. 148, The Magellanic Clouds, ed. R. Haynes & D. Milne, 202

Indebetouw, R., Johnson, K. E., & Conti, P. 2004, aj, 128, 2206

Indebetouw, R., de Messières, G. E., Madden, S., et al. 2009, apj, 694, 84

Indebetouw, R., Brogan, C., Chen, C.-H. R., et al. 2013, apj, 774, 73

Inoue, T., & Fukui, Y. 2013, apjl, 774, L31

Israel, F. P., de Graauw, T., van de Stadt, H., & de Vries, C. P. 1986, apj, 303, 186

Israel, F. P., Johansson, L. E. B., Rubio, M., et al. 2003, aap, 406, 817

Jameson, K. E., Bolatto, A. D., Leroy, A. K., et al. 2016, apj, 825, 12

Johansson, L. E. B., Olofsson, H., Hjalmarson, A., Gredel, R., & Black, J. H. 1994, aap, 291, 89

Johansson, L. E. B., Greve, A., Booth, R. S., et al. 1998, aap, 331, 857

BIBLIOGRAPHY

Jones, O. C., Meixner, M., Sargent, B. A., et al. 2015, apj, 811, 145

Jones, T. J., Woodward, C. E., Boyer, M. L., Gehrz, R. D., & Polomski, E. 2005, apj, 620, 731

Kato, D., Nagashima, C., Nagayama, T., et al. 2007, pasj, 59, 615

Kauffmann, J., Pillai, T., & Goldsmith, P. F. 2013, apj, 779, 185

Kawamura, A., Mizuno, Y., Minamidani, T., et al. 2009, apjs, 184, 1

Kennicutt, R. C., & Evans, N. J. 2012, araa, 50, 531

Kim, S., Staveley-Smith, L., & Sault, R. J. 2001, in Astronomical Society of the Pacific Conference Series, Vol. 240, Gas and Galaxy Evolution, ed. J. E. Hibbard, M. Rupen, & J. H. van Gorkom, 435

Klassen, M., Pudritz, R. E., & Kirk, H. 2017, mnras, 465, 2254

Krumholz, M. R., McKee, C. F., & Klein, R. I. 2005, nat, 438, 332

Kwon, W., Fernández-López, M., Stephens, I. W., & Looney, L. W. 2015, apj, 814, 43

Lada, C. J. 1985, araa, 23, 267

Lada, C. J. 1987, in IAU Symposium, Vol. 115, Star Forming Regions, ed. M. Peimbert & J. Jugaku, 1–17

BIBLIOGRAPHY

Lada, C. J., Lombardi, M., & Alves, J. F. 2010, apj, 724, 687

Lada, C. J., Muench, A. A., Rathborne, J., Alves, J. F., & Lombardi, M. 2008, apj, 672, 410

Lada, E. A. 1992, apjl, 393, L25

Larson, R. B. 1981, mnras, 194, 809

Lejeune, T., & Schaerer, D. 2001, aap, 366, 538

Leroy, A. K., Bolatto, A., Gordon, K., et al. 2011, apj, 737, 12

Lopez, L. A., Krumholz, M. R., Bolatto, A. D., Prochaska, J. X., & Ramirez-Ruiz, E. 2011, apj, 731, 91

Madau, P., & Dickinson, M. 2014, araa, 52, 415

Marsh, K. A., Kirk, J. M., André, P., et al. 2016, mnras, 459, 342

Martín-Hernández, N. L., Vermeij, R., & van der Hulst, J. M. 2005, aap, 433, 205

McKee, C. F., & Zweibel, E. G. 1992, apj, 399, 551

Meixner, M., Gordon, K. D., Indebetouw, R., et al. 2006, aj, 132, 2268

Meixner, M., Panuzzo, P., Roman-Duval, J., et al. 2013, aj, 146, 62

Meynadier, F., Heydari-Malayeri, M., Deharveng, L., et al. 2004, aap, 422, 129

Mezger, P. G., & Henderson, A. P. 1967, apj, 147, 471

BIBLIOGRAPHY

Minamidani, T., Mizuno, N., Mizuno, Y., et al. 2008, apjs, 175, 485

Molinari, S., Swinyard, B., Bally, J., et al. 2010, aap, 518, L100

Nakajima, Y., Kato, D., Nagata, T., et al. 2005, aj, 129, 776

Nayak, O., Meixner, M., Fukui, Y., et al. 2018, apj, 854, 154

Nayak, O., Meixner, M., Indebetouw, R., et al. 2016, ArXiv e-prints

Nishimura, A., Tokuda, K., Kimura, K., et al. 2015, apjs, 216, 18

Ochsendorf, B. B., Meixner, M., Roman-Duval, J., Rahman, M., & Evans, II, N. J. 2017a, apj, 841, 109

Ochsendorf, B. B., Zinnecker, H., Nayak, O., et al. 2017b, Nature Astronomy, 1, 784

Oey, M. S., & Massey, P. 1995, apj, 452, 210

Onishi, T., Kawamura, A., Abe, R., et al. 1999, pasj, 51, 871

Panagia, N., Romaniello, M., Scuderi, S., & Kirshner, R. P. 2000, apj, 539, 197

Pellegrini, E. W., Baldwin, J. A., & Ferland, G. J. 2011, apj, 738, 34

Peretto, N., André, P., Könyves, V., et al. 2012, aap, 541, A63

Peretto, N., Fuller, G. A., Duarte-Cabral, A., et al. 2013, aap, 555, A112

Pillai, T., Kauffmann, J., Wyrowski, F., et al. 2011, aap, 530, A118

Podio, L., Codella, C., Gueth, F., et al. 2015, aap, 581, A85

Rathborne, J. M., Longmore, S. N., Jackson, J. M., et al. 2014, apjl, 795, L25

Reipurth, B., Pedrosa, A., & Lago, M. T. V. T. 1996, aaps, 120, 229

Riebel, D., Boyer, M. L., Srinivasan, S., et al. 2015, apj, 807, 1

Robitaille, T. P., Whitney, B. A., Indebetouw, R., & Wood, K. 2007, apjs, 169, 328

Robitaille, T. P., Whitney, B. A., Indebetouw, R., Wood, K., & Denzmore, P. 2006, apjs, 167, 256

Romaniello, M. 1998, PhD thesis, , Scuola Normale Superiore di Pisa, (1998)

Romita, K. A., Carlson, L. R., Meixner, M., et al. 2010, apj, 721, 357

Rosolowsky, E. W., Pineda, J. E., Kauffmann, J., & Goodman, A. A. 2008, apj, 679, 1338

Rubio, M., Barbá, R. H., Walborn, N. R., et al. 1998, aj, 116, 1708

Sabbi, E., Anderson, J., Lennon, D. J., et al. 2013, aj, 146, 53

Sabbi, E., Lennon, D. J., Anderson, J., et al. 2016, apjs, 222, 11

Saigo, K., Onishi, T., Nayak, O., et al. 2017, apj, 835, 108

Salpeter, E. E. 1955, apj, 121, 161

Schaefer, B. E. 2008, aj, 135, 112

BIBLIOGRAPHY

Scowen, P. A., Hunter, D. A., Hester, J. J., Shaya, E., & Wf/Pc Idt. 1993, in Bulletin of the American Astronomical Society, Vol. 25, American Astronomical Society Meeting Abstracts, 1309

Seale, J. P., Looney, L. W., Chu, Y.-H., et al. 2009, apj, 699, 150

Seale, J. P., Meixner, M., Sewiło, M., et al. 2014, aj, 148, 124

Selman, F. J., & Melnick, J. 2013, aap, 552, A94

Sewiło, M., Indebetouw, R., Charnley, S. B., et al. 2018, apjl, 853, L19

Shetty, R., Beaumont, C. N., Burton, M. G., Kelly, B. C., & Klessen, R. S. 2012, mnras, 425, 720

Shimonishi, T., Onaka, T., Kawamura, A., & Aikawa, Y. 2016, apj, 827, 72

Smartt, S. J., Eldridge, J. J., Crockett, R. M., & Maund, J. R. 2009, mnras, 395, 1409

Smith, K. W., Lewis, G. F., Bonnell, I. A., Bunclark, P. S., & Emerson, J. P. 1999, mnras, 304, 367

Smith, L. J., Norris, R. P. F., & Crowther, P. A. 2002, mnras, 337, 1309

Solomon, P. M., Rivolo, A. R., Barrett, J., & Yahil, A. 1987, apj, 319, 730

Sousa, A. P., Alencar, S. H. P., Bouvier, J., et al. 2016, aap, 586, A47

Subramanian, S., & Subramaniam, A. 2009, aap, 496, 399

Swings, J. P., & Andrillat, Y. 1979, aap, 74, 85

Tachihara, K., Toyoda, S., Onishi, T., et al. 2001, pasj, 53, 1081

Tan, J. C., Kong, S., Butler, M. J., Caselli, P., & Fontani, F. 2013, apj, 779, 96

Tan, J. C., & McKee, C. F. 2002, in Astronomical Society of the Pacific Conference Series, Vol. 267, Hot Star Workshop III: The Earliest Phases of Massive Star Birth, ed. P. Crowther, 267

Tan, J. C., & McKee, C. F. 2003, ArXiv Astrophysics e-prints

—. 2004, apj, 603, 383

Testor, G., Lemaire, J. L., Field, D., & Diana, S. 2006, aap, 453, 517

Torii, K., Enokiya, R., Sano, H., et al. 2011, apj, 738, 46

Torii, K., Hasegawa, K., Hattori, Y., et al. 2015, apj, 806, 7

Tosaki, T., Kohno, K., Harada, N., et al. 2016, ArXiv e-prints

Walborn, N. R., Barbá, R. H., & Sewiło, M. M. 2013, aj, 145, 98

Walborn, N. R., & Blades, J. C. 1987, apjl, 323, L65

Walborn, N. R., & Parker, J. W. 1992, apjl, 399, L87

Weidner, C., Bonnell, I. A., & Zinnecker, H. 2010, apj, 724, 1503

BIBLIOGRAPHY

Whitney, B. A., Sewilo, M., Indebetouw, R., et al. 2008, aj, 136, 18

Wienen, M., Wyrowski, F., Schuller, F., et al. 2012, aap, 544, A146

Williams, J. P., de Geus, E. J., & Blitz, L. 1994, apj, 428, 693

Wong, T., Hughes, A., Ott, J., et al. 2011, apjs, 197, 16

Woosley, S. E., Heger, A., & Weaver, T. A. 2002, Reviews of Modern Physics, 74, 1015

Xu, J.-L., Li, D., Zhang, C.-P., et al. 2016, apj, 819, 117

Yeh, S. C. C., Seaquist, E. R., Matzner, C. D., & Pellegrini, E. W. 2015, apj, 807, 117

Yorke, H. W., & Sonnhalter, C. 2002, apj, 569, 846

Zapata, L. A., Palau, A., Galván-Madrid, R., et al. 2015, mnras, 447, 1826

Zapata, L. A., Palau, A., Ho, P. T. P., et al. 2008, aap, 479, L25

Zaritsky, D., Harris, J., & Thompson, I. 1997, aj, 114, 1002

Zhang, Q., & Fall, S. M. 1999, apjl, 527, L81

Zinnecker, H., & Yorke, H. W. 2007, araa, 45, 481

Vita

D.1 Refereed Papers

Nayak, O., Meixner, M., Fukui, Y., et al. 2018, 'Molecular Cloud Structures and Massive Star Formation in N159,' ApJ, 831, 32

Nayak, O., Meixner, M., Indebetouw, R., et al. 2016, 'Studying Relation Between Star Formation and Molecular Clumps on Sub-parsec Scales in 30 Doradus,' ApJ, 831, 32

Ochsendorf, B., Zinnecker, H., **Nayak, O.**, Bally, J., Meixner, M., Jones, O., Indebetouw, R., Rahman, M., 2017, 'The Star Forming Complex LMC-N79 as a Future Rival to 30 Doradus', NatAs, 1E, 260

Saigo, K., Onishi, T., **Nayak, O.**, Meixner, M., Tokuda, K., Harada, R., Morioka,

VITA

Y., Sewilo, M., Indebetouw, R., Torii, K., Kawamura, A., Ohama, A., Hattori, Y., Yamamoto, H., Tachihara, K., Minamidani T., Inoue, T., Madden, S., Galametz, M., Lebouteiller, V., Chen, R., Mizuno, N., Fukui Y., 2017, 'Kinematic Structure of Molecular Gas around High-mass Star YSO, Papillon Nebula, in N159 East in the Large Magellanic Cloud', ApJ, 835, 108

Lee, M. Y., Madden, S., Lebouteiller, V., Gusdorf, A., Godard, B., Wu, R., Galametz, M., Cormier, C., Le Petit, F., Roueff, E., Bron, E., Carlson, L., Chevance, M., Fukui, Y., Galliano, G., Hony, S., Huges, A., Indebetouw, R., Israel, F., A., Kawamura, Le Bourlot, J., Lesaffre, P., Meixner, M., Muller, E., **Nayak, O.**, Onishi, T., Roman-Duval, J., Sewilo, M., 2016, 'Radiative and mechanical feedback into the molecular gas in the Large Magellanic Cloud. I. N159W', A&A, 596, A85

Fukui, Y., Harada, R., Tokuda, K., Morioka, Y., Onishi, T., Torii, K., Ohama, A., Hattori, Y., **Nayak, O.**, Meixner, M., Sewilo, M., Indebetouw, R., Kawamura, A., Saigo, K., Yamamoto, H., Tachihara, K., Minamidani, T., Inoue, T., Madden, S., Galametz, M., Lebouteiller, V., Mizuno, N., Chen, R., 2015, 'High Mass Star Formation Triggered by Collisions between CO Filaments in N159 West in the Large Magellanic Cloud', ApJ, 807, L4

D.2 Papers In Preparation

Nayak, O., Meixner, M., Indebetouw, R., et al., in prep, 'ALMA Reveals Disk Around the Most Luminous Young Stellar Object in the LMC'

Nayak, O., Meixner, M., Okada, Y., et al., in prep, 'SOFIA/GREAT Observations of H72.97-69.39: Probing the PDR Near the Most Luminous Young Stellar Object'

D.3 Talks

February 2018, 'Extreme Star Formation in the Large Magellanic Cloud', NASA Ames Weekly Colloquia (San Jose, California)

January 2018, 'Analysis of Extreme Star Formation Environments in the LMC', American Astronomical Society Meeting (Washington, D.C.)

August 2017, 'The Most Luminous YSO in the LMC', Star Formation in Different Environment (Quy Nhon, Vietnam)

October 2016, 'Multi-Wavelength Analysis of the Most Luminous Young Stellar Object in the LMC', Star-Formation and Feedback in the SOFIA Era (Asilomar, California)

VITA

June 2016, 'The Relation Between Massive Star Formation and the Structure of CO Clumps in the LMC', Space Telescope Science Institute Summer HotSci Colloquium Series (Baltimore, Maryland)

January 2016, '30 Doradus ? Relating Young Stars to the CO Molecular Gas Observed with ALMA', American Astronomical Society Meeting (Orlando, Florida)

March 2015, 'ALMA Observations of the Large Magellanic Cloud', Soul of High Mass Star Formation (Puerto Varas, Chile)

April 2013, 'Modeling of Emission of Quasar Winds', Pennsylvania State University Local Group Meeting (College Park, Pennsylvania)

February 2012, 'Geometry of Spinor Condensates with Large Spins', American Physics Society Meeting (Boston, Massachusetts)